Extraction of top-Yukawa coupling from $t\bar{t}$ cross-section in single-leptonic final state with $\sqrt{s} = 13$ TeV data from the ATLAS detector

DISSERTATION

zur Erlangung des akademischen Grades
Doctor rerum naturalium (Dr. rer. nat.)

im Fach Physik, Spezialisierung Experimentalphysik

eingereicht an der
Mathematisch-Naturwissenschaftlichen Fakultät der
Humboldt-Universität zu Berlin

von

MSc. Supriya Sinha

geboren am 26 März, 1997 in Neu Delhi

Präsidentin der Humboldt-Universität zu Berlin
Prof. Dr. Julia von Blumenthal

Dekanin der Mathematisch-Naturwissenschaftlichen Fakultät
Prof. Dr. Caren Tischendorf

Gutachter/innen:

1. PD Dr. Klaus Mönig

2. Prof. Dr. Thomas Lohse

3. Prof. Dr. Stephanie Hansmann-Menzemer

Tag der mündlichen Prüfung: 04.07.2024

Erklärung

I declare that I have completed the thesis independently using only the aids and tools specified. I have not applied for a doctor's degree in the doctoral subject elsewhere and do not hold a corresponding doctor's degree. I have taken due note of the Faculty of Mathematics and Natural Sciences PhD Regulations, published in the Official Gazette of Humboldt-Universität zu Berlin no. 42/2018 on 11/07/2018.

Berlin, 15 April 2024

Supriya Sinha

Abstract

In the Standard Model (SM) of particle physics, the interaction of fermions with the Higgs field is referred to as the Yukawa interaction, the strength of which is proportional to the mass of the fermions. The top quark, being the heaviest fermion, exhibits the largest value of the Yukawa coupling strength. Conventionally, the $pp \rightarrow t\bar{t}H$ process has been extensively used to extract the top-Yukawa coupling. However, this thesis aims to measure the ratio of the top-Yukawa coupling strength over its SM value, i.e., $Y_t = g_t/g_t^{\text{SM}}$ using differential distributions of the $t\bar{t}$ cross-section. This method has an advantage that the obtained Y_t is independent of the Higgs coupling to other particles. The analysis is conducted on the single-leptonic decay channel using $2015 - 2018$ data with a centre-of-mass energy of $\sqrt{s} = 13$ TeV from the ATLAS detector at the Large Hadron Collider (LHC), corresponding to an integrated luminosity of 140 fb^{-1}.

The presence of a virtual Higgs boson between the two top quarks modifies the $t\bar{t}$ differential cross-section. The electroweak correction, which is a function of Y_t, starts to enter the cross-section at one-loop order. The largest Y_t sensitivity is observed in the regions close to the $t\bar{t}$ production threshold energy, i.e., at low $t\bar{t}$ invariant mass ($m_{t\bar{t}}$) regions. An angular dependence is also observed on the scattering angle of the top quark in the $t\bar{t}$ rest frame, at large $m_{t\bar{t}}$ values. Events are reconstructed with at least four jets in the final state, two of them with a requirement that they originate from a B-hadron decay. An algorithm is devised to specifically reconstruct the $m_{t\bar{t}}$ for each event. A detailed statistical analysis is then conducted, taking into account all relevant backgrounds, whose contribution to the total Monte Carlo prediction is very small. A profile likelihood fit is performed on data using binned $m_{t\bar{t}}$ distributions for different Y_t values. Due to a linear dependence of the electroweak corrections on Y_t^2, the fit is performed with Y_t^2 as the parameter of interest. The analysis is dominated by systematic uncertainties, with the jet energy modelling and resolution uncertainties contributing the most to the resultant error on Y_t^2. This is followed by theoretical modelling uncertainties on the $t\bar{t}$ sample. The fit results in an expected Y_t^2 of $1.0^{+1.8}_{-1.7}$, with the observed Y_t^2 of $2.3^{+1.8}_{-1.7}$. An upper limit on Y_t at 95% confidence level is extracted using the obtained Y_t^2. An observed upper limit of 2.32 on Y_t is thus achieved, with the expected upper limit of 2.06. The resulting Y_t from this method is less precise, but complementary to the Y_t obtained from other measurement methods due to its sensitivity to a heavy Higgs sector.

Zusammenfassung

Im Standardmodell (SM) der Teilchenphysik wird die Wechselwirkung von Fermionen mit dem Higgs-Feld als Yukawa-Wechselwirkung bezeichnet, deren Stärke proportional zur Masse der Fermionen ist. Das Top-Quark, das schwerste Fermion, hat entsprechend die stärkste Yukawa Kopplung. Normalerweise wird der Prozess $pp \rightarrow t\bar{t}H$ genutzt, um die top-Yukawa-Kopplung zu messen. Diese Arbeit zielt jedoch darauf ab, das Verhältnis der Top Yukawa-Kopplung zu ihrem SM-Wert, d. h. $Y_t = g_t/g_t^{\text{SM}}$ unter Verwendung differentieller Verteilungen des $t\bar{t}$-Wirkungsquerschnitts zu messen. Diese Methode hat den Vorteil, dass das erhaltene Y_t unabhängig von der Higgs-Kopplung an andere Teilchen ist. Die Analyse wird für den einfach-leptonischen Zerfallskanal unter Verwendung der Daten auf den Jahren $2015 - 2018$ bei einer Schwerpunktsenergie von $\sqrt{s} = 13$ TeV mit dem ATLAS Detektor am Large Hadron Collider (LHC) durchgeführt, was einer integrierten Luminosität von 140 fb^{-1} entspricht.

Der Austausch eines virtuellen Higgs-Bosons zwischen den beiden Top-Quarks verändert den differentiellen Wirkungsquerschnitt der $t\bar{t}$-Produktion. Die elektroschwache Korrektur, die eine Funktion von Y_t ist, geht ab der ein-Schleifenordnung in den Wirkungsquerschnitt ein. Die größte Y_t Sensitivität liegt im Bereich nahe der Schwellenenergie der $t\bar{t}$-Produktion, d.h. in der Region mit niedriger invarianter $t\bar{t}$-Masse ($m_{t\bar{t}}$). Bei großen $m_{t\bar{t}}$-Werten wird auch eine Abhängigkeit vom Streuwinkel des Top-Quarks im $t\bar{t}$-Ruhesystem beobachtet. Es werden Ereignisse mit mindestens vier Jets im Endzustand rekonstruiert, zwei davon mit der Bedingung, dass sie aus einem B-Hadron-Zerfall stammen. Ein Algorithmus wurde entwickelt, um $m_{t\bar{t}}$ für jedes Ereignis individuell zu rekonstruieren.

Anschließend wird eine detaillierte statistische Analyse durchgeführt, bei der alle relevanten Untergründe berücksichtigt werden, deren Beitrag zur gesamten Monte-Carlo-Vorhersage allerdings sehr gering ist. Die Daten werden mit einer Profil-Likelihood-Anpassung unter Verwendung von gebinnten $m_{t\bar{t}}$-Verteilungen für verschiedene Y_t-Werte analysiert. Aufgrund der linearen Abhängigkeit der elektroschwachen Korrekturen von Y_t^2 wird die Anpassung mit Y_t^2 als dem interessierenden Parameter durchgeführt. Die Analyse wird von systematischen Unsicherheiten dominiert, wobei die Unsicherheiten in der Modellierung der Jetenergie und Auflösung am meisten zum resultierenden Fehler von Y_t^2 beitragen, gefolgt von theoretischen Modellierungsunsicherheiten für das $t\bar{t}$-Signal. Die Anpassung führt zu einem erwarteten Y_t^2 Wert von $1.0^{+1.8}_{-1.7}$, der beobachtete Wert liegt bei $2.3^{+1.8}_{-1.7}$. Anhand des erhaltenen Y_t^2 wird eine Obergrenze für Y_t mit einem Konfidenzniveau von 95% ermittelt. Die beobachtete Obergrenze liegt bei 2,32 für Y_t, während die erwartete Obergrenze bei 2,06 liegt. Das sich aus dieser Methode ergebende Y_t ist weniger präzise, aber aufgrund seiner Seinsitivität auf einen schweren Higgs-Sektor komplementär zu den mit anderen Methoden erhaltenen Y_t-Resultaten.

Acknowledgements

Contents

Introduction

"We are just a slightly advanced breed of monkeys on a minor planet orbiting a very average star. But we can understand the Universe, and that makes us something very special."

- Stephen Hawking

Since the dawn of humanity, the Universe has always been a never-ending source of curiosity and fascination, inspiring us to push the limits of our understanding. Our fascination with the Universe motivates us to seek answers to the most fundamental questions about our existence, inspiring us to perpetually expand our knowledge. Particle physics is a field of study that attempts to address this exact subject. It seeks to find answers to the fundamental questions of nature. How did the Universe begin? What is it composed of? What are the laws of nature? Can we describe nature with a universal theory?

In an attempt to find solutions to these endless sequence of questions, particle physics has evolved to a stage where many of the answers can be found in a single model, known as the Standard Model (SM) [1]. The Standard Model of particle physics encapsulates the best description of the Universe so far. It describes the fundamental particles of nature and their interactions with each other. The matter is composed of spin-half particles, known as fermions, which interact with each other through electromagnetic, weak and strong forces. These interactions are carried out by an exchange of particles known as bosons, which exhibit integer spin values. A fundamental feature of the SM is the existence of a spinless quantum field, known as the Higgs field, that pervades the Universe and provides mass to the elementary particles [2, 3]. With the discovery of the Higgs boson, the particle associated to this field, by the ATLAS [4] and CMS [5] experiments in 2012, all predicted elementary particles in the SM were observed, and the existence of the Higgs field was experimentally established. Subsequently, properties of the Higgs boson have been extensively studied, such as its production and decay modes. The understanding of the interaction of the Higgs boson with other elementary particles has also been one of the key interests. The strength of this interaction, known as the coupling strength, is related to the mass of the particle it is interacting with. The Higgs boson couples to all massive fermions proportionally to their mass and to the massive bosons in proportion to the square of their mass. Its coupling to the fermions, or the Yukawa coupling g_f, is consequently given by $g_f = \sqrt{2}m_f/v$, where m_f is the fermion mass, and $v = 246.22$ GeV [6] is the vaccum expectation value of the Higgs field. Since the top quark is the heaviest elementary particle in the SM, with a mass of $m_t = 172.5 \pm 0.7$ GeV [7], the top-Yukawa coupling is the largest

Yukawa coupling in the SM. Because the Higgs boson mass ($m_H = 125.25 \pm 0.17$ GeV [7]) is smaller than the top quark mass, the top-Yukawa coupling is the only coupling that can not be measured from Higgs decay processes.

Normally, instead of the coupling itself, the ratio of the coupling with respect to the SM value, i.e., $Y_t = g_t/g_t^{\text{SM}}$ is measured. Conventionally, the studies to estimate the Y_t value include the $t\bar{t}H$ process [8, 9], where a $t\bar{t}$ pair is produced and a Higgs boson is radiated from one of the top quarks. However, there are other channels involving virtual particles in loops. The $gg \to H$ production and the $H \to \gamma\gamma$ decay processes involve top quarks in their loops, making them additionally sensitive to new particles that may enter the loop [10]. Another process involving virtual particles is the $t\bar{t}$ production where a virtual Higgs boson can be exchanged between the two top quarks. This virtual Higgs boson modifies the total cross-section, contributing to the electroweak corrections that depends upon the square of the top-Yukawa coupling [11, 12] . This correction shows a strong Y_t sensitivity near the $t\bar{t}$ production threshold energy. It also shows a weak dependence on the scattering angle of the top quark in the $t\bar{t}$ rest frame. Consequently, Y_t can be obtained from the measurement of the $t\bar{t}$ cross-section as a function of the $t\bar{t}$ mass and the scattering angle of the top quark. Moreover, this channel is also sensitive to other new particles beyond the SM, such as the particles belonging to a heavy Higgs sector. This analysis has been performed before by the CMS collaboration in the single-leptonic channel [13] with partial Run-2 luminosity and in the dileptonic channel [14] with full Run-2 luminosity, and a precision of about 40% on Y_t measuement is achieved.

This thesis describes a measurement of the top-Yukawa coupling from the $t\bar{t}$ cross-section using the single-leptonic channel. It uses the full Run-2 data from proton-proton collisions at the Large Hadron Collider (LHC) corresponding to a centre-of-mass energy of $\sqrt{s} = 13$ TeV with an integrated luminosity of 140 fb^{-1} from the ATLAS detector. The thesis is structured as follows. Chapter 2 covers the description of the SM and the particle interactions within it. With the description of proton-proton collisions as well as the interaction between the top quark and the Higgs boson, the theoretical foundation for the analysis is laid out. In Chapter 3, the process of proton-proton collisions at the Large Hadron Collider (LHC) as well as the data collection at the ATLAS detector are explained. The components of the ATLAS detector are also discussed along with their working principles.

The predicted signal and background processes are obtained using Monte Carlo simulations, a brief overview of which is presented in Chapter 4. An outline of the steps involved in the generation of a Monte Carlo event is provided. Chapter 5 explains the reconstruction of physics objects such as leptons and jets in the event, on which selection cuts are applied as required by the analysis. A detailed description of the algorithm to reconstruct the $t\bar{t}$ invariant mass is also presented. Chapter 6 goes on to define the data and Monte Carlo simulation samples used in the analysis. It outlines the generator descriptions used to obtain these samples, and also gives an estimate of the backgrounds.

The electroweak corrections are obtained using a tool called `HATHOR`, a description of which is given in Chapter 7. The obtained corrections are analysed with respect to the di-top mass and the cosine of the scattering angle of the top quark in partonic rest frame. Finally, Chapter 8 lays out the statistical framework for data analysis and describes the corresponding systematic uncertainties. The second half of the chapter analyses the results in detail. Chapter 9 interprets the obtained results and compares them with similar previous measurements. Chapter 10 then goes on to summarise the entire thesis and concludes as the final chapter.

The Standard Model of particle physics

The understanding of nature around us is obtained through the comprehension of its elementary particles [15]. In order to study different particles of nature, one can accelerate them at high energies and collide them in a controlled environment [16]. A number of particles emerge as a result of the collision, which can be tracked and identified using specialised detectors. A dedicated analysis is then conducted to study the properties of the particles so detected. This is the basic principle behind collider experiments. Enormous amount of information has been collected over the past few decades through collider as well as non-collider experiments [7]. These led to the observations of patterns and features resulting to different theories combining the electromagnetic, weak and strong interactions. Several models incorporating these forces of nature have been formulated, the most successful of which is the Standard Model (SM) of particle physics [17, 18]. This chapter overviews the concept of the Standard Model starting from its basic structure, followed by the understanding of the forces described by it, the electroweak and strong interactions. The phenomenon of electroweak symmetry breaking and the interaction of the Higgs boson with other elementary particles of the SM is also explained. This is followed by a description of the underlying theory behind the proton-proton collision process. Since the analysis involves the top quark and the Higgs boson, the last section in this chapter highlights the theories revolving around the top quark and the Higgs boson and their interaction with each other. This chapter concludes with the description of the kinematic variables sensitive to the top-Yukawa coupling, and the effects which can alter those sensitive observables.

2.1 Structure of the Standard Model

The Standard Model [1] is a theoretical framework that categorises fundamental particles according to their intrinsic properties such as their mass, charge and spin. It establishes rules governing permissible interactions between these particles along with the estimation of their interaction rates. To the present date, the SM serves as the best representation of the understanding of elementary particles and their interactions. It does have some limitations which indicate the possibility of the existence of a more complete model which overcomes them all [19]. These shortcomings are discussed later in this chapter. While the SM has undergone rigorous experimental validation in particle-physics experiments, search continues in order to find the measurements that could reveal deviations from the SM predictions, offering insights into new physics beyond the SM [20, 21].

Figure 2.1 summarises the SM showing all the fundamental particles along with their properties. They are broadly classified into *fermions* and *bosons*. Fermions are the particles that make up the visible matter in the universe. They possess half-integer spin and follow Fermi-Dirac statistics

Standard Model of Elementary Particles

		three generations of matter (fermions)			interactions / force carriers (bosons)	
		I	II	III		
mass charge spin		≈2.2 MeV/c² ⅔ ½ **u** up	≈1.28 GeV/c² ⅔ ½ **c** charm	≈173.1 GeV/c² ⅔ ½ **t** top	0 0 1 **g** gluon	≈125.11 GeV/c² 0 0 **H** higgs
QUARKS		≈4.7 MeV/c² −⅓ ½ **d** down	≈96 MeV/c² −⅓ ½ **s** strange	≈4.18 GeV/c² −⅓ ½ **b** bottom	0 0 1 **γ** photon	
		≈0.511 MeV/c² −1 ½ **e** electron	≈105.66 MeV/c² −1 ½ **μ** muon	≈1.7768 GeV/c² −1 ½ **τ** tau	≈91.19 GeV/c² 0 1 **Z** Z boson	
LEPTONS		<1.0 eV/c² 0 ½ **νe** electron neutrino	<0.17 MeV/c² 0 ½ **νμ** muon neutrino	<18.2 MeV/c² 0 ½ **ντ** tau neutrino	≈80.360 GeV/c² ±1 1 **W** W boson	

(SCALAR BOSONS / GAUGE BOSONS / VECTOR BOSONS)

Figure 2.1: The constituent particles of the Standard Model and their properties [22]. The left portion of the chart shows the three generations of fermions, while the right portion shows the gauge bosons.

[23, 24], while the bosons have integer spins and follow Bose-Einstein statistics [25, 26]. The fermions are separated into three generations where the particles in different generations differ in their masses, but share identical properties. The model is structured in increasing order of the particle masses upon going from lower to higher generations. Each fermion has its corresponding anti-particle associated to it, which has an electric charge opposite to its associated particle.

Fermions are further categorised into leptons and quarks. Leptons, which include the charged particles: electron, muon and tau, along with their corresponding neutral leptons, the neutrinos (v), interact through the electroweak force only. The electron, muon and tau have a charge of -1, and their corresponding neutrinos do not carry any charge. The SM allows for only massless neutrinos, and since they do not possess any charge, they do not interact electromagnetically. They are known to only interact through the weak force. Quarks, on the other hand, are the particles which in addition to an electric charge, have a colour charge. This implies that the quarks have an additional ability to interact via the strong force. They also exist in three generations. The first generation comprise of the up and down quark, the second one has the charm and strange quark, and the third generation contains the top and the bottom quark. The quarks in the first row (up, charm and top quarks) have a charge of +2/3, and the ones in the second row (down, strange and bottom quarks) have a charge of -1/3. The top quark has the largest mass among all the particles in the SM.

Quarks do not exist freely in nature. They form colour-neutral bound states called hadrons (detailed in Section 2.3). The particle composed of a quark-antiquark pair is known as a meson,

while a combination of three quark-antiquarks forms a baryon. Heavier bound states with four or five quarks are known to exist, but are usually not very stable in nature [27].

The interaction between fermions is carried out by vector particles. These are the gauge bosons in the SM which possess a unit spin and serve as the force carriers or the mediators of each of the forces described by the SM. The massless gluon g, is the force carrier of the strong force. It has a colour charge by itself, but carries no electric charge. The massless photon γ, is the carrier of the electromagnetic force. It has no charge by itself, but interacts with only charged particles. The $W^{\pm}$ and the Z bosons are the heavy gauge bosons that are the mediators for weak force. The $W^{\pm}$ boson has a charge of ± 1 and a mass of ≈ 80 GeV [7], while the Z boson is neutral in charge, with a mass of ≈ 91 GeV [7]. There is a special boson in the SM called the Higgs boson, H. It is neutral in charge and is a scalar boson, i.e., it has no spin. It is the interaction with the field of this boson that the fermions in the SM obtain their masses from. In other words, the Higgs boson interacts with massive particles (detailed in Section 2.6).

The SM therefore, is able to combine the electromagnetic, weak and strong forces together to form a wholesome model that is able to explain the nature of particles. The graviational force, which is a very weak force is not yet described by this model, as it still is a challenge to combine the general theory of relativity used to define gravity with quantum theory used in the SM context [28]. This is one of the limitations of the SM, which will be highlighted again in Section 2.4. However, since the gravitational force is very weak in the scale of the SM compared to the other forces, the effect of gravity is negligible. The SM still continues to function effectively, despite of the neglection of gravity.

2.2 Electroweak interactions

These interactions refer to a unified theory of electromagnetic (QED), and weak forces. Historically, these two forces of nature were perceived to be different due to their distinct behaviour at low energies. However, Glashow [29, 30], Weinberg [31], and Salam [32] developed a theory which interprets these two interactions as distinct manifestations of the same force. Subsequent sections will provide details about these forces individually and then explain the theory of electroweak unification.

2.2.1 Quantum electrodynamics

Quantum electrodynamics (QED) is a mathematical description of interactions involving electrically charged particles through the exchange of photons. In other words, it explains the interaction of charged matter with light. It is based on an Abelian gauge theory defined by the symmetry group U(1), expressed with the help of the Dirac bi-spinor field ψ representing the free field of spin one-half particles, and the field A_{μ} which is the covariant four-potential of the electromagnetic field generated by the particle itself. A_{μ} is thus the representation of the vector field of photons. The full QED Lagrangian is expressed as follows [33]:

$$\mathcal{L}_{\text{QED}} = \bar{\psi}(i\displaystyle{\not}\partial - m)\psi - \frac{1}{4}F_{\mu\nu}F^{\mu\nu} + q\bar{\psi}\gamma^{\mu}\psi A_{\mu} \tag{2.1}$$

where γ^μ are the Dirac gamma matrices, $\slashed{\partial} = \gamma^\mu \partial_\mu$ is defined according to Feynman's slash notation [1], m is the mass of the particle, and $F_{\mu\nu} = \partial_\mu A_\nu - \partial_\nu A_\mu$ is the electromagnetic field tensor. The parameter q in the last term of the equation represents the electric charge which is related to the fine structure constant as $\alpha = e^2/4\pi \approx 1/137$ [34, 35] (considering unit charge e). This is a significant number that represents the strength of the interaction. The existence of this last term by itself is a direct consequence of the local gauge invariance requirement of the gauge group.

2.2.2 Weak interactions

Formulated in 1934 by Enrico Fermi [36], the theory of weak interactions stood out to explain the beta decay process in an elegant way. He interpreted the beta decay process where a neutron transforms into a proton as a point-like interaction between the fermions. Through this interaction, the particle could change its flavour, eg., a d-quark could transform to a u-quark. The strength of this interaction was denoted by $G_F \approx 1.16 \times 10^{-5}$ GeV^{-2} [37] known as the Fermi constant. However, the obtained cross-section was found to be inconsistent due to its divergent behaviour at high energies [38].

The discovery of parity violation in weak interactions in the famous Wu experiment [39] in 1957 served as a big milestone towards the understanding of weak interactions. The Wu experiment studied the beta decay of Cobalt nuclei polarised by an external magnetic field as follows:

$$^{60}Co \rightarrow \, ^{60}Ni^* + e^- + \bar{\nu}_e \tag{2.2}$$

If the parity were to be conserved, the electrons emitted would have no preferred direction relative to the spin of the nucleus. However, it was observed that more electrons emitted in the direction opposite to the direction of the magnetic field, i.e., the spin projection of the electron prefered the direction opposite to the direction of its momentum. It was therefore noted that the left-handed[2] leptons and the right-handed antileptons are preferred over the right-handed (RH) leptons and the left-handed (LH) antileptons. These observations gave rise to the V-A [3] theory of weak interactions where the interaction is considered to be a linear combination of vector and axial-vector currents ensuring that certain processes involving weak interactions do not exhibit symmetry under parity transformations.

Further developments and modifications of this model gave rise to a more complete renormalisable theory wherein instead of a point-like interaction, heavy bosons act as mediators, similar to the photons acting as mediators in a QED process. Eventually being replaced by a more comprehensive electroweak theory, Fermi's point-like interaction and the V-A theory [40, 41] laid the foundation of the understanding of weak forces.

---

[1] Feynman's slash notation is a convenient way of expressing the product of the gamma matrices and a covariant four vector such that $\slashed{A} \overset{\text{def}}{=} \gamma^1 A_1 + \gamma^2 A_2 + \gamma^3 A_3 + \gamma^4 A_4$. Using Einstein summation notation, it can be expressed as $\slashed{A} \overset{\text{def}}{=} \gamma^\mu A_\mu$

[2] Handedness: Left and right handedness arise from the concept of helicity and chirality. A particle is right (left)-handed if its helicity is positive (negative), that is when the direction of its spin is the same (opposite) as the direction of its motion.

[3] V-A: *Vector − Axial-vector*
Vector quantity: changes sign when rotated by 180°; Axial-vector quantity: same behaviour as a vector, but opposite sign to the vector under parity transformation.

2.2.3 Electroweak unification

Electroweak interaction is a combined description of two fundamental forces, namely the electromagnetic and the weak force. Sheldon Glashow [29, 30], Steven Weinberg [31] and Abdus Salam [32] formulated a theory known as the GWS theory explaining that the weak and the electromagnetic interactions are manifestations of a single force. The challenge in this unification is to accomodate both the parity conserving electromagnetic current as well as the weak charged current exhibiting maximum parity violation. Therefore, the SM of electroweak interactions is based on the gauge group $SU(2)_L \otimes U(1)_Y$, where the left and right handed components are treated differently. Since the generators of $SU(2)$ gauge transformation are 2×2 Pauli spin-matrices, the wavefunction must be written in terms of two components, i.e., a weak isospin doublet analogous to the definition of isospin. The left-handed components of the fermion field (eg. for electrons: $v_e^L = \frac{1}{2}(1 - \gamma_5)v_e$ and $e^L = \frac{1}{2}(1 - \gamma_5)e$), are expressed as $SU(2)$ doublets taking this form:

$$\begin{pmatrix} v_e \\ e \end{pmatrix}_L, \begin{pmatrix} v_\mu \\ \mu \end{pmatrix}_L, \begin{pmatrix} v_\tau \\ \tau \end{pmatrix}_L \tag{2.3}$$

On the other hand, since the observed form of weak charged-current interaction couples only to the LH particles and RH antiparticles, the RH particles and LH antiparticles are placed in weak isospin singlets such that they are unaffected by $SU(2)$ local gauge transformation. Therefore, the RH fields (eg. for electrons: $v_e^R = \frac{1}{2}(1 + \gamma_5)v_e$ and $e^R = \frac{1}{2}(1 + \gamma_5)e$) associated with weak isospin singlets are written as $(l)_R$[4]. It should be noted here that the neutrinos in the SM are treated to be massless and there are in principle, no concrete evidences for SM RH neutrino interactions.

However, for quarks, the quantum state for free propagation differs from their state while participating in weak interactions, i.e., the mass eigenstates of the quarks differ from their weak eigenstates. The relationship among them is described by the Cabibbo-Kobayashi-Maskawa (CKM) matrix, which is a 3×3 unitary matrix [42]:

$$\begin{pmatrix} d' \\ s' \\ b' \end{pmatrix} = \begin{pmatrix} V_{ud} & V_{us} & V_{ub} \\ V_{cd} & V_{cs} & V_{cb} \\ V_{td} & V_{ts} & V_{tb} \end{pmatrix} \begin{pmatrix} d \\ s \\ b \end{pmatrix} \tag{2.4}$$

where the weak eigenstates are represented by d', s' and b', and the mass eigenstates are represented by d, s and b. The CKM matrix describes the probability of a transition from a quark of flavour i to another quark of flavour j, which turns out to be proportional to $|V_{ij}|^2$. This matrix can be described fully if four independent parameters are known. The most widely used parameterisation involves three rotation angles[5] and one CP-violating[6] complex phase [43].

The LH weak isospin doublets for the case of quarks, therefore takes this form incorporating

---

[4] $(l)_R$ represents the RH isospin singlet for leptons:
$(e)_R, (\mu)_R, (\tau)_R, (v_e)_R, (v_\mu)_R, (v_\tau)_R$
[5] also called as mixing angles
[6] CP violation: CP violation is a violation of CP-symmetry, which is a combination is charge (C) and parity (P) symmetry. The laws of physics should be the same if a particle is interchanged with its antiparticle (C-symmetry) along with its spatial coordinates inverted (P-symmetry).

the weak eigenstates d', s' and b':

$$\begin{pmatrix} u \\ d' \end{pmatrix}_L, \begin{pmatrix} c \\ s' \end{pmatrix}_L, \begin{pmatrix} t \\ b' \end{pmatrix}_L \tag{2.5}$$

while the RH singlets are written as $(q)_R$[7].

Therefore, the Lagrangian takes the form:

$$\mathcal{L}_{\text{EW}} = \bar{\psi}_L i \not{D}_\mu \psi_L + \bar{\psi}_R i \not{D}_\mu \psi_R \tag{2.6}$$

where the LH doublets and RH singlets are represented by ψ_L and ψ_R, respectively. Here, the requirement of local gauge invariance on $SU(2)$ symmetry introduces a Yang-Mills field $W^j (j = 1, 2, 3)$ with a coupling factor g. Another gauge invariance requirement on $U(1)$ gauge symmetry gives rise to an additional field B along with a coupling g' associated to the weak hypercharge Y. The resultant covariant derivative takes the form:

$$D_\mu = \partial_\mu - i \frac{g'}{2} Y_W B_\mu - i g W^j_\mu T_j \quad j = 1, 2, 3 \tag{2.7}$$

where Y_W represents the weak hypercharge and it is so defined such that it evaluates to $Y_W = 2(Q - I^3_W)$, wherein Q is the electromagnetic charge, and I^3_W is the third component of weak isospin. For the LH electron and electron neutrino, $I^3_W = -1/2$, and $I^3_W = +1/2$ respectively. And for the RH states, $I^3_W = 0$, implying that for the RH neutrinos (i.e., $Q = 0$), the hypercharge value is zero. In the SM, the RH neutrinos do not exist.

The T_j in Equation 2.7 are the three generators of the $SU(2)$ group which can be written in terms of the Pauli spin matrices as $T_j = \frac{1}{2}\sigma_j$ [44] and the W^j corresponds to the gauge fields associated with three gauge bosons W^1, W^2, W^3. The first two components of this field can be associated to the W bosons as:

$$W^\pm_\mu = \frac{1}{\sqrt{2}}(W^1_\mu \mp i W^2_\mu) \tag{2.8}$$

The remaining fields W^3_μ and B_μ individually do not have any direct physical interpretation. In fact, with their appropriate linear combinations, physical fields can be obtained. This can be achieved by performing a rotation of an angle θ_W, known as the Weinberg angle or the weak mixing angle [45, 46]. Consider the orthogonal transformation:

$$\begin{aligned} A_\mu &= \sin\theta_W W^3_\mu + \cos\theta_W B_\mu \\ Z_\mu &= \cos\theta_W W^3_\mu - \sin\theta_W B_\mu \end{aligned} \tag{2.9}$$

where the newly introduced field A_μ is required to have properties of the electromagnetic field and can be identified with a photon field. The photon exhibits equal couplings to both the left and right handed fermions, with a strength equivalent to the electric charge. Z_μ in the equation represents a new neutral vector field. The Weinberg angle relates the coupling constants of the two fields as: $e = g \sin\theta_W = g' \cos\theta_W$. Hence the couplings of the weak and electromagnetic interactions are related to each other in the GWS model of electroweak unification.

With the introduction of new gauge fields, the Lagrangian requires additional terms to

---

[7] $(q)_R$ represents the RH isospin singlet for quarks: $(u)_R, (c)_R, (t)_R, (d)_R, (s)_R, (b)_R$

incorporate the interaction with each other. Considering gauge invariance and renormalisability, the gauge term in the Lagrangian takes the form [47]:

$$\mathcal{L}_{\text{gauge}} = -\frac{1}{4} B_{\mu\nu} B^{\mu\nu} - \frac{1}{4} W^a_{\mu\nu} W^{\mu\nu}_a \tag{2.10}$$

where

$$
\begin{aligned}
B_{\mu\nu} &= \partial_\mu B_\nu - \partial_\nu B_\mu \\
W^a_{\mu\nu} &= \partial_\mu W^a_\nu - \partial_\nu W^a_\mu + g\epsilon^{abc} W^b_\mu W^c_\nu
\end{aligned}
\tag{2.11}
$$

where ϵ^{abc} is the three dimensional Levi-Civita tensor (totally antisymmetric) describing the commutative relationship among the generators T^a of the $SU(2)$ group, $[T^a, T^b] = i\epsilon^{abc} T^c$. Since the generators of this group do not commute, this is a non-Abelian group, implying that the gauge bosons have a possibility to self-interact, which can be seen from the $W^b_\mu W^c_\nu$ term in the equation.

It is to be noted that the gauge symmetry of the $SU(2)_L \otimes U(1)_Y$ group does not allow any mass terms for the $W^\pm$ and Z bosons. However, these bosons are known to be massive, indicating that the current theory of electroweak interaction is incomplete. The solution to this problem lies in the phenomenon of spontaneous breaking of electroweak symmetry, as explained in the following section.

2.2.4 Spontaneous symmetry breaking

The bosons associated with the electroweak interaction, i.e., the W as well as the Z boson have a finite mass. In the SM, their mass terms are introduced via a spontaneous symmetry breaking mechanism without disrupting its unitarity and renormalisability. A symmetry is said to be spontaneously broken when the vacuum state is not invariant under its symmetry group. Formulated independently by Brout and Englert[48]; Higgs[49]; and Guralnik, Hagen, and Kibble [50] in 1964, this phenomenon is based on the addition of a quantum field leading to spontaneous symmetry breaking during interactions. Hence a new complex scalar doublet field is introduced as follows:

$$\Phi = \begin{pmatrix} \phi^+ \\ \phi^0 \end{pmatrix} \tag{2.12}$$

This scalar doublet field has four degrees of freedom. The Higgs Lagrangian is defined as:

$$\mathcal{L}_{\text{Higgs}} = (D_\mu \Phi)^\dagger (D^\mu \Phi) - V(\Phi) \tag{2.13}$$

where the D_μ is the same covariant derivative that is used in the Lagrangian definition of $SU(2)_L \otimes U(1)_Y$ from Equation 2.7 of electroweak interaction and $V(\Phi)$ equals:

$$V(\Phi) = \mu^2 \Phi^\dagger \Phi + \lambda(\Phi^\dagger \Phi)^2, \quad \lambda > 0, \mu^2 < 0 \tag{2.14}$$

A degenerate minimum of the Higgs potential is thus obtained when $V(\Phi) = 0$, i.e., $v = \sqrt{-\mu^2/\lambda}$, which is known as the vacuum expectation value (VEV) of the Higgs field. These ground states are related to each other by gauge transformations such that a change in the phase of the complex field Φ does not affect its modulus. When the system selects one of the minimum

configurations, it no longer stays symmetric under the gauge symmetry. Thus the symmetry is said to be spontaneously broken. However, the Lagrangian still maintains its gauge invariance. With symmetry breaking, Φ can be expanded around the minimum by choosing an appropriate gauge to obtain only real scalar field as:

$$\Phi(x) = \begin{pmatrix} 0 \\ \frac{1}{\sqrt{2}}[v + h(x)] \end{pmatrix} \tag{2.15}$$

Here, the field $h(x)$ corresponds to the Higgs field, which is indeed a physical field. The remaining three degrees of freedom get used up by the massive $W^{\pm}$ and Z^0 bosons, giving them the longitudinal degrees of freedom. This phenomenon is known as the Higgs mechanism. The vacuum state thus chosen corresponds to the VEV such that $\Phi_0 = \frac{1}{\sqrt{2}} \begin{pmatrix} 0 \\ v \end{pmatrix}$. The resultant potential $V(\Phi)$ therefore contains the term:

$$\frac{1}{2}(2\lambda v^2)h^2 + \lambda v h^3 + \frac{\lambda}{4}h^4 \tag{2.16}$$

pointing out that the scalar field h gets a mass of $m_H^2 = 2\lambda v^2$. There are also cubic and quartic terms indicating cubic and quartic self couplings of the Higgs boson. Thus the gauge sector is described by just four parameters, the gauge couplings g and g', and the two free parameters μ and λ of the Higgs potential. The full Lagrangian therefore becomes [51]:

$$
\begin{aligned}
\mathcal{L}_{\text{Higgs}} = {} & \frac{1}{2}\partial_\mu h \partial^\mu h - \frac{1}{2}m_H^2 h^2 - \lambda v h^3 - \frac{\lambda}{4}h^4 && \left.\right\} \text{massive } h \text{ scalar, } h \text{ self-interactions} \\
& + \frac{g^2}{8}(h^2 + 2hv)\left[\frac{1}{\cos^2\theta_W}Z_\mu Z^\mu + 2W_\mu^+ W^{-\mu}\right] && \left.\right\} h, W^{\pm}, Z \text{ interactions} \\
& + \left(\frac{gv}{2}\right)^2 W_\mu^+ W^{-\mu} + \frac{1}{2}\frac{(g^2 + g'^2)v^2}{4}Z_\mu Z^\mu && \left.\right\} \text{massive } W^{\pm}, Z
\end{aligned}
\tag{2.17}
$$

Thus, the masses acquired by the $W^{\pm}$ and Z^0 gauge bosons are:

$$m_W^2 = \frac{g^2 v^2}{4}, \quad m_Z^2 = \frac{(g^2 + g'^2)v^2}{4} = \frac{m_W^2}{\cos^2\theta_W} \tag{2.18}$$

Using this relation and the measured values of m_W and g, the VEV of the Higgs field is found to be $v = 246$ GeV. Discovery of the Higgs boson in 2012 by the ATLAS [52] and the CMS [53] collaborations at CERN approximated the mass of the SM Higgs boson to be 125 GeV. This marked a huge achievement in the particle physics community as it confirms the theory of electroweak symmetry breaking and the existence of the Higgs field.

2.2.5 Yukawa coupling

So far, the defined Higgs Lagrangian does not contain any term that relates to the mass of the fermions. A direct mass term of the form:

$$m_f \bar{\psi} \psi = m_f (\bar{\psi}_R \psi_L + \bar{\psi}_L \psi_R) \tag{2.19}$$

breaks the $SU(2)_L \otimes U(1)_Y$ gauge symmetry due to different transformation properties of the left- and right- handed particle states. Hence, a term of this type can not be included in the SM Lagrangian directly, and must be introduced in a gauge invariant manner. Representing the LH fermions of the $SU(2)$ doublet as L, and the RH fermions of the $SU(2)$ singlets as R, the combination $\bar{L}\phi$ turns out to be invariant under $SU(2)_L$ gauge transformation. Combining with a RH singlet, $\bar{L}\phi R$, it becomes invariant under $SU(2)_L \otimes U(1)_Y$ gauge transformations. Hence a term of the form $-g_f(\bar{L}\phi R + \bar{R}\phi^\dagger L)$ can be added to the SM Lagrangian. Considering only the electron doublet for simplicity, the Lagrangian takes the form [38]:

$$\mathcal{L}_e = -\frac{g_e}{\sqrt{2}} v (\bar{e}_L e_R + \bar{e}_R e_L) - \frac{g_e}{\sqrt{2}} h (\bar{e}_L e_R + \bar{e}_R e_L) \tag{2.20}$$

The first term here now fulfils the requirement for lepton masses in a gauge invariant form. The coupling factor g_e is called the ***Yukawa coupling*** and is expressed as: $g_e = \sqrt{2}\frac{m_e}{v}$. Therefore, this Yukawa coupling g_e signifies the strength of the interaction of electrons with the Higgs field, and is found to be proportional to the mass of the electron. The Lagrangian can now be written as:

$$\mathcal{L}_e = -m_e \bar{e}e - \frac{m_e}{v} \bar{e}e h \tag{2.21}$$

where the first term represents the coupling of the electron to the Higgs field giving mass to the electron, while the second term represents the coupling between the electron and the Higgs boson itself.

Similarly, massive quarks can be introduced into the Lagrangian. Considering u-quark for simplicity, the Lagrangian corresponds to:

$$\mathcal{L}_u = -m_u \bar{u}u - \frac{m_u}{v} \bar{u}u h \tag{2.22}$$

Hence, the general expression for the Yukawa coupling for fermions become: $g_f = \sqrt{2}\frac{m_f}{v}$. Considering the heaviest quark, which is the top quark with mass $m_t \approx 173$ GeV, one obtains the largest value of the Yukawa coupling g_t, which turns out to be unity. The later chapters focus on the measurement of the ratio of the top-quark Yukawa coupling over its SM value, represented by Y_t, which is equivalent to the ratio g_t/g_t^{SM}.

2.3 Strong interactions

The theory of strong interactions is given by the domain of particle physics called quantum chromodynamics (QCD). It is a non-Abelian gauge theory based on a non-Abelian gauge group $SU(N_C)$ where N_C is the number of colours, which are three in nature, called as *red, blue* and *green*. This non-Abelian structure allows for the massless gluons, which are the mediators of strong interactions, to interact among themselves, which in QED was not seen (photons do not

self-interact). The QCD Lagrangian is defined by [54]:

$$\mathcal{L}_{\text{QCD}} = \sum_{j,k=1}^{N_C} \bar{q}_f^j(x)(i\slashed{D}_{jk} - m_f)q_f^k(x) - \frac{1}{4}G_{\mu\nu}^a G^{a,\mu\nu} \tag{2.23}$$

where $q_f^j(x)$ is the quark field indexed by j going from 1 to 3 representing a summation over all quark colours. The subscript f corresponds to the flavour of the quark. m_f is the mass of the quark of flavour f. The gauge covariant derivative D_{jk}^μ is defined as:

$$D_{jk}^\mu = \delta_{jk}\partial^\mu + ig_s T_{jk}^a A_a^\mu \tag{2.24}$$

where g_s is the coupling constant for strong interactions. T^a are the generators of the $SU(3)$ gauge group where a ranges from 1 to $N_C^2 - 1 = 8$. These matrices are Hermitian and traceless and are related to the Gell-Mann matrices λ^a as $T^a = \lambda^a/2$ [55]. The commutation relation among the generators follow $[T^a, T^b] = if^{abc}T^c$ where f^{abc} are the fully antisymmetric structure constants of the $SU(3)_C$ group. A_a^μ in the equation are coloured vector fields known as gluon fields.

$G_{\mu\nu}^a$ in Equation 2.23 are the non-Abelian field strength tensor given by:

$$G_{\mu\nu}^a = \partial_\mu A_\nu^a - \partial_\nu A_\mu^a - g_s f^{abc} A_\mu^b A_\nu^c \tag{2.25}$$

Due to the fact that the generators of this $SU(3)$ group do not commute, QCD becomes a non-Abelian gauge theory. And as a consequence, the last term appears in the above equation giving rise to gluon self-interactions. This term therefore allows for the presence of cubic and quartic gluon vertices.

To recall, in the SM, quarks come in 6 flavours namely u, d, c, s, t and b. However, experimental observations so far have been unable to directly observe them freely[8]. Instead, they are known to form pairs creating a meson or a baryon. This observation is explained by a concept called *colour confinement*, which states that coloured objects are always restricted to colour singlet states and that no object with non-zero colour charge can exist as independent particles. The theory of colour confinement is strongly supported by experimental observations.

Another term is widely used in the context of strong interactions, which is called as the strong coupling constant α_s, the same name as used for g_s before. They are related to each other as $\alpha_s = g_s^2/4\pi$. This is actually not a constant, rather at leading order in perturbative expansion, it follows the relation:

$$\alpha_s(Q^2) = \frac{1}{b_0 \log\left(Q^2/\Lambda_{QCD}^2\right)}, \, b_0 = \frac{11N_C - 2N_f}{12\pi} \tag{2.26}$$

where Q^2 is the energy scale, and Λ_{QCD} represents an energy scale below which non-perturbative effects begin to dominate ($\Lambda_{QCD} \approx 250$ MeV.). This is known as the running of the coupling in QCD and is closely related to the concept of renormalisation. $N_C = 3$ is the number of colour charges, and N_f is the number of quark flavours. Hence, α_s decreases with an increase in energy, which can also be seen in Figure 2.2.

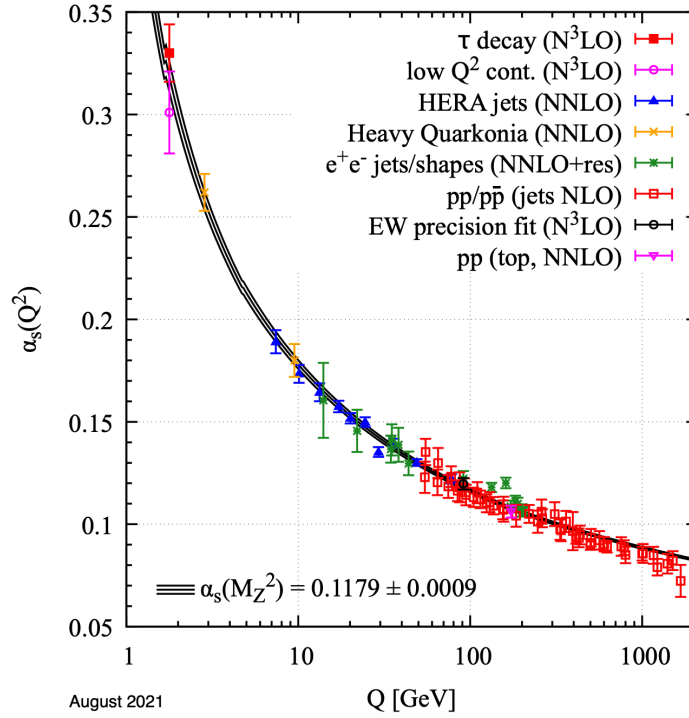[8] Top quark is special in this regard due to its large mass. It is not observed to form stable bound states.

Figure 2.2: Experimental measurements of the strong coupling α_s is shown in this plot as a function of energy Q. The respective degree of QCD perturbation theory used in the extraction of α_s is indicated in brackets (NLO: next-to-leading order; NNLO: next-to-next-to-leading order; NNLO+res.: NNLO matched to a resummed calculation; N3LO: next-to-NNLO) [7]

For large energy values, i.e., $Q^2 \to \infty$, α_s gets smaller, the coupling weakens up and the particles start to move freely in space. This is known as *asymptotic freedom* and perturbative QCD best describes the physics for this scenario. This is depicted in Figure 2.2 in the high Q region of the plot, where the α_s is small.

At low energy scale, i.e., $Q^2 \to 0$, α_s increases, and the coupling gets significantly stronger. Hence, it does not allow for free particles to exist. This phenomenon is called as *quark confinement*, and only bound states of quarks can be observed in this case. The large α_s values do not allow for perturbative expansions. For this non-perturbative regime, computational techniques of lattice QCD are used, involving intensive calculations. This can be observed in Figure 2.2 at low Q values where α_s starts to diverge.

2.3.1 Probing the proton structure

In 1969, to better understand the structure of hadrons at high energies, Feynman put forth the concept of the parton model [56]. For the scattering of an electron with a proton, this model interpreted the components of protons that got scattered by the incident electron as point-like constituents called *partons*.

The scattering process of an electron with a proton can therefore be understood as the scattering of an electron with a parton carrying a momentum fraction x of the proton momentum p. The probability of observing this parton with a momentum of xp is given by the *parton density*

function[9] (PDF), $f(x)$. These functions can not be calculated directly due to a large value of QCD coupling constant, i.e., $\alpha_S \sim O(1)$ around the values of which, perturbative theories break down [38, 57]. Primarily, these distributions are extracted from deep inelastic scattering experiments such as the eletron-proton scattering experiment at the HERA[10] collider.

Initial observations of these PDF values indicated no dependence on the momentum transfer Q^2 at high energies. This observation is termed as *Bjorken scaling*. However, it was later established that the PDF has an energy dependence as well, which is known as the scaling violation. It is one of the clearest manifestations of radiative effects predicted by QCD. It can be explained through the understanding that the proton is composed of one *down*-type and two *up*-type quarks, which interact with each other through the exchange of gluons. The three quarks which are the constituents of a proton are the *valence* quarks. These valence quarks are embedded in a sea of quark-antiquark pairs referred to as *sea* quarks which are constantly getting created and annihilated via their interactions with gluons. Hence the energy carried by a proton is distributed inside the proton amongst these quark and gluon constituents.

QCD can not describe the shape of the PDF, and thus the PDF needs to be measured from experimental observations. However, as the energy scale of the scattering process is modified, the PDFs evolve, which is described by the Dokshitzer- Gribov-Lipatov-Altarelli-Parisi (DGLAP) equations [58–60]. Given the x-dependence of the parton densities at some input scale Q_0^2, these evolution equations can be solved to determine the PDFs at another higher Q^2 value. Figure 2.3 shows the PDFs and their dependence on energy in the two plots. The μ indicated in the
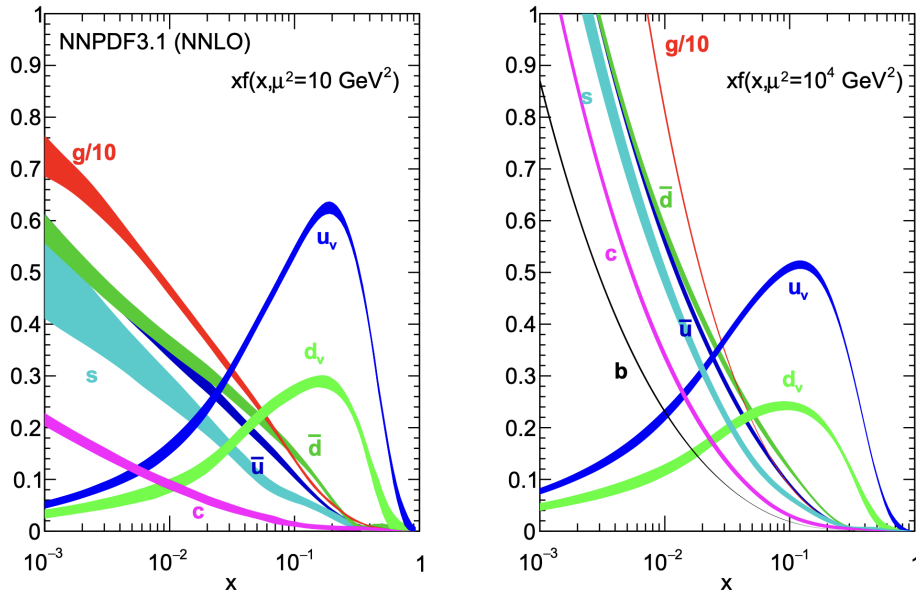

Figure 2.3: PDFs for different partons inside a proton, from the NNPDF Collaboration [57] showing two different energy scales. The left plot shows the PDFs corresponding to a factorisation scale of 10 GeV^2, while the right one corresponds to a value of 10^4 GeV^2. The y-axis corresponds to the term $xf(x, \mu^2)$.

plot refers to a *factorisation scale* μ_F. It is introduced in the equation in order to absorb the collinear singularities into the PDFs, which ends up being dependent on μ_F [61]. From the left

---

[9] Also called as *parton distribution function*

[10] HERA is an electron-proton collider at DESY (Deutsches Elektronen-Synchrotron) laboratory. It operated in the years 1991-2007 and gave significant contributions to the measurements of PDFs

plot (for $\mu^2 = 10 \text{ GeV}^2$), it can be noted that the contribution to the total proton momentum mainly comes from the gluons as well as the valence quarks. The two valence *up* quarks in the proton result in twice the contribution from *down* quark. However, moving to higher μ^2 values (right plot), the contribution from the sea partons become significantly large at low momentum fraction values, as compared to the valence quarks.

2.3.2 Proton-proton collision process

Since the thesis focuses on proton-proton collision where effective interactions occur among the partons from the two protons, the PDFs play a crucial role in determining the cross-section of such a collision process. With the use of the *factorisation theorem* [62], the total inclusive cross-section for a proton-proton *hard scattering* producing particles X and Y can be written as:

$$\sigma_{pp \to XY} = \sum_{i,j} \int \int dx_i dx_j f_i(x_i, \mu_F^2) f_j(x_j, \mu_F^2) \sigma_{ij \to XY}(i, j, \mu_R^2, \mu_F^2) \qquad (2.27)$$

where the total cross-section can be factorised into the individual cross-section contribution from parton-parton interactions $\sigma_{ij \to XY}$, and their initial state parton PDFs $f_i(x_i, \mu_F^2), f_j(x_j, \mu_F^2)$ corresponding to the two initial state protons. The factor μ_F is the factorisation scale which helps in the transition of the expression from parton evolution to hard scattering. The term involving PDFs is called the soft part, and is non-perturbative while the partonic cross-section corresponds to the hard interaction, which is fully perturbative [63]. In addition, there is also a dependence on μ_R, which is called the *renormalisation scale* and is introduced to account for the divergence of higher order corrections. While the physical cross-section σ does not depend on this scale, the truncation of the perturbative series introduces a scale dependence. The choice of the scales μ_R and μ_F is arbitrary. In many analyses, they are set to $\mu = \mu_R = \mu_F = \sqrt{m_{\text{top}}^2 + p_{\text{T, top}}^2}$, and variations around these values are used to estimate the uncertainty in theoretical predictions [64]. This entire product is summed over all pairs of partons (i, j) inside the two colliding protons. The partonic cross-section can be expanded in a fixed-order series in the strong coupling constant $\alpha_s(\mu_R)$ as:

$$\sigma_{ij \to XY} = \alpha_s^2 \left(\underbrace{\sigma_{ij}^{(0)}}_{\text{LO}} + \underbrace{\frac{\alpha_s}{\pi} \sigma_{ij}^{(1)}}_{\text{NLO}} + \underbrace{\frac{\alpha_s^2}{\pi^2} \sigma_{ij}^{(2)}}_{\text{NNLO}} + \dots \right) \qquad (2.28)$$

where the different terms represent different orders at which the cross-section is measured. The first term corresponds to the leading order (LO), the second term is called as next-to-leading order (NLO), the third term as next-to-next-to-leading order (NNLO), and so on [65].

2.4 Shortcomings of the Standard Model

Described by the gauge group $SU(3)_C \otimes SU(2)_L \otimes U(1)_Y$ as briefed in the previous section, the SM stands out to be the best description of our understanding of the fundamental particles in the universe so far. It has been continuously tested and no deviations from the SM predictions have been discovered to date. However, as noted earlier, it does have its limitations and falls short in explaining a number of key points, some of which are detailed below:

- Inclusion of gravity: SM unifies three of the four fundamental forces of nature namely, electromagnetic force, weak force and strong force very elegantly. However, it fails to describe the gravitational force as it has been found to be incompatible with Einstein's theory of general relativity[66]. Hence no reliable *theory of everything* is known to exist till date that successfully incorporates all four fundamental forces of nature.

- Matter-antimatter asymmetry problem: The Big-Bang theory[11] predicts the creation of equal amounts of matter and antimatter in the universe. Contrary to that, the observation of the visible universe reveals the presence of more matter than antimatter [67]. An explanation to this asymmetry was proposed by Sakharov as a set of three conditions known as *Sakharov conditions*, which requires baryon number violation, C- and CP-symmetry violation, and interactions out of thermal equilibrium. These conditions are observed in the SM, but the effects are not strong enough to explain the current matter-antimatter imbalance.

- Hierarchy problem: A vast difference can be observed in the scales of the weak forces and gravity. There is no explanation as to why the weak force is $\sim 10^{24}$ times stronger than gravitational force. Considering the mass of the Higgs boson, there is no known feature in the SM preventing it from receiving large radiative corrections. This means that there exists a *fine tuning* of the Higgs mass in a way that the mass is reduced to the order of $\sim 10^2$ GeV, which would otherwise reach a value as high as Planck mass ($\sim 10^{19}$ GeV). SM provides no explanation to this so called *hierarchy problem* [68, 69].

- Observation of neutrino mass and oscillations: Neutrinos in the SM are massless, and hence they can not perform oscillations from one flavour to another. However, neutrino oscillation is an observed phenomenon which acts as evidence of neutrinos possessing a non-zero mass. The SM can be extended to include mass terms for neutrinos in a way similar to the charged fermions [7], but it fails to explain why its mass is much smaller than its corresponding fermion. Other theories for the source of neutrino mass also exist, but which theory if at all is correct is yet to be established.

- Existence of dark matter and dark energy: The SM explains only 5% of the matter present in the Universe. From cosmological observations, it is known that the remaining 95% of the matter in the Universe is composed of dark matter and dark energy [70]. The SM does not contain any possible candidate for dark matter. Though, there exist theories beyond the SM (BSM) which attempt to incorporate dark matter, the explanation for dark energy is still not clear.

2.5 Top quark: production and decay

The heaviest quark in the SM is the top quark with a mass of approximately 173 GeV [71]. It is an up-type quark from the third generation of fermions. After the discovery of bottom quark [72] of the third generation in 1977, the existence of a sixth quark to complete the pair with the bottom quark was strongly suggested. In 1995, the top quark was finally discovered at the Tevatron[12]

---

[11] Big Bang theory is a widely accepted theory regarding the creation of the Universe that happened around 13.8 billion years ago. It predicts that the Universe expanded from a very hot and dense state.

[12] Tevatron was a proton-antiproton circular particle collider at FermiLab, USA that operated from 1980-2011

collider by the CDF [73] and the D0 [74] collaborations marking a significant milestone in particle physics as this particle had been predicted to exist since long before. Because of its heavy mass, the decay width of the top quark is considerably large ($\Gamma_t \approx 1.5$ GeV [75]), and hence, it has a very small lifetime $O(10^{-25}$s). This short lifetime does not allow for the top quark to hadronise to form bound states, and thus it decays almost immediately as it is formed. A brief overview on the production and decay of top quarks is outlined below:

- **Production**: A large quark mass implies more energy is required to produce it. This is achieved through collisions of particles at high energies. More details on how this is achieved in colliders will be discussed in Chapter 3. At colliders, top quarks are primarily produced in pairs or as a single top quark along with an additional particle. Mainly two initial states govern the top quark production at hadron colliders, namely quark-antiquark annihilation, or gluon-gluon fusion. Quark-gluon initial states are also possible, but only at NLO (ref. Section 2.3.2). At the Tevatron collider, where the top quark was first discovered, the energy of operation was $\sqrt{s} = 1.96$ TeV [76]. At these energy values, the dominant production mode for $t\bar{t}$ pair production is via a quark-antiquark annihilation, marking $\sim 85\%$ of the total cross-section [77]. On the other hand, the centre-of-mass energy at the Large Hadron Collider (ref. Chapter 3) at CERN is much larger, ranging from 7 to 13.5 TeV in different running periods. At these energies, the dominant production mechanism is the gluon–gluon channel since higher energies allow the partons with small momentum fractions to produce a $t\bar{t}$ pair. From Figure 2.3, it can be seen that for higher energies, the gluons dominate for small momentum fractions. The Feynman diagrams corresponding to these processes is shown in Figure 2.4.
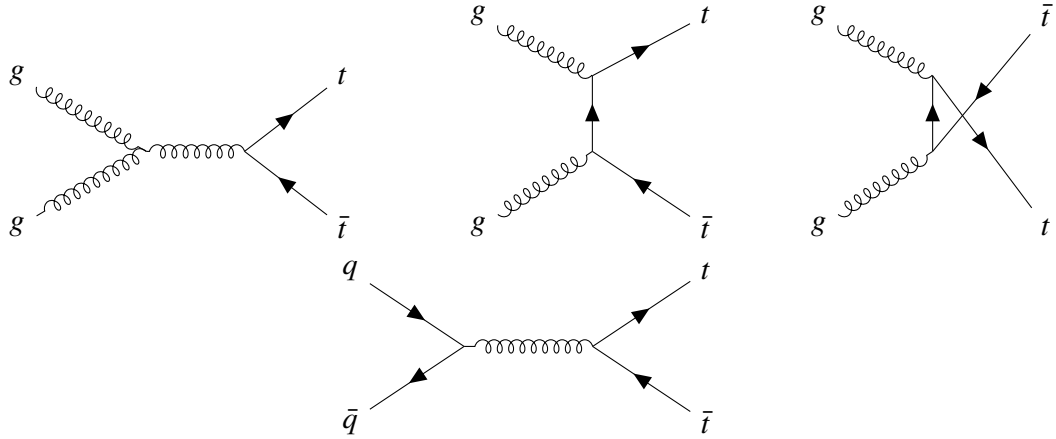

Figure 2.4: Examples of Feynman diagrams for tree-level $t\bar{t}$ pair production process.

An overview of the inclusive cross-section measurements at the Tevatron and the LHC is shown in Figure 2.5 corresponding to different centre-of-mass energies [78–87] along with a comparison to their theoretical predictions [88]. The experimental observations seem to match well with the theoretical predictions. The latest value for the inclusive cross-section from theoretical predictions at the centre-of-mass energy of 13 TeV yields a value of

$$\sigma_{t\bar{t}}^{\text{NNLO+NNLL}} = 832^{+20}_{-29} \text{ (scale)} \pm 35 \text{ (PDF} + \alpha_s) \text{ pb} \tag{2.29}$$

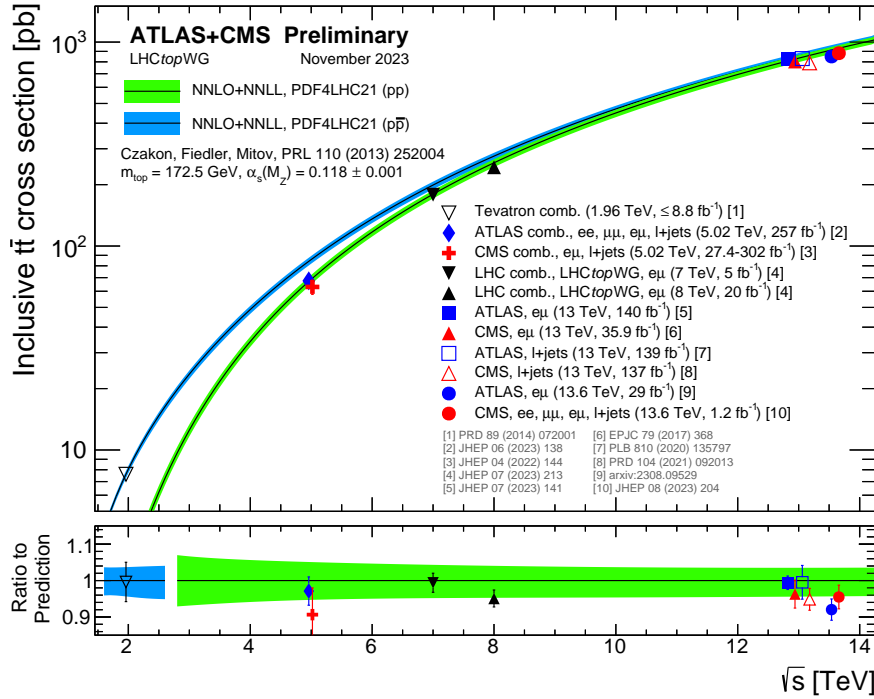which has been calculated at NNLO accuracy in QCD calculations, with soft-gluon

Figure 2.5: Overview of the top-pair production cross-section measurements as a function of the centre-of-mass energy for the LHC and Tevatron colliders. This is compared to the NNLO QCD calculation complemented with NNLL resummation. Both the measurements and the theory calculations are quoted at $m_{\text{top}} = 172.5$ GeV (references [78–88]). The plot has been compiled by the LHC Top Working Group [89].

resummations at next-to-next-to-leading logarithmic (NNLL) order. In addition to these QCD calculations, there exist some electroweak corrections which come into effect at NLO.

- **Decay**: Due to its large mass, the top quark can not hadronise to form stable bound states which are observed for the case of charm and bottom quarks with a resonant production of charmonium ($c\bar{c}$) and bottomium ($b\bar{b}$), respectively. The top quark can decay to a W-boson and a lighter quark. Since the decay of quarks is governed by the CKM matrix, revisiting Equation 2.4, the probability of transition of a quark with flavour i to a quark with flavour j is proportional to the square of the CKM matrix element $|V_{ij}|$. Using the fact that $|V_{tb}| >> |V_{ts}| > |V_{td}|$, the top quark decays almost exclusively to a bottom quark and a W-boson. Hence, the final state particles of a top quark decay process is dictated by the decay modes of the W-boson.

The W-boson can decay hadronically to quarks with a branching fraction[13] of $\sim 68\%$, or leptonically to a lepton and its associated neutrino with a branching fraction of $\sim 32\%$. Thus, considering a $t\bar{t}$ decay, the possible final products can be classified as:

1. **Fully hadronic**: both of the W-bosons decay into quarks, i.e.,
   $t\bar{t} \rightarrow (W^+b)(W^-\bar{b}) \rightarrow (q_1\bar{q}_2 b)(q_3\bar{q}_4\bar{b})$

---

[13] Branching ratio or branching fraction is defined as the fraction of times a particle decays into a particular final state.
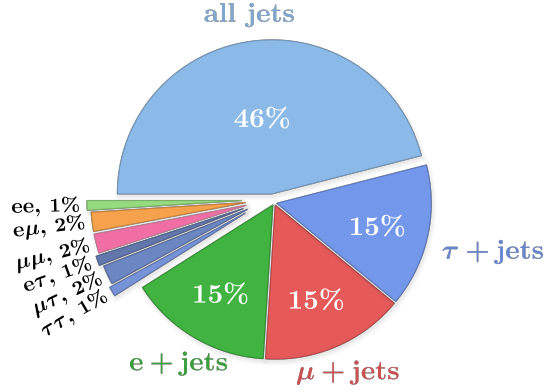
Figure 2.6: Branching fraction for each of the modes of the $t\bar{t}$ decay. The label "all jets" refers to the fully hadronic channel, the labels "τ+jets", "μ+jets" and "e+jets" collectively refer to the single-leptonic channel, and the rest combine to give the branching fraction for the dileptonic decay mode. Figure taken from reference [90].

2. **Single-leptonic**: one of the W-boson decays into quarks and the other decays into a lepton and a neutrino, i.e.,
$$t\bar{t} \rightarrow (W^+ b)(W^- \bar{b}) \rightarrow (q_1 \bar{q}_2 b)(l\bar{\nu}_l \bar{b})$$

3. **Dileptonic**: both the W-bosons decay into a lepton and a neutrino, i.e.,
$$t\bar{t} \rightarrow (W^+ b)(W^- \bar{b}) \rightarrow (\bar{l}\nu_l b)(l'\bar{\nu}_{l'}\bar{b})$$

The branching ratio of each of the decay channel is depicted in Figure 2.6. This shows that $\sim 46\%$ of the times the $t\bar{t}$ decays via the fully hadronic channel, and $\sim 44\%$ of the times it decays via a single-leptonic channel, while the decay via a dileptonic channel is only $\sim 10\%$.

2.6 Higgs boson and its interaction with the top quark

The Higgs boson, as discussed in Section 2.2.4, is one of the special particles in the SM. It interacts with all the massive particles in the SM in different ways. The first type is the interaction of the Higgs boson with the gauge bosons, i.e., the $W^\pm$ and the Z bosons. For this case, the coupling strength of the interaction is proportional to the square of the mass of the boson. The second type is the interaction of the Higgs boson with fermions, which is known as Yukawa interaction, for which the coupling strength is proportional to the mass of the fermion. Hence, for the top quark with the largest mass in the SM, the top-Yukawa coupling is also the largest. The third category is the self interactions of the Higgs boson. As noted earlier, the Higgs boson is capable of exhibiting cubic and quartic self couplings.

Instead of the usual couplings, a more commonly used term is the reduced coupling strength modifier defined as $\sqrt{k_V g_V / 2\, v} = \sqrt{k_V}(m_V/v)$ for bosons ($W^\pm, Z$) with a mass m_V and $k_F g_F/\sqrt{2} = k_F m_F/v$ for fermions with a mass m_F, where g_V and g_F are corresponding absolute coupling strengths and v is the vacuum expectation value of the Higgs field. Figure 2.7 shows the reduced coupling strength as a function of particle masses, which clearly shows the mass proportionality with its corresponding coupling values. Figure 2.8 shows the Higgs boson decay modes as a function of its mass, which shows that the most probable decay mode is $H \rightarrow b\bar{b}$ with a BR of $\sim 58\%$ at $M_H = 125$ GeV. Values of the coupling strengths shown in
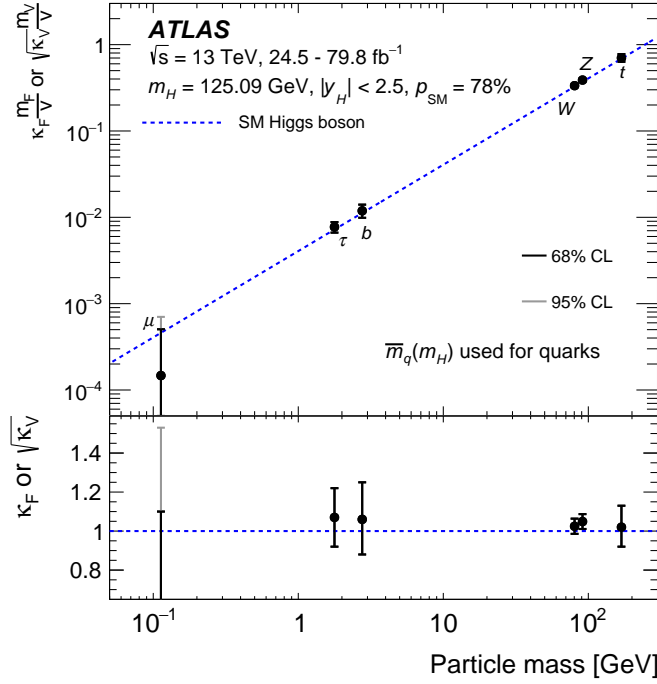
Figure 2.7: Reduced coupling-strength modifiers for fermions ($F = t, b, \tau, \mu$) and for weak gauge bosons ($V = W^\pm, Z$) as a function of their masses m_F and m_V, respectively. The SM prediction for both cases is shown as a dotted line. Plot taken from [91]

Figure 2.7 would predict the BR for the decay to weak gauge bosons to be larger than the values shown in Figure 2.8. The decays to weak gauge bosons are suppressed due to the mass of the Higgs boson. The decay to VV requires one of the bosons to be produced off-shell. The BR for $H \rightarrow VV$ is about $\sim 21\%$. This is followed by its decay to gg, the process of which requires a loop, since the Higgs boson does not directly couple to gluons. $H \rightarrow gg$ has a BR of $\sim 9\%$. The next in the BR plot is its decay to two *tau* leptons, $H \rightarrow \tau^+\tau^-$ with a BR of $\sim 6\%$. It also decays to a pair of photons, also not directly. It can only decay to two photons via a fermion or boson loop. This has a very small BR of $\sim 0.2\%$. It is nevertheless, an important channel as it produces a very clear signature for experimental analysis.

For the case of a top quark, the mass turns out to be too heavy for it to be a product of a Higgs boson decay. Therefore one way to study top-Yukawa coupling is via the introduction of a loop.

2.6.1 top-Yukawa coupling and the electroweak correction

The conventional experimental ways of top-Yukawa coupling measurement relies on the $t\bar{t}H$ process as shown in Figure 2.9(a) where a $t\bar{t}$ pair is produced along with a Higgs boson. This is regarded as a direct method for top-Yukawa coupling (Y_t) measurement since a tree-level top-Higgs vertex is observed here [2, 3, 8, 9]. Another channel studied so far also include gluon-gluon fusion process, where the Higgs boson is indirectly coupled to the top quark via a loop as shown in Figure 2.9(b) (no new physics is assumed). The results of these studies have been found to be compatible with the SM expectation so far. However, this analysis focuses on the measurement of Y_t using an approach different to the conventional approaches, wherein
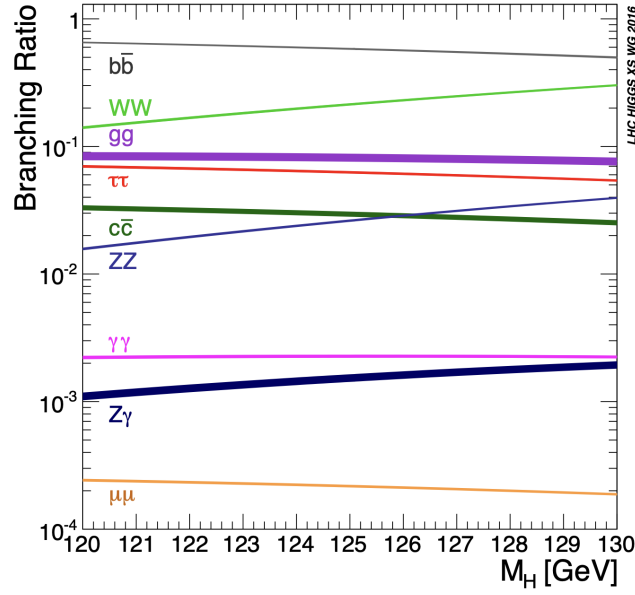
Figure 2.8: Branching ratios for Higgs decay as a function of Higgs boson mass. Plot taken from [92].

the electroweak corrections to $t\bar{t}$ cross-section is evaluated to obtain the Y_t value. Previous measurement done by the CMS collaboration using the same idea placed an upper limit of 1.67 on the Y_t value at 95% confidence level [13].
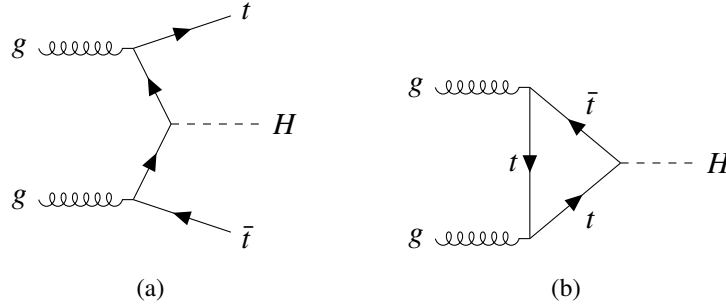

Figure 2.9: Feynman diagrams for ttH production as well as gluon fusion process that are conventioanlly used to obtain top-Yukawa coupling strength.

Considering a $t\bar{t}$ production process, the main Born level Feynman diagrams have been shown previously in Figure 2.4, with Born cross-section of the order α_s^2 [11]. Weak corrections start entering the cross-section at loop-induced order $\alpha_s^2 \alpha_{\text{weak}}$ only. Examples for the diagrams for weak corrections to quark as well as gluon induced amplitudes are shown in Figure 2.10. As can be seen from the figures, the virtual electroweak corrections are considered. Amplitudes that are linear in Y_t would arise from the s-channel Higgs boson production which is depicted in the s-channel diagram at centre in Figure 2.10(b). These amplitudes may be ignored since a b-quark is present in the loop and the mass of a b-quark is small. However, in the other diagrams in Figure 2.10(b), the amplitude of the Higgs boson contribution to the loop is proportional to Y_t^2, since these diagrams always involve two of the $t\bar{t}H$-type vertices.

Taking into account the interference of this EW diagram with the Born-level $t\bar{t}$ production

process, the term ends up being proportional to $\alpha_s^2 Y_t^2$. In some kinematic regions, these Y_t corrections become large and may lead to significant distortions of differential distributions.
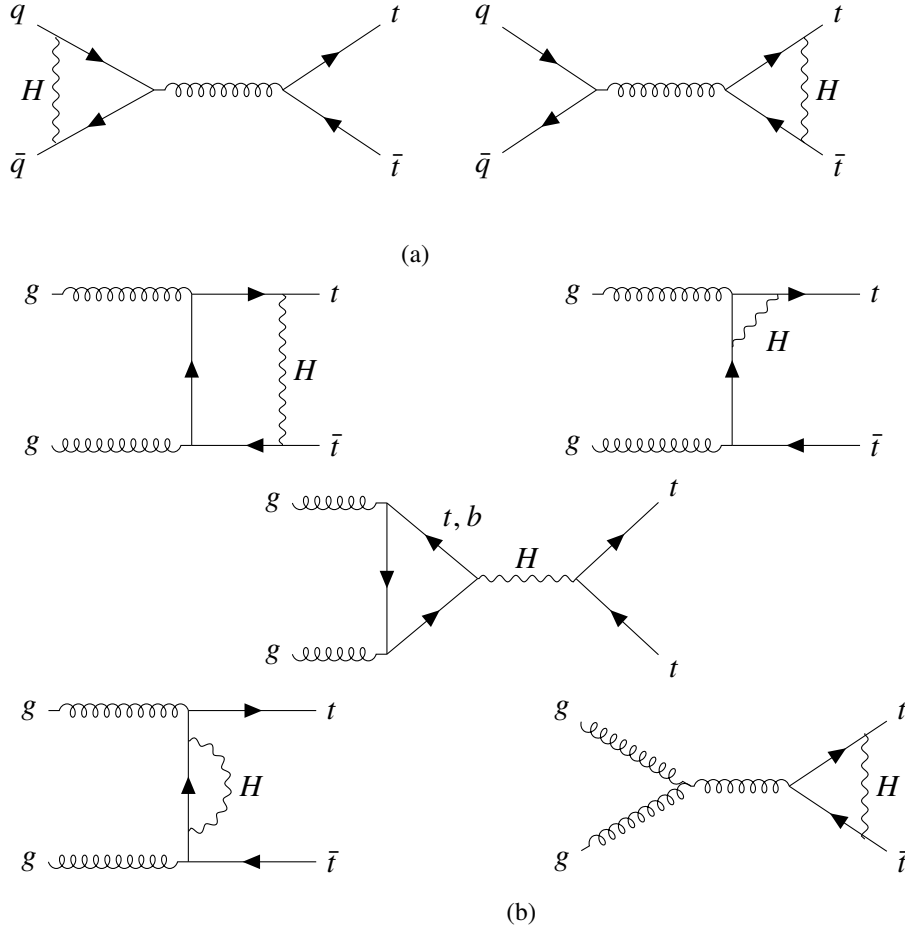

(a)

(b)

Figure 2.10: Examples of Feynman diagrams for virtual corrections through a Higgs boson in 2.10(a) a quark-induced process, and in 2.10(b) a gluon-induced process.

2.6.2 Observables sensitive to Y_t corrections

Since the analysis focuses on the measurement of top-Yukawa coupling via a measurement of the virtual corrections to $t\bar{t}$ cross-section, it is important to search for the observables that are sensitive to this virtual correction. From reference [11], it can be understood that weak corrections affect the cross-section values at hard scattering events where the momentum transfer is large. There are also some effects at the threshold of $t\bar{t}$ production that modify the differential distributions. Analysing different kinematic observables, the weak corrections for the total cross-section turns out to be only a small value. However, certain regions of the differential cross-section distribution show a sizable effect for weak corrections.

Figure 2.11 shows the differential cross-section distributions with respect to the parton-parton centre-of-mass energy, where it is plotted for two different Higgs mass hypotheses for quark and gluon induced processes separately. Focusing on $M_H = 126$ GeV, large corrections at low $\sqrt{\hat{s}}$ can be seen for both the quark as well as gluon induced processes.
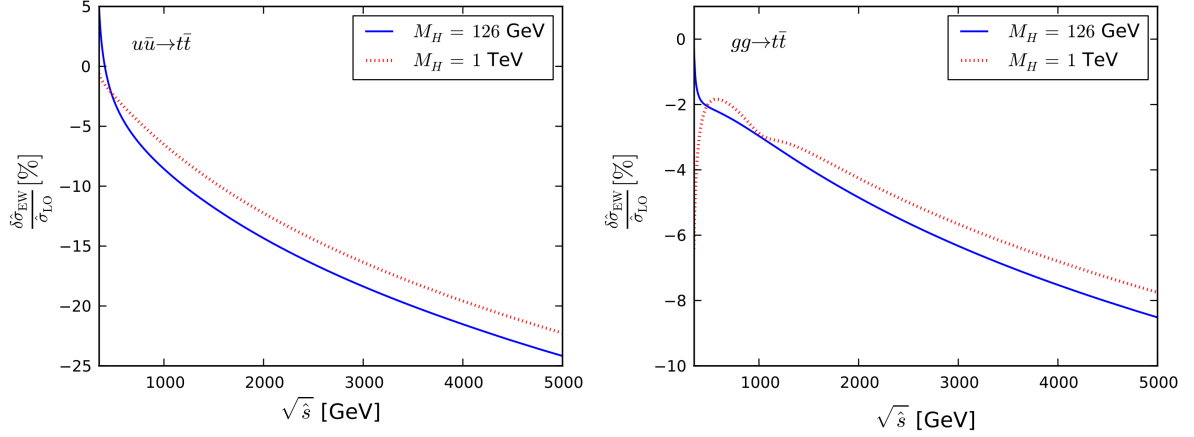
Figure 2.11: Weak corrections as a function of parton-parton centre of mass energy, for quark-induced as well as gluon-induced processes. They are plotted for a Higgs mass of of 126 GeV (in blue line), and for 1 TeV (dotted red line). Plots taken from [11].

Observing the angular dependence of the differential cross-section, the weak corrections show a considerable effect at large energies. This is shown in Figure 2.12, where the differential cross-section as a function of the scattering angle of the top quark is plotted for an energy close to the threshold of $t\bar{t}$ production, i.e., at $\sqrt{s} = 370$ GeV, and for $\sqrt{s} = 3$ TeV. The correction
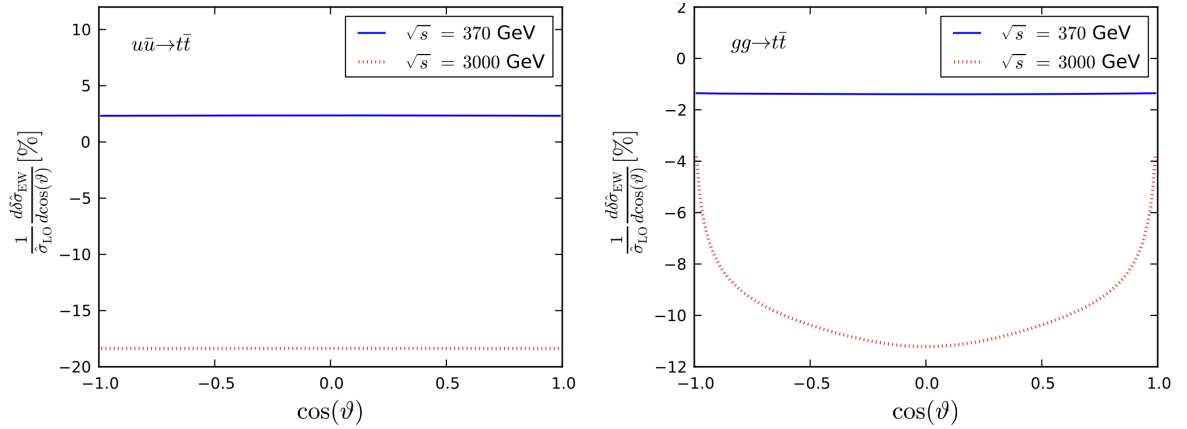

Figure 2.12: Weak corrections as a function of scattering angle for quark-induced as well as gluon-induced processes. They are plotted for centre of mass energy of 370 GeV (in blue line), and for 3 TeV (dotted red line). They correspond to parton-level differential distributions. Plots taken from [11].

can be observed to be uniform over the different scattering angle values apart for the case with gluon-induced processes at high energies. For the gluon-induced process, since both s- and t-channel diagrams contribute, a strong angular dependence can be seen moving from a scattering angle of 0 to 90 degrees at large energies.

Previous analyses using similar methods for obtaining top-Yukawa coupling focused primarily on the invariant mass of the two top quarks, and the scattering angle of the top quark [13]. A detailed analysis for the evaluation of the weak corrections is made in Chapter 7, where the sensitivity for different values of the top-Yukawa coupling is also described.

The ATLAS experiment at the LHC

One of the ways to study the fundamental particles is by probing the structure of hadrons. Through the collision of highly energetic hadrons, a number of particles are created, which can be tracked and identified using specialised detectors. To achieve this, a dedicated collider is required which can accelerate the hadrons at high energies and perform the collision process. The **L**arge **H**adron **C**ollider (LHC) [93] is such a collider which will be covered in detail in the following section. It uses several specialised detectors to collect the collision data. One of these detectors is the ATLAS [94] detector, the data collected at which is used in this analysis. The structure and operation of this detector will be described in detail in Section 3.2.

3.1 The Large Hadron Collider

Built by the European Organisation for Nuclear Research (CERN) [95], the Large Hadron Collider [93] currently stands as the world's largest particle collider. It is situated in a circular tunnel 27 kilometres in circumference and is buried at a depth of about 100 metres underneath the France-Switzerland border near Geneva [96].

The LHC is primarily designed to conduct proton-proton collisions, but in addition, it can also collide beams of heavy ions, performing lead–lead and proton-lead collisions. The collider tunnel is equipped with two parallel beam pipes placed close to one another, each containing a beam that moves in opposite directions around the ring. The proton beams within the LHC are not continuous; instead, they are grouped into distinct bunches, with each bunch containing $\approx 10^{11}$ protons. They are bunched together because the acceleration technique utilises radio-frequency (RF) cavities. The interactions between the two beams occur at discrete intervals, which under nominal operating conditions are 25 nanoseconds apart, with a bunch collision rate of 40 MHz. As they travel through the LHC ring, the beams encounter several magnets that are capable of generating a magnetic field of approximately 8 T [93]. Dipole magnets are used to curve the trajectory of the beams, while quadrupole magnets squeeze and focus the beams in order to prevent them from diverging as well as to raise the probability of collisions. Other higher magnetic multipoles are also used to further correct the effects from the previous magnets.

Achieving a center-of-mass energy of the order of TeV is not a straightforward task. During the second LHC run (2015-2018), the centre-of-mass energy of collision was kept at 13 TeV. To accomplish this, particles were regulated using a chain of accelerators that progressively boost their energy before being injected into the primary LHC ring. Figure 3.1 illustrates the layout of the collider. The acceleration process begins with the linear particle accelerator LINAC 2, which generates 50 MeV protons and feeds them into the Proton Synchrotron Booster (PSB). The PSB accelerates the protons to 1.4 GeV and injects them into the Proton Synchrotron (PS).
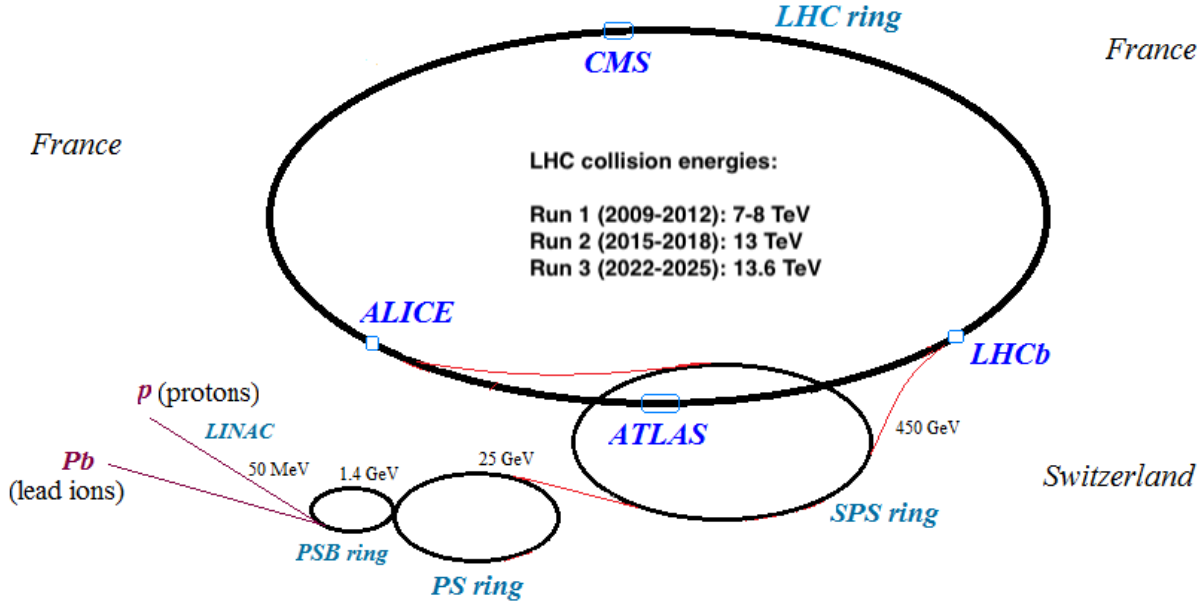
Figure 3.1: Pictorial representation of the LHC setup depicting the chain of accelerators used to achieve the high energy collisions. Adapted from [97].

The PS accelerates the protons further to 26 GeV, and finally, the Super Proton Synchrotron (SPS) increases their energy to 450 GeV before finally injecting them into the main ring. In this LHC ring, proton bunches are accumulated and accelerated to their peak energy of 6.5 TeV each, and are made to collide at four main intersection points. There are four major experiments set up at the LHC at these four interaction points: ATLAS[1][98, 99], CMS[2][100, 101], ALICE[3][102, 103] and LHCb[4][104]. LHCb is an experiment that utilises a forward detector to concentrate on the physics of B-hadrons. The ALICE experiment is designed to study the physics revolving around the quark-gluon plasma using heavy ion collisions at the LHC. The ATLAS and CMS experiments are the two big general-purpose experiments which are utilised to investigate the SM and search for new physics.

3.1.1 Luminosity

One of the crucial parameters of the collider is its instantaneous luminosity, which is a measure of the rate of interactions in the collider. It is described as the ratio of the number of events detected (N) per unit time (t) to the interaction cross section (σ) [105]:

$$L = \frac{1}{\sigma}\frac{N}{t} = \frac{N_b f_r n_1 n_2}{4\pi\sigma_x\sigma_y} \tag{3.1}$$

---

[1] A Toroidal LHC ApparatuS
[2] Compact Muon Soleniod
[3] A Large Ion Collider Experiment
[4] Large Hadron Collider beauty

where N_b is the number of bunches, f_r is the revolution frequency of the beams at the LHC (40 MHz), n_1, n_2 are the numbers of particles per bunch in each of the two beams ($\approx 10^{11}$), σ_x and σ_y represent the transverse beam sizes in the horizontal and vertical directions [106], assuming Gaussian beam profiles. The LHC is designed to achieve a peak luminosity of $10^{34} \mathrm{cm}^{-2}\mathrm{s}^{-1}$ [93]. Another quantity of interest is the integrated luminosity, $\mathcal{L}$, defined as $\mathcal{L} = \int L dt$. Both of these quantities are useful for assessing the performance of a particle accelerator. Their knowledge is essential for the measuement of the cross-section of any physics process at the LHC. In particular, all collider experiments aim to maximise their integrated luminosities, since the higher the integrated luminosity, the more is the statistics for the data available for analysis [107].

Figure 3.2 shows the integrated luminosity at the ATLAS detector over the full Run-2 period (2015-2018) of data taking, achieving a centre-of-mass energy $\sqrt{s}$ = 13 TeV. This is the data which is used in this analysis. The LHC delivered $\approx$ 156 fb^{-1} of luminosity during this period, out of which $\approx$ 147 fb^{-1} of luminosity was recorded at the ATLAS detector [108]. The ATLAS recorded luminosity is lower than the LHC delivered value due to detector performance efficiencies which reduces the amount of data that is actually good for physics analysis. The luminosity that is actually good for physics and is used in the ATLAS Run-2 analyses including the analysis presented in this thesis evaluates to 140.1 ± 1.2 fb^{-1} [108].
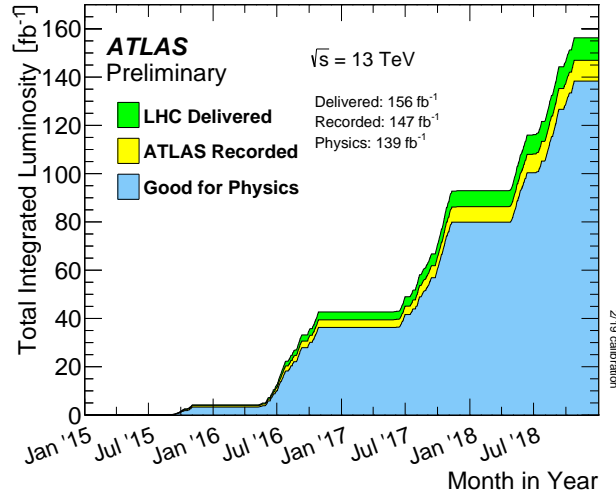

Figure 3.2: The total integrated luminosity over the period from 2015-2018 (Run-2) data as delivered by the LHC (in green), as recorded by the ATLAS detector (in yellow), and as recorded to be usable for physics analyses (in blue) [109].

3.1.2 Pileup

From the expression in Equation 3.1, to obtain higher collision rate, higher luminosity can be achieved if the number of bunches or the number of protons in the bunch are incresased, or the beams are squeezed further. While attaining high luminosity values is ideal for collider experiments, it brings up new challenges alongwith. When particles are bunched, the collision rate increases, leading to multiple proton-proton collisions happening at the same time in a single bunch crossing. The collisions may also include inelastic proton-proton interactions. The phenomenon of multiple collisions occurring simultaneously is referred to as *pileup* [110]. The

average number of pileup interactions for the period of Run-2 data as collected by the ATLAS detector (discussed in detail in Section 3.2) is compiled in Figure 3.3. For the years 2015 and 2016, the average number of pileup interactions was only $< \mu >= 13.4$ and $< \mu >= 25.1$, while for the years 2017 and 2018 this number increased to $< \mu >= 37.8$ and $< \mu >= 36.1$, respectively.
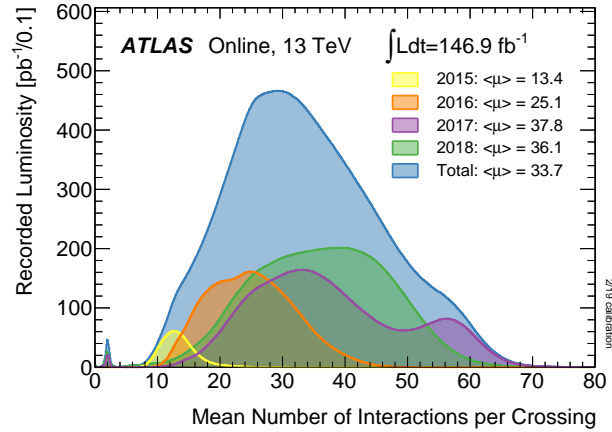
Figure 3.3: The distribution for the average number of interactions per bunch crossing in the different years for Run-2 data collected by the ATLAS detector [111].

3.2 Introduction to the ATLAS detector

One of the detectors at the LHC is the ATLAS detector. The abbreviation "ATLAS" stands for **A T**oroidal **L**HC **A**pparatu**S**. It is designed with a layered structure, much like the layers of an onion, with each layer serving a specific purpose in detecting and reconstructing particle information. The concept that particles lose energy as they travel through a medium serves as the basis of operation. Particles may also interact with the medium within the detector space or the detector material itself. The sub-components of ATLAS identify the results of the interactions.

The detector is built with different materials keeping in mind the harsh radiation environment during the LHC runs. The structure of the ATLAS detector is shown in Figure 3.4. The apparatus itself is 7000 tonnes in weight, 44 metres long and 25 metres high. It can be categorised into four major components [99]. The first one is the inner detector containing the pixel detector, transition radiation tracker, and the semiconductor tracker. It is used for the reconstruction of charged particle tracks. The second is the magnet system that consists of a solenoid magnet placed just outside of the inner detector layers, and a toroid magnet that surrounds the cylindrical part as well as the ends. These magnets help bend the particle tracks to obtain a momentum measurement. The third component is the calorimeter, the structure of which relies on two types of techniques to meet the requirements which will be described in detail later. The particles deposit their energies, which are then measured using these calorimeters. The final component is the muon spectrometer, which specialises in muon detection. The trigger and data acquisition system is an additional component which serves actually one of the most important purposes for the ATLAS detector. It manages the massive amount of data that the detector collects and saves only those events that are useful and interesting for physics analysis.
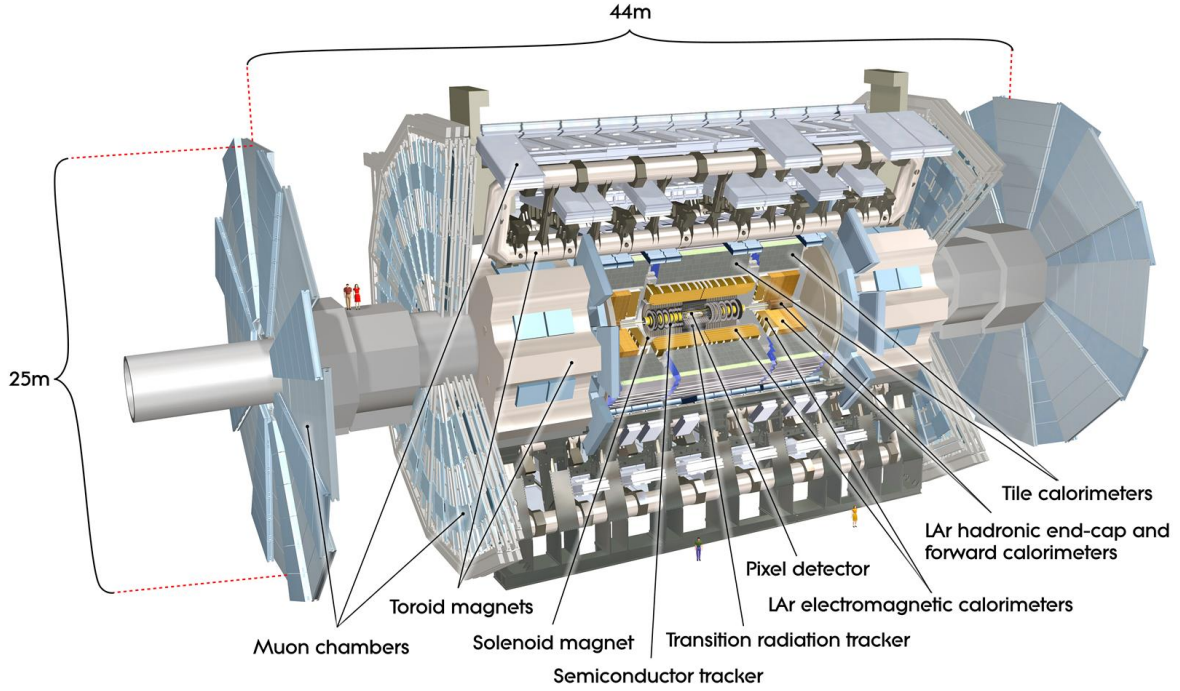
Figure 3.4: Cut-way view of the ATLAS detector situated at CERN [112]

3.3 ATLAS detector components

This section will go into detail about each of the detector components. However, before going into the details about the detector, it is important to first discuss the coordinate system used in ATLAS.

3.3.1 ATLAS Coordinate system

Instead of Cartesian coordinates, a more convenient system based on spherical corrdinates is used in ATLAS. The point where the proton-proton collision takes place is called as the Interaction Point, and it serves as the central point in the coordinate system. Figure 3.5(a) shows the depiction of the convention. In terms of Cartesian coordinates, the central line along the LHC beam pipe is considered as the z-axis. The plane transverse to it is the xy-plane, where the y-axis points upwards and the x-axis points towards the centre of the circular LHC ring.

Considering the geometry of the detector, it is convenient to follow the spherical coordinate system, where two angles are introduced. One is the polar angle, θ which is the angle between the particle trajectory and the z-axis, and the other is the azimuthal angle, ϕ corresponding to the angle between the projection of the particle track in the xy-plane with respect to the x-axis. This xy-plane is called the *transverse plane*, and the quantities in this plane are frequently used in ATLAS analyses. Since the proton-proton collisions take place along the z-axis, the vectorial sum of the momentum of all final particles must evaluate to zero in this plane. The measure of particle momentum in this plane is termed as its *transverse momentum*, $p_T = \sqrt{p_x^2 + p_y^2}$.
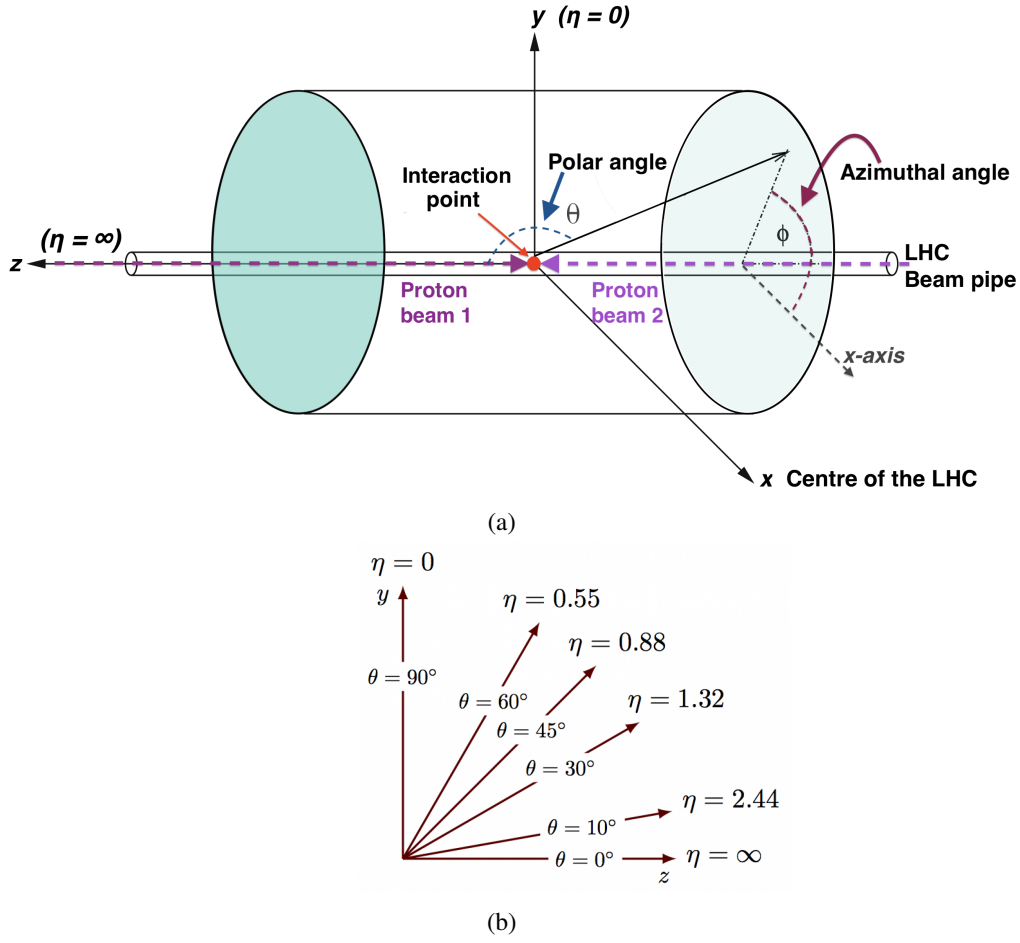
(a)

(b)

Figure 3.5: The coordinate system of the ATLAS detector is shown in this figure. Sketch 3.5(a) shows the cartesian coordinate system marked for the detector's geometry. The sketch 3.5(b) shows the values of pseudorapidity at different polar angles θ. Figure (b) is taken from reference [113].

Rapidity and pseudorapidity

In place of the polar angle θ, quantities like rapidity y and pseudorapidity η are used. For a particle with energy E and three momentum (p_x, p_y, p_z), rapidity of a particle is defined as

$$y = \frac{1}{2}\ln\left(\frac{E + p_z}{E - p_z}\right) \tag{3.2}$$

Differences in rapidity values are invariant under Lorentz boosts parallel to the z-axis. Under the approximation that particle masses are small, rapidity y simplifies to pseudorapidity η. It has a value of zero for particle trajectories that are perpendicular to the beam, i.e., along the xy-plane, and has positive or negative values for those at an angle to the beam, as can be seen from Figure 3.5(b). It is described as:

$$\eta = -\ln\left(\tan\frac{\theta}{2}\right) \tag{3.3}$$

which is not correlated to the energy measurement. η is a more convenient variable to deal with compared to the polar angle θ, as the angular distribution of final state hadrons increases strongly in the forward direction. The detector region lying within a small $|\eta|$ value is considered as the *central* region, while the ones corresponding to larger values is termed as the *forward* region of the detector. In the ATLAS detector, leptons are best detected in the angular range of $|\eta| < 2.5$, and the jets in the range of $|\eta| < 5$. If the mass of the particle is neglected, the differences in pseudorapidity values are also invariant under Lorentz boosts parallel to the z-axis.

Azimuthal angle and the angular distance

As the polar angle by itself is not a meaningful quantity anymore, the use of angular distances is not very common. But since, for a massless particle, differences in azimuthal angle $\Delta\phi$ and pseudorapidity $\Delta\eta$, are invariant under Lorentz boosts along the direction of the beam axis, a quantity

$$\Delta R = \sqrt{(\Delta\eta)^2 + (\Delta\phi)^2} \tag{3.4}$$

is defined as a general distance dimension, or the *angular distance*. This quantity is also invariant under Lorentz boosts along the z-axis if the particle mass is neglected.

3.3.2 Magnet system

A charged particle under the influence of a magnetic field curves the path it follows. This phenomenon of deflection of the particle in the influence of the magnetic field is exploited by the detectors to estimate the momentum of particles passing through it. The direction of the trajectory of the particle also gives information about the charge of the particle. The system of magnets used by ATLAS include a solenoid [114, 115], as well as a toroid [116, 117] magnet. They are made up of superconducting coils cooled down to a temperature of 4 K using liquid Helium.

The solenoid magnet is oriented along the beam axis and generates a 2 T axial magnetic field for the inner detector. The arrangement is carefully optimised to keep the material thickness in front of the calorimeter as small as possible, such that the solenoid assembly contributes a total of only ≈ 0.66 radiation lengths at orthogonal incidence. The magnet spans 5.3 m along the beam axis and has an outer diameter of 2.6 m [98]. Figure 3.6 depicts the geometry of the magnet system.

In contrast, toroid magnets are located in the barrel as well as the two end-caps. The barrel toroid spans the dimensions of the ATLAS detector, reaching 26 m along the beam axis with an outside diameter of 22 m. The end-cap toroids extend the magnetic field for the particles entering the forward region of the detector. They consist of eight radially-oriented rectangular superconducting coils. In the barrel and the end-cap sections, they reach a peak magnetic field of 3.9 and 4.1 T, respectively, which is primarily employed for the muon spectrometer.

3.3.3 Inner Detector

Being the first component of ATLAS to observe the decay products of the collision, the inner detector (ID) [119–121] is constructed to be extremely sensitive and compact. The primary function of this 6-meter-long, 2-meter-high detector is to retrace the tracks of particles that emerged from the collision. Since it is placed very close to the LHC beam pipe, it is highly
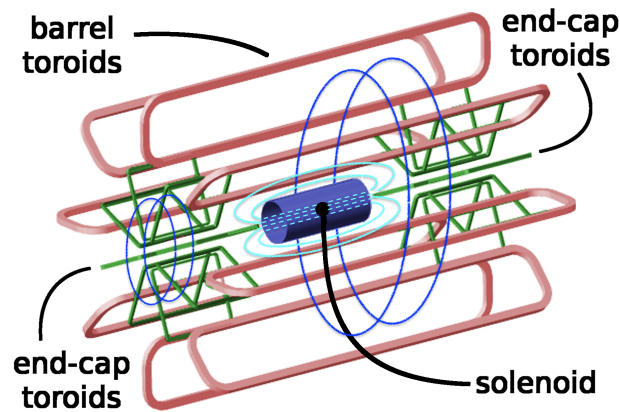
Figure 3.6: The magnet system of the ATLAS detector consisting of (i) central core-solenoid (whose magentic field lines are shown in light blue curve), (ii) Eight barrel toroid coils (magnetic field lines shown in blue curve), and (iii) Eight end-cap toroid coils on both ends. Figure adapted from [114, 118].

susceptible to radiation damage. Furthermore, due to high particle density in this region, it needs to have a good resolution in order to reconstruct the particle tracks correctly. A diagram depicting the structure of the ID is shown in Figure 3.7. It consists of three distinct detector systems namely, the silicon pixels, silicon strips and drift tubes. They measure the direction, momentum, and charge for the electrically charged particles generated from the collision. All three subsystems consist of a barrel and two end-caps. The barrels are made up of numerous cylindrical layers of sensors, while the end-caps are made up of a number of sensor disks or wheels. The complete system resides in a superconducting solenoid coil that generates a magnetic field of 2 T. The innermost part is the pixel detector, followed by a semiconductor tracker (SCT). These are highly granular silicon-based detectors. It is followed by the Transition Radiation Tracker (TRT), which is a gas-based detector as explained later.

The fundamental working principle of semiconductor-based detectors like the pixel and the SCT detectors is the creation of electron-hole pairs when a particle travels through [122]. The p-doped portion of the pn-junction diode in these silicon detectors has an excess of free holes, while the n-doped part has an excess of electrons. When the p- and n-parts are joined together, there is an imbalance of electrons and holes at the junction, which causes the creation of a *depletion zone*. Free charge carriers diffuse into the other layer at the boundary, recombine there, and result to the formation of a field that opposes the diffusion current. As a result, a depletion zone—where free charge carriers are no longer present—is created. This depletion zone can extend under the influence of an external electric field increasing the effective portion that aids in particle detection. The electrons or holes produced by the incident particles induce a charge at the electrodes, which are the contacts across which the voltage is provided to the diode [123]. Readout electronics then process this induced charge. Once the signal is detected in different layers, particle tracks are reconstructed.

- **The Pixel Detector:**
  It is the innermost layer of the ID [124] which measures the trajectories of the charged particles very precisely. It offers full 2π coverage in the ϕ-direction and a coverage up to $|\eta| \leq 2.5$ for the silicon section of the detector. It was initially intended as a three-layer structure. Another layer was added later in 2014 during the long shutdown of the LHC, and was positioned around 3.3 cm from the center of the beam pipe. Each module of this
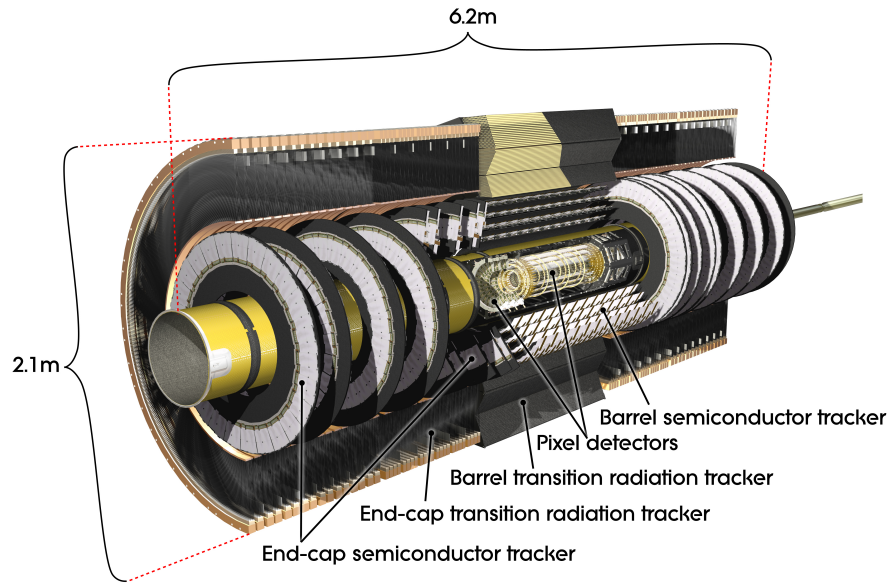
Figure 3.7: Longitudinal view of the ATLAS inner detector [119].

layer has a pixel size of $50 \times 250 \ \mu m^2$. This is known as the Insertable B-layer (IBL) and has a spatial resolution of 10 μm in the $r\phi$-plane and 66.5 μm along the z-direction [125]. Following the IBL are the other layers: Layers 0, 1, and 2, which include both the barrel and the end-cap regions, as opposed to the IBL, which is exclusively a barrel layer. With a size of $50 \times 400 \ \mu m^2$, they have a resolution of 10 μm in the $r\phi$-plane and 115 μm in the z-direction. Overall, the pixel detector contains 92 million readout channels. Each pixel has its own circuit, which aids in determining the particle tracks.

- **The Semi-Conductor Tracker (SCT):**
  The SCT is similar to the pixel detector, but uses long, narrow strips instead of pixels. It consists of a silicon microstrip sensor with over 6 million implanted readout strips (6 million channels). It surrounds the pixel detector and is placed in a stereo-layer formation with back-to-back sensors placed at a small angle of 40 mrad between each other. With this structure, all charged particles leave their tracks in the SCT. Readout strips exist every $80\mu m$ on the silicon, allowing the positions of charged particles to be recorded with a resolution of $17\mu m$ perpendicular to the strip and 580 μm in the parallel direction, per layer [124].

- **The Transition Radiation Tracker (TRT):**
  Serving as the outermost layer of the inner detector, the TRT uses drift chambers and the principle of transition radiation to detect and identify particles. It is made up of straw tubes, each 4 mm in diameter, filled with a gas mixture. A gold-plated tungsten wire runs through the center of the tube. When a charged particle travels through a drift chamber, it ionises the gas within the chamber, resulting in what are known as ionisation clusters, which create electrons. These electrons then drift to the anode wire, where they create an avalanche producing an observable signal [126].

  The other concept that it uses is the phenomenon of transition radiation (TR). When an ultra-relativistic charged particle traverses the interface between two media with different

dielectric constants, it emits transition radiation. The Lorentz factor γ determines whether the particle emits this radiation or not. The TRT was designed to use this phenomenon, specifically to discriminate between electrons and pions up to momentum levels of ~ 100 GeV. To achieve this, the tubes are filled with a noble gas mixed with carbon dioxide and oxygen. In Run-2, a mixture of 70% Xe, 27% CO_2, and 3% O_2 was mainly used. Transition radiation photons (soft X-rays) emitted in the process are typically absorbed by the gas inside the straw tube. Xenon is the first choice, due to its high efficiency in absorbing TR photons, which was the case during Run-1 and most of the Run-2 as well. However, it was substituted by Argon in straws of the modules with large gas leaks in Run-1. Argon has a much lower efficiency to absorb the TR photons in this energy range, but has similar tracking capabilities as xenon. The additional ionisation from TR increases the electric pulse height obtained in the straw tube. The signal is amplified and sent to a shape discriminator, which contains two independent discriminators that are set to different thresholds [127]: a low threshold (300 eV) for registering the passage of minimum ionising particles and a high threshold (6 keV) to flag the absorption of TR X-rays.

There are two distinct geometric configurations of straws in the TRT. The longitudinal region $|z| < 712$ mm and the radial region $560 < r < 1080$ mm are covered by the barrel section, where the straws are oriented parallel to the direction of the beam axis [126]. In the two end-cap portions, covering the regions $644 < r < 1004$ mm and $827 < |z| < 2744$ mm, the straws are oriented perpendicular to the beam axis and pointed outward in a radial manner. The TRT acceptance range is only $|\eta| < 2.0$ and has a point resolution of 130 μm [127].

From the inner detector, a momentum estimate of the particle can be obtained. The extent of the bending of the track due to the applied magnetic field gives the momentum. The final momentum resolution (p_T in GeV) is thus given by [124]:

$$\frac{\sigma_{p_T}}{p_T} = 0.05\% p_T \oplus 1\% \tag{3.5}$$

3.3.4 Calorimeters

Calorimeters measure the amount of energy a particle loses as it passes through the detector. It is designed to stop or "absorb" the majority of particles resulting from the collision, forcing them to deposit all of their energy within the calorimeter through a shower of particles. They are made up of "passive" or "absorbing" high-density material, like lead, alternating with layers of an "active" medium, such as plastic scintillator or liquid argon. The absorber reduces the energy of the particle and the active medium allows for the energy of the particle to be measured. They can be mainly categorised into *homogeneous* and *sampling* calorimeters. Homogeneous calorimeters are composed of a single material throughout the calorimeter volume, which acts as both the active medium and the absorber. The particle is observed through scintillation light or Cherenkov radiation, or in the form of an ionisation signal. Sampling calorimeters on the other hand, have different layers of absorber and active detector material sandwiched between each other.

The basic calorimetric system in ATLAS uses sampling calorimeters with alternating absorber and active material layers. ATLAS calorimeters can be categorised into two types:

the electromagnetic calorimeter (ECAL) and the hadronic calorimeter (HCAL). The ECAL, covering the pseudorapidity region $|\eta| < 3.2$ is mainly used for electrons and photons, while the HCAL, covering $1.5 < |\eta| < 3.2$ in the end-cap and $3.1 < |\eta| < 4.9$ in the forward region, is able to estimate the energy of hadrons [128] as well. Unlike the inner detector which can only detect charged particles, the calorimeter also estimates the energy of neutral particles.

- **The Electromagnetic Calorimeter (ECAL):**
  The energy of electrons and photons inside the detector is measured by the electromagnetic calorimeters. It consists of thin ionising chambers filled with liquid Argon as detection layers, alternating with the lead layers where particles form showers. It has an accordian geometry which provides a complete symmetry in the ϕ-plane without any azimuthal cracks [112].
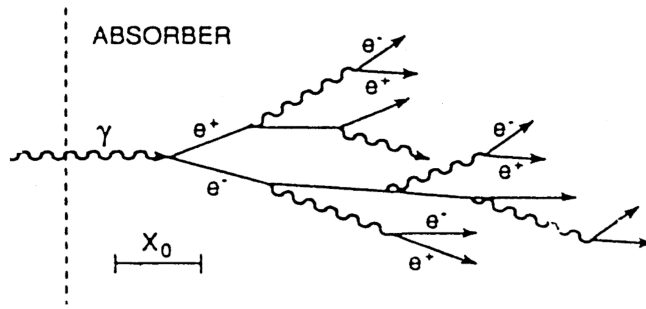
Figure 3.8: Schematic diagram of the electromagnetic shower [129].

When a photon travels through the calorimeter, it produces an electron-positron pair. The electrons produced in this manner, as well as those resulting from the collision, undergo a bremsstrahlung process, generating a photon. This photon further produces an electron-positron pair and as a result, this chain multiplies further. This process is depicted in Figure 3.8. The distance that an electron covers losing $1/e$ of its initial energy due to bremsstrahlung, is known as the radiation length X_0. It is a property of the material of the absorber. The EM calorimeter has a total thickness of $> 24X_0$ in the barrel region and $> 26X_0$ in the end-caps, providing sufficient length to contain the majority of the EM shower [119]. As soon as the energy reduces to what is known as the crititcal energy E_C, the energy losses through ionisation take over compared to the breamsstrahlung happening before. It lacks the energy to continue the process, and slowly the number of particles in the shower decrease and this *electromagnetic shower* stops.

The energy resolution of an ECAL for a particle with energy E passing through it is given by [130]:

$$\frac{\sigma_E}{E} = \frac{a}{\sqrt{E}} \oplus \frac{b}{E} \oplus c \tag{3.6}$$

where a is the stochastic term caused by fluctuations related to the physical development of the shower, for example, the event-by-event fluctuation in the energy deposition in the active medium; b is referred to as the noise term, which originates from the electronic noise of the readout chain and depends on the detector technology and on the features of the readout circuit; and c is a constant term that includes contributions which do not depend on the energy of the particle, such as imperfections in the detector mechanical structure and radiation damage effects. The three terms are added in quadrature (using $\oplus$)

in order to obtain the net energy resolution. For the ATLAS ECAL, the stochastic term is of the order 10%, and the constant term is around 0.7%. The noise term is usually small of the order of MeVs [131].

- **The Hadronic Calorimeter (HCAL):**
  Hadronic calorimeters sample the energy of hadrons as they interact with atomic nuclei, inelastically. This primary interaction produces secondary hadrons, which can interact again, producing a shower. Hadronic cascades are much more complex than the EM ones due to the presence of strong interactions, as shown in Figure 3.9.
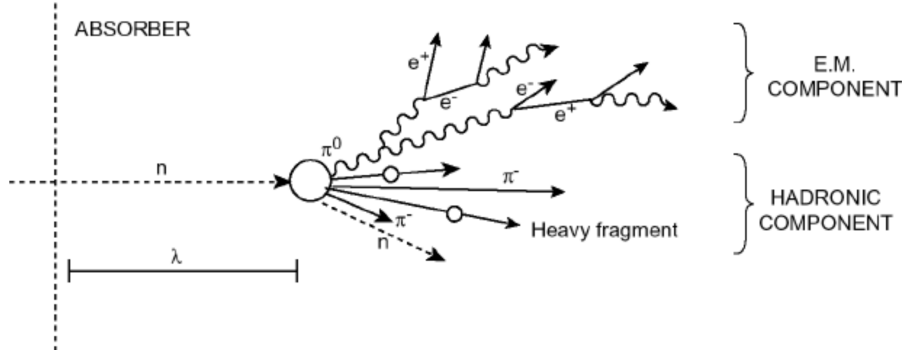
Figure 3.9: Schematic diagram of the hadronic shower [129].

The shower produced in the HCAL is expressed in terms of interaction length λ instead of X_0 used in case of the ECAL. It is a property of the absorber medium defined as the average distance traveled by a high-energy hadron inside that medium before a nuclear interaction occurs [132]. It is inversely proportional to the total cross-section of the nuclear reactions. The HCAL consists of much more material than the ECAL, ensuring that the hadrons are absorbed completely. To detect shower particles in the barrel region, scintillation tiles are put into use, and in the forward sections, liquid Argon chambers are used for detection. Hence, there are two types of calorimeters that are used as HCAL namely, the tile calorimeter, as well as the liquid Argon (LAr) calorimeter.

The tile calorimeter envelops the ECAL. The barrel covers the region $|\eta| < 1.0$, whereas the two extended barrels cover the range $0.8 < |\eta| < 1.7$. Steel serves as the absorber in this sampling calorimeter, while the active material is scintillating tiles. Azimuthal partitioning of the barrel and extended barrels yields 64 modules. The total detector thickness at the outer edge of the tile-instrumented region is 9.7λ at $\eta = 0$ [112].

LAr hadronic calorimeters are present in the forward region as well as the end-caps. Built approximately 10 interaction lengths deep, the LAr forward calorimeter (FCal) covers a region of $3.1 < |\eta| < 4.9$. It is made up of three layers, the first with copper as an absorber and the latter two with tungsten. It utilizes LAr as the active medium. The one in the end-caps is called as the LAr hadronic end-cap calorimeter (HEC) covering a region of $1.5 < |\eta| < 3.2$. It consists of two independent wheels per end-cap, located directly behind the end-cap ECAL. Copper plates with a thickness of 25-50 mm act as an absorber, which is interleaved with 8.5 mm LAr gaps, providing the active medium for this sampling calorimeter.

The energy resolution follows the same expression as given in Equation 3.6. The complex shower in the HCAL has the electromagnetic component as well as the hadronic component,

which makes the resolution worse compared to the ECAL. For the barrel and end-cap regions, the factor *a* is 50% for HCAL, and the constant term is 3%. For the forward region, the resolution becomes much worse, with *a* corresponding to 100%, and the constant term to 10%.

3.3.5 The Muon System

Muons usually pass through the calorimeters undetected. Therefore, a specialised muon spectrometer is designed for muon detection which is placed as the outermost layer of the ATLAS detector. It is based on the deflection of muon tracks in the presence of an applied magentic field using large superconducting air-core toroid magnets. The magnet design generates a field that is predominantly orthogonal to the muon trajectories, while minimising the loss of resolution resulting from multiple scattering[5] [112, 133].
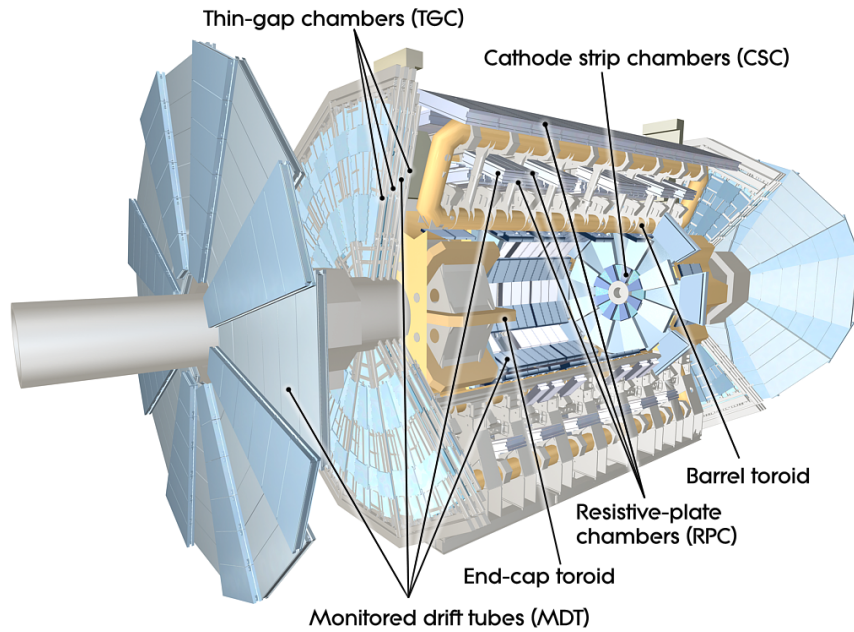
Figure 3.10: Layout of the muon spectrometer highlighting the different components used to measure muon properties [119].

Equipped with high-precision tracking chambers, the muon spectrometer is designed to measure the transverse momentum of muons with $p_T > 30$ GeV and has a resolution of 3% for $p_T < 250$ GeV and an increased resolution of 10% for 1 TeV muons [133]. It consists of four components: monitored drift tubes (MDTs) for precision tracking, Resistive Plate Chambers (RPCs) and Thin Gap Chambers (TGCs) for triggering in barrel and end-cap regions, respectively, and Cathode Strip Chambers (CSCs) for precision measurements in the high-rate endcap inner layer where MDTs would have occupancy issues. Figure 3.10 illustrates the positioning of each component in the ATLAS detector.

---

[5] Multiple scattering is a phenomena that happens when a particle starts interacting with nuclei of the detector material. This deviates the particle tracks from their original path.

- **Monitored Drift Tube (MDT):** (Resolution: 35 μm (z))

  These are pressurised drift tubes with a diameter of 29.97 mm, filled with a gas mixure of 93% argon and 3% CO_2 at a pressure of 3 bars. A 50 μm thick gold-plated tungsten-rhenium wire passes through the centre of the tube which acts as the anode. It is present in the barrel as well as the end-cap region covering a range of $|\eta| < 2.7$. Each tube has a standalone resolution of 80 μm. To perform a precise tracking, they are layered with 3 to 8 tubes, achieveing a resolution of 35 μm per chamber.

- **Cathode Strip Chamber (CSC):** (Resolution: 40 μm (R) $\times$ 5 mm (ϕ) $\times$ 7 ns (t))

  To support the MDT operation at high pseudorapidity values, an extra detector CSC is inserted, spanning the forward area of $2 < |\eta| < 2.7$. The CSCs use the geometry of a *Multi-Wire Proportional Chamber* (MWPC) with a segmentation of the cathode planes into strips. MWPC is a grid of regularly spaced anode wires stretched inside an extended gas volume, enclosed by two cathode planes. In this setup, a uniform drift field can be obtained. Once a particle ionises the gas, the charges split and drift in the nearly uniform electric field. As the parallel field lines approach the wire grid, they change into a radial configuration with increased field intensity at small anode distances. It triggers the amplification process, and a signal is detected on the readout structures at the cathode [134]. Using a gaseus mixture of argon and CO_2 in 80:20 ratio, CSC reaches a spatial resolution of 40 μm.

- **Thin Gap Chamber (TGC):** (Resolution: 2-6 mm (R) $\times$ 3-7 mm (ϕ) $\times$ 4 ns (t))
  & Resistive Plate Chamber (RPC): (Resolution: 10 mm (z) $\times$ 10 mm (ϕ) $\times$ 1.5 ns (t))

  TGCs and RPCs are primarily used for *trigger* purposes to provide fast information (within 15-25 ns) on whether there is a muon traversing the detector. They additionally also provide information about the trajectory followed by it.

  The muon trigger in the barrel region ($|\eta| < 1.05$) consists of RPCs. It is a gaseous detector with 2 mm gas-gaps in between two parallel resistive plates made of Bakelite. The plates are operated at a voltage difference of 9.8 kV, as a result of which a charged particle crossing the gas-gap creates an avalanche of electrons drifting towards the anode [135], and a signal is read out.

  For the end-cap region ($1.05 < |\eta| < 2.4$), a TGCs are chosen, which are multiwire proportional chambers. With a gas-gap of 2.8 mm, 50μm wires are operated at 2.9 kV, using a gas mixture $CO_2 : \text{n-}C_5H_{12} = 55 : 45$. This is a special gas mixture because it is a purely quenching gas that helps reduce the dead time of the detector. The electric field configuration and the small wire distance provide for a short drift time and hence a good time resolution. This is important for bunch crossing identification for which it only has a time window of 25 ns.

3.3.6 Trigger and data-aquisition system

The proton-proton collisions at the LHC take place at a rate of 40 MHz, which leaves a time of merely 25 ns between two bunch-crossings [98]. At that high interaction rate, it is impossible to record and save the entire data with current technology. Furthermore, it also not necessary because a substantial portion of data observed at the collision point holds no information that could be of interest. A trigger system is thus needed, which manages the process of data

collection, serving one of the most essential requirements of the detector. It helps filter out the events which are not intersting from physics side and saves only the data that is usable. Figure 3.11 gives an overview of the trigger strategy used in ATLAS. The ATLAS trigger and data-acquisition (TDAQ) system is based on three levels [136, 137], each of which refines the decisions made at the previous level.
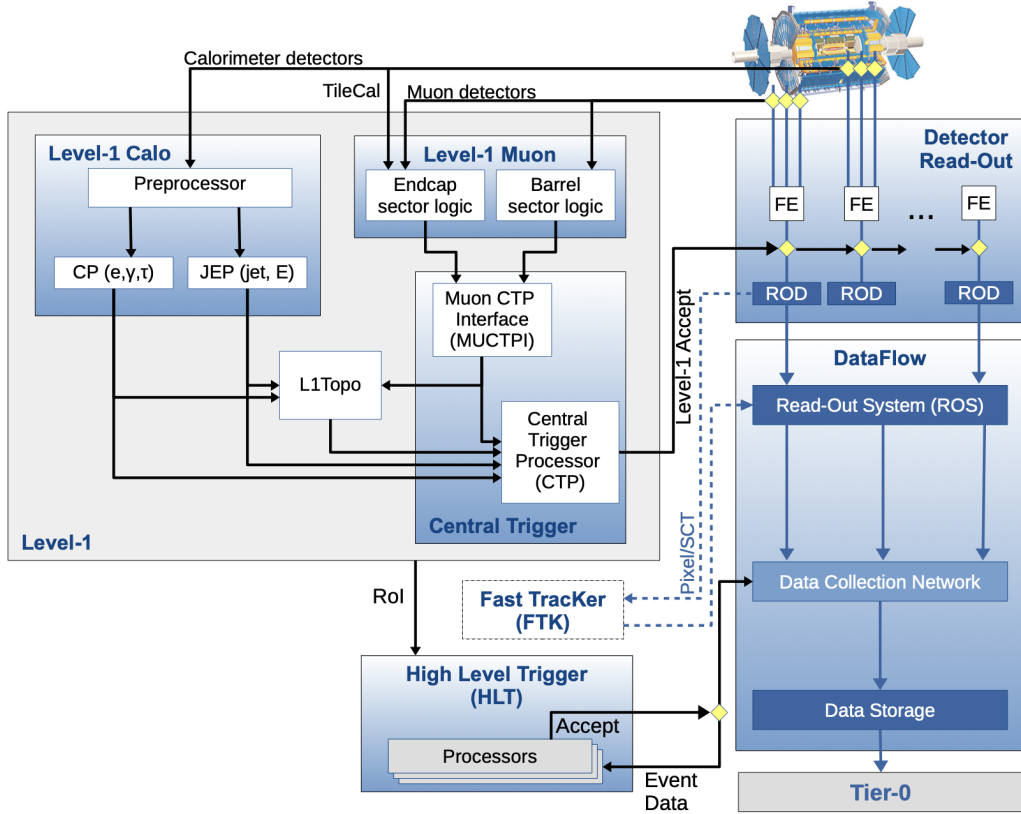

Figure 3.11: Flowchart of the ATLAS trigger and data acquisition system. The upper block shows the events within Level 1 (L1) trigger, and the lower block shows the second level, the High Level Trigger (HLT). On the right, the flow of data is shown, as passing from L1 to HLT to the final storage unit. Figure taken from [138].

The first stage is the hardware-based Level 1 (L1) trigger that receives reduced-granularity information from the calorimeter and muon detectors and makes a selection [139]. Muons with high p_T are identified by the trigger chambers in the muon spectrometer (L1Muon). Calorimeters search for coarse information such as the high p_T and large transverse energies (L1Calo) and provides it to the dedicated processors. The Cluster Processor (CP) identifies the electron, photon and τ-lepton candidates above a certain threshold, and the Jet/Energy-sum Processor (JEP) identifies the jet candidates and produces total and missing transverse energy values. All this information is sent to the central trigger processor (CTP) which makes the decision whether or not to further process the event. The data for the events that are approved by the L1 trigger is then read out by the Front End (FE) electronics for all detectors. Before being transmitted to the ReadOut System (ROS) to be buffered, the data are first sent to ReadOut Drivers (RODs), which handle the first formatting and processing. Additionally, L1 triggers identify specific regions in η and ϕ within the detector, known as the Regions-of-Interest (RoIs) which are sent further to be

investigated by the second trigger stage. The majority of physics requirements can be satisfied by applying this relatively straightforward selection criteria at the L1 trigger level itself. The L1 trigger, which receives information at the rate of 40 MHz, with these selection criteria can reduce the amount of data to get an event rate of around 75-100 kHz [137].

The second stage is the software based High Level Trigger (HLT) [140], which uses complex CPU-intensive algorithms to make the final selection. It receives the data from the ROS as well as ROIs and provides an early rejection using fast trigger algorithms. As the next step, it executes the algorithms on a dedicated computing farm with around 40000 processing units (PUs). In this way, the HLT is able to further reduce the event rate from 75-100 kHz to around 1.2 kHz [138], making it practically possible to store.

The data are then saved coresponding to different requirements through the application of *trigger chains*. These trigger chains select events using L1 trigger items and HLT algorithms to reconstruct physics objects and to apply kinematic selections. Each chain is designed to select specific physics signatures such as leptons, jets, missing transverse momentum, and *B*-meson candidates. Subsequently, the physics analysis can make use of the data associated with a particular trigger chain.

Monte Carlo simulations

The production cross-section of different particle states from proton-proton scattering can be theoretically estimated as described in Section 2.3.2. However, as one progresses through higher orders in perturbation theory, computation of the corresponding scattering amplitudes gets increasingly difficult. Many additional partons enter the process in the form of initial- and final-state radiation. Moreover, for the perturbative part, the calculations can be done theoretically using Feynman graphs, but for the non-perturbative part, the solutions using Feynman graphs break down due to large α_s values [141]. There have been many developments in the past devising techniques to simplify the calculation process. Since the non-perturbative part can not be calculated from the first principles as of now, one needs phenomenological approaches to get an estimate. This complex task can be accomplished through computer simulations using Monte Carlo techniques. Because the cross-section computations are factorisable, they can also be made more accurate by replacing them with a more advanced hadronisation model or a more precise perturbative calculation when they become available.

In experimental studies, often the entire analysis is first prepared on the Monte Carlo simulated events. Additional simulation for the detector response, which simulates the condition of particles inside the detector, such as their interaction with the detector material and the generation of signal in the subdetectors, are therefore incorporated into the Monte Carlo samples, and a *predicted result* is obtained. This result can then be compared with the results from the analysis of data collected from the detector. Event simulations thus act as a bridge between the theoretical expectations and the experimental observations.

This chapter focuses on the techniques used to perform the cross-section calculations and event generation through Monte Carlo simulations. Beginning with the calculation of the collision process, this chapter moves on to the details of the parton shower and hadronisation. Consequently, particles stable enough to be observed in the detector are obtained. Thereafter, detector information is used to simulate particle interactions within the detector. A brief description of the generators used in this thesis is also provided. The theoretical description used in these sections are majorly based on the reference [141].

4.1 Event generation

The modelling of an event should include the description of all the processes taking place to create the final states as seen by the detector. In a proton-proton interaction, the partons from the protons interact and create new partons. Revisiting Equation 2.27, the cross-section of this interaction, known as the hard interaction, is described by a calculation based on Feynman graphs, also referred to as the matrix element calculation. This however, does not describe the
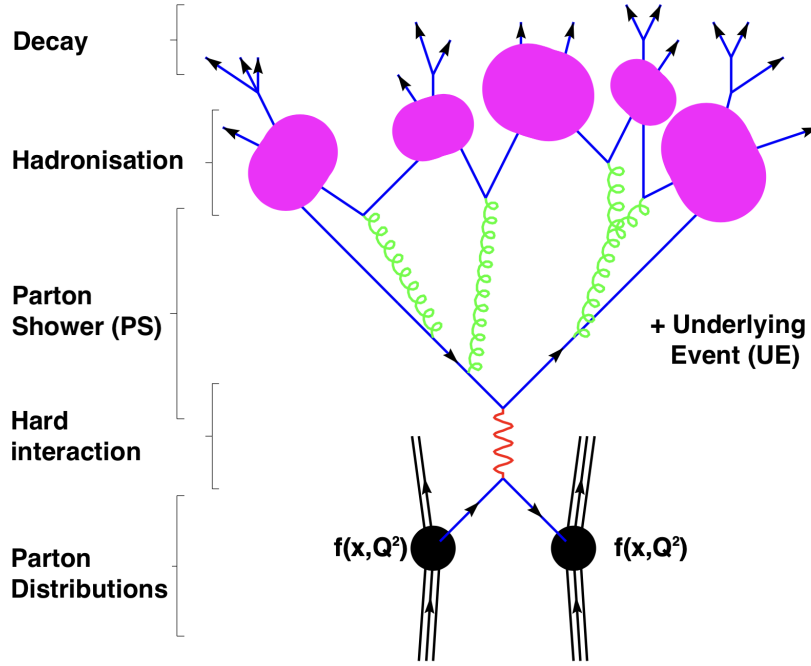
Figure 4.1: Illustration of the processes contributing to a Monte Carlo event generation. Figure adapted from [142].

cross-section fully, rather there are additional interactions which need to be included in order to get the entire picture. Figure 4.1 gives a flowchat of the processes taking place in the event of a proton-proton collision. The leftover partons inside the proton which are not considered in the calculation of the hard interaction would also interact and contribute to the final state. This contributes to the so-called underlying event (UE). Particles exhibiting charges, electric or colour, may emit additional particles in the initial or final states in the form of initial state radiation (ISR), and final state radiation (FSR). Further evolution of these partons with increasing α_s values are described in the so-called parton shower (PS). Moving further to even larger α_s, the perturbative QCD breaks down, and phenomenological models are considered to describe the process of fragmentation of the partons. In this process, partons combine or hadronise to form colour neutral particles, which may decay further to form more stable states. The following sections will give an overview of each step that is necessary to generate a Monte Carlo sample which can be used for physics analyses, specifically motivated in the context of this thesis.

4.1.1 Matrix element

Hard interaction corresponds to the part of an event involving large momentum transfers, implying that particles with high p_T or large masses can be produced. As a result, it serves as the primary contribution to the final cross-section value. In a proton-proton collision process, the cross-section can be written in terms of the PDFs of individual partons from the proton and the cross-section of the parton-parton interaction. This represents the hard interaction and the

equation can be decomposed into a form as shown below [141]:

$$
\sigma_{pp \to XY}^{\text{hard int.}} = \sum_{i,j} \int \int \underbrace{dx_i dx_j}_{\text{Initial State phase space}} \times \underbrace{f_i(x_i, \mu_F^2) f_i(x_i, \mu_F^2)}_{\text{Parton Distribution Functions}} \times
$$
$$
\underbrace{\frac{1}{2\hat{s}}}_{\text{incoming flux}} \times \int \underbrace{d\Phi_{XY}}_{\text{Final State phase space}} \underbrace{|\mathcal{M}_{ij \to XY}|^2 (\Phi_{XY}; \mu_R^2, \mu_F^2)}_{\text{Matrix Element}}
$$

(4.1)

where $\hat{s}$ corresponds to the square of the centre-of-mass energy of the hadrons. The terms in the second line of the equation originate from the parton-level cross-section for the production of the final states X, Y from the initial partons i, j. It is dependent upon the momenta provided by the factorisation scale μ_F, the renormalization scale μ_R, and the final-state phase space Φ_{XY}. The parton-level cross-section is given by the product of the corresponding squared ***Matrix Element*** (ME) (averaged over initial-state spin and colour degrees of freedom) $|\mathcal{M}_{ij \to XY}|^2$, and the parton flux $1/(2\hat{s}) = 1/(2x_i x_j s)$, integrated over the final phase space Φ_{XY}.

Under the assumption that partons are asymptotically free at such high energies, the ME calculation can be described by the perturbation theory upto all orders. However, calculation of the ME above the LO, brings up several difficulties including divergent integrals. Thus, most Monte Carlo generators consider only NLO matrix elements. Because of the significant higher-order corrections, the differential cross-section distributions are not well-defined. For this reason, while comparing outcomes from event generators with experimental data, a so-called *K-factor* is frequently seen, which is multiplied to the NLO cross-section. It is obtained by dividing the total NNLO cross section[1] for the relevant process by its NLO cross section.

4.1.2 Parton shower

Partons and gluons involved in the collision process radiate additional gluons. Owing to the colour charge of the gluons, this radiation causes further gluon radiations, and the creation of quark-antiquark pairs, and this process continues creating a *shower* of particles. The simulation of parton shower allows for the inclusion of the corresponding soft terms arising from possible low momentum emissions, as well as collinear terms emerging from small angle emissions. It effectively aims to simulate higher order effects not described by the LO or NLO matrix element, and thus includes the resummation of leading logarithmic contributions. Higher order diagrams are therefore treated the same as the NLO diagram with additional emissions from the parton shower. When the emissions take place after the collision process, they are referred to as ***final-state radiation*** (FSR). It is also possible to emit these radiations before the collision and have this parton showering in the initial state. They are termed as ***initial-state radiation*** (ISR).

An energy-dependent scale μ, also referred to as the "evolution scale", is used to order the new emissions in the PS following the DGLAP evolution equations. Depending on the PS model, the evolution scale has a different meaning. A term called Sudakov form factor gives the probability that a parton does not split between the two energy scales μ_1 and μ_2, where $\mu_1 > \mu_2$. A user-defined scale μ_{max}, often selected based on the hard process, determines where the PS evolution begins. By using the input scales $\mu_1 = \mu_{\text{max}}$ to solve the Sudakov form factor, the scale μ_2 of the new emission may be determined, leading to the generation of the corresponding

---

[1] It is usually possible to obtain the total cross-section an order higher than the differential cross-section.

emission. Up until the energy reaches the so-called cut-off scale $\mu_{\min}$, the PS iteratively evolves. Generally, perturbation theory is not relevant below Λ_{QCD}, or at the order of 1 GeV, defining it as the $\mu_{\min}$ [143, 144].

4.1.3 Matching of matrix element with the parton shower

Matching is a procedure that connects the hard-scatter generator to the parton shower such that it encompasses the full evolution of the event, from the partonic process to the inclusion of additional radiations by initial and final state particles. Care needs to be taken so as to cover the full phase space without leaving holes or doubly counting the regions of the radiation phase-space. In matching approaches, the processes from the matrix element at a given order which are matched to their corresponding parton shower are *vetoed* from an additional calculation in the parton shower [145].

4.1.4 Fragmentation and hadronisation

The particles produced after the parton shower must form colour neutral states to create more stable composite particles, mesons or baryons. Approaching the cut-off scale $\mu_{\min}$, the parton shower evolution enters a non-perturbative regime where the strong coupling constant reaches larger values ($\alpha_s \approx 1$) [144]. The process of hadronisation, or the formation of hadrons from the available partons in the event, is the direct result of colour confinement below this cut-off scale. Since the perturbative theory is unable to describe the hadronisation process, it is modelled phenomenologically [144].

The two most commonly used models are the string model and cluster model. In the *Lund string model* [146–149], when a quark and an antiquark separate, a colour field of narrow width is stretched between them. This field is usually represented by a relativistic string that can be broken repeatedly producing quark-antiquark pairs. These pairs combine to form a jet of hardons travelling in two separate directions. Partons are arranged in colour along the string, and a quark is analogous to the string's endpoints and a gluon to a kink on it. The main limitation of this model is that it relies on data to determine numerous characteristics linked to flavour properties.

The preconfinement theory [150] of parton shower serves as the foundation for the other widely used hadronisation model, the *cluster model* [151]. In this model, gluons are splitted non-perturbatively into quark-antiquark pairs carrying colour charges. Since parton showers are usually formulated in the limit of infinitely many colours, each coloured quark can be paired with an anti-quark of the same anti-colour. The colour-anti-colour pair then creates a colour-singlet cluster i.e. a cluster with no colour charge. Upon combining with an appropriate PS, the cluster model provides a reasonably good description of the decay to form stable state particles.

4.1.5 Underlying event

In a collision process, the hard interaction takes place among partons from each of the two incoming protons involving a large momentum transfer. However, the residual partons may suffer additional scattering not directly associated to the hard interaction, known as the underlying event (UE) [152]. These processes usually involve soft collisions (with low momentum transfer), but they can still contribute to the final state producing new particles.

In summary, the final cross-section is a result of the convolution of several effects. Parton shower, which comprises the ISR, FSR, and higher order effects, must be added to the ME computation for the hard interaction. It is also necessary to imitate the UE as accurately as possible. Ultimately, the generated particles hadronise to produce colour-neutral particles, which may further decay to form more stable particle states.

4.2 Available MC generators

While some MC generators only simulate the ME and must be interfaced with a PS modelling in order to get the full picture, some others have the possibility to simulate the ME, PS, hadronisation as well as the UE. A short overview of the Monte Carlo generators used in this thesis is given below.

- POWHEG-BOX [153]: This software framework implements the construction of the hard process using matrix element calculations with NLO accuracy. It needs to be interfaced with a parton shower and hadronisation generator following POWHEG[2] approach [154, 155] for matrix element matching to obtain a description of the collision process.

- MADGRAPH5_AMC@NLO [156, 157]: Similar to POWHEG-BOX, this framework can also perform the matrix element calculations at NLO. The simulation of parton shower and hadronisation can be convoluted via an interface through a general purpose MC generator.

- PYTHIA [158]: It is a general-purpose event generator that has the provision to include the hard interaction for a number of processes, but is extensively used for its parton shower and hadronisation capabilities. It uses the Lund string model for hadronisation simulation, and can be interfaced with the outputs of various external matrix element generators such as POWHEG and MADGRAPH5_AMC@NLO.

- HERWIG [159, 160]: This is also general-purpose event generator which features automatic generation of hard processes and has a built-in matching of many hard processes at NLO with the POWHEG method. It implements the cluster method for hadronisation process, and is widely used as a parton shower and hadronisation tool interfaced with other matrix element generators.

- SHERPA [161]: Yet another general-purpose MC event generator, SHERPA exhibits a NLO matrix element calculation with additional emissions described through a parton shower model. Like HERWIG, it uses the cluster model to simulate the hadronisation process. This generator includes its own matrix element as well as parton shower calculations, and does not have the flexibility of being used in combination with other matrix element or parton shower generators.

- EVTGEN [162]: This is a MC simulation package that provides a framework for the implementation of physics processes specifically relevant to decays of heavy flavour resonances, such as the *B*-meson decays which has a complex decay chain.

There are several free parameters in each of these models, which can be optimised in order to obtain a description that better explains the observables. This optimisation process is known as

---

[2] abbreviated for "Positive Weight Hardest Emission Generator"

MC tuning, and the resulting parameter sets are called MC generator tunes [163]. These free paramters can tune, for example, the ISR/ FSR contribution, shower damping (with a parameter called h_{damp}), multiple parton interactions, so as to provide a good description of data.

4.3 Detector simulation

The MC generators described thus far replicate a proton-proton collision event. However, the simulation at this stage does not describe the state of events inside the detector, and hence it must be made to match the conditions from raw data collection at the detector. The introduction of a detector around the interaction point induces a variety of effects on the generator output. The produced particles may interact with the detector's material, which may vary depending upon the geometry of the detector and the position of the particle in space. Long-lived particles may cause secondary interactions which may impact the observed final state. There are several more scenarios that can influence the detector response. As a result, a detailed simulation must be implemented that modifies the events from event generator to create an output in a format that incorporates the conditions inside the detector. The output so produced is saved in a digitised format containing information on the signal produced inside the detector as a consequence of the traversing particles. The events are then passed through the triggers for filtering purposes, and the processing on the simulation is identical to that on the data.

ATLAS uses GEANT v4 [164–166] simulation toolkit to simulate the detector response. Two main types of simulation procedures used in ATLAS. The first procedure is the full simulation (FULLSIM) which investigates the effects due to noise, calibration and intercalibration of calorimeters, shower development, pile-up, cracks, etc. in detail. The other commonly used one is the fast simulation which provides an overview of the event topology in a simplified format. Instead of using a detailed description of the showering process, it relies on the parametrisation of the detector information. This type of simulation is typically used for quick estimates of signal and background rates for specific channels. For some cases, the fast simulation ATLFAST-II [167] (AFII) is the only practical tool for high statistic analyses of complex background processes.

After the simulation process finishes, the response signals from different parts of the detector are digitised into a readable format. The simulations are processed in different stages and a few definitions are frequently used to account for these stages of simulation development. One of the stages is the *truth level* or the *generator level*, which contains no information regarding the detector simulations. The other stage most commonly used is the *detector level* or the *reconstruction level*, which comes after the GEANT v4 detector simulation is processed and the reconstruction of the physics objects is completed. This stage is used to conduct the analysis which requires a comparison with data. Truth level on the other hand, serves many other useful purposes. It is used in this thesis, for example, to obtain event weights for Y_t corrections corresponding to different Y_t values, which is one of the key ingredients for this analysis.

Object reconstruction and event selection

Particles pass through a sequence of subdetectors inside ATLAS, each subdetector designed to measure specific parameters such as the particle's energy, momentum, position, etc. A signal is generated in these subdetectors as the particles traverse through them. These electronic signals are read out from each component of the detector and combined together to reconstruct primarily the particle's track, momentum, and energy. Additionally, this information is combined to construct so-called *jets*, which are collimated sprays of hadrons, usually associated with the production of quarks and gluons [168]. This is also used to identify the particle and distinguish it from the rest of the particles in the event which may appear from the underlying event and pile-up.

This chapter covers the concept of how these parameters of interest, known as *physics objects*, are reconstructed in the ATLAS detector. Starting from the definition of tracks and vertices, this chapter goes on to explain the reconstruction of electrons and muons. Since coloured particles hadronise, their signature in the detector is different (roughly a bundle of particles instead of one, forming a *jet*), and hence their reconstruction follows a dedicated algorithm which will be covered in detail in Section 5.1.4. Once the objects have been obtained, the events required for the analysis must be selected. A chain of fast reconstruction algorithms from the triggers are used to perform the first filtration, after which analysis-specific selections must be applied. The last section (Section 5.3) is dedicated to the reconstruction of the parameter of interest used in this thesis, which is the invariant mass of the two top quarks.

5.1 Object reconstruction

The reconstruction of physics objects is a result of the interpretation of the raw signals collected at the detector. Figure 5.1 shows the path of different particles and their interactions as they traverse through the ATLAS detector. Electrons and photons exhibit electomagnetic showers in the calorimeter and deposit almost their entire energy inside the ECAL. Muons, on the other hand, do not exhibit energy loss in the same manner as electrons. Due to their minimal interaction in the inner and middle regions of the detector, their properties are often reconstructed by combining the data additionally from the muon spectrometer. The heavier particles such as the protons and neutrons lose some part of their energies in the electronic calorimeter and the rest in the hadronic calorimeter, where they are almost completely stopped.

Additionally, the electrically charged particles show bent trajectories due to the Lorentz force [170] experienced by them in the applied solenoidal magnetic field. The force acting on
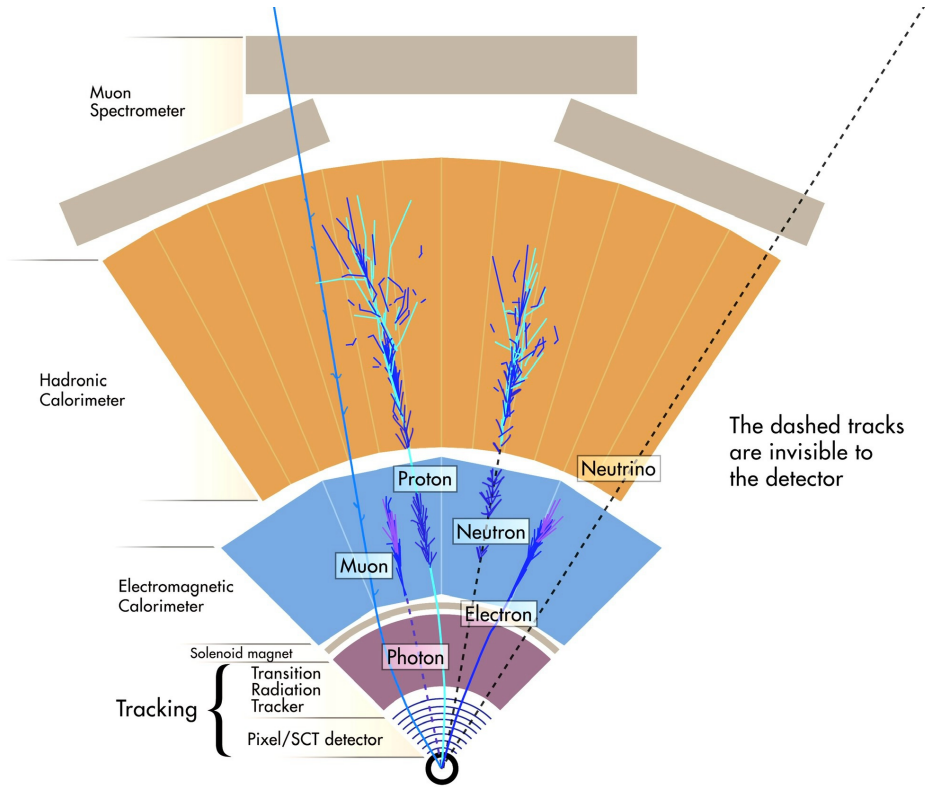
Figure 5.1: Tracks of particles as they travel through the different components of the ATLAS detector. Dashed lines in the figure show the tracks which are not observed by the detector. They may only be reconstructed back using complete data for that event. Figure adapted from [169].

the particles determines their direction of motion based on their charge, causing oppositely charged particles to be bent in opposite directions. In this thesis, where the signal sample is the production of a top and an antitop quark in the final state via a single-leptonic decay channel, the reconstruction of certain objects is necessary. The following sections cover the reconstruction of electrons, muons, jets (originating from quarks), and neutrinos, i.e., the objects that are important for the analysis. Starting with the basic information about the tracks and vertices, further details about the identification of jets containing a b-quark is provided. Additionally, Section 5.1.5 describes how to eliminate repeated counting of events which may occur due to misidentification of particles.

5.1.1 Tracks and vertices

Tracks in the ATLAS detector are expressed using five parameters $(d_0, z_0, \phi, \theta, q/p)$, defined as follows:

- d_0: impact parameter of the track in the transverse plane (xy-plane) defined as the distance of closest approach of the track to a reference point in the xy-plane

- z_0: impact parameter of the track along the longitudinal axis (along the z-axis) defined as the z-position of the point where the d_0 is assumed

- ϕ, θ: the azimuthal and the polar angle of the track, respectively

- q/p: ratio of the electric charge over the momentum of the particle

The point with respect to which these parameters are evaluated, the reference point, is usually chosen to be the *beamspot*, which is defined as the average position of the proton-proton interaction. Later when more information is retrieved, the primary vertices for the interactions in the event are also reconstructed.

Track reconstruction

Tracks of charged particles are reconstructed by combining the information from different layers of the inner detector. When a charged particle interacts inside a subdetector creating a signal, it is said that a *hit* has been recorded. In the pixel and the SCT sensors, the hits which deposit a charge above a certain threshold are grouped into clusters. These clusters provide three-dimensional measurements known as space-points [171], which indicate the locations traversed by the charged particle in the active material of the ID. Clusters in the SCT need to be combined from both sides of a strip layer in order to yield a three-dimensional measurement, while in the pixel detector, each cluster represents one space point. Specialised clustering techniques [172] are used to identify complicated clusters, such as the clusters for tracks in dense environments where the spatial separation between different particles is small.

Thereafter, the track reconstruction algorithm consists of several steps. An iterative track finding algorithm gets the so-called track seeds from the clustering process. Sets of three space-points act as track seeds or inputs to the algorithm. This algorithm follows an *inside-out* [173] approach that relies on the track seeds starting from the innermost pixel layer. Once the seeds are formed, a rough estimation of seed parameters (d_0, z_0, etc. as defined above) are obtained. A selection is applied on the seeds so as to improve the fraction of seeds resulting in good quality tracks. These selected seeds are passed to a combinatorial Kalman fitter [174] which builds track candidates from the chosen seeds while incorporating additional compatible space-points from the remaining layers. If there are several compatible space-point extensions on the same layer, it creates multiple track candidates per seed. Based on certain track quality measures, a score is given to each track candidate. The candidates with a greater potential of correctly describing the particle's trajectory are assigned a higher score, for example, the candidates with large energies are assigned a better score as the lower energy candidates are more probable to be associated with an incorrectly assigned space-point. If the χ^2 of the track fit is poor, the candidate is assigned a lower score. After considering a number of such track quality measures, the track score is finalised. Subsequently, at the *ambiguity solver* stage, the cases with multiple track candidates assigned to the same cluster are resolved using a sequence of requirements. A cluster can not be shared by more than two tracks. There can be at most two shared clusters associated to a track. The candidates must pass several additional selections [171] so as to be sent to the next stage at which it is compared with the information collected in the TRT subdetector. At this step of extension to the TRT, a test is done to check if the selected track candidate left a hit in the TRT confirming the particle track. The quality of this test is evaluated using a fitting procedure and a track score is obtained similar to the ambiguity solver stage.

In the next iteration, an *outside-in* approach is applied where TRT segments are defined in the regions seeded by the electromagnetic calorimeter. Combining the information from the

inside-out approach on the leftover hits in the inner detector and the SCT, these TRT segments are extended back and the track is obtained.

Vertex reconstruction

For an event, knowing the vertex of origin for particles that may interact or decay further is a valuable information. Reconstructing the vertices also provides a better description of the decay chain for heavier particles like the *B*-hadrons, which decay travelling a certain distance after getting produced. Vertex reconstruction follows a specific algorithm as described in the reference [175]. It involves a selection of tracks based on a predetermined quality criteria. Vertex seeds are generated from the crossing-point of two or more tracks. Thereafter, the vertex position is determined from the vertex seeds and the nearby tracks using an iterative χ^2 fitting approach that looks for the compatibility that all tracks originate from the same point. The tracks incompatible with the vertex are removed so as to be assigned to a new vertex based on the χ^2 of the fit.

In this way a number of vertices corresponding to the proton-proton interactions are found, which are called primary vertices (PVs). Among these vertices, the vertex for the hard interaction corresponds to the one which has the largest sum of squared transverse momenta of all tracks belonging to that vertex [175, 176], i.e., with the largest $\sum_{\text{track}} (p_T^{\text{track}})^2$. All other PVs are termed as pile-up vertices.

5.1.2 Electrons

As described in Section 3.3.4, the electrons exhibit showers in the electromagnetic calorimeter with hardly any residual desposits in the hadronic calorimeter. These narrow clusters of energy deposits are then associated with the tracks pointing to them in order to reconstruct the electron. This is depicted in Figure 5.2 where the path of an electron can be seen pointing to an energy cluster in the EM calorimeter.
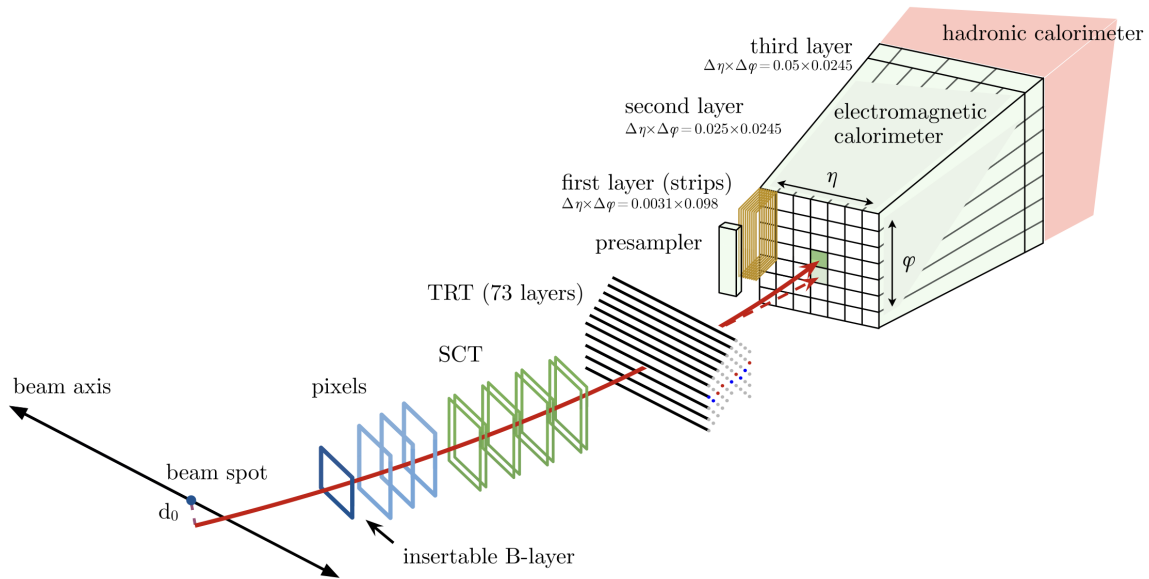
Figure 5.2: Pictorial representation of an electron traversing through the inner detector (pixel, SCT and TRT) and depositing its energy in the electromagnetic calorimeter. Figure taken from [177].

The process of electron reconstruction starts with the creation of the so-called topological clusters or *topo-clusters*. The algorithm for these topo-cluster reconstruction [178] relies on the *cell significance* which is defined as the ratio of the absolute cell[1] energy (at the EM scale[2]) over the expected cell noise. As the first step, a set of noise thresholds are defined on the cell significance. Clusters known as *proto-clusters* are formed by merging nearby cells with abosolute energies above a certain noise threshold as described in detail in reference [180]. Following the initial formation of proto-clusters, those with two or more local maxima of deposited energy above a certain threshold can be divided into separate clusters. In order to ignore the clusters originating from pile-up interactions, a lower threshold of 400 MeV on the transverse energy is set to be considered as a topo-cluster. The subsequent stage involves the matching of the topo-clusters roughly qualifying the shower and shape requirements for an electron with tracks from the inner detector. Track pattern reconstruction is performed as described in the previous section, allowing upto 30% energy loss [181] at each material intersection due to bremsstrahlung. In the next step, an *ambiguity solver* resolves the case of multiple tracks matching to a single cluster following a sequence of requirements. Once the topo-clusters are matched with the tracks, the ones with energies above 1 GeV act as seeds to the *supercluster* reconstruction algorithm. They must be associated to a matched track with at least four hits in the silicon detectors. In the following stage of *satellite finding*, the topo-cluster qualifies as a satellite if it lies within a $\Delta\eta \times \Delta\phi$ range of 0.075×0.125 around the cluster barycentre. This allows for the secondary particles showered from the same electron to be included. A broader range of 0.125×0.300 around the barycentre is also considered and if a cluster has at least one matched track within this region, the cluster is considered as a satellite. All the cluster seeds and their associated satellites then form a supercluster. In the end, multivariate algorithms are used to calibrate the energy of the electron so obtained by comparing the reconstructed electrons from data and simulation.

Due to the construction of the tracker, the $|\eta| > 2.5$ region is not covered, hence the electron reconstruction is restricted to $|\eta| < 2.47$. The region of transition between the barrel and the end-caps ($1.37 < |\eta| < 1.52$) is also excluded from physics analyses due to the presence of extra material.

Identification

Special quality criteria are used to differentiate the signals corresponding to electrons from the electron-like signals generated from other effects such as hadronic jets, noise, or converted photons [182]. Dedicated electron identification algorithms [180] are used to improve the purity of the selected electron objects. A likelihood discriminant is constructed using the track from the inner detector, the shower in the EM calorimeter, and the combined information from them both. It includes the information such as the track conditions, track-cluster matching, TRT extension of the track and the shower width in the calorimeter. From this likelihood, three working points are defined based on the average electron efficiencies. These working points (WPs), called as *Loose, Medium* and *Tight*, correspond to an average electron efficiency of 93%, 88%, and 80%, respectively at $E_T = 40$ GeV. For the *Medium* and *Tight* WPs with smaller electron efficiencies, the rejection of the background processes is better by a factor of around 2 and 3.5 with respect to the *Loose* WP, respectively.

---

[1] A cell inside the calorimeter is usually defined as the component or segment of a calorimeter equipped with its individual readout channel [179].

[2] EM scale or the electromagnetic scale corresponds to the assumption that the particle interaction is purely electromagnetic in nature.

Isolation

Considering the channel of interest in this analysis, where one of two top quarks decays via a leptonic channel, the leptons from the *W*-boson decay are the particles of interest. Hence, a presence of any particle signature other than that of a lepton is not expected. A term called *isolation* is thus defined, so as to isolate the particle of interest (also known as *prompt* particles) from the close-by objects.

Therefore, sets of isolation requirements are applied to reduce the background contribution, primarily to isolate *prompt* electrons from the *non-prompt* objects. The electrons arising from the converted photons produced in a hadronic decay and from the decay of heavy flavour hadrons come under the non-prompt category. A mis-identification of light hadrons as electrons also fall under the definition of non-prompt electrons.

The discriminating variables used for isolation purposes are based on the idea that the prompt electrons exhibit relatively little activity in their proximity. Therefore, the isolation variables rely on the sum of transverse energies from the calorimeter or the sum of transverse momenta of topo-clusters (excluding the candidate cluster) from the tracker in a certain region around the candidate electron cluster. Selections applied to these variables help to reject the background contribution to a large extent.

5.1.3 Muons

Muon information is obtained from not just the inner detector (ID), but also from the dedicated subcomponent, the muon spectrometer (MS). Being a minimum ionising particle (MIP[3]), the interaction rate of a muon is low, which is the main signature of muon identification inside the detector. For its track reconstruction, algorithms are used to obtain independent tracking from the ID, from the MS, as well as using the combined information from both the trackers. The reconstruction of a muon track inside the inner detector follows the same procedure as described in Section 5.1.1. For the standalone track reconstruction from the MS, firstly, short straight-line local *track segments* are reconstructed from the hits recorded in individual MS subdetectors [183]. These segments from different components are then combined to form preliminary track candidates. This combination of track segments is required to follow a parabolic trajectory requirement for the bending of a muon track in the magnetic field, as well as a constraint of being originated from the interaction point. After obtaining a global χ^2 fit on the muon track, the outlier hits are removed and the hits not assigned to the track candidate, but falling on the preliminary trajectory are added. The fitting is then repeated with the updated hit information. Detailed information on the reconstruction process is provided in reference [184].

A global muon reconstruction is then performed using the standalone reconstruction from the ID and the MS, as well as by adding the calorimeter information. As a result, the reconstructed muons are classified into different categories based on the subdetector primarily used for the reconstruction. *Combined muons* (CB) are identified by matching MS tracks to ID tracks and performing a combined track fit based on ID and MS hits. For $|\eta| > 2.5$, MS tracks can be combined with short track segments from pixel and SCT detectors, instead of fully reconstructed tracks. *Inside-out combined muons* (IO) are reconstructed using an inside-out algorithm, extrapolating the ID tracks to the MS. It recovers efficiencies in regions with limited

---

[3] Minimum ionising particles correspond to the particles which lose very little energy during their path, and hence are able to pass the calorimeter and reach the muon spectrometer in the ATLAS detector. These particles have a typical $\beta\gamma > 3$, where $\beta = v/c$ and $\gamma = \frac{1}{\sqrt{1-\beta^2}} = \frac{E}{m}$.

MS coverage and for low-p_T muons which do not reach the MS. If no matching ID track is found, muons can still be reconstructed by extrapolating a MS track to the beamline. These muons are called as *muon-spectrometer extrapolated muons* (ME) and are mainly intended to use the full coverage of the MS ($2.5 < |\eta| < 2.7$), which is not covered by the ID. *Segment-tagged muons* (ST) are reconstructed by matching an ID track to one or more short segments in the MS. Finally, the *calorimeter-tagged muons* (CT) are reconstructed from ID tracks of charged particles with a signature in the calorimeters consistent with a minimum ionising particle.

Identification

A number of quality requirements are applied on the reconstructed muons based on the number of hits in the subdetectors, χ^2 of the track fit, q/p significance[4], ρ' ratio[5], etc. These requirements help to differentiate the muons from the background arising from the hadronic decay particles such as the pions and kaons. Based on these specifications, different working points, *Loose, Medium* and *Tight*, are defined.

The *Medium* WP allows to minimise the muon reconstruction and calibration uncertainties. Only the CB and ME muon tracks are considered for this selection along with other requirements such as a q/p significance smaller than 7. This serves as the default WP in ATLAS. The *Loose* WP maximises the reconstruction efficiency while providing good quality muon tracks. All muon types are used and all *Medium* quality muons qualify as *Loose* muons. *Tight* WP is designed to maximise the muon purity with a compromise in efficiency. Only CB muons with hits in at least two stations of the MS and satisfying the *Medium* selection criteria are considered. Selection cuts are applied on quantities such as the q/p significance, ρ', χ^2 of the fit, to remove pathological tracks. The WP corresponding to *High p_T* muons aims to improve the momentum resolution for tracks with $p_T > 100$ GeV. It results into an efficiency of $\sim 80\%$. The other WPs have an efficiency of $\sim 98\%$ for *Loose*, $\sim 96\%$ for *Medium* and $\sim 92\%$ for *Tight* muons in $20 < p_T < 100$ GeV range [184].

Isolation

The prompt muons can be differentiated from the non-prompt muons arising from the hadronic decays in a similar way as done for electrons, by measuring the amount of hadronic activity in their vicinity [183]. The main selections for isolation are applied on the ratio of the transverse energy reconstructed in a cone around the muon over the muon p_T.

5.1.4 Jets

As mentioned before, particles with colour charges, the quarks and gluons, are not observed directly. They undergo fragmentation and hadronisation to produce additional particles, as a result of which a shower of well-collimated colourless hadronic particles is obtained, which is known as a *jet*. In order to reconstruct the jet, one needs to identify whether or not the hadron candidate observed in the detector is a part of that jet. This task is accomplished using jet

---

[4] q/p significance is defined as: $\frac{|q/p_{ID} - q/p_{MS}|}{\sqrt{\sigma^2(q/p_{ID}) + \sigma^2(q/p_{MS})}}$, where q/p_{ID} and q/p_{MS} are the q/p measurements of the track curvatures in the ID and the MS, and the σ are their corresponding uncertainties.

[5] ρ' ratio $= \frac{|p_{T,ID} - p_{T,MS}|}{p_{T,CB}}$, where $p_{T,ID}$ and $p_{T,MS}$ are muon p_T measurements in the ID and in the MS, and the $p_{T,CB}$ is the p_T value from the resulting cmbined track fit.

clustering algorithms which identify which energy signals (or some other identifiable entity) belong to a particular jet, and combine them to obtain the jet information.

Jet clustering algorithm

One of the most important features of a jet clustering algorithm is its *infrared* and *collinear* (IRC) safety, the understanding of which lies in the theory of perturbative QCD. Low energies introduce a divergence called infrared (or soft) divergence in the calculation of the gluon emission probability. Collinear divergence on the other hand, is introduced at small-angle gluon emissions. These divergences imply that an initial high energy quark radiates soft gluons along the same axis as that of the initial quark with an infinite probability. Thus, the IRC safety [185] of a jet algorithm refers to its ability ro create a final set of hard jets which can not be modified by an arbitrary collinear or soft gluon emission.

The most frequently used algorithm in ATLAS is the anti-k_t [186] jet clustering algorithm, which creates jet cones based on a sequential recombination of closest cluster entities according to a distance measure. This distance measure is defined as:

$$d_{ij} = \min\left(p_{\mathrm{T},i}^{2m}, p_{\mathrm{T},j}^{2m}\right)\frac{\Delta R_{ij}^2}{R^2},$$
$$d_{iB} = p_{\mathrm{T},i}^{2m} \tag{5.1}$$

where d_{ij} is the distance between the entities i and j, and d_{iB} is the distance between the entity i and the beam. The parameter R is called as the jet radius, which is the only free parameter in the algorithm. The parameter ΔR_{ij} represents the distance between entities i and j in the $y\phi$-plane, i.e., $\Delta R_{ij}^2 = (y_i - y_j)^2 + (\phi_i - \phi_j)^2$, where y_k is the rapidity of entity k and ϕ_k is its corrsponding azimuthal angle. The parameter m is an integer that defines different types of algorithms with $m = 1$ representing the k_t *algorithm* [187]; $m = 0$ representing the *Cambridge/Aachen algorithm* [188]; and $m = -1$ defining the *anti-k_t algorithm*.

This algorithm may be appplied to the entities with a defined four momenta, such as topo-clusters or particles. This entity can be seen as a hadron with a four-momentum given by the sum of the four-momenta of the constituents. The procedure of finding jets goes as follows:

(i) Fix a value for R in the denominator of Equation 5.1 and compute the distance d_{ij} between each entity i and j using their corresponding p_{T} values. Evaluate d_{iB} for each entity i as well.

(ii) Find the smallest d_{ij},i.e., $\min(d_{ij})$ and the smallest d_{iB}, i.e., $\min(d_{iB})$ among all combinations obtained from the previous step, and proceed as follows:

- If $\min(d_{ij}) < \min(d_{iB})$: combine the two entities i and j to form a new entity. Remove the entities i and j from the procedure and add this new entity so created.

- If $\min(d_{ij}) > \min(d_{iB})$: recognise the entity i as a jet and remove it from the iteration.

(iii) Repeat the procedure until no entities are left.

The procedure so performed results into almost perfect conical jets, as shown in Figure 5.3. This algorithm is collinear and infrared safe as any soft or collinear particle generated at a small distance will be merged with the other particle. The jets used in this thesis are clustered using anti-k_t algorithm with $R = 0.4$. This is also the default case of ATLAS jet clustering, which is achieved with the help of the FASTJET [189] package.
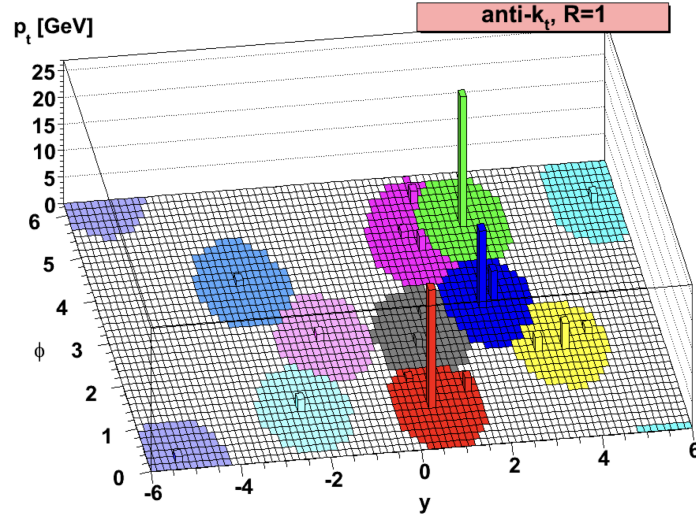
Figure 5.3: Depiction of a sample parton-level event using the anti-k_t algorithm with $R = 1$ used for the clustering procedure. Figure taken from [186].

Jet reconstruction

ATLAS jet reconstruction strategy relies on a spohisticated *Particle Flow* [190] algorithm that applies the anti-k_t algorithm to the tracks from the inner detector and the topo-clusters (Ref. Section 5.1.2) from the calorimeters and combines them together to reconstruct the hadronic jets and soft activity[6][191]. The particle flow algorithm is designed to better distinguish the charged particles from the neutral ones. In this tracker-calorimeter matching, energy deposits in the calorimeter originating from charged particles are identified and subtracted from the calorimeter using a cell-based energy subtraction algorithm to identify the neutral signals better. In order to subtract the right amount of energy, an estimation of the energy deposits from charged tracks is made using the energy of the topo-cluster (E^{clus}), and the momentum of the reconstructed track (p^{trk}). The ratio $E^{\mathrm{clus}}/p^{\mathrm{trk}}$ is evaluated using a single pion sample simulated without pileup, as a reference sample. This is a reasonable reference as most of the charged particles in a jet are pions. Thereafter, the energy deposited by the cluster is calculated. If this energy is more than the topo-cluster energy, the entire topo-cluster is removed. Otherwise, the cell subtraction is performed.

After the track-topo-cluster matching, *Particle Flow Objects* (PFOs) are created for neutral as well as charged particles. The neutral PFOs contain those topo-clusters which do not get matched to any track, as well as the the ones which are left after the energy subtraction of charged particles. Charged PFOs, on the other hand, are created from isolated tracks matched to the primary vertex, and from the matched track-topo-cluster objects. The matching to the PV helps remove a large fraction of tracks and their associated calorimeter energies from pile-up interactions. Thereafter, these objects are fed to the anti-k_t algorithm to finally get reconstructed jets.

---

[6] Soft activity refers to the additional hadronic recoils below the threshold used in the jet reconstruction procedure. This is important to be reconstructed because the missing transverse energy calculation is effected by these soft terms.

Jet calibration and pileup suppression

Once the jets are reconstructed, they need to be corrected for the known effects which may alter the properties of the reconstructed jets, for instance, the pileup effects and the primary vertex matching. Techniques to reduce the pile-up begins with a so-called *ρ-area subtraction*, which uses the median p_T density of the jets within a detector volume $|\eta| < 2$, and subtracts it from the jet based on the area covered by it in the $y\phi$-plane. It is then adjusted on an event-by-event basis. An additional *residual correction* uses the number of interaction per bunch crossing μ, as well as the number of primary vertices N_{PV} to account for any residual pileup dependencies after the ρ subtraction.

The four-vector of the jet is then corrected to match the particle-level jet via a MC-driven calibration approach. This corrects the jet so that it agrees in energy and direction with truth jets and is termed as the *jet energy scale* (JES) correction. In addition, the *global sequential calibration* (GSC) [190], using a MC-driven approach, is used to improve the jet p_T resolution and associated uncertainties. It does so by identifying the variables sensitive to the initial state information from the detector subcomponents and correcting them sequentially. A final *in-situ* calibration is peformed to account for the differences between the data and simulation. The p_T of a jet is balanced against a well-calibrated reference object, which can be leptonically decaying Z-bosons or photons. The term *jet energy scale* is defined as the mean of the Gaussian fit made to the core of the p_T ratio of the reconstructed over the generated p_T distribution. This fit further gives the *jet energy resolution* (JER) [192] associated with the jet reconstruction from the width of the distribution and smears the jets in the MC to better match their resolution with data.

The jet calibration techniques as defined so far introduce different uncertainties associated with them, which need to be incorporated in physics analyses. These uncertainties constitute a major portion of the systematics for this thesis and will be covered in a dedicated section on systematic uncertainties along with the description of the other systematics (Ref. Section 8.2.1).

Jet Vertex Tagger (JVT)

To supress the jets originating from pile-up interactions, a discriminant is prepared that determines how likely it is for a jet to be originating from the primary vertex. This discriminant is termed as the *jet vertex tagger* (JVT) [193] which takes into account the sum of p_T of the tracks associated to the jet originating from the hard-scatter vertex as well as from the pile-up vertices.

***b*-flavoured jet identification**

In many physics analyses involving a b-quark, the knowledge of whether a jet comprises of a b-quark or not is one of the most crucial physics information. This identification of a b-quark in a jet is known as b-tagging. Dedicated algorithms are used in ATLAS to serve this purpose, which rely on the distinctive properties of a B-hadron.

B-hadrons are heavy particles with a mass greater than 5 GeV [7]. Typical lifetime (τ) of a B-hadron lies around 1.5 picoseconds, meaning that the B-hadron decays after travelling a distance ($c\tau$) of approximately 450 μm. This implies that a B-hadron decay can be observed inside the detector. One of the dominant decay modes for B-hadrons produces lighter hadrons comprising of c-quarks, which further decays to even lighter particles after traversing a short distance inside the detector. Consequently, the B-hadrons leave at least one secondary vertex, which is typically not seen for lighter hadrons. This acts as a signature to identify the presence of a b-quark in a jet.

Different algorithms based on these properties are used in the ATLAS experiment. In this thesis, the DL1r [194] b-tagging algorithm is used to tag the b-quark jets. This is an algorithm that utilises neural networks [195] to combine the information from several other algorithms as described below:

- **Impact parameter based algorithms (IP2D and IP3D)**:

  Since a B-hadron travels a distance before it decays, it exhibits tracks with large transverse as well as longitudinal impact parameter values d_0 and z_0. These values differ significantly from zero as compared to the other jets with lighter quarks, which typically are consistent with a value close to zero. Therefore, a quantity *impact parameter significance* is defined as the ratio of the impact parameter over its uncertainty, i.e., d_0/σ_{d_0} in the transverse plane and z_0/σ_{z_0} along the longitudinal direction[7].

  IP2D and IP3D taggers [196, 197] are based on this approach using impact parameter significance to differentiate between the jets originating from a b-quark, a c-quark, or any other lighter quark. The IP2D considers only the transverse impact parameter significance, while the IP3D also uses the longitudinal impact parameter significance in addition. This information is used to construct a likelihood ratio so as to differentiate between the different jet types.

- **RNNIP**:

  In addition to the concept of the IP2D and IP3D taggers, the Recurrent Neural Network Track-based (RNN) tagger [198] utilises the information on the dependencies of the impact parameter significance among the tracks associated to a jet. It uses the information such as the fraction of p_T carried by the tracks relative to the jet p_T and the angular distance between the track and the jet (ΔR(trk,jet)) as inputs to the neural network which gives the probabilty of a jet being a b, c or *light*-quark jet as an output.

- **Secondary vertex based algorithms (SV1 and JetFitter)**:

  The secondary vertex created by the B-hadron decay can be reconstructed from the tracks of its daughter particles. The distance between the primary and the secondary vertex can then be used to identify the b-flavoured jets. Specialised algorithms are used in ATLAS to exploit this feature. The SV1 algorithm [199] explicitly reconstructs a single displaced secondary vertex in a jet, while the JetFitter algorithm [200] reconstructs the entire decay chain of the B-hadron allowing for a multi-vertex reconstruction.

DL1r is therefore, a sophisticated algorithm which provides a b-tagging discriminant that helps set different working points for physics analyses. The peformance of the algorithm is given by the so-called b-tagging efficiency which is defined as the efficiency to correctly identify a jet as a b-flavoured jet. A working point of 77% b-tagging efficiency is used in this thesis. In this context, a term known as the rejection factor is defined, which is the inverse of the efficiency for a background jet to pass the given selection requirement. The rejection factors for the c-jets and light-quark jets corresponding to the 77% b-tagging efficiency working point lie around 5 and 170 in simulated $t\bar{t}$ events, respectively [194].

---

[7] Usually, the quantity used for the longitudinal direction is defined to be: $z_0 \sin\theta/\sigma_{z_0 \sin\theta}$.

5.1.5 Overlap removal

The object reconstruction procedures which have been described so far do not consider any correlation between the reconstruction of the same track using two distinct reconstruction techniques for distinct objects. For instance, the EM calorimeter clusters are used to reconstruct both the jets and the electrons, allowing the electron signature to appear twice in the collection of reconstructed objects– in the jet as well as electron containers. These ambiguities may result in a double counting or erroneous reconstruction of an object. It is resolved using a specialised overlap removal procedure which establishes requirements on the objects. If an electron is found within a distance of $\Delta R_y(\text{jet}, e) < 0.2$ (in $y\phi$-plane) around a jet, the jet is removed, avoiding the counting of the electron energy deposits twice. After this, the electrons and muons found within a $\Delta R_y(\text{jet}, e/\mu) < 0.4$ from any remaining jet are also removed, thereby reducing the non-prompt electrons arising from heavy flavour decays. For muons in this case, there is an additional requirement that the associated jet must have at least three tracks for the muon to be removed, otherwise the jet is removed instead. If an electron and muon share the same track in the ID within $\Delta R_y(e, \mu) < 0.02$, the electron is removed.

5.1.6 Missing transverse momentum

In the collision of partons in the LHC, the partons do not carry any momentum in the transverse plane, hence the observed final state should also not have any contribution of the total momentum in the transverse plane. Any imbalance in the observed transverse momenta in the final state points to the presence of particles that went undetected from the detector, i.e., this contribution must originate from the particles which traverse the detector without exhibiting observable interactions. This is termed as *missing transverse energy* (MET) or E_T^{miss}. In this analysis, this is assumed to be originating from the neutrino in the final state.

Since the sum of the detected as well as the undetected transverse momenta must be zero, the $\mathbf{p}_T$ of undetectable particles evaluates to the negative sum of the $\mathbf{p}_T$ of the all detectable particles. Therefore, the missing $\mathbf{p}_T$ is evaluated to [201]:

$$
\begin{aligned}
\mathbf{p}_T^{\text{miss}} &= -\mathbf{p}_T^{\text{detected}} \\
&= -\underbrace{\sum_{\text{electrons}} \mathbf{p}_T^e - \sum_{\text{photons}} \mathbf{p}_T^\gamma - \sum_{\text{muons}} \mathbf{p}_T^\mu - \sum_{\text{taus}} \mathbf{p}_T^\tau - \sum_{\text{jets}} \mathbf{p}_T^{\text{jet}}}_{\text{Hard term}} - \underbrace{\sum_{\substack{\text{unused} \\ \text{tracks}}} \mathbf{p}_T^{\text{soft}}}_{\text{Soft term}}
\end{aligned}
\tag{5.2}
$$

where the summations run over the vectorial sum of the selected and calibrated objects– the *hard term* comprising the electrons, photons, muons, taus, jets, along with an additional *soft term*. The soft term in the evaluation refers to the particles which do not participate in any of the object reconstruction processes. It is estimated from the calorimeter topo-clusters not associated to any hard object (calorimeter-based soft term), or from the tracks associated to the hard-scatter primary vertex, but not associated to any hard object (track-based soft term). Therefore, the final value of the E_T^{miss} is equal to the magnitude of the $\mathbf{p}_T^{\text{miss}}$ vector, i.e., $E_T^{\text{miss}} = |\mathbf{p}_T^{\text{miss}}| = \sqrt{(E_{T,x}^{\text{miss}})^2 + (E_{T,y}^{\text{miss}})^2}$ and the azimuthal angle ϕ corresponding to it is given by $\phi^{\text{miss}} = \tan^{-1}(E_{T,y}^{\text{miss}}/E_{T,x}^{\text{miss}})$.

5.2 Event selection

In accordance with the requirement of different analyses, specific selections are imposed on the physics objects. These selections help to enhance the signal and reduce the background contribution to the final state. This section covers the selection criteria used in this thesis, starting with the trigger requirement on the data and the Monte Carlo simulated samples. The remaining selection criteria are described in the section that follows.

5.2.1 Trigger selection

Collecting data from a collision process at the LHC requires sophisticated triggers as explained in Section 3.3.6. These triggers, which are primarily required for data collection, need to be applied also on the Monte Carlo samples in order to keep them in accordance with the data. In this analysis, the events passing a single-electron or a single-muon trigger are used.

Object	Data period	$\geq p_T$ GeV	ID	Isolation	Trigger name
Electron		24	Medium	Gradient	e24_lhmedium_L1EM20VH
	2015	60	Medium	-	e60_lhmedium
		120	Loose	-	e120_lhloose
		26	Tight	Loose	e26_lhtight_nod0_ivarloose
	2016-2018	60	Medium (no d_0 cut)	-	e60_lhmedium_nod0
		140	Loose (no d_0 cut)	-	e140_lhloose_nod0
Muon	2015	20	Loose	-	mu20_iloose_L1MU15
		50	-	-	mu50
	2016-2018	26	Medium	Gradient	mu26_ivarmedium
		50	-	-	mu50

Table 5.1: Triggers used for the electron and muon objects for different years, depicting their corresponding p_T threshold, the identification (ID) working point and the isolation working point, along with the name of the trigger.

The trigger requirements are summarised in Table 5.1, showing the triggers corresponding to the different data-taking periods. The 2015 data has comparitively a looser set of trigger requirements compared to the rest of the data from the 2016-2018 period. The table also shows the p_T threshold, the identification as well as the isolation working points corresponding to the different triggers used for this thesis. For electrons, a logical OR of three single-electron triggers is used, while for muons, a logical OR of two single-muon triggers is considered. The *Loose, Medium* and *Tight* working points correspond to the WPs explained in Sections 5.1.2 and 5.1.3. More details about the individual WP definitions can be found in the references [202, 203].

5.2.2 Object selection

Since the channel of interest is the $t\bar{t}$ decay via the semi-leptonic mode, the final state is described by two b-quarks (one decaying from a top and the other from an anti-top quark), a charged lepton and its corresponding neutrino (from the decay of one of the W-bosons), and two additional quarks (from the decay of the other W-boson), as shown in an example Feynman diagram in Figure 5.4. All four quarks in the final state are reconstructed as jets, and b-tagging can be applied on the two b-quark jets using the DL1r algorithm as explained in Section 5.1.4.
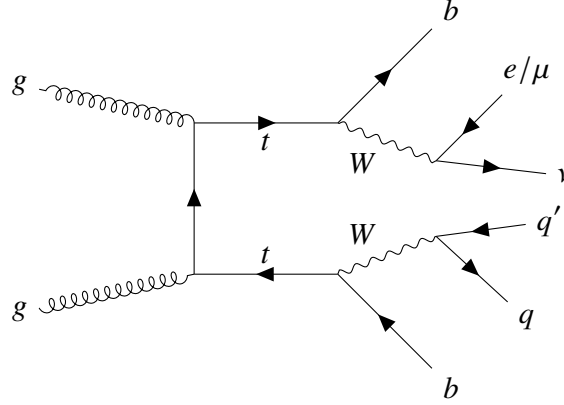
Figure 5.4: Example of a Feynman diagram for $t\bar{t}$ decay process via a single-leptonic decay channel.

After the selection is applied on the trigger-level, a next stage of selection is applied on the kinematic quantities. Exactly one electron or muon is required in each event. The electrons are required to have a $p_T > 27$ GeV and $|\eta| < 2.47$, while removing the transition region between the end-caps and the barrel, specifically the $|\eta|$ region within $1.37 < |\eta| < 1.52$. Cuts are applied on the transverse as well as the longitudinal impact parameters such that $|d_0|$ is smaller than 5 times the uncertainty in its measurement (σ_{d_0}), and the $|\Delta z_0 \sin\theta| < 0.5$ mm. This is applied to make sure that the electron tracks are close to the primary vertex. The electron events are required to have an $E_T^{miss} \geq 30$ GeV and a transverse mass of the W-boson,[8] m_T^W larger than or equal to 30 GeV as well.

Muons, on the other hand, are required to have $p_T > 27$ GeV and $|\eta| < 2.4$. Similar to the electrons, selections on impact parameters are applied. While the transverse impact parameter d_0 is required to be smaller than $3\sigma_{d_0}$, the z_0 requirement stays the same as for the electrons. The sum of the E_T^{miss} and transverse W-boson mass for muon events is required to be at least 60 GeV. For 2015 data-taking period, both the electrons as well as muons have the p_T requirement loosened to 25 GeV, instead of 27 GeV used for the other years.

Jets are reconstructed using the anti-k_t algorithm using a radius of $R = 0.4$ as explained in Section 5.1.4. They must have a p_T greater than 25 GeV and $|\eta| < 2.5$. Quality criteria are imposed such that the jets arising from pile-up can be suppressed. Hence, a jet vertex tagger (JVT) discriminant larger than 0.5 is required for the jets with $p_T < 60$ GeV and $|\eta| < 2.5$ (Section 5.1.4). DL1r algorithm is used to tag the b-flavoured jets in the final state. A working point corresponding to 77% efficiency of b-tagging is used. The events are required to have at

---

[8] $m_T^W = \sqrt{2p_T^l E_T^{miss}(1 - \cos\Delta\phi)}$, where $\Delta\phi$ is the angle between the lepton and the E_T^{miss} direction in the azimuthal plane.

Object	Electron	Muon	Jets
p_T	$p_\text{T}^{e/\mu} > 25$ GeV (2015), $p_\text{T}^{e/\mu} > 27$ GeV (2016-2018)		$p_\text{T}^\text{jet} > 25$ GeV
η	$|\eta| < 2.47$, excluding $1.37 < |\eta| < 1.52$	$|\eta| < 2.4$	$|\eta| < 2.5$
d_0/σ_{d_0}	≤ 5	≤ 3	-
$|\Delta z_0 \sin\theta|$	≤ 0.5 mm	≤ 0.5 mm	-
$E_\text{T}^\text{miss}, m_\text{T}^W$	$E_\text{T}^\text{miss} \geq 30$ GeV, $m_\text{T}^W \geq 30$ GeV	$E_\text{T}^\text{miss} + m_\text{T}^W \geq 60$ GeV	-
Count, N	N(electron + muon) = 1		N(jets) ≥ 4, N(b-tagged jets) ≥ 2

Table 5.2: Summary of the selection criteria on physics objects applied on each event.

least four jets with at least two of them b-tagged. Table 5.2 gives a summary of all the selections applied on the events.

5.3 Reconstruction of $t\bar{t}$ mass

As described in Section 2.6.2, the invariant mass of the $t\bar{t}$ pair serves as an observable which can be used to extract the Y_t information from data. Since this reconstructed observable provides the basis for this analysis, it becomes crucial to extract this quantity as accurately as possible. The information from the final state needs to be combined to reconstruct the $t\bar{t}$ mass, i.e., the information on the neutrino, lepton, and the four jets involved in the decay process need to be used. The only available neutrino information is the transverse missing energy as well as the ϕ of the transverse energy component. Therefore, as a first step towards the $t\bar{t}$ mass reconstruction, the z component of the neutrino momentum is reconstructed. In the following sub-section, the process of obtaining the di-top mass is explained, after which the algorithm to obtain the neutrino p_z is described. The final part of this section shows the methods used to optimise the final observable.

5.3.1 $t\bar{t}$ invariant mass reconstruction algorithm

In order to correctly obtain the top quark mass, the first step is to identify the objects that are originating from the top quark. However, as the object of interest is the $t\bar{t}$ invariant mass, the individual assignment of the final state objects to the top and the anti-top quark specifically, is not necessary. As mentioned before, the algorithm requires at least four jets to be present in the event, along with one lepton and a missing energy component. The flow-chart shown in Figure 5.5 displays this reconstruction algorithm.

The first two leading b-tagged jets are considered as the b-jets arising from the decay of the two top quarks in the $t\bar{t}$ system. For the case where the event has only two jets in addition to these two b-tagged jets, the hadronic W-boson candidate is reconstructed from these two jets.

```
┌─────────────────────────────────────────┐
│   Events with number of jets ≥ 4        │
│   and number of b-tagged jets ≥ 2       │
└─────────────────────────────────────────┘
                    │
                    ▼
┌─────────────────────────────────────────┐
│      Select the hadronic W-decay jets   │
└─────────────────────────────────────────┘
                    │
                    ▼
┌─────────────────────────────────────────┐
│ Associate a b-jet to the hadronically decaying │
│   W-boson => hadronic top-quark obtained │
└─────────────────────────────────────────┘
                    │
                    ▼
┌─────────────────────────────────────────┐
│   Obtain neutrino p_z values from the   │
│   solutions to the quadratic equation   │
└─────────────────────────────────────────┘
                    │
                    ▼
┌─────────────────────────────────────────┐
│  Associate the leftover b-tagged jet to the │
│         lepton+neutrino pairs           │
└─────────────────────────────────────────┘
                    │
                    ▼
┌─────────────────────────────────────────┐
│    Select the neutrino solution that    │
│ results to the top-quark mass closest to the │
│        nominal top-mass value           │
└─────────────────────────────────────────┘
```

HADRONIC
DECAY SIDE

LEPTONIC
DECAY SIDE

Figure 5.5: A flowchart for the reconstruction of $t\bar{t}$ invariant mass, giving a brief overview of the reconstruction algorithm.

For the case where the event has has three or more additional jets, the three jets with the largest p_T are taken under consideration and the two which give the invariant di-jet mass closest to the W-boson mass [7] are considered as the hadronic W-boson decay products. The resultant mass of the reconstructed W-boson is shown in Figure 5.6(a), showing a peak at ≈ 80 GeV. Thereafter, one of the two b-tagged jets is associated to this reconstructed hadronic W-boson, depending on which b-tagged jet results in a better nominal top quark mass value [7]. The resultant top-quark mass is obtained as shown in Figure 5.6(b), depicting a peak around the nominal value of the top quark mass.

For the leptonic-top reconstruction, the lepton, the leftover b-jet and the reconstructed neutrino are combined. The neutrino reconstruction is described in detail in the next section (Section 5.3.2). As a result of the neutrino reconstruction method, two possible solutions are obtained. Both the solutions are tested at this stage, and the one that produces the best top-quark mass is taken to be the final solution for the reconstructed neutrino p_z. As a result, the $t\bar{t}$ mass is fully reconstructed. Figure 5.6(c) shows the reconstructed mass of the leptonically decaying W-boson, as well as the mass of its associated top-quark (Figure 5.6(d)). One can observe a clear peak at ≈ 80.38 GeV from the W-boson mass plot. This stems from the neutrino reconstruction strategy which imposes a mass restriction on the leptonic W-boson. It will be explained in more detail in the following section. On the other hand, the mass of the top-quark contains a big contribution from the b-tagged jet, resulting in a broad distribution.

(a)

(b)

(c)

(d)
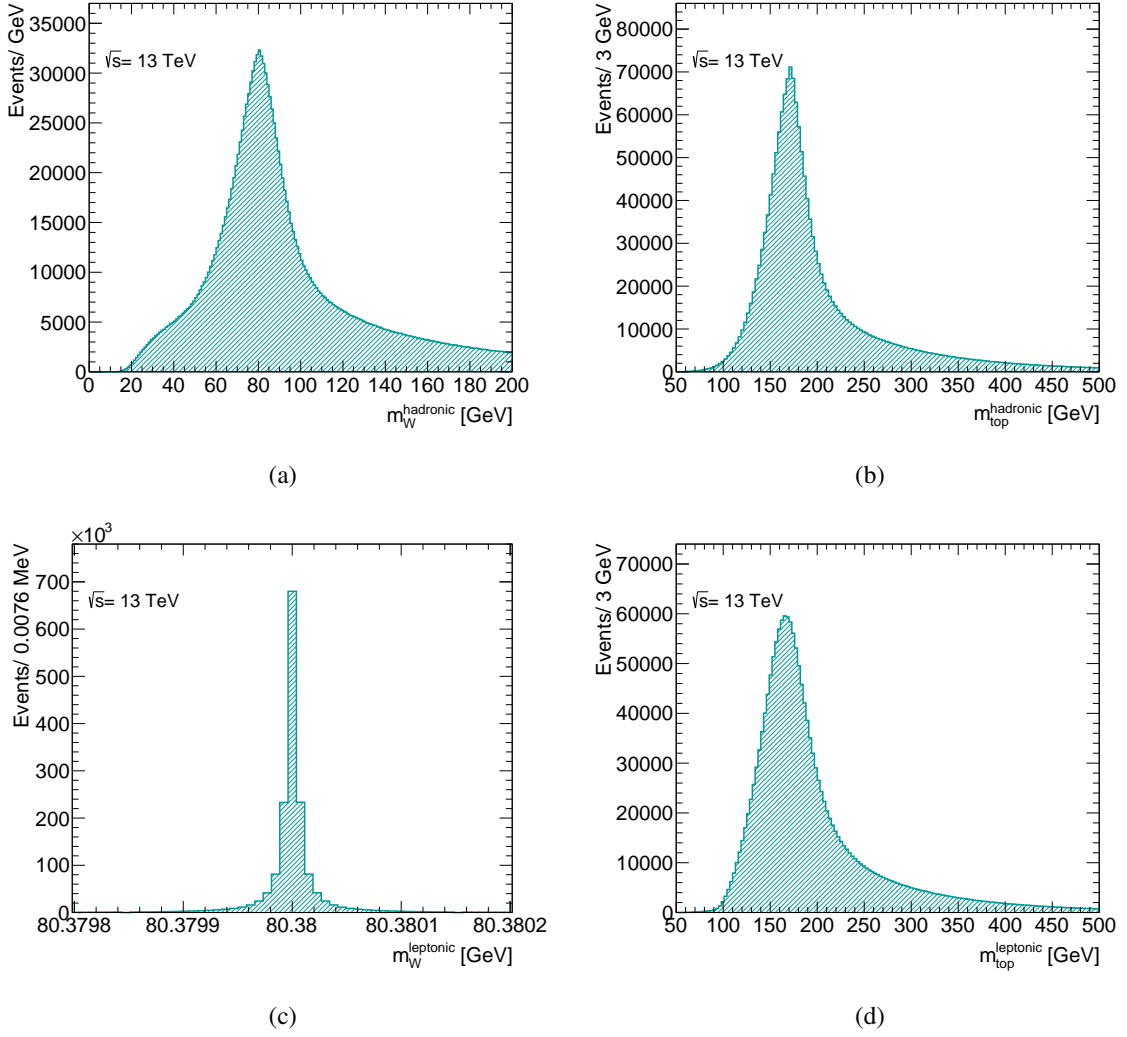
Figure 5.6: Reconstructed masses of the hadronically decaying 5.6(a) W-boson, as well as for the corresponding reconstructed 5.6(b) top-quark; Leptonically decaying W-boson mass corresponds to Figure 5.6(c), as well as the same for the corresponding reconstructed top-quark is shown in 5.6(d).

Figure 5.7 shows the reconstructed mass of the di-top pair, i.e., the $m_{t\bar{t}}$ distribution as obtained using the algorithm explained. It also shows a two-dimensional plot for the reconstructed $m_{t\bar{t}}$ versus the generated $m_{t\bar{t}}$, which depicts a correlation between the two mass distributions. However, the correlation appears poor at smaller values of generated $m_{t\bar{t}}$ mass, where the reconstructed $m_{t\bar{t}}$ shows a broader spectrum, inclining to a large $m_{t\bar{t}}$ value. The correlation among them can be expressed in terms of a resolution, which is defined as the ratio of the difference between the reconstructed and the generated di-top masses, over the generated di-top mass value, i.e.,

$$m_{t\bar{t}}^{\text{resolution}} = \frac{m_{t\bar{t}}^{\text{reco}} - m_{t\bar{t}}^{\text{gen}}}{m_{t\bar{t}}^{\text{gen}}} \qquad (5.3)$$

where $m_{t\bar{t}}^{\text{reco}}$ corresponds to the reconstructed di-top mass value and the $m_{t\bar{t}}^{\text{gen}}$ refers to the

(a) (b)
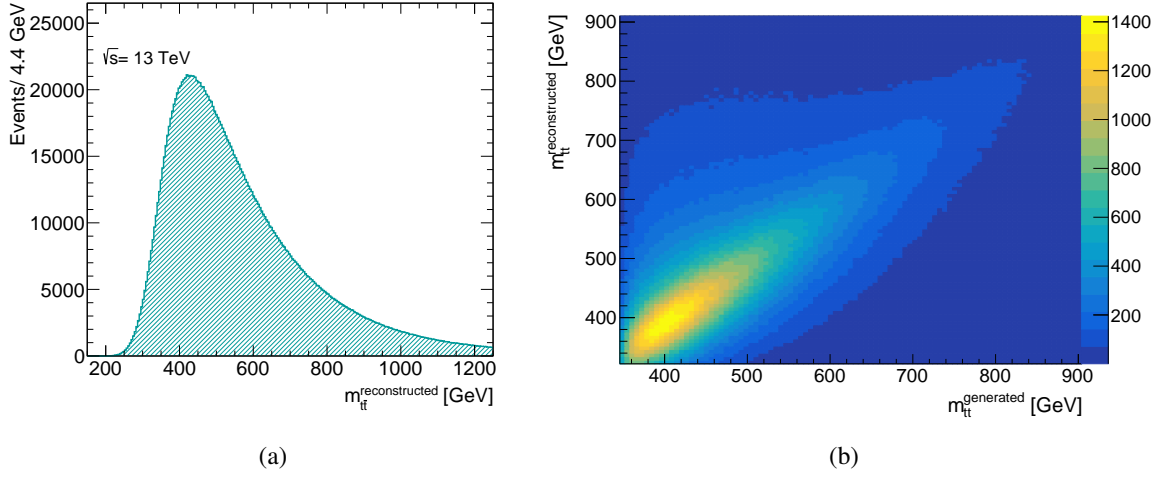
Figure 5.7: Reconstructed masses of the 5.7(a) di-top pair, as well as 5.7(b) the corresponding two-dimensional distribution for the reconstructed versus the generated di-top mass.

generated one. The resolution of the reconstructed mass ($m_{t\bar{t}}^{\text{resolution}}$) is shown in Figure 5.8(a). The distribution is centered around zero, but it can be noted that the it has a tail on the positive side, indicating that on an average, the $m_{t\bar{t}}^{\text{reco}}$ tends to be larger than the $m_{t\bar{t}}^{\text{gen}}$. Figure 5.8(b) shows this resolution corresponding to different ranges of generated $m_{t\bar{t}}$ values. Moving from the di-top production threshold to larger $m_{t\bar{t}}^{\text{gen}}$ values, the distribution gets more symmetric around zero, and an improvement in the mean of the corresponding distribution can be observed.

(a) (b)
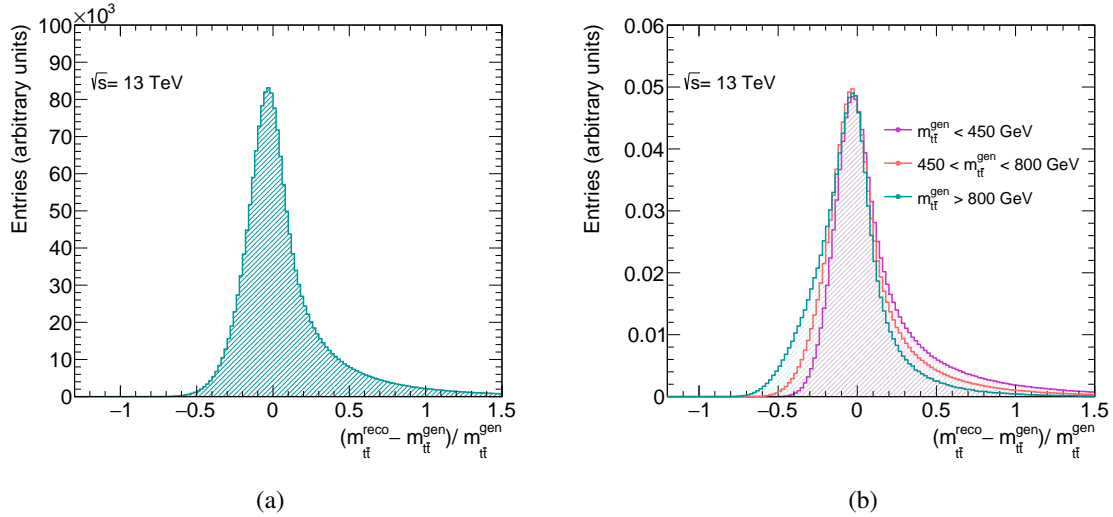
Figure 5.8: Resolution of the reconstructed $t\bar{t}$ mass. Figure 5.8(a) shows the resolution inclusive of all mass values, whereas, 5.8(b) shows the same resolution splitted in different generated $m_{t\bar{t}}$ mass ranges.

5.3.2 Reconstruction of neutrino momentum

The only information about the neutrino is present in the form of $E_{\mathrm{T}}^{\mathrm{miss}}$ and the corresponding ϕ^{miss} of the system. The value of the z-component of the neutrino momentum is not available since the boost in the z-direction is not known. Hence the neutrino p_z needs to be evaluated using the already known quantities, assuming energy-momentum conservation. Taking into account that the lepton and the neutrino originate from a W-boson decay, and using the on-shell constraint of the W-boson mass in the lepton+$E_{\mathrm{T}}^{\mathrm{miss}}$ system, one can obtain an equation of the form:

$$A(p_z^\nu)^2 + B p_z^\nu + C = 0 \tag{5.4}$$

where,

$$
\begin{aligned}
A &= (p_z^l)^2 - (E^l)^2 \\
B &= \alpha p_z^l \\
C &= -(E^l)^2[(p_x^\nu)^2 + (p_y^\nu)^2] + \frac{\alpha^2}{4} \\
\text{with} \quad &\alpha = m_W^2 - m_l^2 + 2(p_x^l p_x^\nu + p_y^l p_y^\nu)
\end{aligned}
\tag{5.5}
$$

This quadratic equation leads to two solutions for the neutrino momentum p_z, which are:

$$p_z^\nu = \frac{-B \pm \sqrt{B^2 - 4AC}}{2A} \tag{5.6}$$

The detailed derivation of this equation is shown in Appendix A. The quantity $D := B^2 - 4AC$ is called as the *discriminant* of the quadratic equation solution. Depending upon the value of the discriminant, one can classify the solutions into three types:

1. $D = 0$: one real solution
   There is no ambiguity in this case. The obtained value is $p_z^\nu = -b/2a$.

2. $D > 0$: two real solutions
   The final solution is chosen depending on which one of them provides the top-quark mass closest to the nominal value, as explained in the previous section. Figure 5.9(a) shows the two solutions in the plot. It depicts the solutions corresponding to $(-B + \sqrt{D})/2A$ (called as Root+), and $(-B - \sqrt{D})/2A$ (called as Root-). The third curve in the figure belongs to the final value of the p_z^ν that is obtained after combining the lepton and the b-tagged jet information and verifying which solution results in the top-quark mass closest to its nominal value. Figure 5.9(b) then plots the difference between this chosen p_z solution and the generated neutrino p_z.

3. $D < 0$: imaginary solutions
   The solution with a real value is retrieved using special methods as explained in detail below.

For the case with $D < 0$, the solution is not straightforward, because it results in two imaginary solutions. In practice, around 45% of the total number of cases belong to this category. These non-physical results arise from detector resolution effects leading to an incorrect measurement of the p_{T} of lepton, or the missing transverse energy.

One possibility here is to ignore the imaginary part and only take the real part of the solution as the value of p_z^ν. This will be called as "*Algorithm 1*" in the text.

(a)   (b)
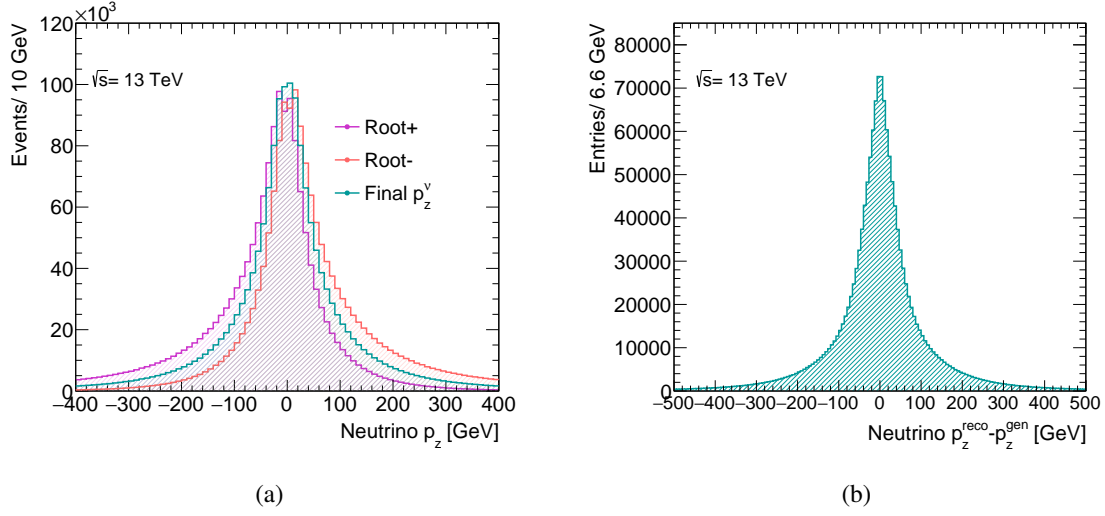
Figure 5.9: Reconstructed neutrino p_z, depicting the solutions corresponding to the quadratic equation, along with the final neutrino p_z obtained. Plot 5.9(b) shows the difference between the reconstructed and the generated neutrino p_z.

Since the origin of these imaginary solutions is the mismeasurement of the lepton p_T or the missing transverse energy, ignoring the imaginary component only serves as an approximation. As the p_T of the lepton is obtained more precisely as compared to the E_T^{miss}, one could scale or rotate the E_T^{miss} components by a small value such that it results in a real solution. Therefore, the E_T^{miss} value is reduced by 100 MeV and the discriminant is recomputed. This process of
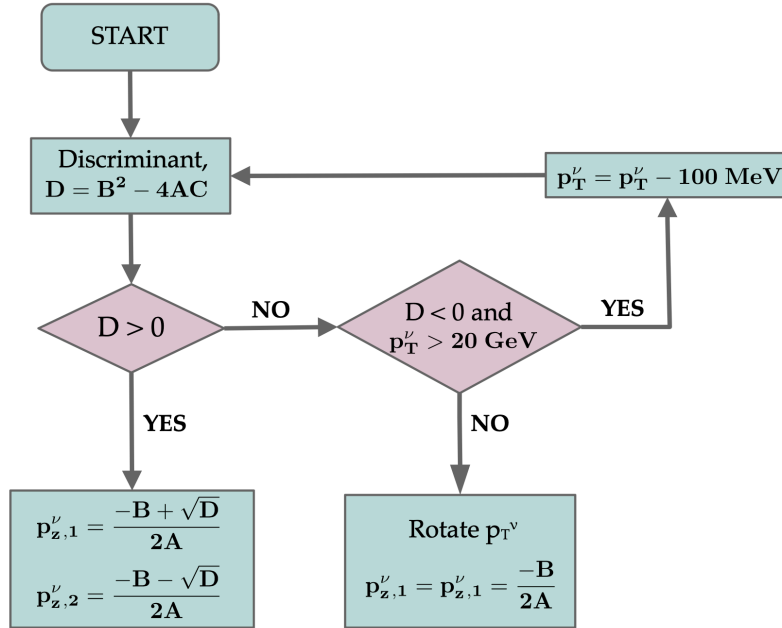
Figure 5.10: The algorithm for the reconstruction of the z component of the neutrino momentum, depicting the conditions for which the E_T^{miss} is scaled and rotated.

scaling-down of the E_T^{miss} is repeated until a real solution is obtained, or the E_T^{miss} reduces to 20 GeV. In the very small number of cases where still no solution is obtained and the E_T^{miss} has already reduced down to 20 GeV, the E_T^{miss} is rotated at a certain angle to obtain a real solution. A flowchart explaining this algorithm is shown in Figure 5.10. This method of neutrino p_z reconstruction will be called as "**Algorithm 2**" in the text.
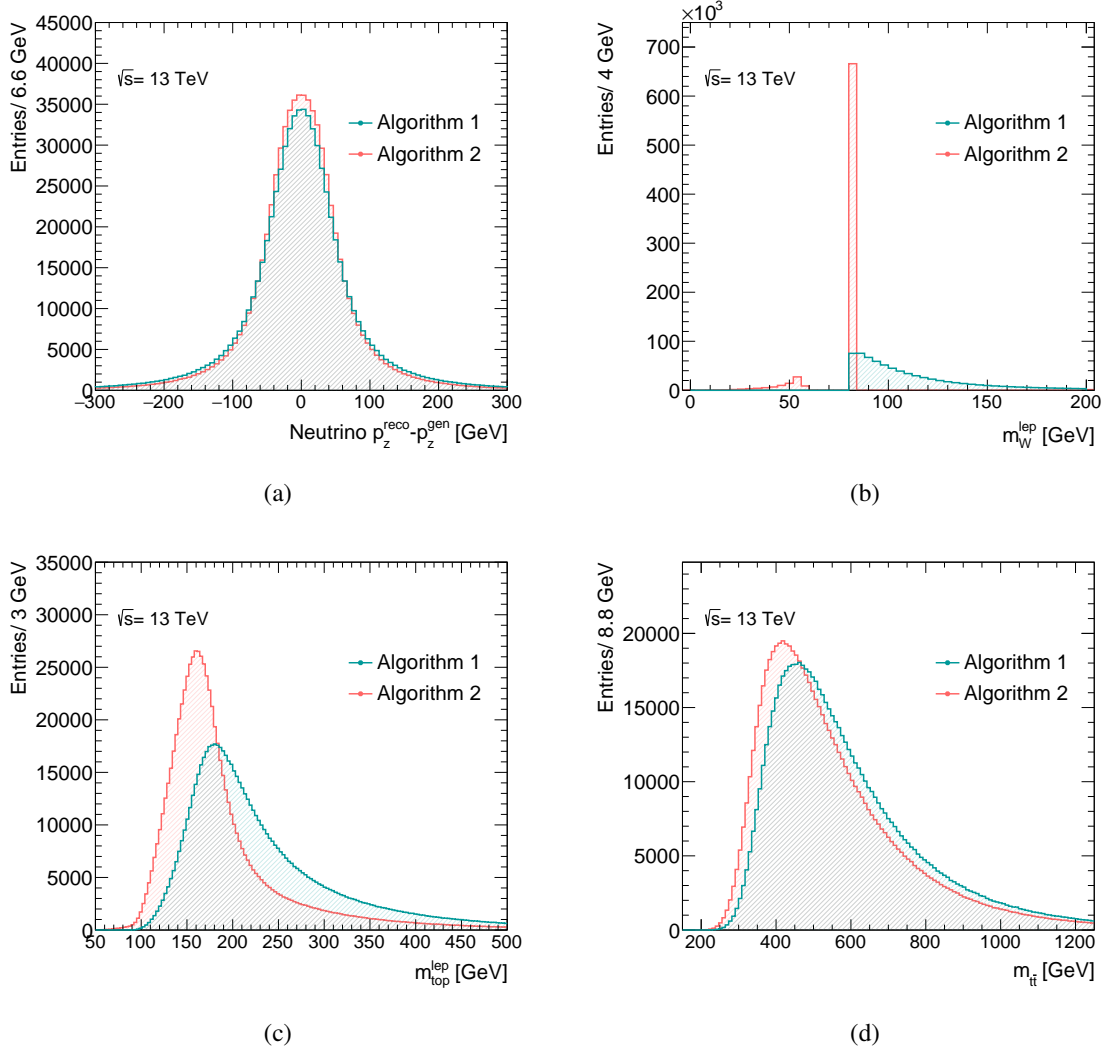
Figure 5.11: A comparison of the two algorithms of neutrino reconstruction for $D < 0$. Plot (a) shows the difference between the obtained and the generated p_z^{ν}; (b) corresponds to the reconstructed m_W^{lep}; (c) shows the mass of the reconstructed leptonically decaying top-quark; (d) shows the reconstructed $m_{t\bar{t}}$.

Figure 5.11 shows the difference between the obtained and the generated p_z^{ν} for $D < 0$, for the case where the imaginary component of the solution is ignored (*Algorithm 1*), as well as for the case where the p_z^{ν} is scaled and rotated (*Algorithm 2*). The resultant W-boson mass is shown as well (Figure 5.11(b)), where the scaling and rotation method recovers the m_W^{lep} from a distribution above 80 GeV to a distinct peak at 80 GeV, along with a small distribution at $m_W^{lep} < 80$ GeV. This small peak corresponds to the cases where the scaling algorithm fails to obtain a positive discriminant, as well as the rotation is unable to recover a reasonable result.

The mass of the corresponding top-quark is shown in Figure 5.11(c), where the average mass becomes smaller moving from *Algorithm 1* to *Algorithm 2*, recovering the events with imperfect $E_{\mathrm{T}}^{\mathrm{miss}}$ values. The same can be seen for the reconstructed $m_{t\bar{t}}$ distribution. Therefore, the final $m_{t\bar{t}}$ reconstruction utilises the neutrino reconstruction as explained in the flowcharts shown in Figures 5.5 and 5.10.

5.3.3 Jet-to-parton association and optimisation of $m_{t\bar{t}}$ distribution

Revisiting Figure 5.6, one can observe long tails in the mass distributions for the hadronically decaying W-boson, as well as the two top quarks. Hence the resultant $m_{t\bar{t}}$ distribution is expected to reflect these long tails as well. In addition to the intrinsic resolution of the mass distributions, one of the reasons the events enter this long-tailed region is the wrong assignment of the jets, for example, only one of the jets reconstructed as the W-boson decay candidate is in reality originating from the W-boson. One approach towards eliminating them is by excluding the events located in the tail region. If it is known where the bulk of these poorly reconstructed events lie, one may place efficient selection cuts. Therefore, in this section, a study is performed, associating the jets with quarks from the generator to identify the kinematic regions where this parton-matching does not describe the events well. Such an identification would help find a suitable region to apply a cut selection.

Each of the four jets involved in the $m_{t\bar{t}}$ reconstruction is matched to one of the quarks (from the generator) such that the ΔR [9] between the jet and the matched quark is the smallest. The requirement for the event to be fully matched at the parton level is that the ΔR between the jet and the matched quark is smaller than 0.4, i.e., $\Delta R(\text{jet, quark}) < 0.4$. In a fully matched event, each of the four jets is uniquely matched with a $\Delta R(\text{jet, quark}) < 0.4$ to its one of the quarks at generator level. The jets stemming from the decay of the W-boson are referred to as the W-decay jets, and the jet associated to this hadronically decaying W-boson, resulting in a hadronically decaying top-quark, is referred to as the hadronic b-jet. Similarly, on the leptonic side, the jet associated to the leptonically decaying W-boson, resulting into a leptonically decaying top-quark, is referred to as the leptonic b-jet.

If the leptonic b-jet matches correctly with the generator-level b-quark associated to the leptonically decaying top-quark, then it is referred to as a ***"correct b-jet association"***. For the case where it fails to match, it is called as an ***"incorrect b-jet association"***. Figure 5.12(a) shows the reconstructed mass of the leptonically decaying top-quark for *correct* as well as the *incorrect b-jet associations*. It also shows the ***"all associations"*** case, where no parton-matching requirement is applied. A clear top-quark mass peak can be seen for the correctly matched case, whereas the tail of the total distribution can be seen to be mostly covered by the *incorrectly*-associated jets. The contribution to the tail in the distribution comes primarily from either the wrongly chosen b-jet, or a jet which does not have a good match to a quark at the parton level. Similar conclusion can be made for Figure 5.12(b), which shows the mass of the hadronically decaying W-boson. For the *correct* jet association, a peak at ≈ 80 GeV can be seen, while the contribution to the tails arise from the *incorrect* associations.

Figure 5.13 shows the reconstructed top-quark mass for the hadronic side. Unlike the masses shown in Figure 5.12, for the hadronic top-quark, the correct jet combinations have to be made both for the two jets from the W-boson decay, as well as for the b-tagged jet associated with this

---

[9] $\Delta R(\text{reco jet, generated quark}) = \sqrt{(\Delta\eta)^2 + (\Delta\phi)^2}$
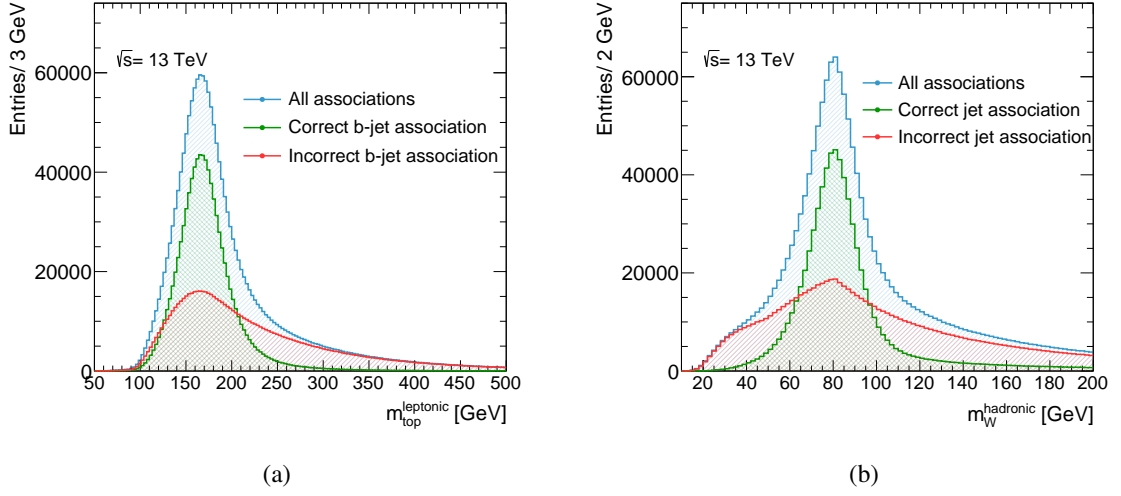
Figure 5.12: Reconstructed masses of the leptonically decaying top-quark, as well as for the hadronically decaying W-boson. Additionally, the distributions are shown after parton-matching, showing the cases for correctly as well as incorrectly matched jets.

top-quark decay. The plot shows the distribution scaled to unity. For the correct association, the mass distribution shows a distinct peak around the top-quark mass value, cutting away the tails.
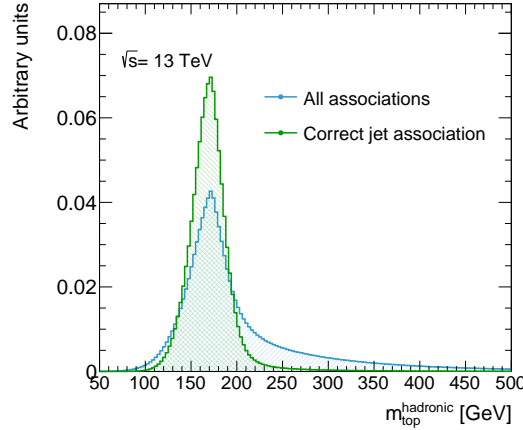
Figure 5.13: Reconstructed mass of the top-quark decaying hadronically, is compared to the case where the jet is correctly matched to the top-quark at parton level.

These figures show that one of the reasons the tails appear in the mass distributions is through the events for which the reconstructed objects are not associated correctly with the partons. Therefore, by applying cuts on the tails of the distribution, one should be able to increase the fraction of correctly matched events in the sample, thereby improving the resolution of the di-top mass. Hence, a test is done to check the impact of removal of the events lying in the tails of the mass distributions for the reconstructed objects. For the leptonic W-boson, the requirement on the mass is already imposed from the neutrino reconstruction procedure, as seen from Figure

5.6(c), and hence, no selection cuts are applied on the reconstructed leptonic W-boson mass. For the other objects, selection windows can be applied on the masses, $m_{top}^{\text{hadronic}}$, $m_{top}^{\text{leptonic}}$, and m_W^{hadronic}. A few quantities are consequently defined, which can help optimise the selection criteria. The parameter *acceptance efficiency* (ϵ_{acc}) is defined as the fraction of the total number of events passing the selection cuts.
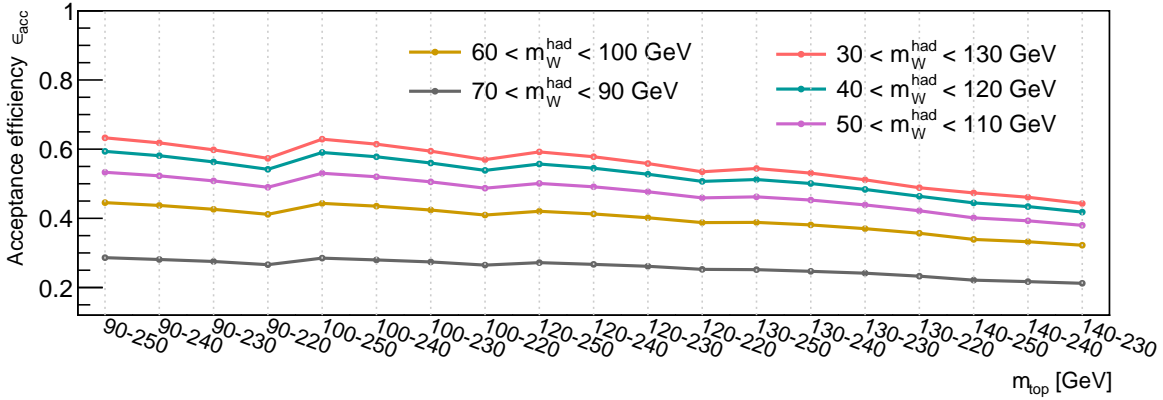
Figure 5.14: The *acceptance efficiency* values corresponding to different m_W^{hadronic} selections, represented by the lines of different colours. The x-axis shows the various ranges of m_{top} values for which the *acceptance efficiency* is evaluated.

Different mass windows are considered for m_W^{hadronic}, i.e., [30,130], [40,120], [50,110], [60,100] and [70,90] GeV. Corresponding to each of these selections, the *acceptance efficiency* is evaluated for different m_{top} ranges. This is plotted in Figure 5.14. As the cuts are tightened, the ϵ_{acc} reduces. The maximum ϵ_{acc} is seen for $m_W^{\text{hadronic}} \in [30, 130]$ GeV with almost identical values for the two m_{top} ranges: $m_{top} \in [90, 250]$ GeV and $m_{top} \in [100, 250]$ GeV. Looking back into the W-boson and top-quark masses, it can be noted that these mass windows cover almost the entire distribution where the jet-to-parton association is correct.

Similarly, a quantity called *parton matching efficiency* (ϵ_{match}) is defined, which gives the fraction of the total number of events that are parton-matched with correct jet-associations for all four jets involved in the $m_{t\bar{t}}$ reconstruction process. For the same set of selection windows as used for ϵ_{acc}, the ϵ_{match} is shown in Figure 5.15. The better the ϵ_{match}, the better is the $m_{t\bar{t}}$ resolution. An improvement in the ϵ_{match} can be observed as the selection windows on m_W^{hadronic} are made smaller. However, for a given m_W^{hadronic} selection, the efficiency does not differ too much with varying m_{top} ranges.

Figure 5.16 shows the $m_{t\bar{t}}$ resolution for three cut windows namely, $m_{top} \in [130, 220]$, [120, 230], [100, 250] GeV, where all three of them contain an additional loose selection on $m_W^{\text{hadronic}} \in [40, 120]$ GeV. It also depicts the resolution without any cut selection application, consisting of a long tail in its distribution. It can be seen from the distributions that by applying any of the three cut selections, the resolution gets much better compared to the case where no cuts are applied. The three distributions with cut windows however, show a similar resolution, thus, concluding that it is reasonable to apply some cuts rather than not applying any.

Considering the parameters *acceptance efficiency* and the *parton matching efficiency*, the tighter the selection window is made, the worse is the ϵ_{acc}, but the better is the ϵ_{match}. Therefore, to combine these two information together, another quantity is defined, which is simply a product
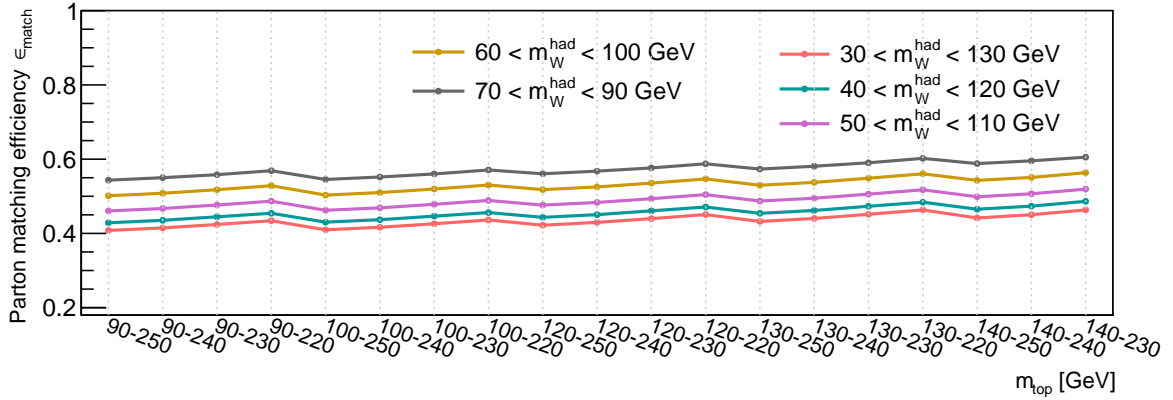
Figure 5.15: The *parton matching efficiency* values corresponding to different m_W^{hadronic} selections, represented by the lines of different colours. The *x*-axis shows the various ranges of m_{top} values for which the *parton matching efficiency* is evaluated.
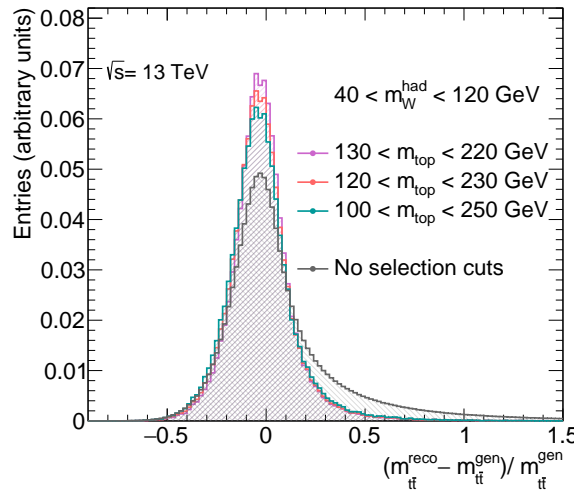
Figure 5.16: The $m_{t\bar{t}}$ resolution distributions are shown for different cut windows. The three lines for the m_{top} cut have an additional cut $m_W^{\text{hadronic}} \in [40, 120]$ GeV applied. The line corresponding to "No selection cuts" has no cuts applied on either the m_{top} or the m_W^{hadronic}.

of the *acceptance efficiency* and the *parton matching efficiency*, i.e., *acceptance efficiency* × *parton matching efficiency*. This is plotted in Figure 5.17. The larger the value of this product, the more sensible is the compromise between the number of events passing the cuts, and the efficiency of parton-matching. As can be noticed from the plot, moving to a tighter m_{top} region only makes this product smaller due to a highly reduced *acceptance efficiency*. Two of the tightest selections on m_W^{hadronic} used in this comparison, [30, 130], and [40, 120] GeV do not make a huge difference in this product and almost overlap in the plot, because their net *parton matching efficiency* effect is cancelled out by its poor *acceptance efficiency*. Therefore, amongst these two, $m_W^{\text{hadronic}} \in [40, 120]$ GeV, with a better *parton matching efficiency* is selected to use. Looking at the m_{top} ranges in the same plot, the one with the largest value of this product has
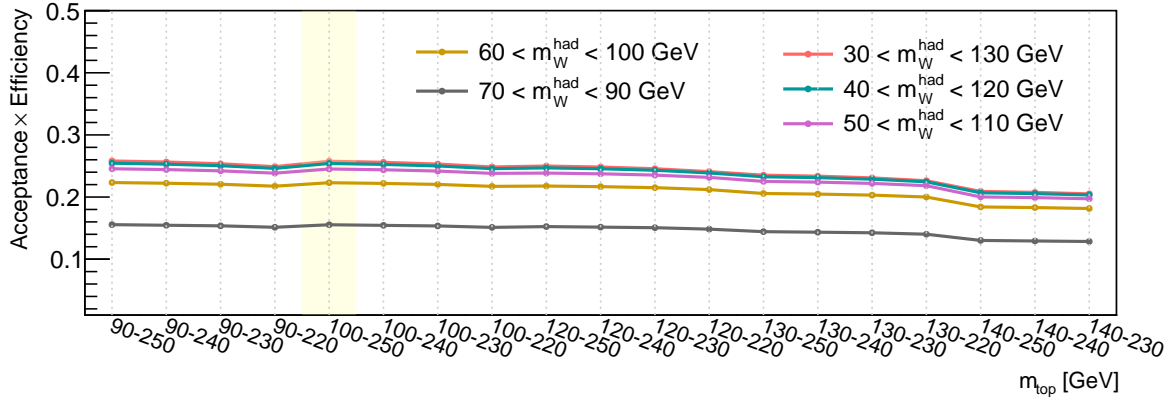
Figure 5.17: The *acceptance efficiency × parton matching efficiency* values corresponding to different m_W^{hadronic} selections, represented by the lines of different colours. The x-axis shows the various ranges of m_{top} values for which this product is evaluated. The yellow band highlights the favoured selection.

the range of $[100, 250]$ GeV, which is highlighted in yellow. Hence, for the $m_{t\bar{t}}$ optimisation, the final selections that are applied on the reconstructed observables (without any parton-level matching) correspond to $m_W^{\text{hadronic}} \in [40, 120]$ GeV and $m_{top} \in [100, 250]$ GeV. The resultant $m_{t\bar{t}}$ after these selections is then compared with the generated $m_{t\bar{t}}$, and the corresponding two-dimensional histogram is shown in Figure 5.18. A clear correlation between the two di-top masses can be observed, confirming that the reconstruction method along with these selection cuts results in an $m_{t\bar{t}}$ distribution comparable to the generated $m_{t\bar{t}}$.
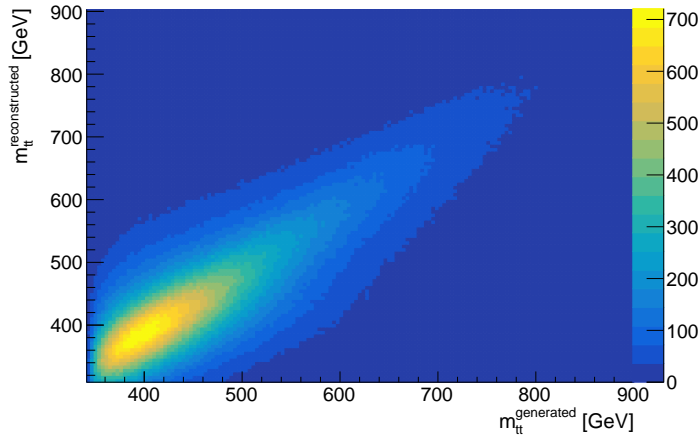
Figure 5.18: The reconstructed $m_{t\bar{t}}$ after applying the selection of $m_W^{\text{hadronic}} \in [40, 120]$ GeV and $m_{top} \in [100, 250]$ GeV, plotted against the generated $m_{t\bar{t}}$.

This can be compared with the two-dimensional plot obtained before the optimisation procedure, i.e., Figure 5.7(b), which depicts a reconstructed $m_{t\bar{t}}$ with a much broader distribution as compared to the optimised reconstructed $m_{t\bar{t}}$ in Figure 5.18.

Data and Monte Carlo samples

This chapter provides information on the data and Monte Carlo samples utilised in the analysis. Section 6.2.1 describes the channel that is considered as the signal sample. The other processes, which have a potential to exhibit a similar final state in the detector as that of the signal, known as backgrounds, are described in the following section. It also highlights the Monte Carlo generators used to simulate each MC sample, as well as the *weights* that are required to be considered while using them in the analysis.

6.1 Data information

The analysis is performed on Run-2 data collected by the ATLAS detector in the period from 2015 to 2018. This data corresponds to the proton-proton collisions at the LHC with a centre of mass energy of $\sqrt{s}$ = 13 TeV. The integrated luminosities (ref. Section 3.1.1) collected for each year is tabulated in Table 6.1 [108]. A total integrated luminosity of $\mathcal{L}$ = 140.1 ± 1.2 fb^{-1} is

Data sample	Integrated luminosity (fb^{-1})
2015	3.24 ± 0.04
2016	33.40 ± 0.30
2017	44.63 ± 0.50
2018	58.79 ± 0.64
Total	140.07 ± 1.17

Table 6.1: Summary of the integrated luminosities at the ATLAS detector for each individual year of the Run-2 pp data sample at $\sqrt{s}$ = 13 TeV [108].

collected at the ATLAS detector during the full Run-2 period. The data preparation follows a sequence of processes as described in the previous chapters along with the implementation of object and event selection requirements as described in Section 5.2.

6.2 Monte Carlo samples

This section describes the signal and background processes for the analysis. It also covers the details of the simulated samples used to estimate the signal and the background processes, i.e.,

the information about the generators used for their production and any approximations assumed to produce them.

6.2.1 Signal sample

The process of interest, or the signal in this analysis is the $t\bar{t}$ production (ref. Section 2.5), where one of the top quarks decays to a b-quark and a W-boson, that further decays to an electron or a muon along with its corresponding neutrino; and the other top quark decays to a b-quark and a W-boson which further decays hadronically. The signal process can be obtained from a gluon-gluon fusion or a quark-antiquark annihilation at leading order as shown previously in Figure 2.4. The Feynman diagram for one of the signal processes is shown in Figure 6.1 illustrating the final state.
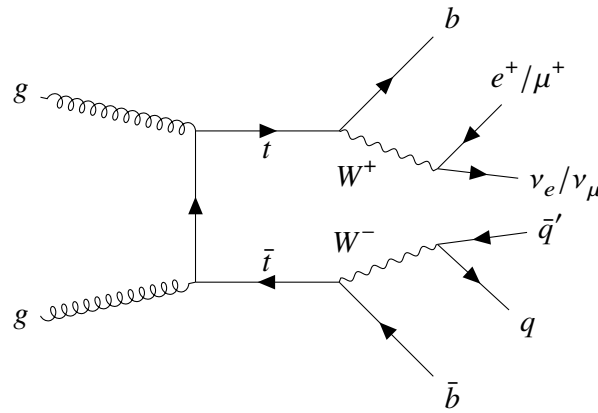
Figure 6.1: Example of a Feynman diagram for $t\bar{t}$ decay process via a single-leptonic decay channel (the signal in this analysis).

The nominal signal $t\bar{t}$ MC sample is generated using Powheg-Box-v2 [153] generator, which is based on the NLO QCD matrix calculations. This matrix element (ME) generator is interfaced with Pythia v8.230 [158] generator which simulates the parton shower, fragmentation and the underlying event. The ME calculation uses the NNPDF3.0LO [204] set for the parton distribution functions with a top-quark mass of 172.5 GeV. A value of 1.5 times the top-quark mass is set as the damping parameter h_{damp} in the MC. This is the parameter that controls the emission of the first gluon. The renormalisation and factorisation scales are set to $\mu = \mu_R = \mu_F = \sqrt{m_{\mathrm{top}}^2 + p_{\mathrm{T,\,top}}^2}$, which is calculated using the top-quark mass and the p_{T} before radiation. The parton shower from the Pythia v8.230 generator uses the A14 set of tunable parameters together with NNPDF2.3LO [204] PDF set.

The samples for different Yukawa coupling values are obtained via a reweighting technique used on this nominal sample. This is based on a leading order calculation for the full electroweak corrections from HATHOR v2.1–b3 [205] where the Yukawa coupling is a free parameter. A detailed explanation is provided in a dedicated section, in Chapter 7.

Top++ v2.0 [206] is used to calculate the total inclusive top pair production cross-section and using that, the events are normalised to the NNLO cross-section including the resummation of soft gluon emissions at next-to-next-to-leading-logarithmic (NNLL) accuracy. Heavy flavour decays are modelled using the EvtGen v1.6.0 [162] program, and the detector response is

simulated using Geant v4 [164] framework. All Monte Carlo samples in the analysis use Geant v4 for their detector simulations with the full simulation procedure (FullSim) unless stated otherwise, in which case the other approach of fast simulation (AFII) (ref. Section 4.3) is used instead.

Alternative $t\bar{t}$ samples

The signal $t\bar{t}$ sample is obtained using a particular combination of matrix element, parton shower and hadronisation model, tunable parameters and PDF sets. A variation in the choice of these parameters may lead to a change in the final cross-section distribution. These are known as modelling parameters which appear as sources of uncertainties in the MC prediction, and hence, alternative samples of MC are used to account for these uncertainties, which are defined as follows:

- **Parton shower and hadronisation:** The Monte Carlo sample to account for differences in the parton shower and hadronisation in the event uses the same matrix element calculation (from Powheg-Box-v2) with an h_{damp} value of 1.5 times the top-quark mass of 172.5 GeV, as the nominal sample. However, it is interfaced with Herwig v7.1.3 [159, 160] generator for the simulation of the parton shower and hadronisation process that uses the MMHT2014lo [207] PDF set, instead of the Pythia v8.230 shower as used in the nominal sample.

- **NLO matching:** The matching between the matrix element and the parton shower is modified using the same generator-combination as the nominal $t\bar{t}$ sample, but with an alternative matching scheme between Powheg-Box-v2 and Pythia v8.230 that alters the matching using a p_T^{hard} [208] parameter. The value of p_T^{hard} for the alternative sample is set to unity, instead of zero which is set as default for the nominal case. More details are covered in Section 8.2.2.

- **Top-quark mass and h_{damp} variation:** The same generator-combination is used to simulate the effect of variation of top-quark mass, as the nominal signal sample, with a difference of 0.5 GeV from the nominal top-quark mass value. Samples corresponding to a mass value of 172 GeV and 173 GeV are used in the analysis to assess the effect of the variation of the top-quark mass. To estimate the effect of h_{damp} variation, again, the same generator-combination as the nominal $t\bar{t}$ sample is used to obtain the simulation, but with an h_{damp} value of 3 times the top-quark mass, as opposed to 1.5 times the top-quark mass in the nominal one.

- **Variation of the initial and final state radiation:** Additional variations to be taken into account use the same nominal signal MC sample, but with a tuning of different parameters to generate the impact of the variation of initial state radiation (ISR) and the final state radiaton (FSR). The ISR variation is estimated by varying the μ_R and μ_F scales in the ME by a factor of 2.0 and 0.5 with respect to their nominal values. The μ_R scale of a parameter called Var3c [163] in the A14 tune is varied by a factor of 0.5 and 2.0, which also accounts for the ISR. The FSR variation alters the μ_R scale related to the QCD-induced emissions in the parton shower by a factor of 0.5 and 2.0.

- **PDF variation:** The effect of a variation in the parton distribution function for the $t\bar{t}$ sample is obained using the PDF4LHC15 [209] error set consisting of a combination of

several different PDF sets as explained in reference [210]. It gives a set of PDF variations with 30 components, all of which are used in the analysis.

6.2.2 Background samples

There are several processes which contribute to the background in this analysis. These backgrounds and their corresponding generators used to simulate them are covered in this section.

- **Single-top-quark processes:**
  This is the source of the largest contribution to the background for this analysis. These processes are split into s-channel, t-channel and Wt-channel contributions. A few examples of Feynman diagrams corresponding to such processes is shown in Figure 6.2. All of these three processes are generated using POWHEG-BOX-v2 ME generator, interfaced with PYTHIA v8.230 using the A14 tune. They use the NNPDF2.3LO for the PDF description. The samples are normalised to the approximate NNLO precision [211, 212]. The t-channel single-top quark process uses the ATLFAST-II [167] estimation for fast simulation of the detector response. The Wt-final state uses a diagram removal (DR) technique [213] which ignores the interference between the $t\bar{t}$ and Wt final states. This interfernce arises considering the NLO Wt-channel which may produce the exact same final state as that of the LO signal $t\bar{t}$ sample.
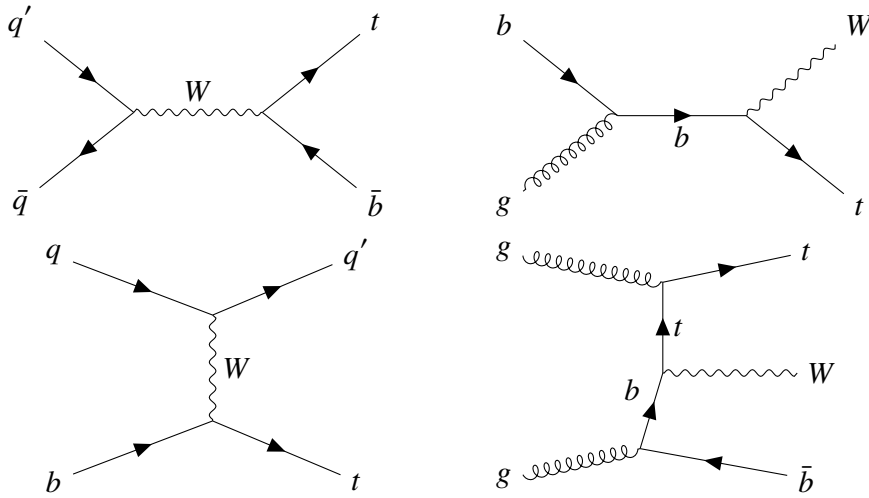
Figure 6.2: Examples of Feynman diagrams for LO s-channel, t-channel, Wt-channel single-top quark production processes, as well as an NLO Wt process for the same.

Sample variations: The ISR and FSR variations corresponding to these samples are also generated as internal weights to the nominal single-top quark sample. The nominal sample uses the diagram removal (DR) scheme to get rid of the overlap between the $t\bar{t}$ and the Wt channel processes. However, other schemes exist, and therefore, an alternative sample of diagram subtraction (DS) scheme is taken as an uncertainty in the Wt background estimation, which is produced using the same generator combination and the same PDF description as the nominal Wt sample.

- **V+jets production:**
  The next important background is the Z or W boson production in association with additional jets. A few Feynman diagrams are shown in Figure 6.3 as examples corresponding to these processes. These samples are simulated using SHERPA v2.2.11 generator [161, 214], which includes both the simulation of hard interaction as well as the hadronisation process. The NNPDF3.0LO PDF set us used with a dedicated tune specific to the SHERPA generator. The samples are nomalised to the NNLO cross-section [215].
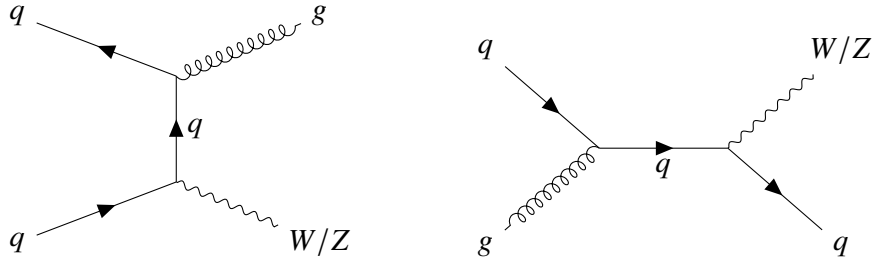
Figure 6.3: Examples of Feynman diagrams corresponding to W+jets and Z+jets processes.

A variation of μ_R and μ_F corresponding to the W+jets background is obtained from the same generator as used for the nominal sample, but with a corresponding μ_R and μ_F varying simultaneously by a factor of 0.5 as well as 2 times the corresponding values used in the nominal sample generation.

- **Diboson processes:**
  A small background contribution also comes from the diboson processes such as WW, WZ, and ZZ production. Examples of Feynman diagrams corresponding to these processes is shown in Figure 6.4. Their MC samples are generated using SHERPA v2.2.1 with the dedicated tune from SHERPA authors. The simulation of up to two additional jets is calculated at NLO precision, while it has only LO precision for additional jets. The NNPDF3.0NNLO set is used to describe the PDF. Only the processes with at least one lepton in the final state are considered. The samples are normalised to the NLO QCD theoretical cross-section [216].
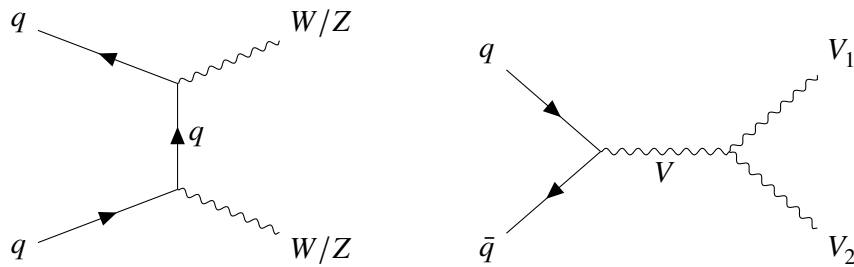
Figure 6.4: Examples of Feynman diagrams corresponding to the diboson processes, i.e., WW, WZ, and ZZ production processes. The representation $V/V_1/V_2$ refers to the bosons W or Z. Photon propagator γ can also qualify as V in the diagram.

- **Other processes:**
  Other small processes such as $t\bar{t}$ associated with a boson production, $t\bar{t}W$, $t\bar{t}Z$, $t\bar{t}H$ as well

as *tH* production individually contribute to a very small fraction of the total background. A few examples for these backgrounds are shown as Feynman diagrams in Figure 6.5.
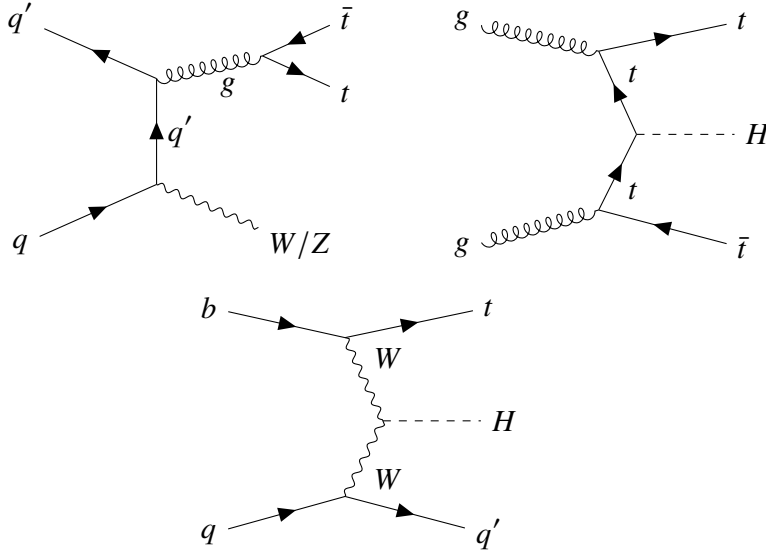
Figure 6.5: Examples of Feynman diagrams corresponding to the *ttV* and *tH* processes.

The *t̄tW* and *t̄tH* samples are generated using Powheg-Box-v2 for the ME, interfaced with Pythia v8.230 for the parton shower and hadronisation. The background *t̄tZ*, on the other hand, uses MadGraph5_aMC@nlo v2.3.3 for the ME interfaced with Pythia v8.230 for the shower and hadronisation. All three of them use the NNPDF2.3lo PDF set using the A14 tune. Events are produced at the LO precision only. The *tH* sample is simulated using aMC@NLO that calculates the ME, which is interfaced with Pythia v8.245 for parton shower and hadronisation using the H7.1 tune. NNPDF3.0nlo PDF for the ME, and MMHT2014lo PDF set for the shower are used. The events are generated at NLO accuracy. This process uses the AtlFast-II estimation for fast simulation of the detector response.

A summary of the signal and background MC samples along with the information on the generators used to simulate them is shown in Table 6.2.

6.2.3 MC event weights

The generated MC simulation samples do not match the data and must be reweighted to their corresponding cross-sections as well as the required integrated luminosity values before being used in the analysis. This is achieved by obtaining a weight w for each event, resulting from a product of the cross-section of the process σ_{MC} (at NLO for $t\bar{t}$ signal), branching ratio $\mathcal{B}$ of the MC process, as well as the integrated luminosity $\mathcal{L}_{int}$ value for which the MC needs to be used for the comparison with data. Additionally, a k-factor[1] value, k_{factor} needs to be taken into account to rescale the cross-section value to a higher order cross-section precision. A

---

[1] k-factor refers to the ratio of the cross-section calculated at a higher order precision over the cross-section obtained by the generator (which is represented by σ_{MC} in the text). For $t\bar{t}$ signal, the k_{factor} equals to the ratio of the NNLO+NNLL precision over the NLO cross-section calculated by the generator.

MC process	Generator	ME PDF	Shower	PS Tune	Cross-section normalisation
$t\bar{t}$ signal	Powheg-Box-v2 + EvtGen v1.6.0	NNPDF3.0LO	Pythia v8.230	A14	NNLO+NNLL
Single top (Wt)	Powheg-Box-v2 + EvtGen v1.6.0	NNPDF2.3LO	Pythia v8.230	A14	(app.)NNLO
Single top (t)	Powheg-Box-v2 + EvtGen v1.6.0	NNPDF2.3LO	Pythia v8.230	A14	(app.)NNLO
Single top (s)	Powheg-Box-v2 + EvtGen v1.6.0	NNPDF2.3LO	Pythia v8.230	A14	(app.)NNLO
W+jets	Sherpa v2.2.11	NNPDF3.0LO	Sherpa v2.2.11	Sherpa default	NNLO
Z+jets	Sherpa v2.2.11	NNPDF3.0LO	Sherpa v2.2.11	Sherpa default	NNLO
Diboson	Sherpa v2.2.1	NNPDF3.0NNLO	Sherpa v2.2.1	Sherpa default	NLO
$t\bar{t}H$	Powheg-Box-v2 + EvtGen v1.6.0	NNPDF2.3LO	Pythia v8.230	A14	LO*
$t\bar{t}W$	Powheg-Box-v2 + EvtGen v1.6.0	NNPDF2.3LO	Pythia v8.245	A14	LO*
$t\bar{t}Z$	MadGraph5_aMC@NLO v2.3.3 + EvtGen v1.2.0	NNPDF2.3LO	Pythia v8.210	A14	NLO*
tH	aMC@NLO+ EvtGen v1.7.0	NNPDF3.0NLO	Pythia v8.245	H7.1-MMHT2014LO	NLO*

Table 6.2: A summary of the MC generator settings used to simulate various processes used in the analysis. Samples marked with a "*" are normalised to the generated cross-section, i.e., they correspond to a k_{factor} of unity.

so-called *filter efficiency*, ϵ_{filter} of the MC needs to be incorporated as well, which takes into account the efficiency of the event selection criteria applied on the generator level. In addition to this, the MC saves individual weights for each event, represented by w_{MC}. These individual weights summed over all events give the total weighted number of MC events in the sample, $N_{\text{gen}} = \sum_{\text{all events}} w_{\text{MC}}$. Hence, the weight that needs to be applied for each event, takes the form:

$$w = \frac{w_{\text{MC}} \times (\sigma_{\text{MC}} \times \mathcal{B}) \times k_{\text{factor}} \times \epsilon_{\text{filter}} \times \mathcal{L}_{\text{int}}}{N_{\text{gen}}}, \tag{6.1}$$

The modelling inaccuracy of the instrumental effects arising due to lepton reconstruction for example, is incorporated by multiplying this weight w by the product of the scale factors SF^k, appointed to the individual reconstructed objects and the pile-up weight, $w^{\text{pile-up}}$, correcting for the pile-up distribution in the simulated samples. Thus, the total MC weight w_i^{total}, obtained for each event i, is given by Eq. 6.2:

$$w_i^{\text{total}} = w_i \times \prod_k \text{SF}_i^k \times w_i^{\text{pile-up}} \tag{6.2}$$

6.3 Fake lepton background estimation

While specific identification and isolation requirements are applied for lepton reconstruction, a small number of events from the *non-prompt* lepton category may also pass the selection cuts and mimic the signal process. These are the non-prompt or misidentified leptons arising from photon conversions, leptonically decaying heavy-flavour hadrons, as well as from the events where jets get misidentified as leptons. For the case of an electron, most of the contribution to this *multijet background* comes from the low multiplicity jets misidentified as electrons, as well as from the non-prompt decays of hadrons, while for the muons, this background mostly comes from the non-prompt hadronic decays. It is difficult to accurately estimate the rate of fake leptons in the event using MC simulation. This is due to a number of reasons, particularly important of which is the high dependency of the simulation on the modelling of material composition and detector response [217]. Moreover, simulating these processes with sufficiently large sample size would require a significant amount of computational resources. As a result, this background is often determined using data-driven techniques.

This analysis uses a data-driven *matrix method* to estimate this multijet background, mainly based on reference [217]. Two sets of lepton selection criteria are defined, called the *baseline* and the *tight* selection. The tight selection criteria selects the leptons the same way as selected in the physics analysis, whereas, the baseline selection criteria accepts an additional set of candidates which are rich in contribution of the fake/ non-prompt leptons, as well as the tight selection. The candidates which pass the baseline selection, but not the tight selection are termed as *loose* leptons. The selection requirements are summarised in Table 6.3.

Correspondingly, efficiencies are defined, where the fraction of real leptons in the baseline sample that pass the tight selection is termed as the *real efficiency*, ϵ_r, written as:

$$\epsilon_r = \frac{N_{\text{tight}}^{\text{real}}}{N_{\text{baseline}}^{\text{real}}} \tag{6.3}$$

where N represents the number of events, the superscript "real" refers to the prompt leptons

Channel	Electron		Muon	
Selection	Tight	Baseline	Tight	Baseline
Identification	`TightLH`	`LooseAndBLayerLH`	`Medium`	`Medium`
Isolation	`FCTight`	—	`FCTightFixedRad`	—
$d_0/\sigma(d_0)$	< 5	< 5	< 3	< 7
$z_0 sin\theta$ [mm]	< 0.5	< 0.5	< 0.5	< 0.5

Table 6.3: Selection criteria for *tight* and *baseline* leptons. More details about the individual isolation and identification WP definitions can be found in references [202, 203].

passing the tight or baseline selection criteria. The estimate of ϵ_r is taken from MC sample, and is corrected to account for the differences between data and simulation. The fraction of fake leptons in the baseline sample which satisfy the tight selection is referred to as the *fake efficiency*, ϵ_f, which can be expressed as:

$$\epsilon_f = \frac{N_{\text{tight}}^{\text{fake}}}{N_{\text{baseline}}^{\text{fake}}} \tag{6.4}$$

where the superscript "fake" refers to the fake leptons satisfying the tight or baseline selection criteria. The fake efficiency ϵ_f is derived from the data passing the same selections as the signal. However, the contribution from the prompt-leptons need to be subtracted from this sample in order to get a sample enriched in fakes, which is done by applying inverted E_T^{miss} and m_T^W selection cuts.

If the number of events satisfying the tight selection is represented as N_T, and the number of events satisfying the baseline but not tight selection is represented as N_L (loose), then their relationship can be written as:

$$\begin{pmatrix} N_T \\ N_L \end{pmatrix} = \begin{pmatrix} \epsilon_r & \epsilon_f \\ 1 - \epsilon_r & 1 - \epsilon_f \end{pmatrix} \begin{pmatrix} N_{\text{baseline}}^{\text{real}} \\ N_{\text{baseline}}^{\text{fake}} \end{pmatrix} \tag{6.5}$$

where $N_{\text{baseline}}^{\text{real}}$ and $N_{\text{baseline}}^{\text{fake}}$ are the unknown numbers of real and fake leptons in the baseline sample. These unknown numbers are hence, related to the observed yields N_T and N_L via a matrix as shown in the equation. Inverting the matrix, one can obtain the expression corresponding to the number of fake leptons in the baseline sample as:

$$N_{\text{baseline}}^{\text{fake}} = \frac{1}{\epsilon_r - \epsilon_f} \left[(\epsilon_r - 1)N_T + \epsilon_r N_L \right] \tag{6.6}$$

The quantity of interest is the number of fake leptons in the tight sample, which can then be obtained using the relation shown in Equation 6.4 as:

$$N_{\text{tight}}^{\text{fake}} = \epsilon_f N_{\text{baseline}}^{\text{fake}} = \frac{\epsilon_f}{\epsilon_r - \epsilon_f} \left[(\epsilon_r - 1)N_T + \epsilon_r N_L \right] \tag{6.7}$$

In the same way, the number of real leptons satisfying the tight selection can be obtained as:

$$N_{\text{tight}}^{\text{real}} = \epsilon_r N_{\text{baseline}}^{\text{real}} = \frac{\epsilon_r}{\epsilon_r - \epsilon_f} \left[(1 - \epsilon_f)N_T - \epsilon_f N_L \right] \tag{6.8}$$

The efficiencies used in this analysis are obtained from a dedicated study[2] using the ATLAS data as well as Monte Carlo samples used in this thesis. The real efficiency is obtained from the $t\bar{t}$ signal sample itself, while the fake efficiencies are obtained from data. Parametrised as a function of lepton p_T and η, these efficiencies are used to obtain weights for each event, which are later applied on the Monte Carlo to get the fake lepton background estimate.

6.4 Event yields

After the application of selection cuts as explained in the previous chapter, as well as the weights as described in Section 6.2.3, the total number of events is recorded. The corresponding event yield so obtained for each MC sample used in this analysis is summarised in Table 6.4. While the uncertainties shown in the values refer to the statistical uncertainties in the corresponding MC sample, for the case of the fake lepton[3] background, an overall uncertainty of 50% is applied. The single-top-quark background, comprising of the s-channel, t-channel, as well as the Wt production modes sum up to give the largest contribution to the total background, contributing to around 3% of the total MC prediction, and comprising around 55% of the total background. However, the net background fraction itself is observed to be very small, evaluating to only around 5.5% of the total MC yield. The next important background comes from the W+jets production making around 22% of the total background. The fake leptons, however, only contribute approximately 8% to the total background estimate, followed by Z+jets background with a contribution of around 7.5%. The rest of the background contributions arising from the $t\bar{t}Z, t\bar{t}W, t\bar{t}H, tH$ as well as di-boson processes combine to contribute only around 7% to the total background estimate.

For simplicity, the contribution from s-channel, t-channel, as well as the Wt production are collectively considered as the "single-top" background. Similarly, the contribution from the $t\bar{t}Z, t\bar{t}W, t\bar{t}H, tH$ as well as di-boson processes collectively are considered as the "Other" background in the next chapters.

---

[2] The efficiency calculations used in this analysis are done as a separate study in a private communication with Dr. Thorsten Kuhl.

[3] This background is also referred to as the multijet background or the QCD bkg in this thesis.

Process	Yield ($\geq$ 4 j, $\geq$ 2 b)
$t\bar{t}$	2 354 330 ± 3 476
single-top Wt	53 311 ± 506
single-top s-chan	1 793 ± 45
single-top t-chan	19 585 ± 457
W + jets	31 582 ± 1 377
Z + jets	10 576 ± 288
Multijet	12 193 ± 6 096
$t\bar{t}Z$	2 607 ± 58
$t\bar{t}W$	2 506 ± 17
$t\bar{t}H$	2 135 ± 11
tH	45 ± 5
di-boson	2 037 ± 10
Total	2 492 700 ± 12 346

Table 6.4: Yields of the signal and the background samples after applying the mass selection cuts. The errors represent only the statistical error estimate, except for the multijet (fake lepton) background, which is assigned a 50% uncertainty.

Loop corrections and its dependence on Y_t

The cross-section prediction for the $t\bar{t}$ production channel is known at the NNLO QCD prediction [11]. However, as noted in Chapter 2, the contribution from weak force corrections must be considered in order to obtain the $t\bar{t}$ cross-section with the highest precision or at high energy values. It is the impact of these weak correcions that a top-Yukawa coupling dependence can be obtained in the cross-section measurement, which is exploited to obtain the Y_t value. This chapter covers the detailed methodology used to obtain these weak corrections and the implementation of these corrections in the analysis.

7.1 Estimation of the electroweak corrections

The electroweak correction described in Section 2.6.1 is evaluated using a sub-package inside a tool called HATHOR v2.1-b3 [205]. It stands for HAdronic Top and Heavy quarks crOss section calculatoR, providing corrections for the differential cross-sections based on Refs. [11, 218, 219]. While for the $q\bar{q}$ channel, the full set of weak corrections is included, for the gluon fusion process, all dominant corrections are included. Tiny corrections due to box contributions and the corrections from real emissions are neglected. In Ref. [219], it has been shown that these contributions are small.

In order to get these corrections, the events are classified on the basis of the interacting particles, i.e., whether it is a gluon-gluon or a quark-antiquark interaction. The Born-level diagrams originate from gg and $q\bar{q}$ processes , examples of which are shown in Figure 7.1.

Dependence on the di-top mass, $m_{t\bar{t}}$

The partonic leading order QCD cross-section is then obtained from the HATHOR tool as shown in the topmost plot in Figure 7.2, as a function of the parton-parton centre of mass energy $\sqrt{s}$, or, the di-top invariant mass, $m_{t\bar{t}}$. The quark-antiquark annihilation and the gluon-fusion processes are calculated separately, and they show considerably different curves for the partonic cross-sections[1]. For the $q\bar{q}$ annihilation process, the cross-section and the corrections are obtained both for the $u\bar{u} \to t\bar{t}$ as well as $d\bar{d} \to t\bar{t}$ processes. The corresponding cross-sections

---

[1] It should be noted that these plots correspond to the partonic cross-section which is different from the experimentally observed cross-section.
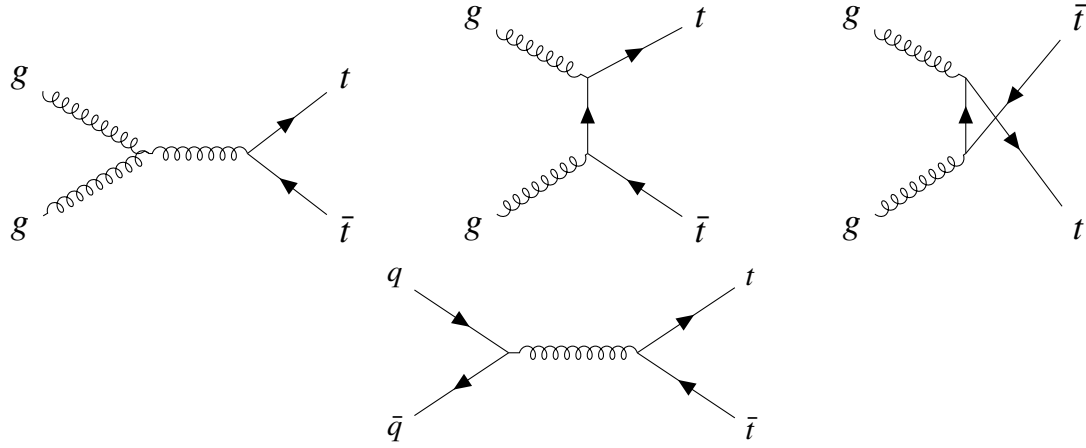
Figure 7.1: Examples of Feynman diagrams for a Born-level $t\bar{t}$ process. The gluon fusion and $q\bar{q}$ processes including these diagrams correspond to ~ 98% of the total number of events in the $t\bar{t}$ sample used in this analysis.
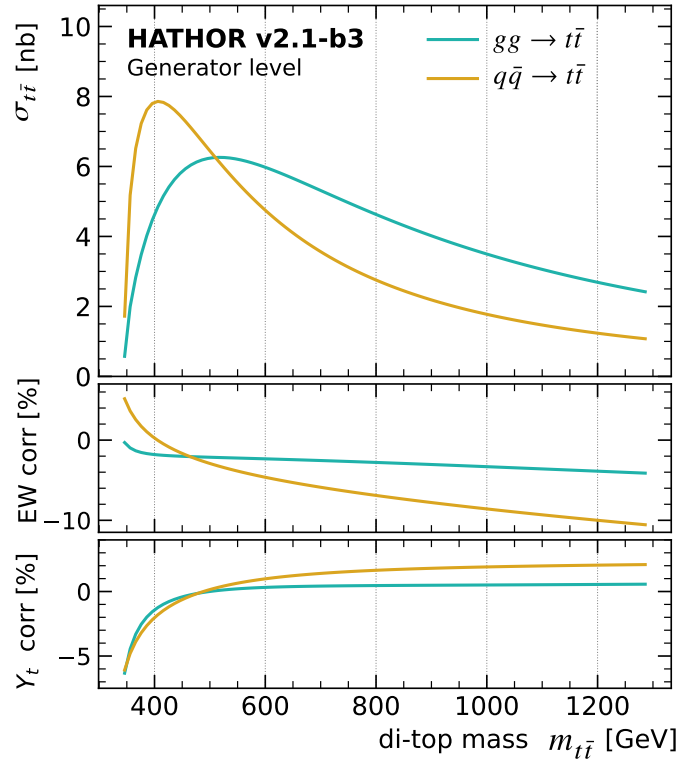
Figure 7.2: Partonic leading order QCD cross-section as well as the electroweak corrections associated to it as functions of the di-top mass, $m_{t\bar{t}}$, or the parton-parton centre of mass energy, $\sqrt{s}$. The topmost plot shows $\sigma_{t\bar{t}}$, the middle plot shows the electroweak correction $\frac{\delta\sigma_{\mathrm{EW}}}{\sigma_{t\bar{t}}}$%, and the bottom one shows the correction due to Y_t, i.e., $\frac{1}{\sigma_{t\bar{t}}}(\delta\sigma_{\mathrm{EW}}^{Y_t=0} - \delta\sigma_{\mathrm{EW}}^{Y_t=1})$ %. The plot is shown for both $gg \to t\bar{t}$ and $q\bar{q} \to t\bar{t}$ processes.

and the corrections obtained for the two processes are almost identical[2]. Hence, for simplicity, only the corrections due to $u\bar{u} \to t\bar{t}$ annihilation is shown, which is labelled as $q\bar{q} \to t\bar{t}$ in the plots. The $q\bar{q} \to t\bar{t}$ process dominates[3] over the $gg \to t\bar{t}$ process for the partonic cross-sections at low $m_{t\bar{t}}$ values. The middle plot shows the percentage ratio of electroweak correction over the leading order QCD cross-section as a function of the di-top mass. Away from the small $m_{t\bar{t}}$ values, the corrections are negative both for the quark- as well as gluon-induced processes, with quark-induced process exhibiting corrections almost twice as large as for the gluon-induced case. Only in the regions close to the threshold of $t\bar{t}$ production, i.e., low $m_{t\bar{t}}$ regions in the plot, a positive correction can be observed, but only for the quark-induced process. The bottom plot in the same figure shows the correction that originates as a consequence of the top-Higgs Yukawa interaction, where it shows the percentage ratio of the difference between the correction obtained using $Y_t = 0$ and $Y_t = 1$ over the LO QCD cross-section. The correction due to Y_t can be seen primarily around the $t\bar{t}$ threshold region. Away from the threshold, the quark-induced process exhibits larger corrections compared to the gluon-induced process.
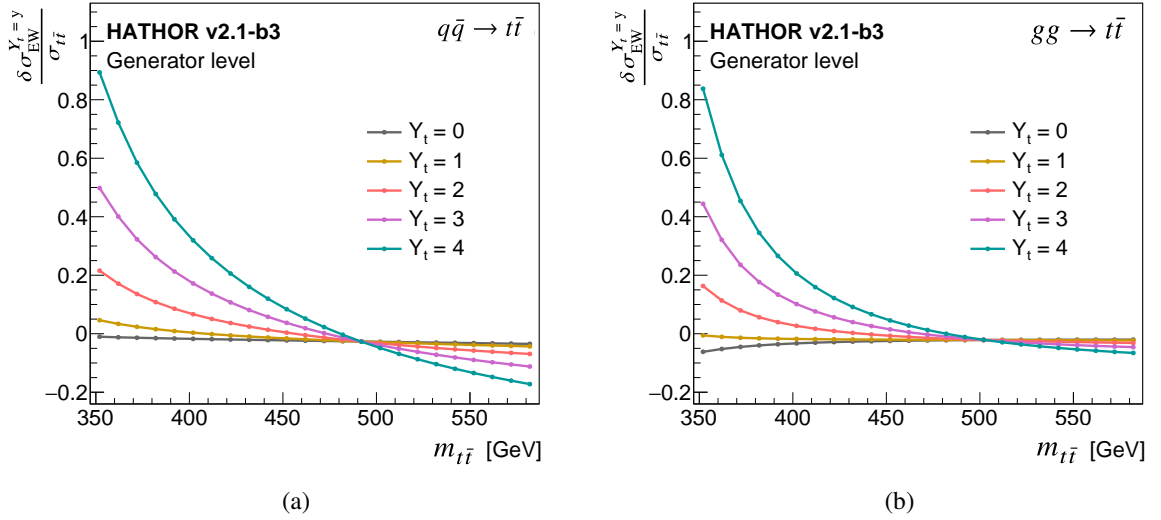
Figure 7.3: Ratio of the electroweak corrections over the leading order QCD cross-section at parton level, i.e., $\frac{\delta\sigma_{EW}^{Y_t = y}}{\sigma_{t\bar{t}}}$, for different Y_t values from (a) quark-antiquark annihilation as well as (b) gluon-fusion processes.

The dependence of the Y_t correction on the di-top mass is shown in Figure 7.3 corresponding to different Y_t values. It shows the ratio of the electroweak correction over the parton-parton LO QCD cross-section as a function of $m_{t\bar{t}}$ to study the impact of enhanced Yukawa coupling values. Figure 7.3(a) and 7.3(b) show the corrections for the $q\bar{q}$ annihilation and the gluon-induced process, respectively. The electroweak corrections corresponding to the Y_t values of 0, 1, 2, 3 and 4 are plotted For the $q\bar{q} \to t\bar{t}$ process, $Y_t = 1$ gives a correction of $\sim 5\%$, $Y_t = 2$ has a correction of $\sim 22\%$, followed by $Y_t = 3$, which shows a correction of $\sim 50\%$ which increases

---

[2] For processes initiated by $c\bar{c}$, the weights for $u\bar{u} \to t\bar{t}$ process is taken, while for the case where $s\bar{s}$ is the initial state, the weights for $d\bar{d} \to t\bar{t}$ process are considered.

[3] However, the total contribution to the cross-section, when convoluted with the parton distribution functions in order to obtain the complete proton-proton to $t\bar{t}$ process, is dominated by gluon-fusion over quark-antiquark annihilation, as described in reference [12].

further going up with larger Y_t values. Hence, a quadratic dependence on different Y_t values can be observed. The same behaviour can be seen for the $gg \rightarrow t\bar{t}$ process, only that the corrections are slightly smaller than the ones obtained for the $q\bar{q} \rightarrow t\bar{t}$ process.

Dependence on the scattering angle, θ

(a)

(b)
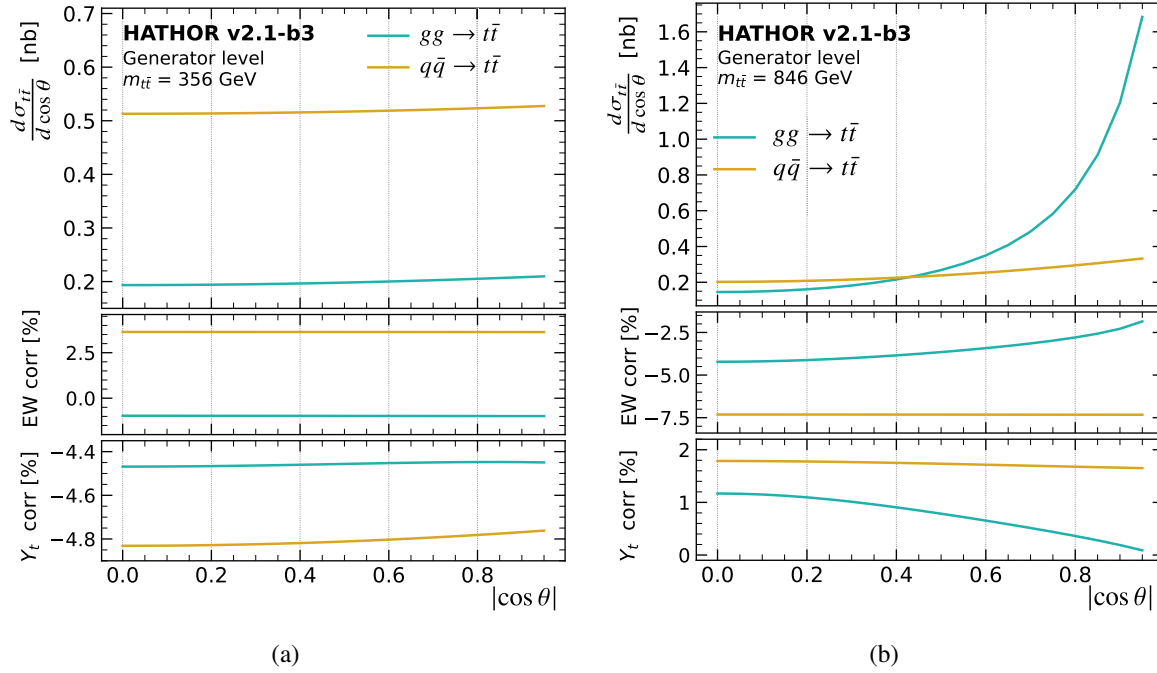
Figure 7.4: Leading order QCD differential cross-section at parton level is shown for $q\bar{q} \rightarrow t\bar{t}$ as well as $gg \rightarrow t\bar{t}$ processes as a function of the cosine of the scattering angle of the top-antitop quark pair. Figure (a) shows the distribution for $m_{t\bar{t}} = 356$ GeV (close to the $t\bar{t}$ production threshold energy), and (b) shows the distribution for $m_{t\bar{t}} = 846$ GeV. In both the figures, the middle plot shows the percentage of electroweak correction over the cross-section: $\left(\frac{d\delta\sigma_{\mathrm{EW}}}{d\cos\theta} / \frac{d\sigma_{t\bar{t}}}{d\cos\theta} \right)$, and the bottom plot shows the percentage of Y_t correction: $\left[\left(1/\frac{d\sigma_{t\bar{t}}}{d\cos\theta} \right) \left(\frac{d\delta\sigma_{\mathrm{EW}}^{Y_t=0}}{d\cos\theta} - \frac{d\delta\sigma_{\mathrm{EW}}^{Y_t=1}}{d\cos\theta} \right) \right]$.

The angular dependence of the cross-section is highlighted in Figure 7.4, where the differential cross-section is plotted for two different $m_{t\bar{t}}$ values. For $m_{t\bar{t}} = 356$ GeV, i.e., close to the $t\bar{t}$ production threshold, plot 7.4(a) shows the LO differential cross-section as a function of $|\cos\theta|$, which is the cosine of the scattering angle of the top-quark in the parton-parton centre-of-mass frame. A weak angular dependence can be seen for the Y_t correction both for the quark- as well as gluon-induced processes at this energy. Plot 7.4(b) shows the same distributions at a higher $m_{t\bar{t}}$ value, $m_{t\bar{t}} = 846$ GeV. The cross-section for both the processes have a contribution from the s-channel process, which has a $(1 + \cos^2\theta)$ dependence. This can be directly observed from the distribution for the $q\bar{q} \rightarrow t\bar{t}$ process. The gluon-fusion process, on the other hand, has an additional contribution from the t-channel diagram which manifests itself as a distinctive shape in the differential distribution, dominating over the s-channel contribution. The electroweak and the Y_t correction for the gluon-induced process also show this angular dependence. On the other hand, the quark-induced process at this energy still shows a weak dependence for the corrections

with respect to $\cos\theta$.
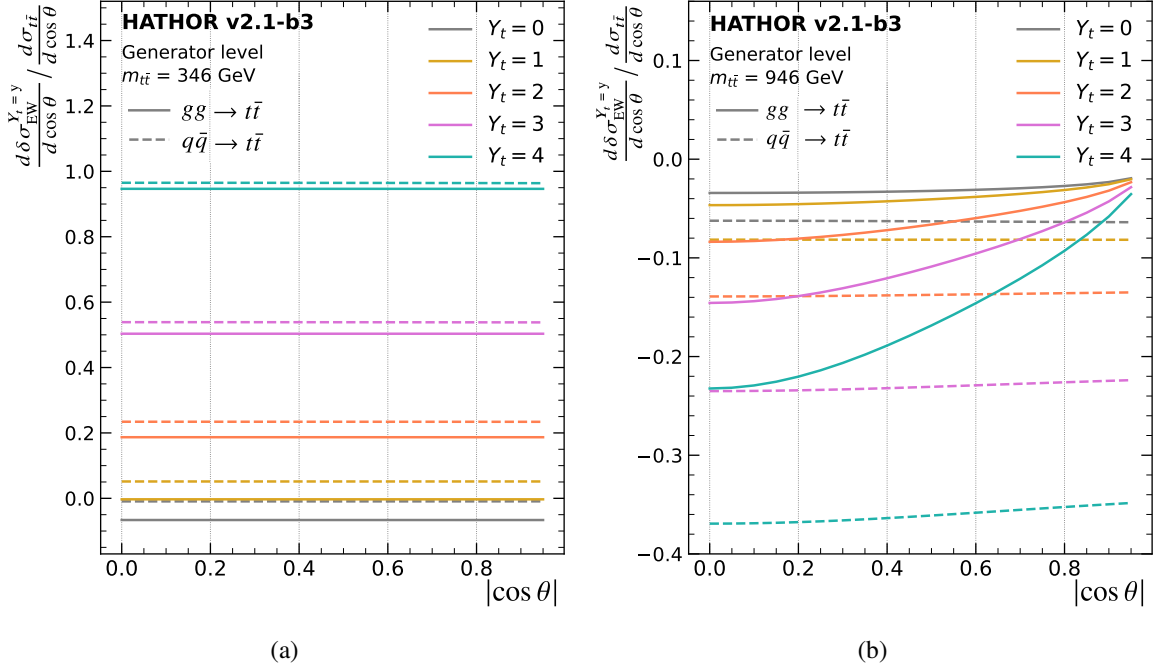
Figure 7.5: The ratio of electroweak correction over the leading order QCD cross-section, i.e., $\left(\frac{d\delta\sigma_{\mathrm{EW}}^{Y_t=y}}{d\cos\theta} \Big/ \frac{d\sigma_{t\bar{t}}}{d\cos\theta}\right)$, is shown in these figures as a function of cosine of the scattering angle, for different Y_t values. Plot (a) corresponds to the electroweak corrections at $m_{t\bar{t}} = 346$ GeV (at the $t\bar{t}$ production threshold energy) which shows no angular dependency, and plot (b) corresponds to a higher $m_{t\bar{t}}$ value ($m_{t\bar{t}} = 946$ GeV) which exhibits an angular sensitivity to the Y_t corrections.

Figure 7.5 shows the impact of enhanced top-Yukawa coupling on the electroweak corrections as a function of $|\cos\theta|$ for two different $m_{t\bar{t}}$ values. Figure 7.5(a) shows the corrections at the threshold, $m_{t\bar{t}} = 346$ GeV, where no angular dependence for any Y_t value is observed for both the quark and gluon induced processes. The electroweak correction increases quadratically as one moves to larger Y_t values. Figure 7.5(b) shows the corrections at a higher $m_{t\bar{t}}$ value, $m_{t\bar{t}} = 946$ GeV. All corrections obtained at this energy contribute negatively to the cross-section. The $q\bar{q}$ annihilation produces larger negative corrections compared to the gluon-fusion process. Moving to larger Yukawa coupling values, the corrections become larger, specifically around the scattering angles of $\pi/2$. As mentioned before, this arises from the involvement of t-channel diagram in the gluon-gluon initial state process. To account for this angular sensitivity, the parametrisation of Y_t correction as explained in the following section, must account for the $\cos\theta$ dependence in addition to the $m_{t\bar{t}}$ dependency.

7.1.1 Y_t correction weights

Electroweak corrections to the parton-level cross-section is incorporated in the analysis by establishing separate weights for each Y_t value based on the initial parton information, as well as on the $m_{t\bar{t}}$ and $\cos\theta$ of the corresponding event. The electroweak correction results from HATHOR are therefore parametrised based on $m_{t\bar{t}}$, $\cos\theta$, and Y_t. A ratio R is defined for different

Y_t values such that:

$$R(m_{t\bar{t}}, \, \cos\theta, \, p, \, Y_t) = \frac{\sigma_{t\bar{t}} \, (m_{t\bar{t}}, \, \cos\theta, \, p, \, (\mathrm{LO} + Y_t + \mathrm{EW}))}{\sigma_{t\bar{t}}(m_{t\bar{t}}, \, \cos\theta, \, p, \, \mathrm{LO})} \tag{7.1}$$

where $m_{t\bar{t}}$ and $\cos\theta$ are the di-top mass and the cosine of the scattering angle of the top quark in the parton-parton centre-of-mass frame, respectively, as explained in the previous section. The cross-section values and the corrections associated to them are calculated from the truth (generator-level) information for the different partonic initial states $p = gg$, $u\bar{u}$, $d\bar{d}$ which is taken after parton shower and initial state radiation. The events are then reweighted for different Y_t values using this ratio for each $t\bar{t}$ signal event in this analysis.

The electroweak part of the cross-section factorises as functions of $\cos\theta$, Y_t, and $m_{t\bar{t}}$ such that:

$$R(m_{t\bar{t}}, \cos\theta, Y_t) = a + b\cos^2\theta + c\cos^4\theta + d\sqrt{1 - \cos^2\theta} \tag{7.2}$$

where a, b, c, d are the coefficients which can be parameterised as functions of Y_t and $m_{t\bar{t}}$. Considering these dependencies, a parametrisation of the coefficients a, b, c, d can be done using a quadratic function in Y_t:

$$x(Y_t, m_{t\bar{t}}) = \alpha + \beta \, Y_t^2 \tag{7.3}$$

with $x = a, b, c, d$. This parameterisation describes the electroweak part of the cross-section perfectly for both the $q\bar{q}$ and gg initial states. The coefficients α and β depend on the centre of mass energy of the two incoming partons ($m_{t\bar{t}}$), and can be parameterised using a sixth order polynomial function in $m_{t\bar{t}}$.
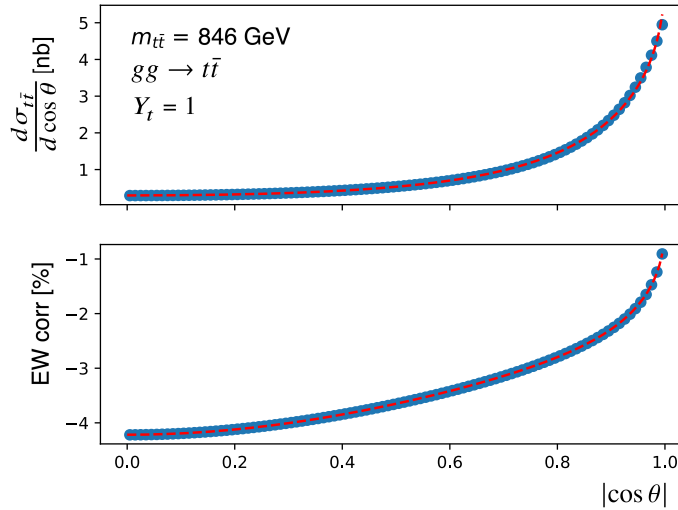
Figure 7.6: Parameterisation of the calculated parton-parton cross-section and the electroweak correction by HATHOR for the gg initial state (dots) with a sixth order ploynominal (dashed red line) for Y_t =1 and a parton-parton centre of mass energy $\sqrt{s}$ = 846 GeV.

Figure 7.6 shows the agreement between the HATHOR calculation and parameterisation for the gg initial state at $m_{t\bar{t}}$ = 846 GeV. It can be seen from the lower plot for the electroweak correction that the fitted function lies on top of the electroweak correction values. Hence, a good

agreement between the fitted function and the electroweak correction can be observed from the plot.

This parameterisation is then applied on the signal $t\bar{t}$ samples at POWHEG generator level. Since POWHEG is a NLO generator, and the parametrisation of the corrections is only at LO, the corrections for the $q\bar{q} \rightarrow t\bar{t}$ and $gg \rightarrow t\bar{t}$ processes can be obtained directly, however, for the case of $qg \rightarrow t\bar{t}$, which does not exist at LO, a direct application of the parametrisation can not be done.

The fraction of each type of event in the $t\bar{t}$ signal sample is evaluated and the majority ($\sim 87\%$) of the events correspond to a gluon fusion process, which is followed by the $q\bar{q}$ channel, with $\sim 11\%$ of the events. Constituting to only $\sim 2.5\%$ of the events, the qg processes only exist at NLO with the possible Feynman diagrams as shown in Figure 7.7. A brief study (described in Appendix B) done to approximate the treatment of qg events show a correlation between the particle associated with the NLO radiation and the initial particles. From these correlation studies, it is seen that these events have a similar behaviour as the gluon-gluon initial state events, where the spectator quark radiates a gluon that interacts with another gluon from the PDF (corresponding to Figure 7.7(a)). This concludes that treating them in parallel with a gluon fusion process serves as a very good approximation.

(a) (b)
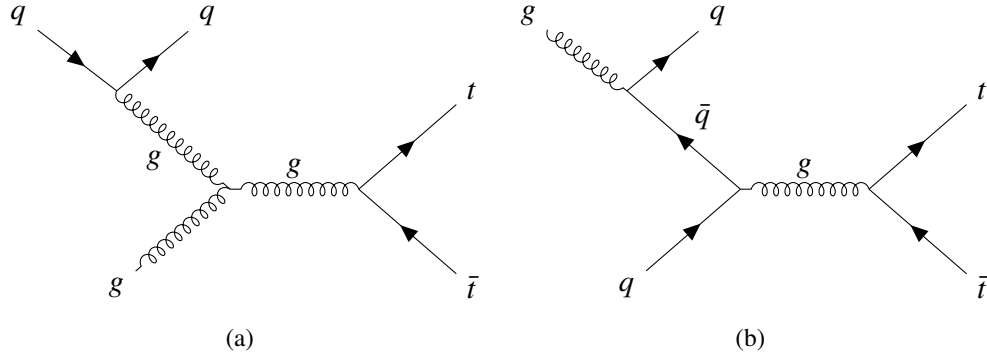
Figure 7.7: Example of possible Feynman diagrams for a qg process from the POWHEG generator.

Figure 7.8 shows the $m_{t\bar{t}}$ distribution from the POWHEG $t\bar{t}$ Monte Carlo sample with the reweighting applied for different Y_t values. The middle and the bottom plot in the figure show the ratio of the distribution with respect to the distribution for $Y_t = 1$. As can be observed from the ratio, the region close to the threshold shows the most sensitivity to the different Y_t values. The bottom plot shows a magnified version of the ratio where one can observe a $\approx 15\%$ correction corresponding to $Y_t = 2$ at the $t\bar{t}$ production threshold compared to the correction for $Y_t = 1$. This reduces further and goes to the negative direction in regions with $m_{t\bar{t}} > 500$ GeV. Higher Y_t values also show the behaviour as expected from the HATHOR calculations, exhibiting a large sensitivity to the top-Yukawa coupling around $t\bar{t}$ threshold energy.

7.1.2 Additive versus multiplicative approach

The corrections to the LO cross-section arise due to the QCD effects as well as the electroweak effects. In general, one may express the cross-sections corrected for the QCD and the electroweak
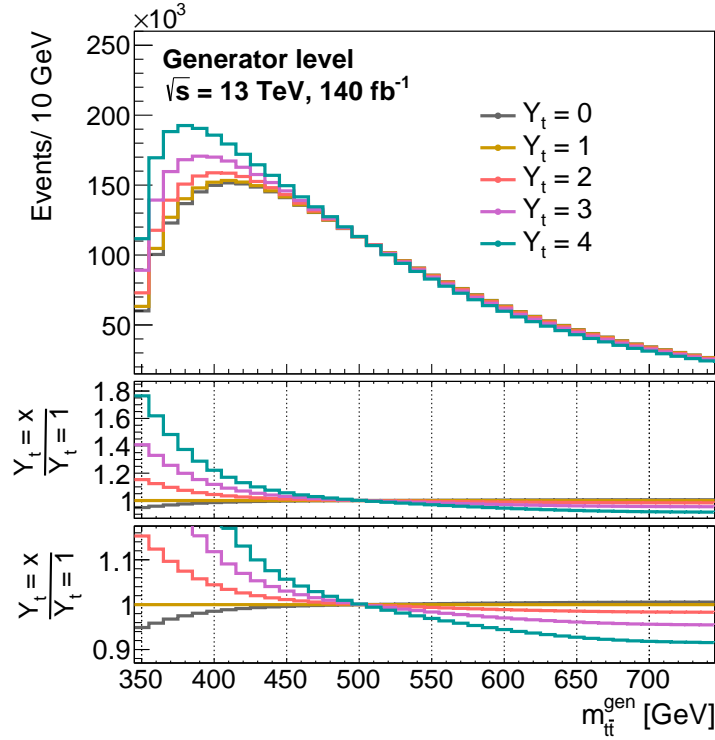
Figure 7.8: $m_{t\bar{t}}$ distribution from the Powheg simulated $t\bar{t}$ signal sample with a reweighting to $Y_t = 0, 1, 2, 3$ according to the HATHOR calculated weights.

effects, represented as σ_{QCD} and σ_{EW}, respectively, as:

$$
\begin{aligned}
\sigma_{QCD} &= \sigma^{LO} + \delta_{QCD}\sigma^{LO} &&= \sigma^{LO}(1 + \delta_{QCD}) \\
\sigma_{EW} &= \sigma^{LO} + \delta_{EW}\sigma^{LO} &&= \sigma^{LO}(1 + \delta_{EW})
\end{aligned}
\tag{7.4}
$$

Therefore, the ratio of the QCD and the EW corrected cross-sections over the leading order cross-sections are expressed as:

$$
\begin{aligned}
\frac{\sigma_{QCD}}{\sigma^{LO}} &= (1 + \delta_{QCD}) \\
\frac{\sigma_{EW}}{\sigma^{LO}} &= (1 + \delta_{EW})
\end{aligned}
\tag{7.5}
$$

The final cross-section can then be obtained in two ways. One of the ways assumes that the QCD and the electroweak corrections factorise with each other, which is known as the multiplicative approach, where the full cross-section is expressed as:

$$
\sigma_{QCD \otimes EW} = \sigma_{LO}(1 + \delta_{QCD})(1 + \delta_{EW}) = \sigma_{LO}(1 + \delta_{QCD} + \delta_{EW} + \delta_{QCD}\delta_{EW}) \tag{7.6}
$$

This analysis uses this multiplicative approach to combine the electroweak and strong corrections. This is driven from the fact that the Powheg generator used for the $t\bar{t}$ sample already includes the QCD corrections, and hence, the electroweak effect can directly be incorporated as a reweighting factor.

In contrast to this approach, the strong and electroweak effects can also be combined by opting

an additive method such that the total cross-section is formulated as:

$$\sigma_{\text{QCD} \oplus \text{EW}} = \sigma_{\text{LO}}(1 + \delta_{\text{QCD}} + \delta_{\text{EW}}) \tag{7.7}$$

The two approaches differ only by a term $\delta_{\text{QCD}}\delta_{\text{EW}}$ which arises from the corrections of $O(\alpha_s\alpha)$, and since it is theoretically challenging to evaluate this correction, both additive and multiplicative approaches are equally justified [220]. Since this analysis uses the multiplicative approach due to its reduced complexity, the difference between the additive and the multiplicative approaches is included as a theoretical uncertainty.
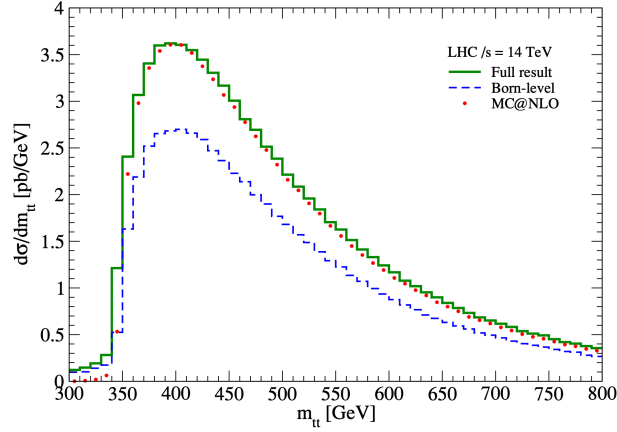
Figure 7.9: Differential cross-section with respect to $t\bar{t}$ invariant-mass in $pp \rightarrow bW^+\bar{b}W^-$ at $\sqrt{s} = 14$ TeV. Green solid line is the full prediction and blue dashed line is the Born-level prediction. The NLO $t\bar{t}$ production computed by MC@NLO is also plotted in red dots. Plot taken from reference [220].

To obtain the cross-section through additive approach, the electroweak corrections need to be applied to the LO cross-section instead of the NLO cross-section from Powheg sample (which includes the QCD corrections). The estimate of the LO cross-section is achieved using the plots from reference [220], shown in Figure 7.9. The $t\bar{t}$ invariant-mass $m_{t\bar{t}}$ is defined as the invariant-mass of the final $WbWb$ system. The green solid line represents the full result which including higher order corrections, and the blue dashed line represents the Born-level result (the LO prediction in the conventional perturbative QCD approach).

It can be seen that the Born level prediction differs from the full cross-section result by a considerable amount. Taking the ratio directly from the plot, one sees that they differ exactly by a factor of 0.75. To obtain the electroweak corrections from the additive method, the electroweak effects obtained from HATHOR are applied on the Born level LO cross-section instead of the full cross-section that contains the QCD effects, which was done in the previous section for the multiplicative approach. This correction is scaled by a factor of 0.75, accounting for the difference between the Born level versus the full cross-section with QCD effects. Using the same fitting procedure as for the multiplicative approach, weights are obtained for the additive method corresponding to different Y_t values.

The results after applying the weights from the additive correction is shown in Figure 7.10, where it is compared with the multiplicative approach for the $m_{t\bar{t}}$ distributions at generator level. It can be observed that the two methods differ from each other by less than 1% for $Y_t = 1$. On the other hand, the same comparison for $Y_t = 2$ shows a difference of approximately 3% in the threshold region, which reduces moving away from the threshold.

(a)   (b)
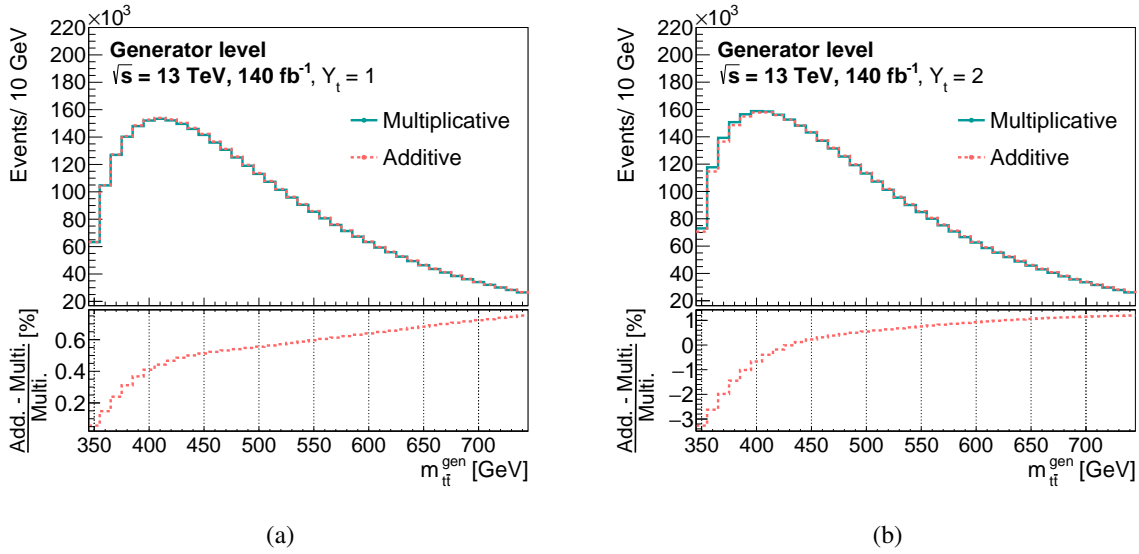
Figure 7.10: These plots show the percentage difference between the additive and multiplicative methods used to combine the electroweak and strong corrections in the cross-section using their generator level $m_{t\bar{t}}$ distributions. Plot (a) shows the comparision for $Y_t = 1$ and plot (b) for $Y_t = 2$.

7.2 Threshold corrections

In the region close to the threshold of $t\bar{t}$ production energy, some additional effects contribute to the cross-section distribution. Near the threshold energy, a color-singlet (quasi-bound) state of $t\bar{t}$ known as toponium is produced as a result of the exchange of gluons between the top quarks in the final state. Although it is not a clearly isolated bound state, its effect is observed in the $t\bar{t}$ cross-section. The current QCD predictions of the MC do not include these bound-state potential contributions around $m_{t\bar{t}} \approx 2m_t$ [221]. These corrections can be systematically resummed to all orders in α_s. Physically, this means that the value of $m_{t\bar{t}}$ can be lower than the $2m_t$ threshold, due to these bound-state effects caused by the virtual gluon exchanges [220]. They are of the form α_s^n/β^m where $\beta = \sqrt{1 - 4m_t^2/m_{t\bar{t}}^2}$ is the speed of the top quark in the $t\bar{t}$ rest frame. In the threshold region where the top and antitop quarks are slowly moving with respect to each other, $\beta \sim 0$, and the α_s^n/β^m contributions are enhanced.

Figure 7.11 shows the same plot as shown in Figure 7.9, but magnified in the threshold region. The cross section (green line) is enhanced over the Born cross-section (dotted blue line) significantly by the bound-state effects, and there appears a shoulder below the threshold corresponding to the color-singlet states in the $t\bar{t}$ channel. In the same figure, a comparison of the prediction with the NLO $m_{t\bar{t}}$ distribution is computed using the MC@NLO generator which includes the full NLO QCD corrections (but not the Coulomb resummation) for the on-shell $t\bar{t}$ productions. Below and near the threshold, the full cross-section is much larger than the MC@NLO prediction, mainly due to the bound-state formation. Above an $m_{t\bar{t}}$ value of 350 GeV, the bound-state effects disappear and the cross section approaches the MC@NLO prediction [220]. The two cross-sections become approximately equal from around $m_{t\bar{t}} \sim 370$ - 380 GeV up to larger $m_{t\bar{t}}$ values.

Figure 7.11 is used to obtain the ratio between the theoretical expectation (including the full effect present at the threshold) and the MC@NLO prediction. The MC@NLO prediction in the
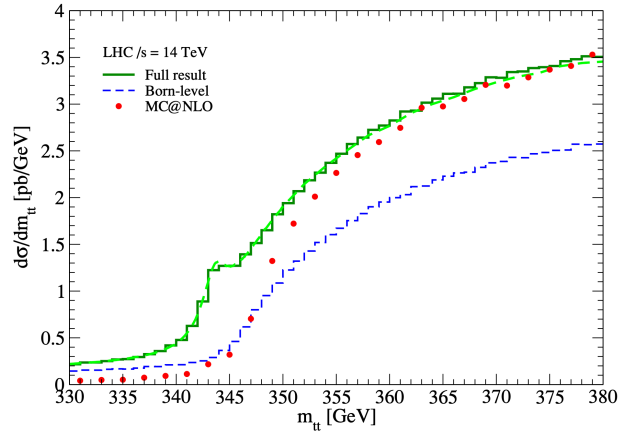
Figure 7.11: Differential cross-section with respect to $t\bar{t}$ invariant-mass in $pp \rightarrow bW^+\bar{b}W^-$ at $\sqrt{s} = 14$ TeV close to the $t\bar{t}$ production threshold energy. This is the same plot (from reference [220]) as shown in Figure 7.9, but magnified in the $t\bar{t}$ threshold region.

figure is considered to be comparable to the $t\bar{t}$ MC sample prediction used in the analysis. In the top-half of Figure 7.12, the two results obtained from the paper are shown. Their ratio is shown in the bottom-half of the figure. A fit is performed on this ratio using a sum of an error function and a Gaussian function centered around 350 GeV. The fitted function is depicted as the blue curve in the figure.
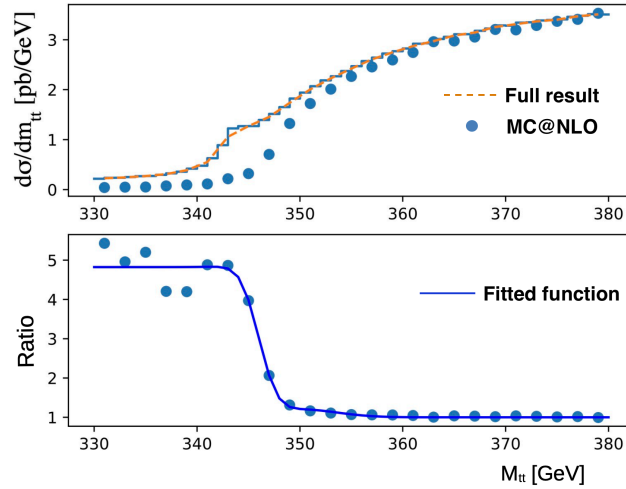
Figure 7.12: The upper plot corresponds to the differential cross-section as a function of $m_{t\bar{t}}$ for MC@NLO sample in blue dots, while the orange dotted line corresponds to the full result as obtained from the paper [220]. The bottom plot is the ratio of the full result to the MC@NLO prediction. The blue curve shows the fitted function on top of it.

The fitted function is used to obtain the correction as weights corresponding to the generator level di-top mass. These weights are evaluated for each event in the $t\bar{t}$ sample, and the resultant $m_{t\bar{t}}$ distribution is obtained as shown in Figure 7.13. As can be observed, the corrections are visible in the threshold region, with a $\sim 15\%$ difference in the first bin with respect to the sample without the application of threshold correction. Note that this 15% correction is in the $m_{t\bar{t}}$ range

of $345 - 355$ GeV where the cross-section itself is very small. Propagating this correction to the $m_{t\bar{t}}$ at detector level, this correction smears out even further.
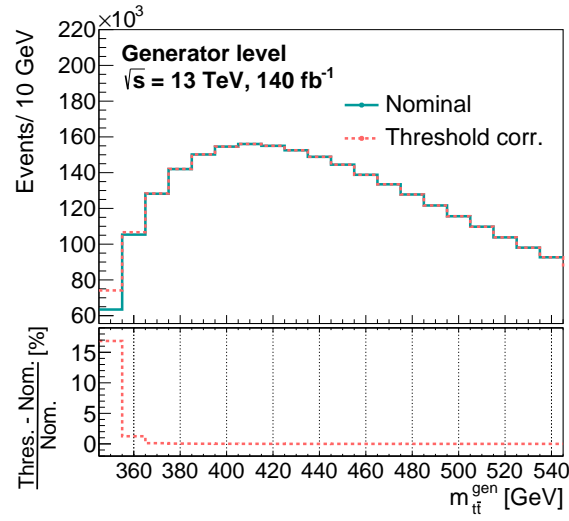
Figure 7.13: Comparison of the generator level $m_{t\bar{t}}$ distribution with as well as without the inclusion of the threshold effects. "Nominal" in the plot refers to the distribution without the threshold correction.

Statistical analysis and results

Ingredients for the analysis have been discussed in the previous chapters where the $t\bar{t}$ mass reconstruction, object definition, event selection, and the creation of the $t\bar{t}$ signal distribution for different top-Yukawa coupling values are explained. The final stage in the analysis procedure combines all information and fits the total Monte Carlo prediction to the Run-2 data from the ATLAS detector so as to obtain the Y_t value.

Starting from the description of the likelihood construction, this chapter discusses the fitting procedure, uncertainty description, and finally, the Y_t results. It also describes the important uncertainties associated with the fitting procedure which affect the final Y_t estimate.

8.1 The fitting approach

The value of top-Yukawa coupling modifier Y_t, which is the ratio of the measured top-Yukawa coupling over its Standard Model value, i.e., $Y_t = \frac{g_t}{g_t^{\text{SM}}}$ is extracted by adjusting the total Monte Carlo prediction for the Run-2 ATLAS data using a *profile likelihood fitting* approach described in this section. The formulation of a *likelihood function* which governs the probability of observed data corresponding to the assumption of different Y_t values, acts as the starting point for the statistical analysis.

8.1.1 Likelihood construction

In a scenario where the optimal value of a parameter of a model has to be determined, the concept of likelihood estimation proves to be extremely useful. Consider a set of n measured values, $(x_1, \ldots, x_n)$, whose probability density function depends upon m unknown parameters $\vec{\theta} = (\theta_1, \ldots, \theta_m)$, such that the probability to observe a variable x_i for given parameter $\vec{\theta}$ is defined by $f(x_i|\vec{\theta})$, where the parameter $\vec{\theta}$ represents a set of real-valued unknown parameters. To estimate the optimal value of the parameter set $\vec{\theta}$, a function is defined, which is represented by a joint probability distribution of the measured values from the random sample:

$$f(x_1, \ldots, x_n|\theta_1, \ldots, \theta_m) = f(x_1|\theta_1, \ldots, \theta_m) \cdots f(x_n|\theta_1, \ldots, \theta_m) \tag{8.1}$$

This joint distribution function $f(x_1, \ldots, x_n|\theta_1, \ldots, \theta_m)$ is known as the *likelihood* function $L(\boldsymbol{x}; \vec{\theta})$, or simply $L(\vec{\theta})$, as it depends upon the vector of unknown parameters, $\vec{\theta}$. The optimal value of $\vec{\theta}$ is defined to be the value of $\vec{\theta}$ for which the likelihood function evaluated on the measured data $(x_i, \ldots, x_n)$ is maximal. Therefore, the optimal value of the parameter can be

obtained by locating the global maximum of the likelihood function $L(\vec{\theta})$ [222]. This method of parameter estimation is termed as the *maximum likelihood estimation*, and the estimated parameter using this method is represented by $\hat{\vec{\theta}}$. Considering that the sample consists of N independent measurements, the likelihood can be represented as:

$$L(\vec{\theta}) = \prod_{i=1}^{N} f(x^i; \vec{\theta}) \tag{8.2}$$

From the equation above, the maximum of the likelihood, described as a product of N terms, needs to be determined. This calculation can be simplified if instead of maximising the likelihood itself, the logarithm of the likelihood is maximised, which would serve an equivalent purpose. This allows for the likelihood to be transformed from a product of N terms into a sum of the logarithms of individual terms, such that:

$$\ln L(\vec{\theta}) = \sum_{i=1}^{N} \ln f(x^i; \vec{\theta}) \tag{8.3}$$

Since a logarithm function is *monotonic*, this transformation of the likelihood by a *log-likelihood* (LL) does not affect the parameter estimation. The optimal parameter value at maximum likelihood stays the same as obtained by maximising the log-likelihood. Hence, the partial derivatives of this function with respect to the individual parameters θ_i should equate to zero, i.e.,

$$\frac{\partial \ln L(\theta_j)}{\partial \theta_j} = 0; \; j = 0, \ldots, m \tag{8.4}$$

This gives a set of simultaneous equations describing solutions at the extremum of the log-likelihood function.

8.1.2 Uncertainty in parameter estimation

The maximum likelihood approach provides an estimate of the parameter value. The information on how accurately the parameter is estimated from the maximum likelihood method is usually expressed in terms of standard deviation of the estimator with respect to its true value, i.e., the variance of the estimator. If the experiment is repeated many times with the same number of measurements per experiment, the variance would determine the spread of the obtained distribution of the parameter.

Numerically, since the likelihood depend upon parameters $\hat{\vec{\theta}}$, the correlation between the possible parameter pairs $(\hat{\theta}_i, \hat{\theta}_j)$ needs to be considered for correct error estimation. Under a Gaussian approximation, the variance is expressed as the inverse[1] of the covariance matrix of the estimators, $\text{cov}[\hat{\theta}_i, \hat{\theta}_j]$:

$$\widehat{V}_{ij} = 1 \bigg/ \left(-\frac{\partial^2 \ln L}{\partial \theta_i \partial \theta_j} \right)\bigg|_{\hat{\theta}_i, \hat{\theta}_j} \tag{8.5}$$

The diagonal elements of the covariance matrix give the variance of the corresponding parameter.

---

[1] This is assuming that the estimator is efficient (such that the minimum variance value can be assumed) and unbiased, i.e., the expected mean value of $\hat{\theta}$ converges to the true value of the parameter.

Hence the variance, or the uncertainty corresponding to a single parameter θ can be expressed in terms of the second derivative at $\theta = \hat{\theta}$ as:

$$\widehat{\sigma^2}_{\hat{\theta}} = \left(-1 \bigg/ \left. \frac{\partial^2 \ln L}{\partial \theta^2} \right) \right|_{\theta = \hat{\theta}} \tag{8.6}$$

This gives symmetric upper and lower uncertainties corresponding to $\hat{\theta}$, which for a sufficiently large data sample holds exactly true. When the likelihood function is approximated to be a Gaussian function of the parameter θ, the log-likelihood becomes a parabolic function of the parameter.

Another way to understand the uncertainty is by using a series expansion. Considering the log-likelihood dependence on a single parameter, the function can be expressed in a Taylor series expansion around the parameter value $\hat{\theta}$ corresponding to the maximum of the log-likelihood function as:

$$\ln L(\theta) = \ln L(\hat{\theta}) + \left[\frac{\partial \ln L}{\partial \theta} \right]_{\theta = \hat{\theta}} (\theta - \hat{\theta}) + \frac{1}{2!} \left[\frac{\partial^2 \ln L}{\partial \theta^2} \right]_{\theta = \hat{\theta}} (\theta - \hat{\theta})^2 + \dots \tag{8.7}$$

By definition, the log-likelihood will be maximum corresponding to the estimator value $\hat{\theta}$; and the first derivative with respect to the parameter at $\theta = \hat{\theta}$ is zero. Ignoring the higher order terms, the equation reduces to:

$$\ln L(\theta) = \ln L_{\text{max}} + \frac{1}{2} \left[\frac{\partial^2 \ln L}{\partial \theta^2} \right]_{\theta = \hat{\theta}} (\theta - \hat{\theta})^2 \tag{8.8}$$

The curvature of the log-likelihood function therefore provides information about the precision of the parameter estimates. Using Equation 8.6, this equation becomes:

$$\ln L(\theta) = \ln L_{\text{max}} - \frac{(\theta - \hat{\theta})^2}{2\widehat{\sigma^2}_{\hat{\theta}}} \tag{8.9}$$

which implies that a deviation of $\hat{\sigma}_{\hat{\theta}}$ from the mean $\hat{\theta}$ can be written in the following form:

$$\ln L(\hat{\theta} \pm \hat{\sigma}_{\hat{\theta}}) = \ln L_{\text{max}} - \frac{1}{2} \tag{8.10}$$

This indicates that if the parameter $\hat{\theta}$ is changed by one standard deviation $\hat{\sigma}_{\hat{\theta}}$ from its maximum likelihood estimate, then the log-likelihood decreases by 1/2 from its maximum value [223].

It is also possible to obtain different values for the upper and lower uncertainties in the parameter estimation. In this case where the log-likelihood plot is asymmetric, it becomes more accurate to extract the uncertainties from the log-likelihood scan corresponding to the parameter. Figure 8.1 shows an example of the log-likelihood function, displaying the 1σ uncertainties corresponding to the best-fitted parameter with different upper and lower uncertainty values. A change of n times σ corresponds to a reduction in $\ln L_{\text{max}}$ by $n^2/2$. The plot shows a reduction of $\ln L_{\text{max}}$ by 1/2, i.e., a shift of 1σ from the estimated $\hat{\theta}$. In this thesis, this graphical approach is used to determine the uncertainties only for the parameter of interest in the fit. All other fit parameters are determined using the numerical approach as described in Equation 8.6.
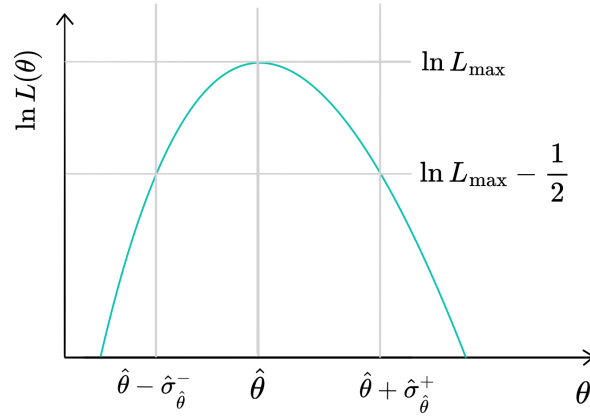
Figure 8.1: Illustration of a log-likelihood scan as a function of parameter θ is shown in this plot. The uncertainty in the parameter estimate $\hat{\theta}$ is given by the parameter values corresponding to the maximum log-likelihood reduced by one half. The lower uncertainty is represented by $\hat{\sigma}_{\hat{\theta}}^{-}$ and the upper uncertainty by $\hat{\sigma}_{\hat{\theta}}^{+}$.

Similar to the case of numerical uncertainty estimation, if the log-likelihood depends upon multiple parameters, the correlation between the parameters need to be considered. Instead of a one-dimensional likelihood scan, a contour is obtained, from which the error is estimated. Fixing all the parameters other than θ_i to their estimated values, as an initial guess, the uncertainty in $\hat{\theta}_i$ is determined by reducing the maximum $\ln L$ by 1/2. However, this does not give a correct uncertainty estimate. Instead, the uncertainty is given by the extreme points on the ellipse in (θ_i, θ_j) plane. This is equivalent to finding the values of θ_j where $\ln L$ changes by 1/2 while maximising the $\ln L$ with respect to all other parameters.

Practically, instead of maximising the log-likelihood function, an equivalent approach is used where the problem transfers to a minimisation of $-\ln L$ instead. Numerical methods are implemented using computing algorithms to perform this minimisation procedure.

8.1.3 Likelihood for binned data

The data are recorded in terms of histograms with a specific number of bins such that each individual data point represents a bin. The number of entries in each bin is generally not expected to follow a Gaussian distribution as this number could also be small for certain bins. It is however reasonable to expect that it obeys a Poissonian distribution instead of a Gaussian, such that the expected number of entries in each bin is estimated from the theoretical prediction which, in turn, depends upon the parameters $\vec{\theta}$. The final likelihood is then a product of the Poissonian distribution from each bin such that the log-likelihood can be expressed in the form:

$$
\begin{aligned}
\ln L &= \ln \prod_{i=1}^{N_{\text{bins}}} \text{Poiss}(n_i; \mu_i(\theta_1, \ldots, \theta_m)) \\
&= \sum_{i=1}^{N_{\text{bins}}} \ln \left(\frac{[\mu_i(\theta_1, \ldots, \theta_m)]^{n_i}}{n_i!} e^{-[\mu_i(\theta_1, \ldots, \theta_m)]} \right)
\end{aligned}
\tag{8.11}
$$

where n_i is the number of entries in bin i, μ_i is the expectation value of the number of entries in bin i, and N_{bins} refers to the total number of bins used in the histogram. This equation can be further simplified by ignoring the terms which do not depend[2] on $\vec{\theta}$ such that the log-likelihood becomes proportional to:

$$\ln L(\theta_1, \ldots, \theta_m) \propto \sum_{i=1}^{N_{\text{bins}}} \left[n_i \ln \mu_i(\theta_1, \ldots, \theta_m) - \mu_i(\theta_1, \ldots, \theta_m) \right] \tag{8.12}$$

The binned approach of likelihood construction considering Poissonian treatment for the bin entries, is much faster than the full likelihood estimation. However, care has to be taken to ensure that the binning is not too wide so as to hide the sensitivity to the parameter of interest.

8.1.4 Incorporating systematics in the likelihood definition

Out of the parameters $(\theta_1, \ldots, \theta_m)$, usually, not all parameters are of direct interest in the analysis, but are necessary so as to model the characteristics of the data sample. These are called *nuisance parameters* which appear as a consequence of various uncertainties associated to the yield of the distribution. All the systematic uncertainties in the analysis will be included as nuisance parameters in the fit. The parameters among $(\theta_1, \ldots, \theta_m)$ which are to be measured are known as the *parameters of interest* (POI) and are represented by μ. This thesis has only one parameter of interest. All remaining parameters are treated as nuisance parameters, represented by $\vec{\theta}$. The full likelihood function can now be expressed as a joint product of the individual likelihood functions from the response model for physics measurement, and the systematic uncertainties associated with the yields, i.e.,

$$L_{\text{full}}(x, \theta^{\text{obs}}|\mu, \vec{\theta}) = L_{\text{phys}}(x|\mu, \vec{\theta}) L_{\text{subs}}(\theta^{\text{obs}}|\vec{\theta}) \tag{8.13}$$

where L_{phys} is the likelihood function for the physics measurement, which describes the distribution of the observables x for each value of μ as well as for each value of the nuisance parameters $\vec{\theta}$; and L_{subs} refers to the likelihood corresponding to the subsidiary measurement of uncertain parameters with θ^{obs} representing the data of the prior subsidiary measurement, and $\vec{\theta}$ referring to the nuisance parameters constrained by the measurement. Thus, in this likelihood, usually referred to as the *profile likelihood*, the term L_{phys} depends upon the parameters μ and $\vec{\theta}$.

On the other hand, the subsidiary measurement must be provided for the experimental uncertainties (from calibration measurements) as well as for the theoretical uncertainties. Considering one of the subsidiary measurements θ for simplicity, the L_{subs} can be approximated by a Gaussian function, $G(\theta^{\text{obs}} = \hat{\theta}|\theta, \sigma_{\hat{\theta}})$ where $\hat{\theta}$ is the best estimate of θ with the corresponding uncertainty of $\sigma_{\hat{\theta}}$. A simple coordinate transformation is made such that $\alpha(\theta) := (\theta - \hat{\theta})/\sigma_{\hat{\theta}}$ so as to transform the function to a Gaussian with zero mean and unit standard deviation, i.e., $\text{Gauss}(\alpha^{\text{obs}} = 0|\alpha, 1)$. This simplifies the likelihood expressed in Equation 8.13 to this form:

$$L_{\text{full}}(x|\mu, \alpha) = L_{\text{phys}}(x|\mu, \alpha)\,\text{Gauss}(0|\alpha, 1) \tag{8.14}$$

In this joint likelihood approach, the nuisance parameters are expressed in terms of the so-called *pull parameters*, α. The data may introduce constraints on these pull parameters, as a

---

[2] The terms that can not be expressed as functions of $\vec{\theta}$ or are simply constants do not contribute to the log-likelihood minimisation procedure and, hence, are not useful in the equation.

consequence of which the fitted values corresponding to these α may result in an uncertainty smaller than unity. This is referred to as a *constrained* parameter. This indicates that the nuisance parameter α experiences a joint constraint from both the terms in the full likelihood expression, leading to the propagation of this reduced uncertainty from α to the POI, μ. The presence of an uncertainty smaller than unity may also mean that this nuisance parameter is important in the fitting procedure. In addition to an uncertainty smaller than unity, the data may also introduce a non-zero mean corresponding to the nuisance parameter α, i.e., the data are shifted away from the nominal value considered in the subsidiary measurement. For both the situations where there is a constraint or a *pull* corresponding to a nuisance parameter, it must be studied carefully to assess its plausability. This will be explained in more detail in Section 8.4.1, where the obtained results are discussed.

In order to account for m nuisance parameters $(\alpha_1, \ldots, \alpha_m)$, the likelihood is modified by a product of the individual Gaussian term for each parameter. Additionally, since the physics measurement in this thesis is done using a binned likelihood approach, the full likelihood is expressed as a product over all bins used in the fit, taking the form:

$$L_{\text{full}}(x|\mu, \alpha) = \prod_{i=1}^{N_{\text{bins}}} L_{\text{phys}}(x^i|\mu, \alpha) \prod_{j=1}^{m} \text{Gauss}(0|\alpha^j, 1) \tag{8.15}$$

8.1.5 Introducing the Y_t dependency

The electroweak corrections are incorporated in the $t\bar{t}$ signal Monte Carlo histograms using the weights obtained from the HATHOR tool as explained in Section 7.1.1. To incorporate the Y_t dependence of the signal sample in the likelihood, the first term L_{phys} in Equation 8.15 can be expressed as a Poisson distribution (ref. Equation 8.11) multiplied over all bins. For bin i, this term can be written as:

$$L_{\text{phys}}(x^i|\mu, \alpha) = \text{Poiss}\left[n_{\text{obs}}^i|s^i(\alpha)R_{\text{EW}}^i(\mu, \alpha) + b^i(\alpha)\right] \tag{8.16}$$

where n_{obs}^i is the observed number of events in bin i with the expected bin count given by the sum of the predicted signal and the background yield. The signal yield is given by a product of the leading order $t\bar{t}$ sample yield as obtained from the POWHEG simulation ($s^i(\alpha)$), and the electroweak reweighting factor[3] $R_{\text{EW}}^i(\mu, \alpha)$ obtained from the HATHOR tool which is a function of the top-Yukawa coupling value.

Y_t templates for the $t\bar{t}$ sample

The Y_t sensitivity observed in the sample is visible through its $t\bar{t}$ invariant mass ($m_{t\bar{t}}$) distribution, which is therefore used for the fit. From the obtained correction weights for different Y_t values, individual templates are obtained for the reconstructed $t\bar{t}$ invariant mass. The fit takes into account these templates using a morphing method. Template morphing, in this context, refers to the method of interpolation between the histogram templates corresponding to different variations of the Y_t values, as well as for the nominal[4] sample with no Y_t variation. The morphing

---

[3] Note that this $R_{\text{EW}}^i(\mu, \alpha)$ is obtained event-wise for the $t\bar{t}$ sample, thereby yielding different bin contents for different Y_t templates.

[4] Nominal sample corresponds to a $Y_t = 1$ template.

algorithm interpolates between these templates to find out the best fitted histogram. In this way, a continuous interpolation for Y_t is obtained from separate histograms for individual points in Y_t space. The simplest interpolation method uses a piece-wise linear interpolation between the templates. A simple morphing[5] technique interpolates between these templates such that each template is assigned a normalisation weight, which is a function of the parameter of interest, μ.

Recalling Equation 7.3, the dependence of the yield on the top-Yukawa coupling is exactly quadratic. Therefore, if the parameter of interest in the fit is made to be Y_t^2 instead of Y_t, the interpolation between different top-Yukawa coupling templates can be made to be an exactly linear function of the parameter of interest. This makes the fit convergence easier and removes any ambiguity arising from the type of interpolation technique used. Hence, Y_t^2 is used as the POI, μ in the fit, which implies that the square root of the fitted result should be evaluated to obtain the value of Y_t.
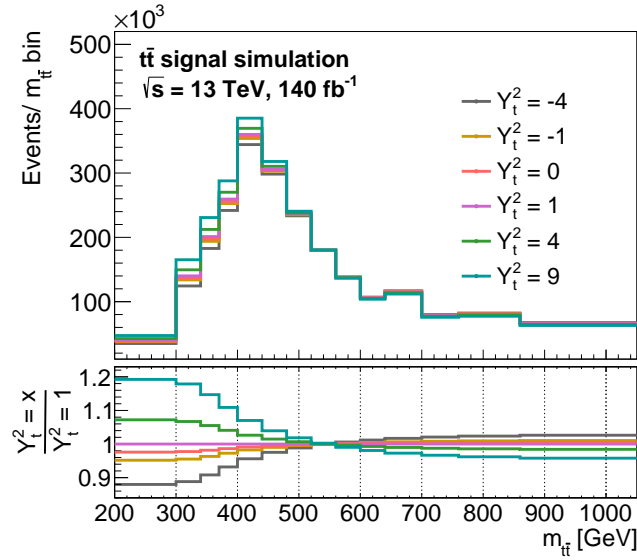
Figure 8.2: $t\bar{t}$ invariant mass histograms (at the reconstruction level) for the $t\bar{t}$ signal sample corresponding to different Y_t^2 templates used in the fit. The lower plot corresponds to the ratio of yield for the template with respect to the $Y_t^2 = 1$ template yield.

Templates for the histograms corresponding to different Y_t^2 values are shown in Figure 8.2, displaying the $t\bar{t}$ signal histograms used in the fit. In addition to the templates corresponding to $Y_t^2 = 0, 1, 4, 9$, histograms corresponding to negative Y_t^2 values can also be seen. These hypothetical Y_t^2 values[6] are introduced in the fit so as to produce a stable fit minimisation with a continuous likelihood function for the situation where the -1σ uncertainty in the fitted Y_t^2 result goes further below zero.

To carefully consider the Y_t-sensitive region, the fit employs an optimised binning strategy. The histogram consists a total of 14 bins. Two bins cover the area below the $t\bar{t}$ production threshold. The binning is made finer for $m_{t\bar{t}}$ near the $t\bar{t}$ threshold to preserve Y_t^2 sensitivity in the otherwise broad bins. Away from the threshold, the binning is adjusted to be wider again

---

[5] This morphing technique is also used to include $\pm1\sigma$ systematic uncertainties described in Section 8.1.4.

[6] These weights for negative Y_t^2 values are produced in a similar way as the ones for positive Y_t^2 values using same reweighting equations.

since no significant Y_t^2 sensitivity is observed in this region.

Figure 8.3 shows the interpolation between the Y_t^2 templates used in the fit for all 14 bins used. The plots show the ratio of the yield obtained for different Y_t^2 templates with respect to the nominal $Y_t^2 = 1$ template yield. Signal yield for each $m_{t\bar{t}}$ bin used in the distribution is plotted as a function of Y_t^2. It can be seen that the interpolation is exactly linear as Y_t^2 is used as the POI. For low $m_{t\bar{t}}$ bins, it can be seen that the fitted straight line has a positive slope as the electroweak corrections increase with inceasing Y_t^2 values. On the contrary, for higher $m_{t\bar{t}}$ ranges, this slope is negative.

8.1.6 Goodness of fit

A measure of how well the fit model describes the observed data is quantified by a parameter known as the *goodness-of-fit*, and it must be noted for any fit procedure used. This metric should be able to incorporate the information on agreement of data and prediction after the fit, as well as the pulls of the nuisance parameters. Since the maximum likelihood value by itself is not an ideal quantity to convey this information, this is achieved by using the maximum likelihood value compared to a reference. Therefore, in this thesis, the likelihoods of two fit models are compared. The first one corresponds to the likelihood of the fitting of data with the nominal model. The other likelihood corresponds to the fit for the same data, but with a so-called *saturated model*. This model is constructed by including an extra free parameter for each data point such that the model fits the data perfectly. A metric λ is constructed which is defined as the ratio of these two likelihoods:

$$\lambda = \frac{L(\hat{\mu}, \hat{\alpha})}{L_{\text{saturated}}} \tag{8.17}$$

This ratio of the likelihood of the nominal model with respect to the likelihood of the saturated model follows a χ^2 distribution in the Gaussian limit. The goodness of fit is then is expressed by its $\chi_\lambda^2 = -2 \ln \lambda$ value. This is quoted along with the number of degrees of freedom ("ndf") [223] used in the fitting approach.

8.1.7 Upper limits using the profile likelihood ratio

The profile likelihood ratio $\lambda(\mu_0)$ is a test statistic defined as the ratio of the likelihood for a conditional best estimate of the parameter which maximises the likelihood over the unconditional maximum likelihood function, i.e.,

$$\lambda(\mu_0) = \frac{L(\mu, \hat{\hat{\alpha}}_\mu)}{L(\hat{\mu}, \hat{\alpha})} \tag{8.18}$$

where $\hat{\alpha}$ in the equation refers to the maximum likelihood estimator, and a $\hat{\hat{\alpha}}_\mu$ corresponds to a constrained maximum likelihood estimator of α obtained by fixing the μ. Hence, in the numerator, only the nuisance parameters α are used in the fit, while the POI μ is fixed to a constant value $\mu = \mu_0$. In the denominator, the $\hat{\mu}$ and $\hat{\alpha}$ are the best fit values of μ and α corresponding to the observed data sample.

Using a likelihood scan for the parameter, a standard error of $\pm 1\sigma$ can be obtained, as described in Section 8.1.2. This is stated as the 1σ uncertainty on the parameter, which corresponds to the standard deviation of the probability density function (PDF) of the estimator. In a large sample
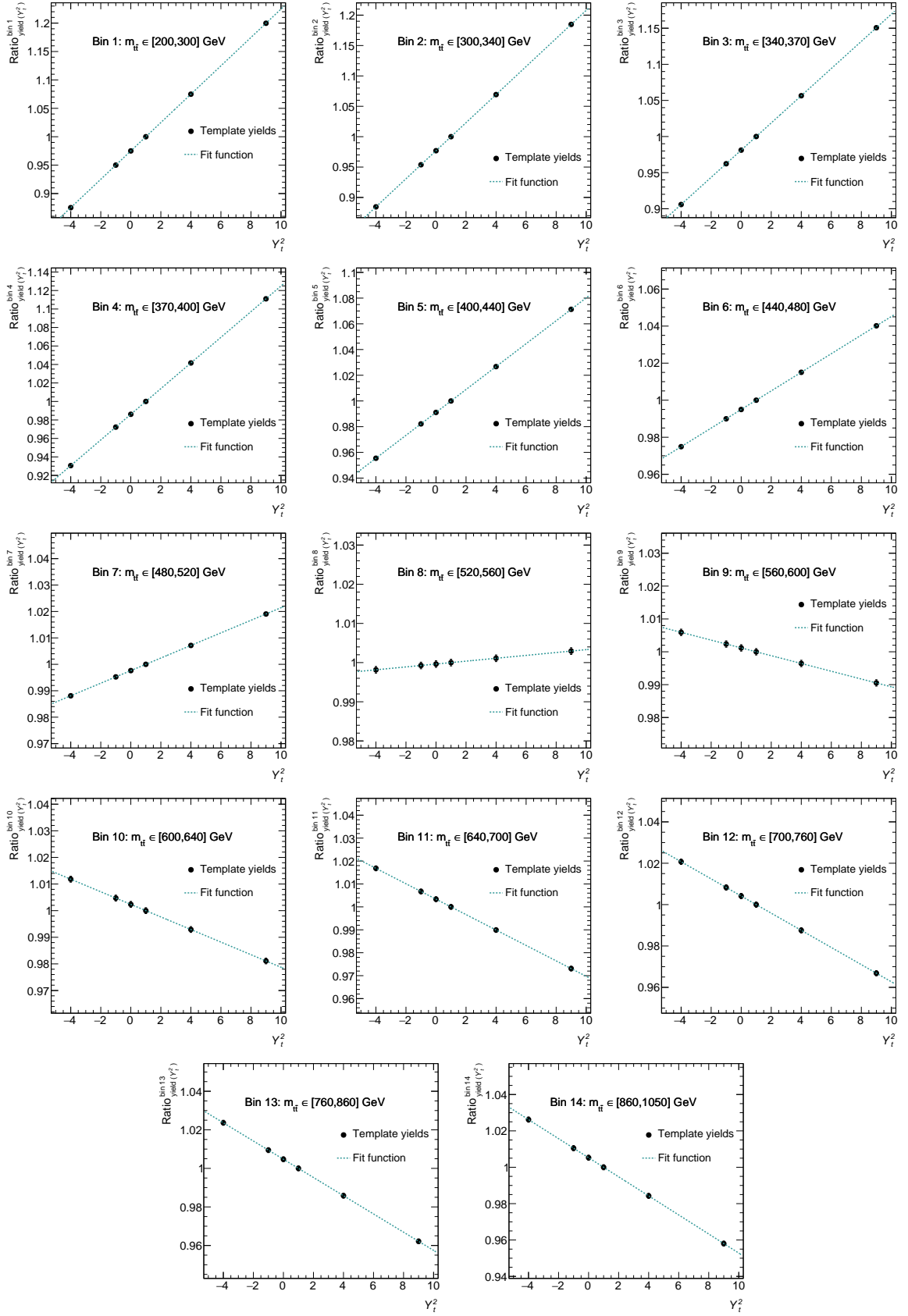
Figure 8.3: The ratio of yield obtained considering the electroweak correction for different Y_t^2 values with respect to the $Y_t^2 = 1$ yield. This ratio is shown as a function of Y_t^2 for the bins used in the $m_{t\bar{t}}$ distribution. The fitted linear function is shown in dotted lines.

limit, the PDF simplifies to a Gaussian function. However, for non-Gaussian PDFs, usually in addition, the *confidence intervals* are stated, which do not make an assumption for the PDF distribution to be a Gaussian.

A confidence interval helps provide a qualitative statement about the fraction of times that such an interval would contain the true value of the parameter in a large number of repeated experiments. In case the estimator has a Gaussian PDF, the standard $\pm 1\sigma$ error corresponds to a so-called 68% confidence level (CL). This interval is defined such that 16% of the distribution sits on both the left and right side of the interval. Figure 8.4(a) shows a PDF $f(\hat{\alpha}, a)$ of an estimator $\hat{\alpha}$ given the true value of the parameter, a. The shaded regions sum up to 32% of the total distribution. This is an example of a two-sided confidence interval.

(a)   (b)
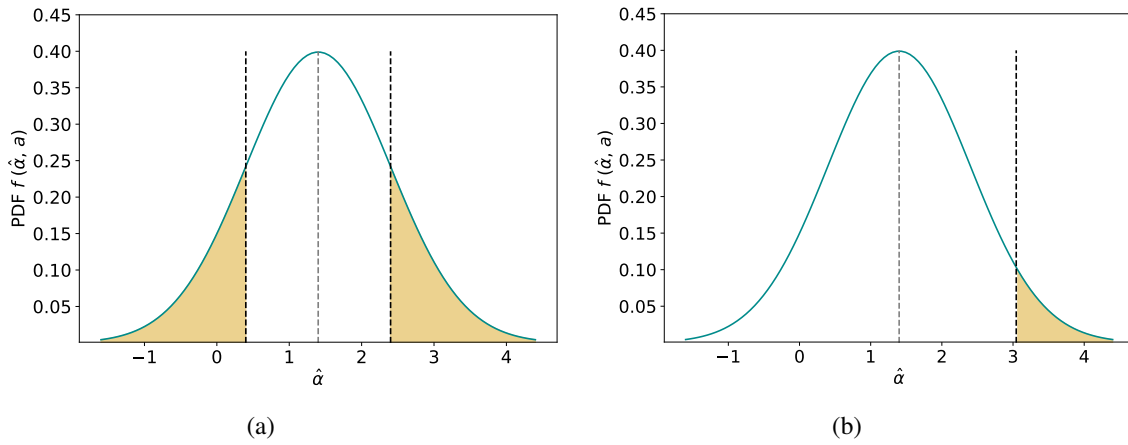
Figure 8.4: Illustration of a two-sided and a one-sided confidence interval/ limit. Figure (a) depicts the probability density function for the estimator $\hat{\alpha}$ for a given value of the true parameter, a. The combined area of the two shaded regions represent a 32% probability that the estimator would lie in this region. Figure (b) shows an upper limit corresponding to the estimator, where the shaded region represents 5% of the total distribution with $\hat{\alpha} > 0$.

However, it is also possible to quote a one-sided confidence interval, or an upper limit. For example, when instead of a 68% central interval, a 95% lower interval is chosen as acceptance region in $f(\hat{\alpha}, a)$, the resulting confidence interval on $\hat{\alpha}$ will be a 95% upper limit as depicted in Figure 8.4(b). This implies that the area of the region above $\hat{\alpha} = a$ amounts to 5% of the total area under the curve. To evaluate this upper limit, additional information can be utilised, such as whether a certain region is physically observable for the analysis or not. If for instance, $\hat{\alpha} < 0$ falls in the unphysical region, only the area of the distribution with $\hat{\alpha} > 0$ is considered in the limit calculation for the 95% upper limit. This is also the definition used in Section 8.4.3 to obtain the upper limit on Y_t^2.

8.1.8 Fitting software

A fitting framework known as TRExFitter is used for this analysis, which is an ATLAS-specific profile likelihood framework that builds statistical models in HistFactory [224] format. In the HistFactory package, RooFit [225] workspaces are produced, creating a statistical model for the fit. RooStats [226] is an additional package providing tools for further statistical inferences regarding the fit performance. The TRExFitter framework inherits the minimisation

procedure from the MINUIT [227] tool, which uses specialised methods to evaluate uncertainties on likelihood estimators.

8.1.9 Pre-fit modelling

Modelling of the kinematic variable used in the fit, i.e., the $m_{t\bar{t}}$ distribution for the data and simulation is shown in Figure 8.5. The signal $t\bar{t}$ distribution included in this plot takes into account the threshold correction as described in Section 7.2. The uncertainy band includes both the statistical as well as systematic errors for each bin. The y-axis has a logarithmic scale so as to obtain a clear picture of the contribution from different backgrounds in the plot. In general, a good agreement between the data and the Monte Carlo prediction can be seen from the ratio pad. However, the data yield below $m_{t\bar{t}} = 400$ GeV has a higher yield compared to the simulation. This is also the region of interest for the Y_t-sensitivity. Above this $m_{t\bar{t}}$, the data yield shows slightly lower values compared to the simulation. Nevertheless, the difference between the data and prediction from the Monte Carlo is fully covered by the uncertainty band.
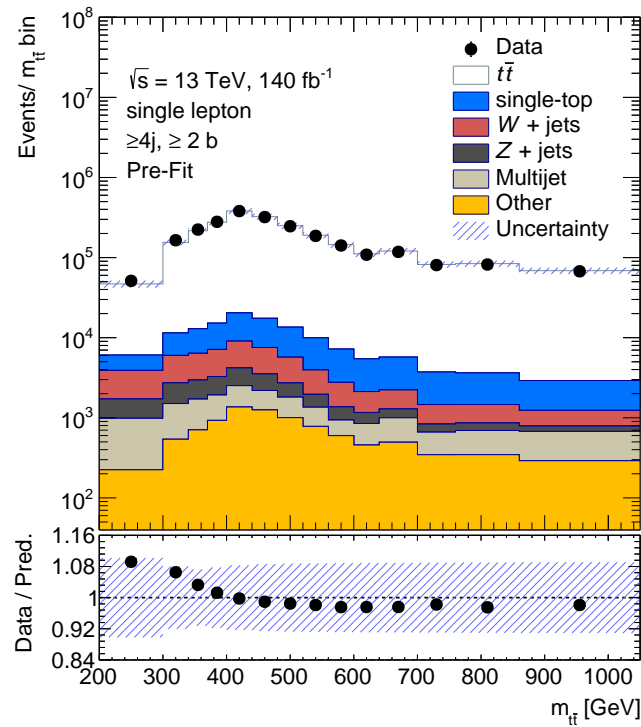
Figure 8.5: The pre-fit $m_{t\bar{t}}$ distribution with the data and the Monte Carlo simulation for signal and the backgrounds considered in the fit. The lower plot shows the ratio of the data to the total Monte Carlo prediction. The uncertainty band plotted in the figure correspond to the full set of systematic and statistical uncertainties. The y-axis is in logarithmic scale, corresponding to the number of events in each variable $m_{t\bar{t}}$ bin.

8.2 Systematic uncertainties

This section discusses the systematic uncertainties considered in the fit. The inclusion of these uncertainties in the likelihood has been described in Section 8.1.4. These systematic uncertainties result from a limited theoretical knowledge or imperfect modelling of the detector response. One can broadly categorise these uncertainties into two types: experimental and theoretical uncertainties. Experimental uncertainties arise from limitations in the experimental precision caused by the detector and can be observed for instance, in the measurement of the luminosity of the collision, or the momentum of a physics object. Theoretical uncertainties, on the other hand, stem from the approximations or simplifications made in the underlying theoretical models, such as the modelling of the signal $t\bar{t}$ Monte Carlo sample. A good enough estimation of these uncertainties is crucial for the analysis, as the impact of these uncertainties will be reflected in the resultant value of the parameter of interest. These uncertainties are included in the fit as up and down distributions corresponding to their $\pm 1\sigma$ variations.

8.2.1 Experimental uncertainties

Sources of systematic uncertainties related to the finite resolution and efficiency of the detector that are taken into consideration for the fit are described below.

Luminosity

The simulated signal and background events need to be reweighted to their appropriate luminosity values as explained in Section 6.2.3. The integrated luminosity corresponding to the full Run-2 data from the ATLAS detector evaluates to $\mathcal{L}_{\text{int}} = 140.07 \pm 1.17$ fb^{-1} [108], which gives a total of 0.83% uncertainty on the value of luminosity used in the analysis. As a result, a uniform overall uncertainty of $\pm 0.83\%$ is applied to all Monte Carlo simulated samples.

Pileup reweighting and suppression

The pileup, as introduced in Section 3.1.2, need to be well-modelled for the simulated samples in order to correctly describe the pileup profile in data. To account for the differences in the pileup distributions for the data and the Monte Carlo simulation, an uncertainty corresponding to it is applied [228] and propagated into the fit as up and down variations.

Additional methods are used to suppress the pileup interactions. The jet vertex tagger (JVT) discriminant is built to classify the jets whether it is orginating from the hard-scattering or the pileup interactions. The differences between the efficiency of this identification of jets in data and simulation are incorporated as scale factors in the event. These scale factors are derived using dedicated pileup enriched Monte Carlo simulation samples, and the statistical uncertainty in the derived scale factors is also taken into account [229]. This uncertainty in the JVT efficiency is implemented as up and down systematic variations in the fit.

Lepton efficiency

The performance of reconstruction, identification, isolation, and trigger for electrons and muons in the detector differ for data and Monte Carlo simulated samples. These differences are corrected by the application of lepton scale factors corresponding to each of these performances. For electrons, one nuisance parameter each for reconstruction, identification, isolation and trigger

efficiency calculations are included. For muons [183], two nuisance parameters each for isolation, identification, trigger and track-to-vertex-association efficiencies are applied corresponding to their statistical and systematic errors.

Other uncertainties for leptons include the measurement of their energies and momenta. The precision of the lepton momentum scale and resolution may be different for the data and the Monte Carlo simulation. For electrons [230], the uncertainties on the energy scale and resolution are included as nuisance parameters in the fit. For the muons, the uncertainties corresponding to the energy scale, as well as the uncertainty in momentum from the sagitta (curvature) measurement of the track are considered. Errors in the momentum scale and resolution of CB muons (originating from the inner detector and the muon spectrometer) are also considered.

Jet energy scale

The measurement of energy and momentum of the jets need to be corrected to account for several effects such as pileup, energy leaks and the underestimation of energy for hadronic jets due to their low-energy interactions in the calorimeters. Uncertainty in its measurement may also arise from the particle composition of the jet, for instance, the shower shapes for quark-initiated jets are different than that for the gluon-initiated jets. A calibration procedure as described in Section 5.1.4 attempts to adjust the energy, momentum and direction of the reconstructed jets so as to match them with their corresponding jets at generator level. The fit must take into account the uncertainties related to this calibration procedure.

The jet energy scale calibration includes the uncertainties from the η-intercalibration using dijet events, calibration using well-calibrated Z+jet and γ+jet events, high-p_T jet calibration using multijet balance, pileup corrections, and jet flavour related systematics. Reference [192] lists the full description of the sources of uncertainties associated with these calibration methods. The uncertainties so obtained lead to a large set of correlated components. Several schemes exist to obtain a reduced set of uncertainties to allow simplified descriptions with a minimum loss of correlation information. An eigenvector decomposition method categorises the uncertainties into separate components based on their origin. The uncertainties are grouped into a number of components arising from the statistics, modelling, the detector, or from a combination of sources. In this thesis, the jet energy scale calibration uncertainties are included in the fit as a set of 34 nuisance parameters.

Jet energy resolution

The jet energy resolution on the transverse momentum is given by a similar relation as shown in Equation 3.6, which is dependent upon a noise term, a stochastic term and a constant term. To measure the JER, the jet momentum must be measured precisely. To achieve this, the jets are balanced against one-another in a well-defined dijet system, meaning that the width of the dijet asymmetry distribution across p_T and η is measured with respect to a well-calibrated (central) region of the detector. JER is then measured by an iterative Gaussian fit to the core of the asymmetry distribution [192]. The systematic uncertainty in its measurement at low p_T is dominated by an imprecise knowledge of the scale of the jets, whereas at high p_T the closure of the dijet balance method is largely dominant. Measurements using zero bias data with *random cones* are used to constrain the noise term. In the *random cones* method, energy deposits in the calorimeter are summed in circular areas analogous to the jet area for anti-k_t jets with $R = 0.4$, and a difference between the p_T cones provides a measure of random fluctuations of deposited

energy. An eigenvector decomposition similar to JES is used to obtain a reduced set of JER uncertainties.

To ensure that the resolution of the jet energy measurement in the simulation matches the data, a smearing procedure is used. For the p_T regions where the resolution in data is larger than in MC simulation, the simulation sample is smeared such that its average resolution matches the data resolution. The uncertainties are then propagated by smearing the jets according to Gaussian distribution with a width σ_smear given by $\sigma_\mathrm{smear}^2 = (\sigma_\mathrm{nominal} + |\sigma_\mathrm{NP}|)^2 - \sigma_\mathrm{nominal}^2$, where σ_nominal is the nominal JER after the smearing of the MC simulated sample, and the σ_NP is the $\pm 1\sigma$ variation of the JER uncertainty component. For the regions with a smaller resolution in data than in MC simulation, no smearing is performed, as the data should remain unaltered. However, the differences between the data and simulation is applied as an additional systematic uncertainty, $\sigma_\mathrm{NP} = \sigma_\mathrm{nominal}^\mathrm{data} - \sigma_\mathrm{nominal}^\mathrm{MC}$. As a result of, a total of 14 nuisance parameters corresponding to JER uncertainties are obtained, which are included in the fit.

Flavour-tagging of the jet

The algorithms used to identify the flavour of the jets give rise to a separate set of uncertainties originating from the calibration applied. The performance of a b-tagging algorithm is character-ised by the probability of identifying a jet as a b-flavoured jet (b-jet tagging efficiency) and the probability of mistakenly identifying a c-flavoured jet or a light-flavoured jet as a b-jet, given by their corresponding mis-tag efficiencies. Scale factors are applied to correct the simulated b-tagging efficiencies in order to match the efficiencies in data. These scale-factors are in general, functions of p_T and η of the jets. Several sources contribute towards the uncertainties in the flavour tagging algorithms for the jets, such as limited statistics for the data and simulated samples and the modelling of the simulated samples used for the derivation of these scale factors. They are determined from variations in the jet flavour components and from the extrapolation of systematics into regions where the measurements are statistically limited, starting around jet $p_\mathrm{T} > 400$ GeV [231]. A large number of correlated variations are thus obtained, from which a reduced set of uncertainties are retrieved using an eigenvector decomposition method. As a result, a set of eigenvalues are used as nuisance parameters in the fit with 9 systematics corresponding to b-flavoured jets, and 4 each for the c-flavoured and the light-flavoured jets. Two additional systematics from the extrapolation method are also included in the fit.

Missing transverse energy

Error in the measurement of the missing transverse energy of the event (ref. Section 5.1.6) is covered by this systematic uncertainty. It is a complex uncertainty, a part of which is propagated through the calibration of physics objects in the final state through JES and JER measurements. The other part of this systematic originates from the uncertainties on the soft terms in the $E_\mathrm{T}^\mathrm{miss}$. The uncertainty on $E_\mathrm{T}^\mathrm{miss}$ is finally propagated in the form of three nuisance parameters in the fit. One of the uncertainties corresponds to the scale of the soft term measurement, and the other two are on the resolution of the p_T projection of the soft term parallel as well as perpendicular to the p_T of the hard term [232].

8.2.2 Theoretical uncertainties

These uncertainties are related to the modelling of the Monte Carlo simulated samples which arise from the assumptions made in the underlying theory of the simulation process. The theoretical uncertainties considered for the signal $t\bar{t}$ sample as well as the backgrounds are described as follows.

$t\bar{t}$ modelling

- **PDF variations:**
  Accurate determination of the parton distribution functions (PDFs) of the proton is crucial for precision measurements. This estimation is provided by a number of dedicated collaborations that extract this information using different methods. Even for PDFs based on similar datasets, the resultant central values and their corresponding uncertainties vary for different groups, indicating that the use of these PDFs from a single group may underestimate the true uncertainties. Hence a combination of individual PDF sets is used to achieve a reliable uncertainty estimate in the LHC cross-sections.

  The signal sample uses the NNPDF3.0LO [204] set as parton distribution functions. The uncertainties in its estimation are evaluated using the PDF4LHC15 [209, 210] error set that uses a combination of the results from different individual groups. A reduced set of uncertainties are obtained using an eigenvector decomposition consisting of 30 components. These components are symmetrised[7] to obtain the up and down systematic variations which are then included in the fit in the form of 30 nuisance parameters.

- **Cross-section normalisation:**
  Theoretical uncertainties on the predicted cross-section value stemming from the variation of PDF, α_s and missing higher orders, is applied as a normalisation systematic to the $t\bar{t}$ signal sample. These uncertainties [233] are obtained using the PDF4LHC15 prescription, and approximate to an overall uncertainty of +3.49% and −4.42%, which is applied on the $t\bar{t}$ sample and is included as a nuisance parameter in the fit.

- **h_{damp} variation:**
  The parameter h_{damp}, which controls the p_{T} of the first additional emission beyond the Born configuration in the POWHEG-BOX-v2 [153–155] generator, is set to 1.5 times the mass of the top quark for the nominal $t\bar{t}$ signal sample. A sample with the same specifications as the nominal one, but with an h_{damp} equal to three times the top-quark mass is taken as a systematic uncertainty. The difference between this systematic and the nominal sample is symmetrised to obtain the up and down variations, which are included as a nuisance parameter in the likelihood.

- **Parton shower and hadronisation:**
  To describe the impact of the uncertainty originating from the chosen hadronisation model, the nominal sample which uses PYTHIA v8.230 [163] showering scheme is compared with another $t\bar{t}$ sample using the HERWIG v7.1.3 [159, 160] showering scheme. The matrix element (ME) generator for both the samples is POWHEG-BOX-v2. The difference between

---

[7] The implementation of the difference between the nominal and the systematic distributions as both up and down systematic variations is referred to as one-sided symmetric uncertainties in this thesis. This approach is used for the systematics for which only one-sided variation is available.

the distributions obtained using the HERWIG v7.1.3 sample and the nominal sample is symmetrised and taken as one nuisance parameter in the likelihood.

- **NLO matching:**
  The nominal $t\bar{t}$ signal sample uses a combination of POWHEG-BOX-v2 matrix element generator along with PYTHIA v8.230 for parton showering. The matching between POWHEG and PYTHIA is called vetoed shower, where PYTHIA produces emissions in the full phase-space but vetoes the emissions in regions of the phase space that are already covered by POWHEG. In both the generators, ordering of the emissions in the event evolution is based on a variable related to the p_T, called "hardness". Double counting or regions in the phase space not modelled by POWHEG or PYTHIA may occur due to differences in the hardness definitions used in the two generators. In this vetoed shower, PYTHIA is required to be aware of the hardness value in POWHEG. This hardness value can be varied by defining a specific p_T^{hard} setting [208]. The default value of the parameter p_T^{hard} in this matching scheme is zero, which is used for the signal sample.

  An alternative sample is obtained by setting the parameter value p_T^{hard} to unity, and the difference between the nominal and $p_T^{\text{hard}} = 1$ distribution is symmetrised to obtain up and down variations. This systematic is included in the fit as one nuisance parameter.

- **Mass variation of the top-quark:**
  Distributions are obtained using alternative simulation samples with the same specifications as the nominal sample, but using a top-quark mass of 172 GeV and 173 GeV, as opposed to the 172.5 GeV used for the nominal $t\bar{t}$ simulation. They are taken as symmetric uncertainties in the fit with the distribution corresponding to $m_t = 172$ GeV as the up variation and the one for $m_t = 173$ GeV as the down variation of the systematic uncertainty.

- **Initial state radiation (ISR):**
  The uncertainty originating from the modelling of ISR is estimated from three sources. The first source is the variation of α_s parameter of the ISR in the parton shower, given by the `var3cUp` and `var3cDown` [163] variations. They are symmetrised and included as a nuisance parameter in the likelihood. The second source of uncertainty on the ISR is the variation of the renomalisation scale, μ_R. The distribution for $\mu_R \times 0.5$ is taken as the up-variation, and the $\mu_R \times 2$ is taken as the down-variation. They are symmetrised and included as one nuisance parameter in the fit. The third component considered for the ISR systematic originates from the factorisation scale, μ_F. The up-variation comes from the $\mu_F \times 0.5$ distribution and the down-variation from the distribution corresponding to $\mu_F \times 2$. This uncertainty is also symmetrised and considered as one nuisance parameter in the likelihood.

- **Final state radiation (FSR):**
  The uncertainty arising from the modelling of the final state radiation is obtained by the variation of the μ_R scale related to the QCD-induced emissions in the parton shower. The distribution for $\mu_R^{\text{FSR}} \times 0.5$ is considered as the up-variation, and the one for $\mu_R^{\text{FSR}} \times 2$ is taken as the down-variation. These variations are symmetrised and included as one nuisance parameter in the fit.

- **Lepton p_T mismodelling:**
  p_T distribution of the top-quark is not modelled well since the generator does not include

higher order NNLO effects. This mismodelling can directly affect the lepton p_T *acceptance*, as well as the $m_{t\bar{t}}$ distribution. To address the missing NNLO effects in the $t\bar{t}$ signal sample, a *stress-test* is conducted on the lepton p_T distribution. In this approach, p_T of the lepton is reweighted and tests are made to examine the *acceptance* effects. Weights are obtained for the $t\bar{t}$ sample so as to match the data with the total prediction. Thereafter, the acceptance, defined as the ratio of the number of events with a lepton p_T cut selection of 27 GeV (used in the analysis) over the number of events without any selection cut on lepton p_T, is evaluated. This is done for the events reweighted to match the data, as well as for the non-reweighted events.

As a first step, a ratio $w_{t\bar{t}}$ of the difference between the two-dimensional ($m_{t\bar{t}}$, lepton p_T) distribution for data and the predicted background over the $t\bar{t}$ prediction, is obtained in bins of lepton p_T and $m_{t\bar{t}}$. This weight $w_{t\bar{t}}$ is defined as:

$$w_{t\bar{t}} = \left[\frac{(n_{\text{data}} - n_{\text{background}})}{n_{t\bar{t}}} \right]_{(\text{lepton } p_T, \, m_{t\bar{t}}) \text{ bins}} \tag{8.19}$$

where n represents the total number of events in a (lepton p_T, $m_{t\bar{t}}$) bin corresponding to the data, background and $t\bar{t}$ samples. The obtained 2D plot is shown in Figure 8.6, where this ratio is seen to vary from ~ 0.85 to ~ 1.1.
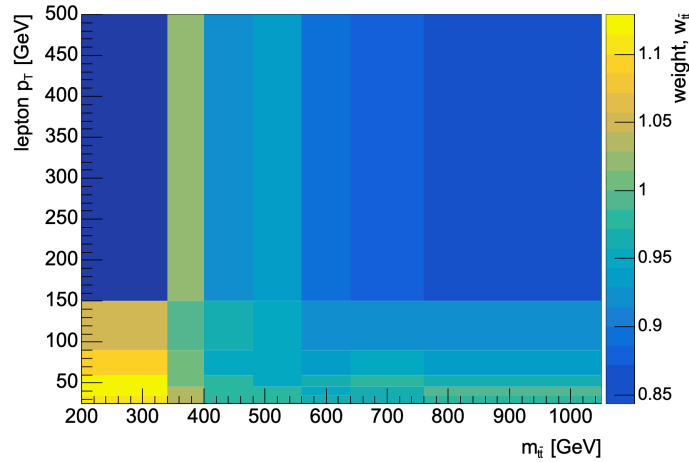
Figure 8.6: Weight $w_{t\bar{t}}$ as a function of $m_{t\bar{t}}$ and p_T^{lepton} at the reconstruction level. The weight is plotted along the z-axis, the scale for which is shown on the right.

In the next step, a fit is performed as a function of lepton p_T in a given $m_{t\bar{t}}$ bin. This straight line fit allows for the prediction of these weights in the lepton p_T values lower than 27 GeV through extrapolation, providing a method to estimate the number of events for no cut selection. Thereafter, the acceptance at generator level is estimated. Two acceptance values are evaluated, defined as:

$$a_{\text{reweighted}} = \frac{n_{\text{reweighted}}^{p_T \text{cut}}}{n_{\text{reweighted}}^{\text{all}}} \quad \text{and,} \quad a_{\text{non-reweighted}} = \frac{n_{\text{non-reweighted}}^{p_T \text{cut}}}{n_{\text{non-reweighted}}^{\text{all}}} \tag{8.20}$$

where $a_\text{reweighted}$ is the acceptance for the case with lepton p_T reweighting done using the straight line fits obtained, while $a_\text{non-reweighted}$ refers to the acceptance without these weights applied, n refers to the number of events, the superscript "$p_T$cut" refers to the case where lepton $p_\text{T} > 27$ GeV, and the superscript "all" refers to the case without any lepton p_T cut selection.

(a)   (b)
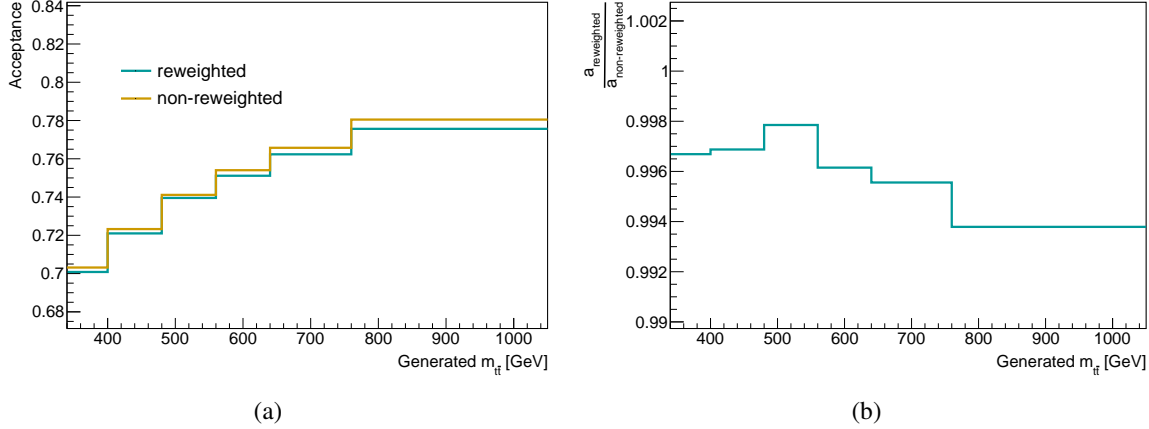
Figure 8.7: Acceptance as a function of generated $m_{t\bar{t}}$. These values are shown for the reweighted and the non-reweighted cases. Plot (b) shows the ratio of the reweighted acceptance to the non-reweighted acceptance as a function of generated $m_{t\bar{t}}$.

Acceptance values for the reweighted and non-reweighted case as a function of generated $m_{t\bar{t}}$ are shown in Figure 8.7(a). The ratio of these two acceptances, i.e., $\frac{a_\text{reweighted}}{a_\text{non-reweighted}}$ is shown in Figure 8.7(b). From this ratio plot, an almost uniform distribution can be observed with a negligible effect of $\sim 0.2 - 0.6\%$, at generator level. This effect when studied at reconstruction level, should smear-out even further to become close to zero. Since no notable difference in shape of the $m_{t\bar{t}}$ distribution is seen from the mismodelling of lepton p_T, as a reasonable approximation, this effect is ignored in the analysis.

Background modelling

The modelling uncertainties on major backgrounds are also estimated. Since most of the contribution comes from the single-top and W+jets background, additional modelling uncertainties are included for them.

- **Normalisation uncertainty:**
  Similar to the $t\bar{t}$ signal, the backgrounds are also assigned a normalisation uncertainty so as to take into account any error in the theoretical prediction of the cross-section. This uncertainty combines the estimated errors from the PDF and α_s variations and is included as a nuisance parameter for that background. The percentage of up and down variations in the cross-section for each background included in the likelihood is shown in Table 8.1. An overall 50% normalisation uncertainty is applied to the data-driven multijet bakground. Two nuisance parameters are included in the fit corresponding to the electron and the muon fake estimation. Since the background contribution from the processes other than single-top (Wt, s-chan and t-chan), W+jets, Z+jets, and the multijet background, is negligible, their normalisation uncertainty will not have any notable impact on the result.

114

Background	Variation up (%)	Variation down (%)
single-top Wt	3.6	-3.5
single-top s-channel	3.8	-3.5
single-top t-channel	1.9	-1.2
W+jets	5.0	-5.0
Z+jets	5.0	-5.0
$t\bar{t}Z$	1.23	-1.42
$t\bar{t}W$	2.2	-2.0
di-boson	5.0	-5.0

Table 8.1: Summary of the up- and down-variations of normalisation uncertainty for the backgrounds. These variations correspond to the percentage with respect to the nominal cross-section values, and are applied as an overall (constant) uncertainty throughout the background distribution.

- **Single-top Wt background:**
  Modelling uncertainties considered for the Wt background include the uncertainties originating from three sources. Similar to the $t\bar{t}$ signal modelling, an uncertainty on the μ_R, μ_F, var3c, and the FSR are considered. These are incorporated as four nuisance parameters in the fit. In addition, an alternative sample for the Wt background is considered to account for the differences in the *diagram-removal* and the *diagram-subtraction* (ref. Section 6.2.2) scheme for Wt Monte Carlo generation. Thus, a one-sided uncertainty is obtained which is symmetrised and included in the fit as a single nuisance parameter.

- **Single-top s- and t-channel backgrounds:**
  Uncertainties corresponding the modelling for these backgrounds include the μ_R, μ_F, var3c and the FSR variations. They are applied in the same way as for the Wt background, and hence, four nuisance parameters corresponding to these uncertainties are included.

- **W+jets background:**
  The variation of renormalisation and factorisation scales, μ_R and μ_F are incorporated as a single nuisance parameter in the fit. The up-variation refers to the distribution obtained with ($\mu_R \times 0.5; \mu_F \times 0.5$) and the down-variation is obtained by using ($\mu_R \times 2; \mu_F \times 2$) values. Hence, for this systematic uncertainty, μ_R and μ_F are varied simultaneously.

8.3 Smoothing and pruning of systematics

8.3.1 Smoothing and symmetrisation

The obtained systematic uncertainties have their own associated statistical fluctuations. Some of the simulated samples themselves have small statistics, while others have systematic variations that are statistically limited. This may result in large statistical fluctuations in the $m_{t\bar{t}}$ distribution, when the variation is compared to that of the nominal sample. If incorporated into the fit, these

distributions could result in an unstable fit performance. Hence, *smoothing* techniques are required to minimise the impact of statistical fluctuations on the systematic uncertainties. This technique provides a smoothed distribution out of a given systematic distribution by merging the neighbouring bins. The adjacent bins for which the combined statistical uncertainty is greater than their combined difference with respect to the nominal sample [8], the bins are merged into one bin, and a single uncertainty is determined for the two merged bins.

Along with the smoothing, symmetrisation is also applied on all one-sided systematics, i.e., where only one variation with respect to the nominal sample is known. For the systematics where both up and down variations are known, symmetrisation is applied on all of them except the JER systematics and the normalisation uncertainties. The symmetrisation of a two-sided systematic effectively averages out the systematic uncertainty in the bin, which further reduces the impact of statistical fluctuations, if any.
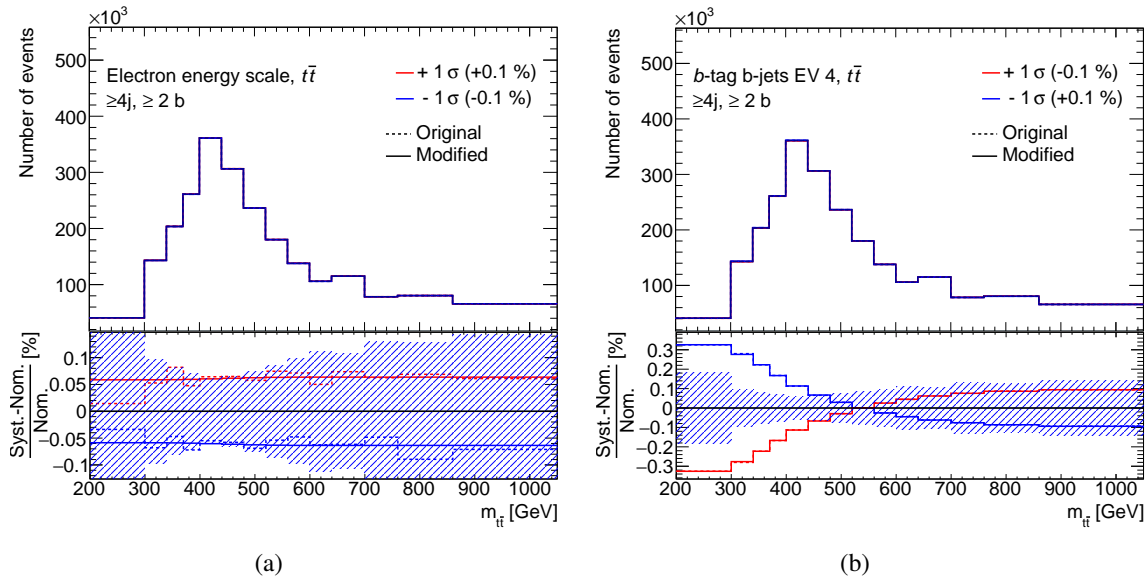
Figure 8.8: The effect of smoothing and symmetrisation on systematic uncertainties for the case with (a) large enough statistical fluctuations, compared to the case with (b) negligible statistical fluctuations. The up variation is given by the red lines $(+1\sigma)$ and the down variation is given by the blue lines (-1σ). The dashed lines correspond to the raw systematic distributions and the solid lines represent the smoothed and symmetrised distributions.

For the case where large statistical fluctuations exist, the smoothing process can modify the distribution considerably. This can be observed from Figure 8.8(a), where the uncertainty on electron energy scale is shown for the $t\bar{t}$ signal sample. The dashed lines correspond to

---

[8] Smoothing procedure first defines a threshold δM for each bin, such that $\delta M = max(\delta S, \delta N)$ for the uncertainty correlated to the nominal sample, and $\delta M = \sqrt{\delta S^2 + \delta N^2}$ for uncorrelated uncertainties. Here, δS refers to the statistical uncertainty on the systematic variation, and δN refers to the statistical uncertainty on the nominal sample. A term $x_{i-1,i}$ is defined to quantify the difference between the systematic variation and the nominal distribution for two neighbouring bins such that $x_{i-1,i} = \left| \frac{S_i - N_i}{N_i} - \frac{S_{i-1} - N_{i-1}}{N_{i-1}} \right|$, with a relative statistical uncertainty defined as $\delta x_{i-1,i} = \sqrt{\frac{\delta M_i^2}{N_i^2} + \frac{\delta M_{i-1}^2}{N_{i-1}^2}}$. If at least one bin satisfies $x_{i-1,i} < \delta x_{i-1,i}$, the algorithm looks for the neighbouring bins $b-1$ and b with the largest ratio $\frac{\delta x_{b-1,b}}{x_{b-1,b}}$ and merges these bins. This process continues until no bin in the distribution satisfies $x_{i-1,i} < \delta x_{i-1,i}$.

the raw systematic distributions and the solid lines to the distributions after the application of smoothing and symmetrisation. Large statistical fluctuation in the bins are identified by the smoothing procedure which in turn, averages out the distribution. On the other hand, for the distributions which have a smooth behaviour and no significant statistical fluctuations, this smoothing procedure does not modify them. Figure 8.8(b) shows one of the uncertainties originating from b-tagging method on the $t\bar{t}$ sample. In this plot, the raw systematic distribution and the smoothed, symmetrised distribution are nearly identical.

8.3.2 Pruning

The total number of systematic uncertainties to be considered for the fit results in a large number. In practice, not all systematics produce a considerable impact on the final result. Some systematics lead to a negligible impact, which can be ignored. Hence, a *pruning* procedure is applied to remove such systematics from the fit. Neglecting them makes the fitting procedure more efficient and fast, without any loss of meaningful information.

The impact of the systematic variation on the nominal sample can be such that it only affects the normalisation of the nominal distribution, or only the shape of the nominal distribution, or both the shape and normalisation of the nominal distribution. Hence, the systematic distributions are factorised into a normalisation component, containing the overall size of the systematic, and a shape component, obtained by normalising the area of the systematic distribution to the nominal distribution. These two components undergo different interpolation strategies in the fit. A pruning threshold of 0.1% is chosen for both the shape and normalisation components. This implies that the uncertainties for which the difference between the shape component and the nominal distribution in each bin is smaller than 0.1% are only considered for normalisation effects. On the other hand, the systematics for which both the normalisation and shape components have an effect smaller than 0.1% are dropped. The pruning threshold of 0.1% has been evaluated and observed to have no significant effects on the final result, making it safe to use for the analysis. Table 8.2 shows a summary of all systematic uncertainties considered for the analysis, showing the number of nuisance parameters associated with them, as well as the type of effect it has on the nominal distribution. Whether the systematic uncertainty impacts the shape or only the normalisation of the distribution, is also shown. The number of nuisance parameters left after the application of pruning procedure is indicated in the last column. It can be noted that a significant number of systematic uncertainties originating from physics objects get dropped after pruning. However, all JER systematic components survive the pruning procedure. Among the modelling systematics, 17 components of uncertainty from $t\bar{t}$ PDF variations, and the uncertainty associated to the single-top t-channel μ_R are dropped after pruning.

8.4 Results

Using $m_{t\bar{t}}$ templates, the fit is carried out, and pulls and constraints on the nuisance parameters are obtained. All systematics below the pruning threshold are ignored from the fit. Due to the large amount of available data, statistical uncertainties are expected to be small and the fit is dominated by systematic uncertainties instead. In the following, firstly the impact of systematic uncertainties are shown, and their shapes are studied. Fit results are discussed in the end.

Systematic Uncertainty	Number of NPs	Effect	Number of NPs after pruning
Pileup reweighting	1	SN	1
Luminosity	1	N	1
Physics objects			
Electrons	6	SN	3
Muons	12	SN	6
Jet energy scale (JES)	36	SN	23
Jet energy resolution (JER)	14	SN	14
Jet vertex tagger	1	SN	1
$E_{\mathrm{T}}^{\mathrm{miss}}$	3	SN	3
b-tagging efficiency	11	SN	5
c-tagging efficiency	4	SN	2
light-jet-tagging efficiency	4	SN	2
$t\bar{t}$ signal modelling			
$t\bar{t}$ normalisation	1	N	1
ISR (μ_R)	1	SN	1
ISR (μ_F)	1	SN	1
ISR (Var3c)	1	SN	1
FSR	1	SN	1
h_{damp} variation	1	SN	1
top-quark mass	1	SN	1
Matrix element $p_{\mathrm{T}}^{\mathrm{hard1}}$	1	SN	1
Parton shower and hadronisation	1	SN	1
PDF	30	SN	13
Background modelling			
Single-top s-, t-chan. normalisation	2	N	2
Single-top s-, t-chan. ISR (μ_R)	2	SN	1
Single-top s-, t-chan. ISR (μ_F)	2	SN	2
Single-top s-, t-chan. ISR (Var3c)	2	SN	2
Single-top s-, t-chan. FSR	2	SN	2
Single-top Wt normalisation	1	N	1
Single-top Wt ISR (μ_R)	1	SN	1
Single-top Wt ISR (μ_F)	1	SN	1
Single-top Wt ISR (Var3c)	1	SN	1
Single-top Wt FSR	1	SN	1
Single-top Wt DS scheme	1	SN	1
W+jets normalisation	1	N	1
W+jets (μ_R, μ_F) variation	1	SN	1
Multijet background normalisation	2	N	2
Z+jets normalisation	1	N	1
Other background normalisation	3	N	3

Table 8.2: Summary of the systematic uncertainties included in the fit. Each component of the uncertainty is represented by a nuisance parameter. These systematics can effect the shape (S) of the distribution, or the normalisation (N), or both (SN). The last column in the table shows the number of nuisance parameters left in each systematic category after the pruning procedure.

8.4.1 Impact of systematics on the fit

As mentioned in Section 8.1.4, pull parameters are defined in the likelihood, which are given by the ratio of the difference between the fitted and the expected parameter values over the uncertainty on the fitted value, i.e.,

$$\text{pull}(\alpha) = \frac{\hat{\theta} - \theta_0}{\Delta\theta} \tag{8.21}$$

These pull parameters correspond to the Gaussian approximated subsidiary measurements. The fit allows the data to put constraints on the subsidiary measurement, i.e., on the nuisance parameters. If a parameter is constrained from the data, then the fit would simply move the parameter to the new value and produce a non-zero pull. This additionally reduces the error corresponding to that parameter.

These pulls indicate how far the fitted value of the nuisance parameter deviates from the expected value, or in other words, how far the nuisance parameter has to be "pulled" in order to achieve the maximum likelihood value. If there is no sensitivity in the data corresponding to a parameter, the fitted value matches the expected value, the pull is zero, and the standard deviation is unity. However, in some other cases, the uncertainties obtained on the fitted parameter is not equal to unity. If the estimated uncertainty is smaller than 1, the nuisance parameter is said to be constrained, and for the case where the uncertainty is larger than unity, the parameter is said to be under-constrained.

In order to improve the fit, constraints are essential and are generally expected in a fit. One only requires a reasonable understanding of these constraints. However, the presence of under-constraints in a fit is a cause of concern. This generally indicates that the under-constrained nuisance parameter has a log-likelihood shape that differs significantly from a smooth parabola, or that it may have multiple minima. It may also emerge as a result of technical issues with the fit minimisation tool or fit instabilities and hence, requires additional examination.

The pulls originating from different systematics are plotted so as to assess the consistency between the observed data and the prediction given the constraints from subsidiary measurements. They are grouped on the basis of their origin as described below.

Cross-section normalisation

Considering uniform overall up and down variations, the uncertainties on the cross-section of the signal and background predictions lead to small pulls as shown in Figure 8.9. The fit constrains the $t\bar{t}$ cross-section normalisation, and a non-zero pull indicates that the normalisation difference between the data and the predicted model is absorbed by this nuisance parameter. Among the normalisations from the backgrounds, no significant pulls and constraints are observed. This analysis is mainly insensitive to these errors since the background contribution is effectively very small.

Modelling systematics

Theoretical uncertainties originating from the modelling of the samples get affected by the fit the most. Figure 8.10(a) shows the pull plots for the $t\bar{t}$ modelling systematics. The parton shower and hadronisation systematic stemming from the differences between PYTHIA v8.230 and HERWIG v7.1.3 showering schemes show the largest pull among the modelling uncertainties.
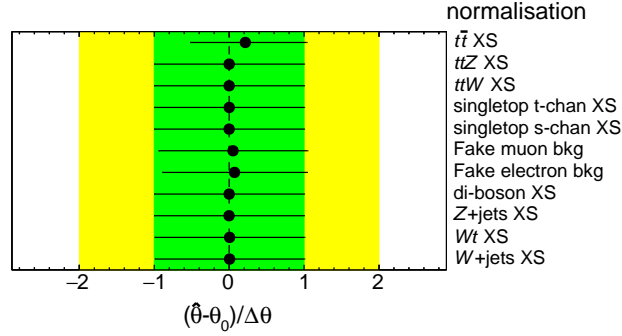
Figure 8.9: Pulls and constraints for nuisance parameters corresponding to the cross-section normalisation of the signal and the backgrounds. The green band refers to a 1σ deviation, while the yellow band corresponds to the 2σ uncertainty on the fitted parameter.

(a)   (b)
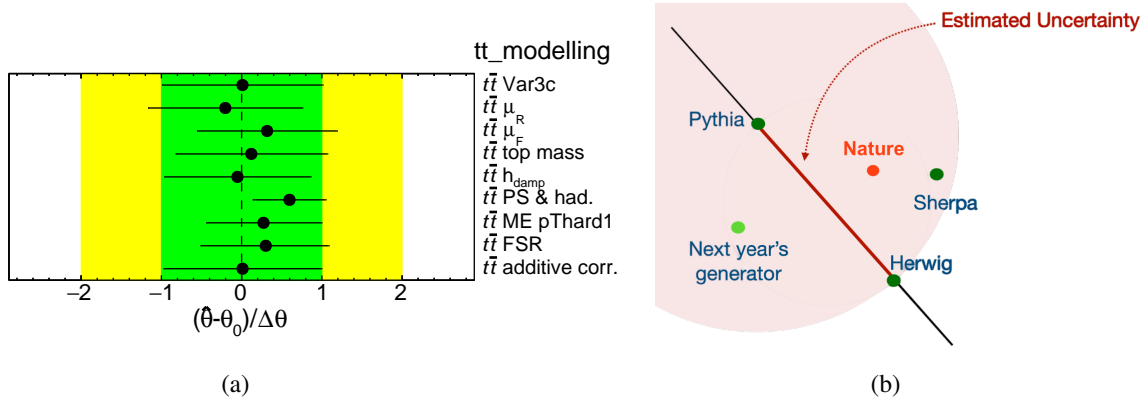
Figure 8.10: Impact of $t\bar{t}$ modelling systematics on the fit. Figure (a) shows the pulls and constraints on the nuisance parameters. Figure (b) depicts the two-point systematic, *Pythia* versus *Herwig* (adapted from [234]). The distance between *Pythia* and *Herwig* is treated as the uncertainty, which covers the true value, i.e., "nature" even if it does not lie on the line connecting *Pythia* and *Herwig*.

This is not entirely unexpected because no generator is known so far which perfectly describes the data. Additionally, this systematic is more difficult to estimate since it belongs to a category of *two-point systematics*, where no parameteric form for the systematic uncertainty is known. The only information available is the implementation of one theory model that differs in its results from the other, which in this case is, *Pythia* versus *Herwig*. Figure 8.10(b) shows a pictorial representation of such a two-point systematic. The information on the magnitude of this uncertainty is obtained by evaluating the POI at these two points in the theory space. However, it remains unclear whether this difference is correctly representing the true underlying theoretical uncertainty. In the likelihood, it is represented by one nuisance parameter that is estimated by an interpolation between the two known points. A one-parameter morphing is unlikely to capture the true degree of uncertainty on the shape of the distribution. From the pull plot, it is clear that none of these two models describes the data well. A constraint can also be seen for this systematic, indicating that the considered parametrisation is inadequate and a better description of this uncertainty would be beneficial. Another example of a two-point uncertainty used in the fit is the $p_{\mathrm{T}}^{\mathrm{hard}}$ variation. However, it exhibits only a small pull and does not show any strong

constraints.

Figure 8.11 shows the pull plots for PDF variations on the $t\bar{t}$ sample. From a total of 30 nuisance parameters, 17 get pruned away before the fit. However, the remaining ones which enter the fit show notable pulls in the plot. PDF variation 5 is seen to be pulled the most. Constraints and pulls can also be observed for a few other variations in the plot, indicating that $t\bar{t}$ modelling uncertainties have a considerable impact on the estimation of the POI.
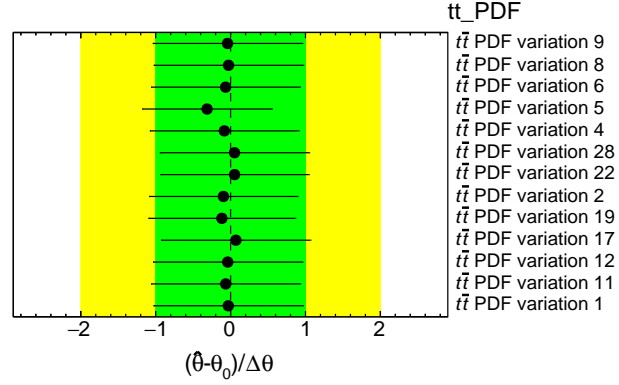
Figure 8.11: Pulls and constraints for nuisance parameters corresponding to the PDF variations on the signal $t\bar{t}$ sample.

Pulls and constraints on the background modelling uncertainties are shown in Figure 8.12. No notable pulls or constraints are observed on these systematics.
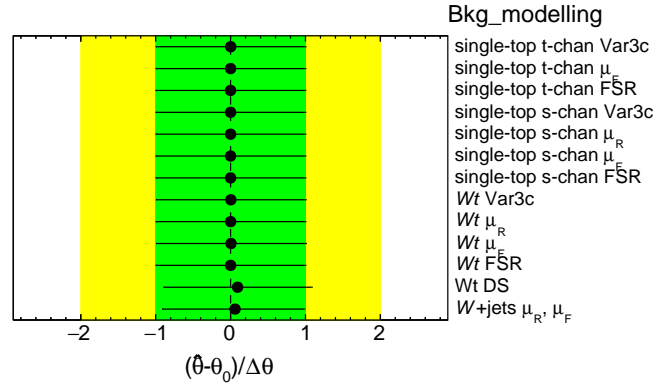
Figure 8.12: Pulls and constraints for nuisance parameters corresponding to the modelling uncertainties on the backgrounds.

Other uncertainties

Jet calibration uncertainties account for the largest number of nuisance parameters in the fit. Pulls and constraints on the JES and JER components are plotted in Figure 8.13. Most of the parameters are consistent with a zero pull with 1σ uncertainty. JES pileup ρ topology, however, shows a small pull along with a constraint.

(a)

(b)

(c)
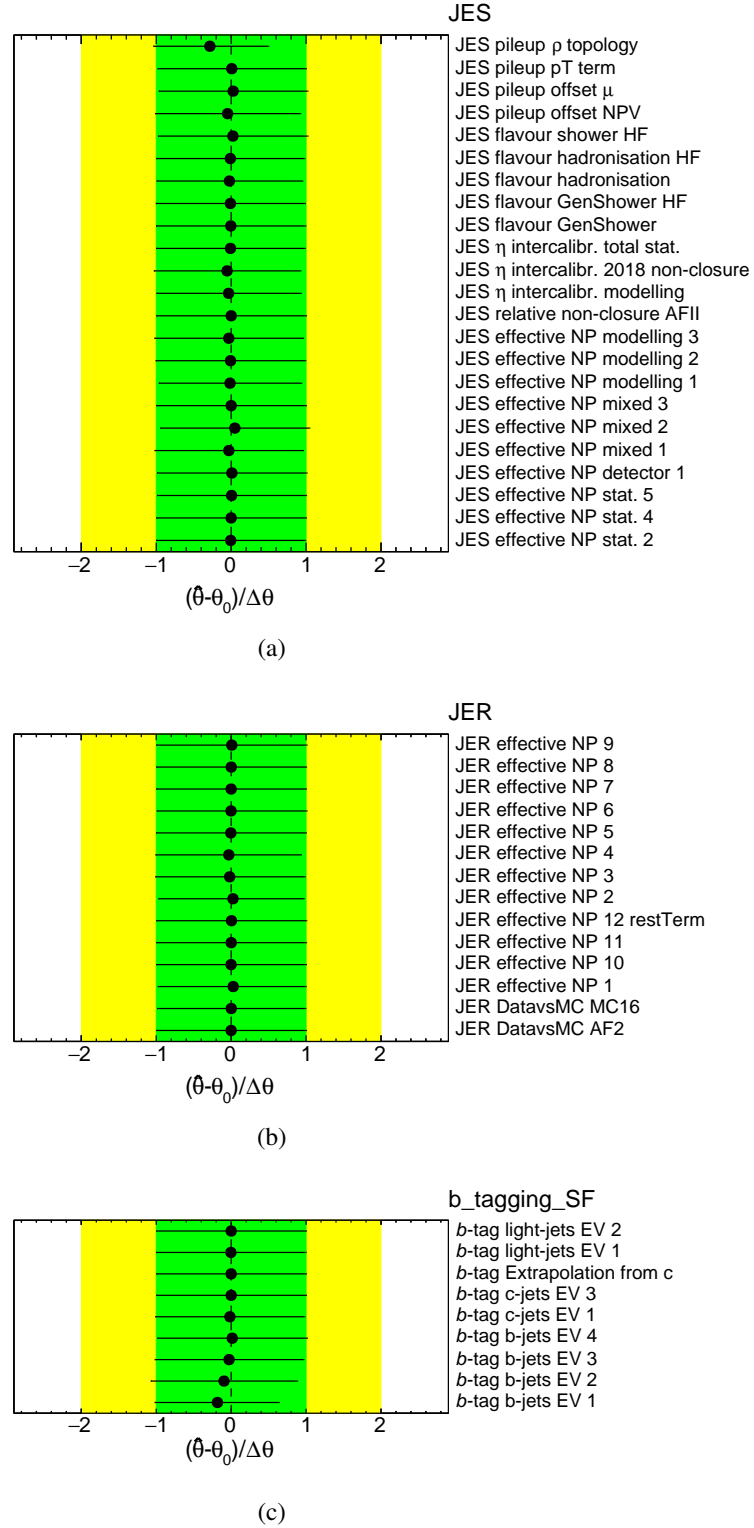
Figure 8.13: Pulls and constraints for nuisance parameters corresponding to the uncertainties on the (a) jet energy scale (JES), the (b) jet energy resolution (JER), as well as on (c) flavour tagging efficiencies.

For the uncertainties corresponding to b-tagging, c-tagging and light-jet-tagging efficiencies, the pulls and constraints are shown in Figure 8.13(c). Apart from a small pull on the first eigenvalue of the b-jet efficiency systematic, no significant pulls are observed for these uncertainties. For the systematics associated to the leptons, missing energy, pileup reweighting, luminosity and JVT efficiency, the plots are shown in Figure 8.14, and no notable pulls or constraints are seen here either.

(a)

(b)

(c)
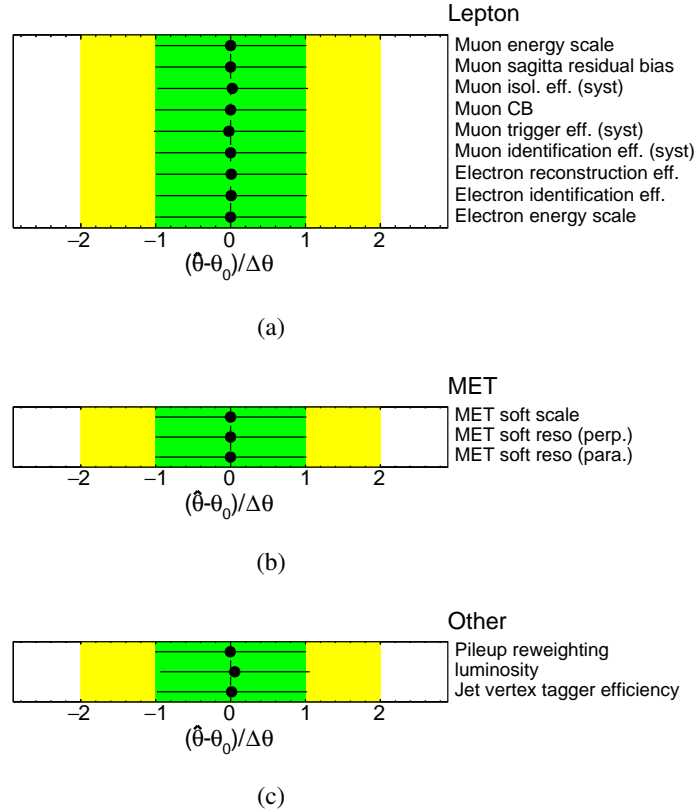
Figure 8.14: Pulls and constraints for nuisance parameters corresponding to the uncertainties on the (a) lepton measurement, reconstruction and identification, the (b) missing energy components, and (c) other uncertainties, namely pileup reweighting, luminosity and JVT efficiency.

8.4.2 Expected results from the SM prediction

A profile likelihood fit is also performed on pseudodata obtained by summing all Monte Carlo predictions, i.e., the sum of the signal and the background distributions. This is known as the *Asimov dataset*, and it gives an estimate of the predicted uncertainty contributions on the Y_t^2 value. The fit is carried out using the $m_{t\bar{t}}$ distributions, which results in a zero pull for all nuisance parameters, as expected. The constraints on the parameters obtained from this fit on pseudodata are found to be in accordance with the constraints obtained from the fit to data, as detailed in the previous section. This suggests that there are no unanticipated consequences from the data which need further investigation.

8.4.3 Resultant Y_t value

Results for the *observed* as well as *expected* Y_t^2 values are obtained. The expected Y_t^2 is extracted by performing a fit on the *Asimov* dataset, as explained earlier. The negative log-likelihood plot for Y_t^2 is shown in Figure 8.15(a). The Y_t^2 values at $-\Delta \ln L = 0.5$ from the likelihood scan gives the $\pm 1\sigma$ uncertainty associated to it. The fitting so performed results to an expected value of $Y_t^2 = 1.00^{+1.81}_{-1.71}$.

The observed value corresponds to the Y_t^2 extracted from the fit using the Run-2 ATLAS data. From the likelihood scan for Y_t^2 in this fit, shown in the plot as a solid line, the observed value results to $Y_t^2 = 2.26^{+1.84}_{-1.75}$.

| (a) | (b) |
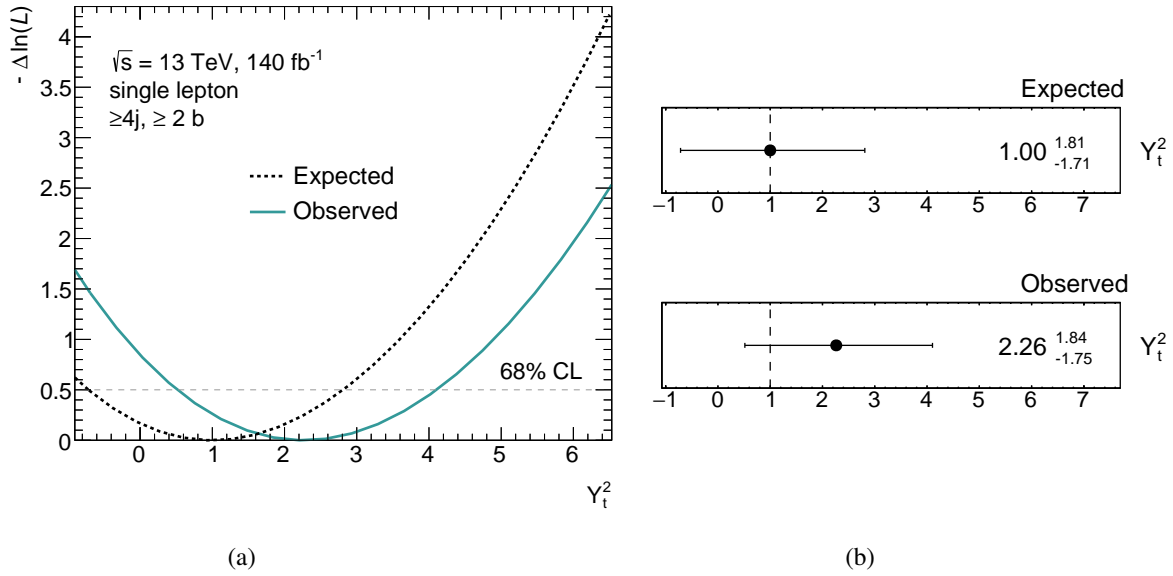
Figure 8.15: The observed and expected Y_t^2 values from the fit. Figure (a) shows the negative log-likelihood scan for the POI, Y_t^2. The value of Y_t^2 at $-\Delta \ln L = 0.5$ gives its corresponding uncertainty. Figure (b) shows the Y_t^2 value along with the uncertainties as obtained from the likelihood scans for the observed and the expected Y_t^2 values.

To obtain an upper limit on Y_t^2, a Gaussian approximation is made for the probability distribution functions (PDFs) for the expected and observed parameters. The extracted Y_t^2 value is taken as the mean of the Gaussian distribution, and an uncertainty of $+1\sigma$ is taken as its standard deviation. Hence, a $\mathrm{Gauss}(\mu = 1, \sigma = 1.81)$ function is constructed for expected Y_t^2, and a $\mathrm{Gauss}(\mu = 2.26, \sigma = 1.84)$ function is constructed for the observed Y_t^2. The distributions so obtained are shown in Figure 8.16. The physical region in the plot corresponds to the region with $Y_t^2 > 0$. Hence, an upper limit x, corresponding to the 95% confidence level (CL) is obtained such that the ratio of the area between $Y_t^2 = 0$ and $Y_t^2 = x$ in the curve, over the net area above $Y_t^2 = 0$, evaluates to 95%. The expected and the observed value of x so obtained, marked by yellow lines in the plot, give the upper limit for expected Y_t^2 to be < 4.27 at 95% CL. Correspondingly, the observed limit on Y_t^2 is determined to be < 5.39. Consequently, the expected 95% CL upper limit on Y_t is 2.06 and the observed limit is 2.32. A summary of these results is shown in Table 8.3.
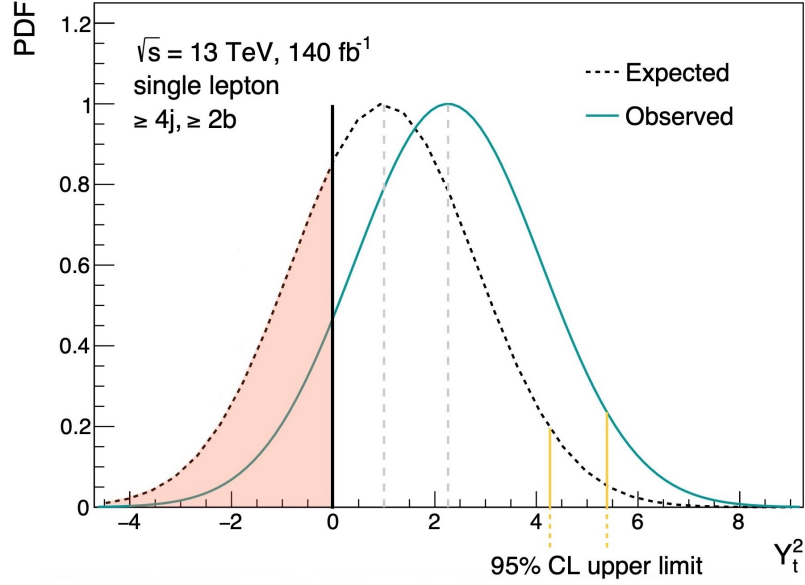
Figure 8.16: Probability density functions corresponding to the maximum likelihood estimator Y_t^2, using their expected and observed values from the likelihood scans. These are Gaussian PDFs with $\mu = Y_t^2$ corresponding to the maximum likelihood value and σ corresponding to the $+1\sigma$ uncertainty on the fitted Y_t^2. Their 95% CL upper limits are marked by yellow lines. The shaded regions below $Y_t^2 = 0$ are not included in the calculation of the 95% CL limit.

| | Fitted Y_t^2 | 95% CL upper limit | |
		Y_t^2	Y_t
Expected	$1.00^{+1.81}_{-1.71}$	< 4.27	< 2.06
Observed	$2.26^{+1.84}_{-1.75}$	< 5.39	< 2.32

Table 8.3: Summary of the results. The observed and expected best fit values for Y_t^2 and their corresponding 95% CL upper limits are shown. The last column shows the 95% CL upper limits on Y_t.

Decomposition of uncertainties on Y_t^2

The uncertainties which contribute the most to the extracted Y_t^2 is quantified in terms of a so-called *ranking plot*, as shown in Figure 8.17. The *impact* ΔY_t^2 of a nuisance parameter θ on the Y_t^2 is expressed by the shift in the Y_t^2 value comparing the nominal fit with another fit where the nuisance parameter is fixed to a value $\hat{\theta} \pm x$. The value $\hat{\theta}$ is the post-fit value of the estimator corresponding to the maximum likelihood. The *impact* of a systematic effectively quantifies the error contribution of the systematic on the resultant Y_t^2 uncertainty. When $x = \Delta\theta = +1$, the resulting impact ΔY_t^2 is called the pre-fit impact. Here, $\Delta\theta = 1$ describes the uncertainty of θ as used for constrained nuisance parameters that add a unit Gaussian term to the likelihood. The post-fit impact refers to the impact corresponding to $x = \Delta\hat{\theta} \leq 1$, where $\Delta\hat{\theta}$ represents the uncertainty on $\hat{\theta}$. Since nuisance parameters can be constrained, the post-fit impact may become smaller than the pre-fit impact.

The nuisance parameters are ranked by decreasing post-fit impacts on Y_t^2. The empty blue and cyan rectangles show the pre-fit impact, with the nuisance parameters fixed to $\hat{\theta} \pm 1$. The filled rectangles show the post-fit impact, with nuisance parameters fixed to $\hat{\theta} \pm \Delta\hat{\theta}$. On the upper axis, the impact ΔY_t^2 is shown. The lower axis shows the nuisance parameter pull $(\hat{\theta} - \theta_0)/\Delta\theta$, comparing the best-fit value to the nominal pre-fit value θ_0, with the difference divided by the pre-fit uncertainty.
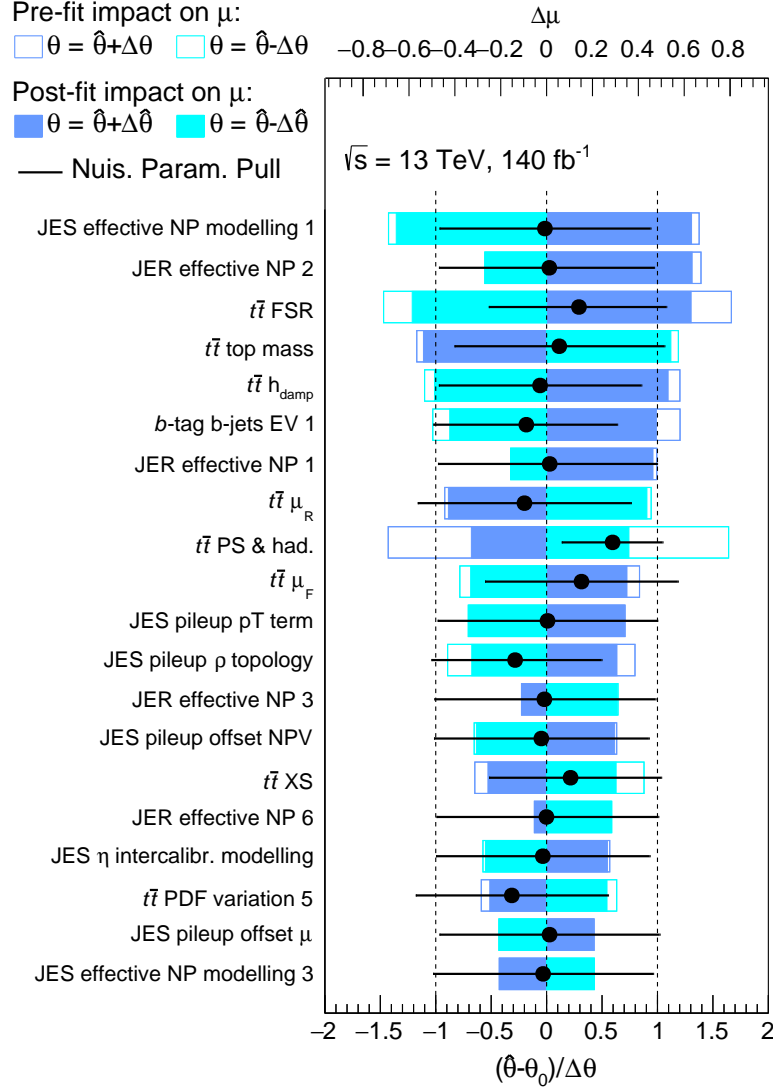
Figure 8.17: Ranking plot depicting the impact of the 20 most significant uncertainty contributions to the extracted POI, $\mu = Y_t^2$. Both the pre-fit $\hat{\theta} \pm \Delta\theta$ (empty boxes) and the post-fit $\hat{\theta} \pm \Delta\hat{\theta}$ (filled boxes) impacts are shown using rectangular boxes, the axis for which is shown on the top. Pulls and constraints $(\hat{\theta} - \theta_0)/\Delta\theta$ on the corresponding nuisance parameters are also plotted (black dots with a horizontal line), with its axis labelled at the bottom.

The most significant post-fit uncertainty contribution comes from the first eigenvalue of the jet energy scale modelling, which is anticipated when the corresponding distribution is studied. Figure 8.18(a) shows the distribution for this systematic for the $t\bar{t}$ sample. Besides being a large uncertainty in itself, it also exhibits a shape closely resembling to the Y_t^2 templates used in the fit.

The ratio pad in the plot shows this effect, as a consequence of which it contributes significantly to the final result. The second systematic in the ranking plot is the second eigenvalue of the jet energy resolution uncertainty, the distribution for which is shown in Figure 8.18(b). It is a difficult uncertainty to study since it shows asymmetric up and down variations. These two variations exhibit a large shape effect in the distribution, which are different for $+1\sigma$ and -1σ uncertainties. As a result, the post-fit impact for these two variations also differ in the ranking plot. In general, this is also true for other JER uncertainty components. Thus, the ranking plot shows an asymmetric impact for JER uncertainties.
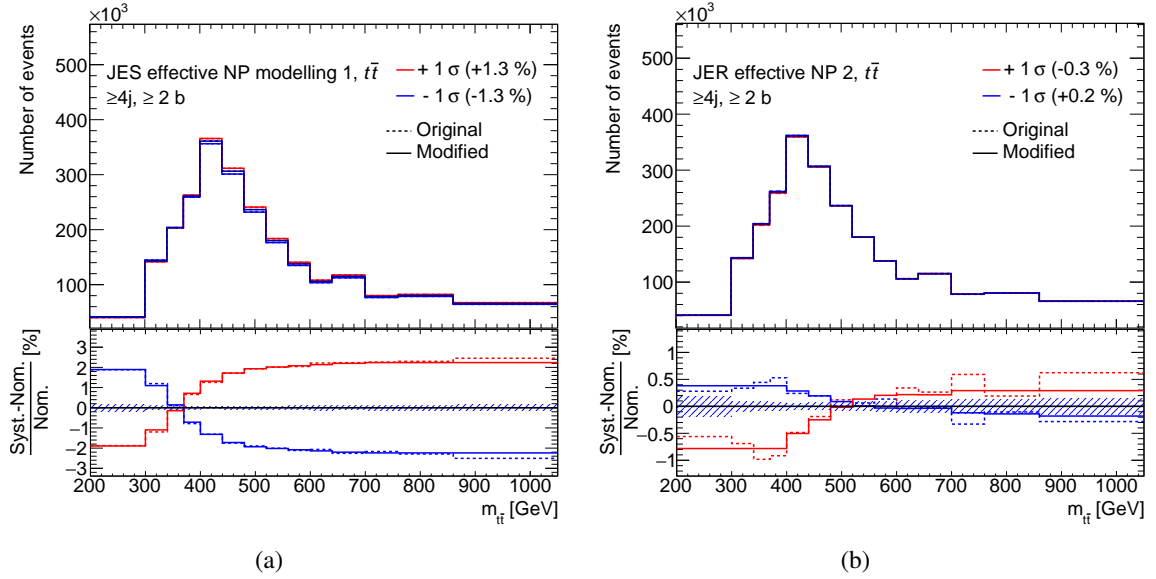
Figure 8.18: Shapes of important systematic uncertainties for the $t\bar{t}$ signal. Figure (a) shows the distribution for the first eigenvalue of jet energy scale modelling uncertainty, (b) shows the second component of the jet energy resolution systematic.

Other important parameters in the ranking plot are the $t\bar{t}$ modelling uncertainties, the FSR and the parton shower and hadronisation, with a distribution as shown in Figure 8.19(a) and 8.19(b). They exhibit a shape effect originating from the low $m_{t\bar{t}}$ region. In the ranking plot, the pre-fit and post-fit contributions differ for both of them, with parton shower and hadronisation constraining itself much more than the FSR. This can be understood better by studying the correlation matrix.

Figure 8.20 shows the correlations[9] between the nuisance parameters used in the fit. This matrix gives an overview of which nuisance parameter could be effected by shifts in other parameters in the likelihood fit and can potentially help explain the nuisance values that can not be explained by their isolated physical behaviour. Large negative correlations can be observed between the FSR and the parton shower and hadronisation uncertainties. The FSR and the JES pileup ρ topology also show a large correlation. JES pileup ρ topology is also constrained from the fit. In general, it can be noted that the presence of correlations effectively reduces the post-fit impact of the systematic uncertainties. Since the parameters contributing the largest to the Y_t^2 uncertainty show large correlations, the uncertainty on Y_t^2 is reduced.

---

[9] The net uncertainty on the POI cannot be obtained by simply adding the post-fit impacts from the ranking plot in quadrature, as correlations between the nuisance parameters must be additionally taken into account.
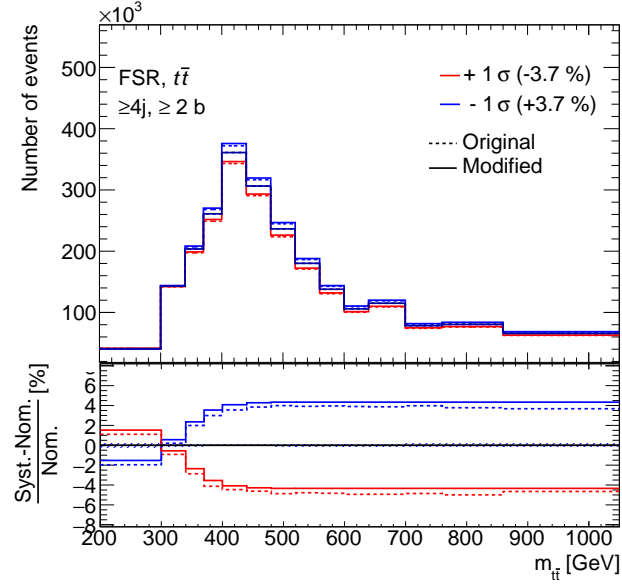
(a)
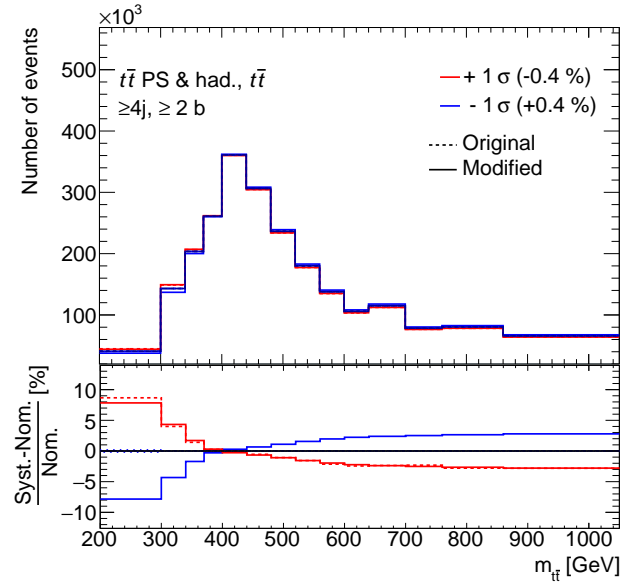
(b)

Figure 8.19: Shapes of important systematic uncertainties for the $t\bar{t}$ signal. Figure (a) shows the theoretical modelling uncertainty due to the final state radiation, and (b) shows the $t\bar{t}$ modelling uncertainty originating from the parton shower and hadronisation.

Figure 8.20: Correlation matrix for the nuisance parameters in the fit. Values (correlation percentage between two NPs) are shown for the NPs which have a minimum of 20% correlation with at least one other parameter in the fit.

8.4.4 Comparison of pre-fit and post-fit distributions

The comparison of data and prediction for the fitted variable $m_{t\bar{t}}$ is shown in Figure 8.21. The uncertainty band for this post-fit distribution is considerably smaller than its corresponding pre-fit uncertainties, as previously shown in Figure 8.5. The matching of data and prediction becomes considerably better after the fit as well.
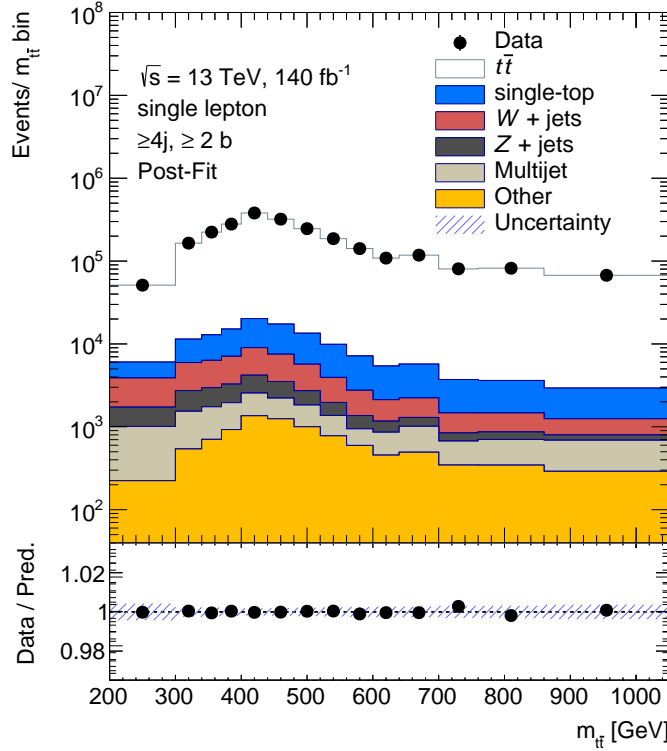
Figure 8.21: The post-fit $m_{t\bar{t}}$ distribution with the data and the Monte Carlo simulation for signal and the backgrounds considered in the fit. The lower plot shows the ratio of the data to the total Monte Carlo prediction. The uncertainty band plotted in the figure correspond to the full set of systematic and statistical uncertainties. The y-axis is in logarithmic scale, corresponding to the number of events in each variable $m_{t\bar{t}}$ bin.

Additional kinematic variables not used in the fit are also studied to ensure that the fit does not lead to any unphysical kinematic behaviour. The distributions for these variables are shown in Figures 8.22 to 8.25. Pre-fit and post-fit distributions for the number of jets, E_T^{miss}, lepton p_T and η, leading jet p_T and leptonic m_W^T of the event are shown. Kinematic distribution for the sum of the transverse momenta of all jets present in the event is given by the observable $H_T^{\text{all jets}}$. In addition, an observable S_T is also shown, which represents the sum of transverse momenta of all objects in the event, including the missing energy. Since the fitting is performed only on the $m_{t\bar{t}}$ observable, no large improvements in the post-fit distributions are expected for these variables. Overall, a good agreement between the data and the Monte Carlo prediction is noted for the observables. The uncertainty bands which include both, the statistical and the systematic uncertainties in each bin, cover most of the discrepancies. These uncertainties reduce considerably after the fit, as explained in the previous section. In general, the post-fit distributions show a slightly better agreement between the data and the Monte Carlo prediction.
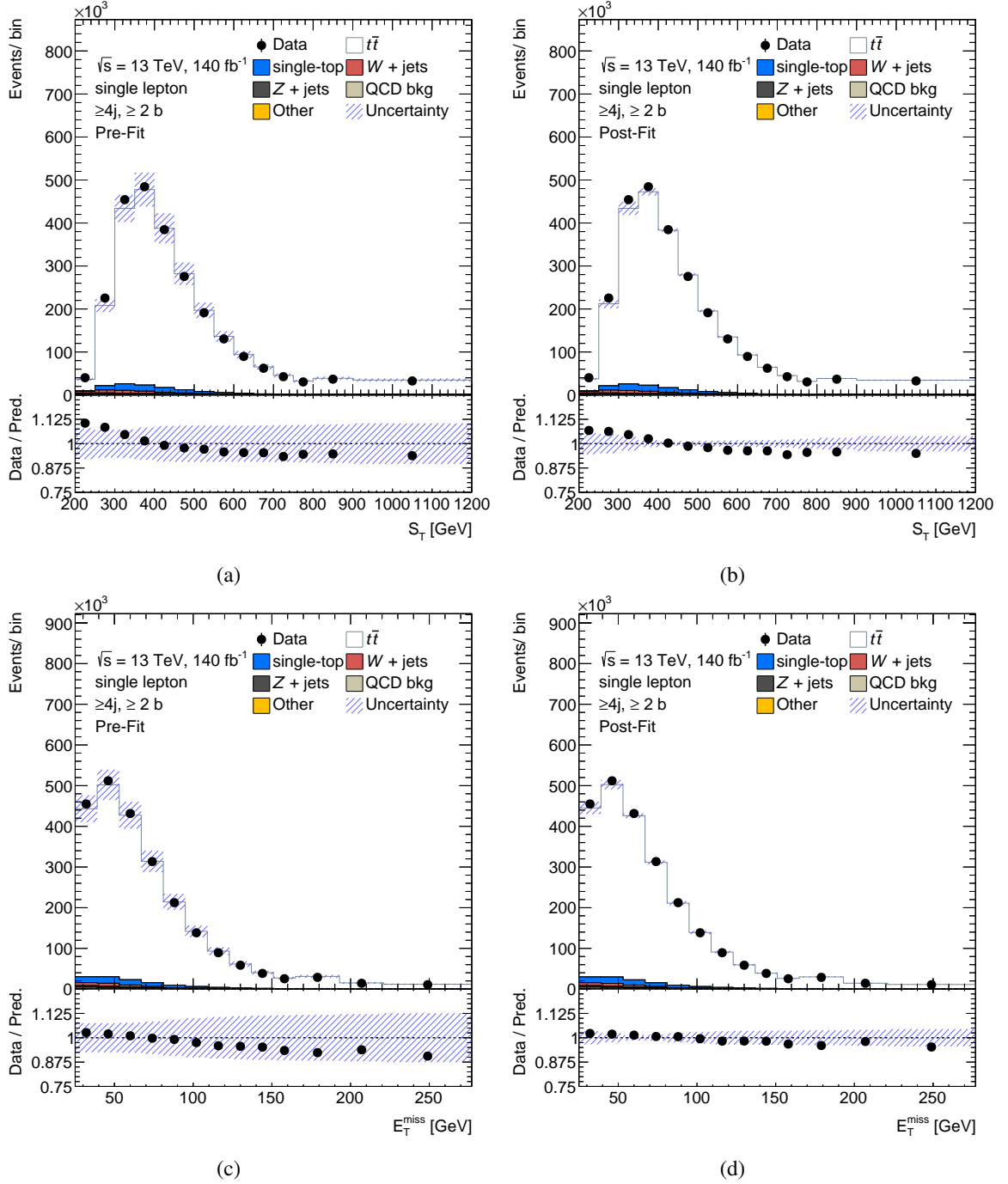
Figure 8.22: Comparison of data and Monte Carlo prediction. Figures (a) and (b) show pre-fit and post-fit distributions, respectively, for the sum of the transverse momenta of all objects in the event, represented by S_T. The E_T^{miss} distribution is shown in Figures (c) and (d) corresponding to the pre-fit and the post-fit distributions, respectively. The uncertainty band includes both, the statistical and the systematic uncertainties.
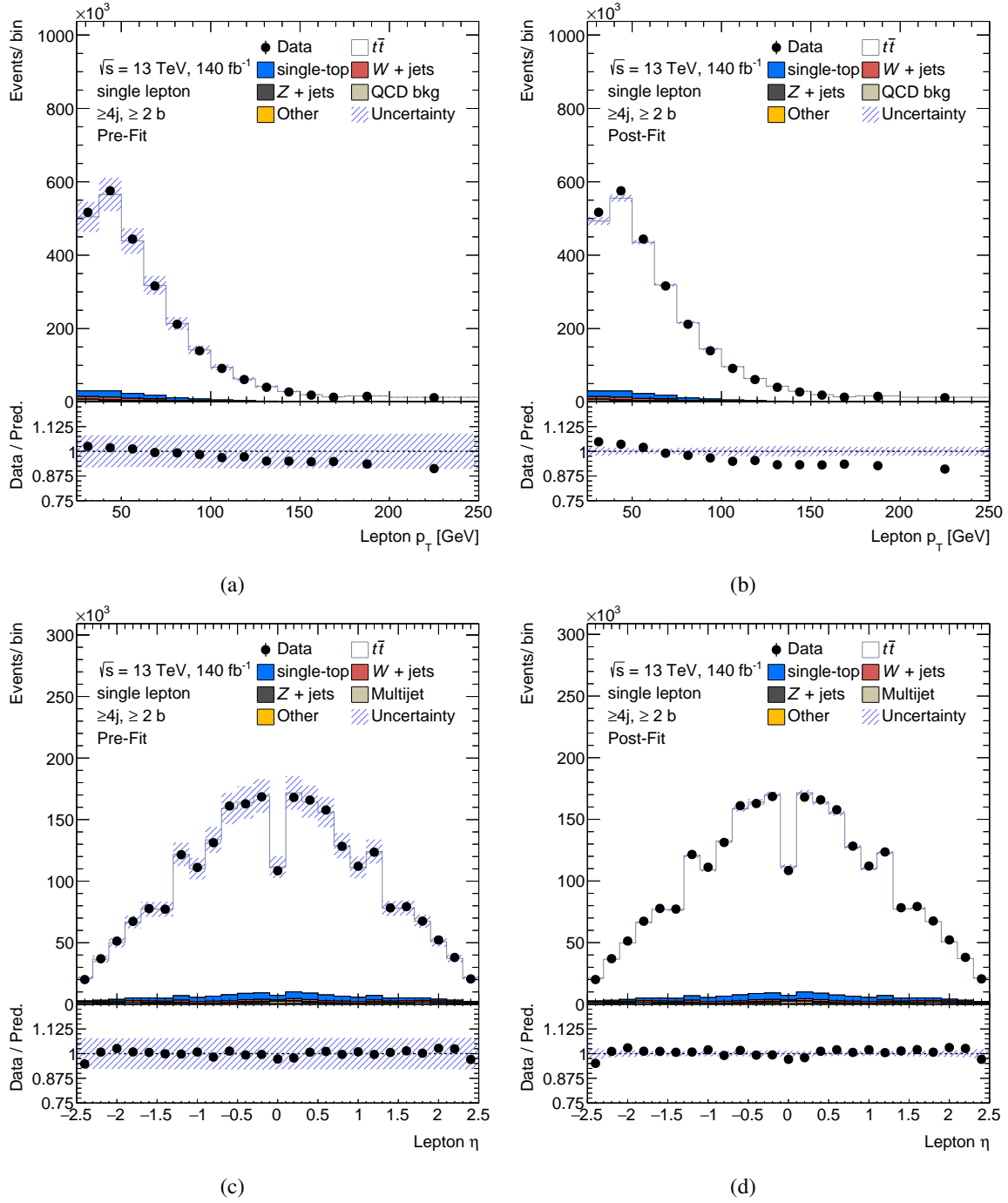
Figure 8.23: Comparison of data and Monte Carlo prediction. Figures (a) and (b) show pre-fit and post-fit distributions, respectively, for the transverse momentum of the lepton. Figures (c) and (d) correspond to the pre-fit and the post-fit distributions, respectively, for the lepton pseudorapidity, η. The uncertainty band includes both, the statistical and the systematic uncertainties.
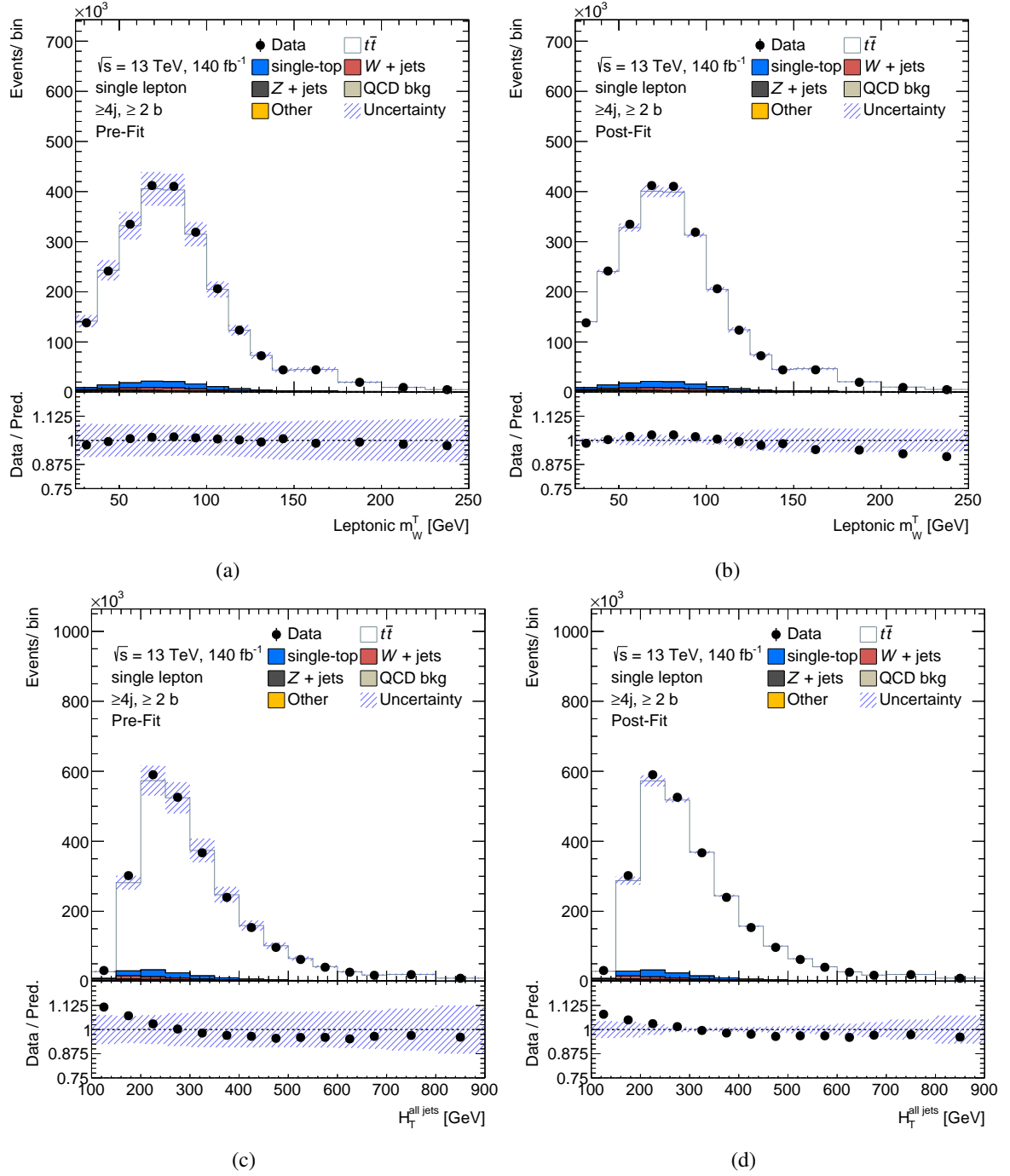
Figure 8.24: Comparison of data and Monte Carlo prediction. Figures (a) and (b) show pre-fit and post-fit distributions, respectively, for the transverse leptonic W-boson mass in the event. Figures (c) and (d) correspond to the pre-fit and the post-fit distributions, respectively, for the sum of the transverse momenta of all jets in the event, $H_T^{\text{all jets}}$. The uncertainty band includes both, the statistical and the systematic uncertainties.
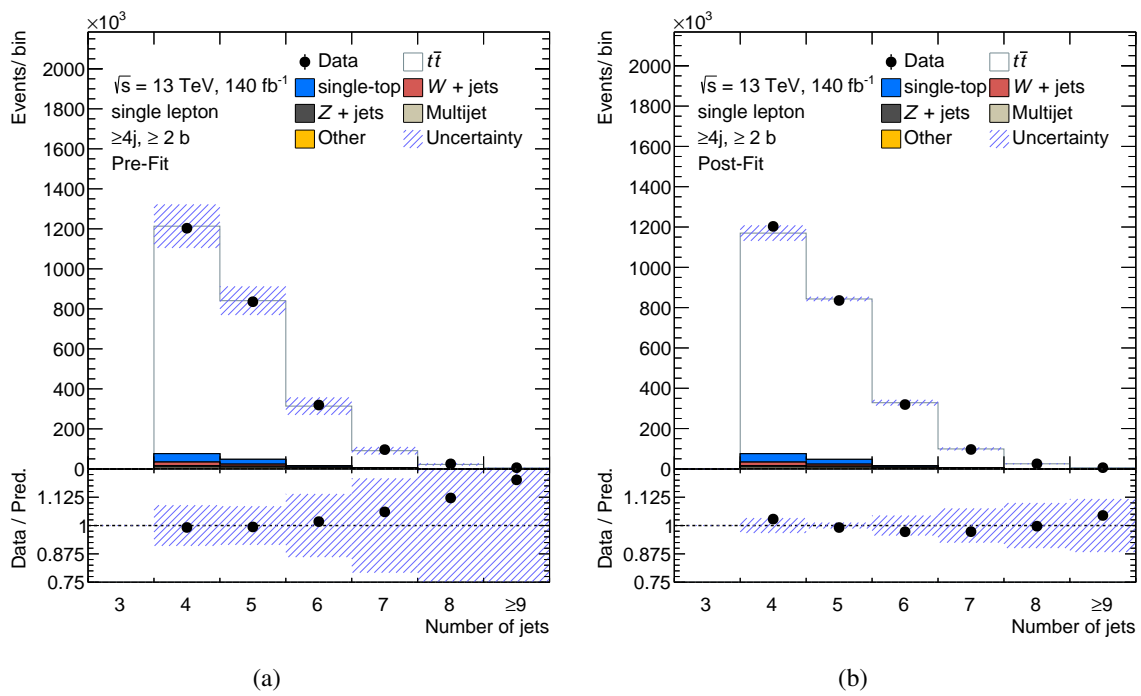
Figure 8.25: Comparison of data and Monte Carlo prediction. Figures (a) and (b) show pre-fit and post-fit distributions, respectively, for the number of jets in the event. The uncertainty band includes both, the statistical and the systematic uncertainties.

Interpretations and conclusions

This analysis measures the top-Yukawa coupling modifier Y_t, defined as the ratio of the top-Yukawa coupling strength over its Standard Model value, i.e., $Y_t = \frac{g_t}{g_t^{SM}}$. An upper limit of 2.32 is observed on this Y_t at 95% confidence level.

Previous studies made on the measurement of this coupling strength focused on several different channels, which can broadly be categorised into *direct* and *indirect* Y_t measurement channels [235]. Indirect measurement here refers to the cases where the Feynman diagram involves an off-shell top quark or an off-shell Higgs boson, while the direct measurement channels contain real top quarks and a Higgs boson.

The main channels used to obtain a direct measurement of Y_t so far include the Higgs production in association with a top quark-antiquark pair, i.e., the $t\bar{t}H$ process [9, 235], as well as its associated production with a single top quark, i.e., the tH process [10, 235]. Constraints on Y_t are obtained using these channels, providing a direct measurement of the Higgs coupling to the top quarks. In both cases, in addition to Y_t, the process depends upon the Higgs boson coupling to the decay products, for instance, the bottom quarks or τ leptons.

Indirect measurement channels, on the other hand, include processes such as the four top production ($t\bar{t}t\bar{t}$) diagrams via a virtual Higgs boson [236]. For these processes, the Higgs boson interaction to particles other than the top quark at leading order does not exist. Hence, the Y_t is effectively measured independently of the Higgs coupling to other fermions or bosons. The analysis in this thesis also falls into this classification, and hence has an advantage that the Y_t measurement does not rely upon other Higgs coupling values. From the indirect measurement using four top quarks, the top-Yukawa coupling strength is constrained to be less than 2.1 [236] times its expected SM value at 95% confidence level. This result is comparable to the upper limit obtained in this thesis. There are several ways in which the thesis results can be improved, which are discussed later in this chapter. In addition, indirect measurements are also sensitive to particles beyond the standard model (BSM) which may be present in the loop with the virtual Higgs boson. This acts as an advantage because it paves the way to further investigate the sensitivity to the heavy Higgs sector with the possible sensitivity to scalar and pseudoscalar particles in the loop.

Using a combined fit of the mesurements from the ATLAS and the CMS collaborations, the ratio of the top-Yukawa coupling to the SM prediction is determined to be 0.87 ± 0.15 [10]. This measurement is more precise than the one obtained in this thesis. However, a comparison of the combined ATLAS and CMS measurements with the results from this thesis is not entirely sensible. This is because it uses a combination of several channels[1] with several

---

[1] $t\bar{t}H$, gluon-gluon fusion (ggF), vector-boson fusion (VBF), WH and ZH

Higgs decay modes[2], including both the direct and indirect measurement methods. On the other hand, this thesis uses a single channel with a single decay mode and measures the Y_t using the indirect method. The direct measurement channels, such as the $t\bar{t}H$ channel, that are used in the combination are not directly sensitive to the BSM sector, while the sensitivity to new BSM heavy particles, carrying electric or colour charge, or both, may manifest in the loop-induced processes in the indirect measurements. Therefore, the two measurements are not equivalent for a comparison to be made between them, but are rather complementary. Hence the results in this thesis could be incorporated as another channel in the combination to further enrich the combined measurement.

CMS has performed the same measurement [13] as shown in this thesis on partial Run-2 data. This results in an expected upper limit of 1.62 on the top-Yukawa coupling compared to the SM value, at 95% confidence level. However, there are a few differences in the analysis definition which may lead to different impacts on the Y_t estimation:

- A two-dimensional fit is used in the CMS analysis using a two-dimensional histogram for $m_{t\bar{t}}$ versus $\Delta y_{t\bar{t}}$. In contrast, firstly, instead of $\Delta y_{t\bar{t}}$, this thesis uses $\cos\theta$ for the angular dependence. This is motivated from the presence of correlations between the $m_{t\bar{t}}$ and $\Delta y_{t\bar{t}}$, interpretation of which would be difficult. Additionally, this thesis uses a one dimensional fit using only the $m_{t\bar{t}}$ distributions since most of the Y_t sensitivity is observed near the $m_{t\bar{t}}$ threshold region where a one dimensional fit seems sufficient. However, the reweighting procedure incorporates both the $m_{t\bar{t}}$ and the $\cos\theta$ dependence and yields a weight for each $m_{t\bar{t}}$ value, without directly using them both in the fit.

- The treatment of systematic uncertainties in the two measurements is different. For instance, in the CMS measurement, the parton shower and hadronisation systematic has different components with different definitions as compared to the $t\bar{t}$ modelling systematics used in this thesis. A full comparison of Pythia is made with the Herwig showering scheme in this thesis, the effect of which is incorporated differently in the CMS analysis. For this reason, in general, it is not reasonable to compare the effects of systematic uncertainties in the two analyses in the same way.

- The CMS analysis is divided into three signal regions, based on jet multiplicities in the final state. Hence, separate fitting is done for the regions with 3 jets, 4 jets, and ≥ 5 jets in the event. The consequences of this separation of regions are multifaceted.

    - In the CMS measurement, in order to increase the efficiency of $t\bar{t}$ events in the threshold region of $t\bar{t}$ production, which is sensitive to Y_t the most, an additional region with exactly 3 jets in the final state is included. However, this requires a specialised method to reconstruct the $m_{t\bar{t}}$ for events with one missing jet which does not pass the event selection cuts [13]. Since the $m_{t\bar{t}}$ reconstruction method is different for the events with exactly three jets, compared to the events with more than three jets, the analysis has to be conducted in separate jet multiplicity bins. However, for the measurement in this thesis, no separation on the basis of jet multiplicity is carried out.

    - While for the CMS measurement, the jet multiplicity based separation helped reduce the effects of well-understood systematic uncertainties [13], for the measurement in this thesis, a few of the two-point systematics, the parton shower and hadronisation

---

[2] Higgs boson decay modes used in this combination: $H \to \gamma\gamma$, $H \to ZZ$, $H \to WW$, $H \to \tau\tau$, $H \to bb$

systematic for instance, show an anti-correlation between the region with four jets and the region with five or more jets. A separation based on jet multiplicity would then lead to a migration of effects which are already not known with a good modelling from one jet multiplicity region to another. As a result, it may cause strong constraints and pulls in the combined fit, the physics of which would not well understood.

Nevertheless, it is possible to improve the results obtained in this thesis. One of the largest contribution to the Y_t uncertainty comes from the jet energy resolution systematic, which has asymmetric up and down variations. A preliminary investigation into the estimation of this uncertainty revealed that the estimate currently employed in this analysis is on the conservative side. It is intuitive that a better determination of this uncertainty will produce a better Y_t result. In addition, the analysis conducted so far includes only the single-leptonic channel for the $t\bar{t}$ decay. However, a preliminary study on the dileptonic channel concludes that it is also highly sensitive to Y_t variations. A combination of the results from this channel with the results from single-leptonic channel would put more constraints on the extracted Y_t. While including this channel would lead to an improvement in the Y_t value, obtaining the $m_{t\bar{t}}$ in this channel is not straightforward due to the presence of two neutrinos. It requires specialised $m_{t\bar{t}}$ reconstruction methods so as to obtain an $m_{t\bar{t}}$ with a good resolution that preserves the Y_t sensitivity. Preliminary studies on other *proxy* variables which can be used in place of $m_{t\bar{t}}$, for instance, m_{bbll} and m_{bl}, indicate that these variables act as good enough proxies to the $m_{t\bar{t}}$ distribution. Preliminary analysis also suggests that this channel is not statistically limited, and most of the uncertainty would stem from the systematics. Undoubtedly, further efforts are needed in this area in order to achieve a definitive result using ATLAS data, but the measurement on this channel [14] done by the CMS collaboration already yields a promising result.

To conclude, the top-Yukawa coupling measurement using electroweak corrections on the $t\bar{t}$ cross-section has the potential to provide a better understanding of the Standard Model by comprehending the interaction of the heaviest fermion, the top quark with the most special Standard Model particle, the Higgs boson. This thesis presented the first ever Y_t measurement with this approach using the ATLAS data. With further improvements in tracking, identification of the b-flavoured jet, and better systematic estimates, an improvement in the result is projected, which can then be combined with other top-Yukawa coupling measurements to yield a more precise result. Inclusion of the dileptonic channel would put additional constraints on the measurement. This analysis also opens the possibility to probe new physics beyond the SM, such as, the heavy Higgs sector.

Summary

The Standard Model (SM) provides the most comprehensive knowledge of particle physics to date. The last missing piece of the SM puzzle was found with the discovery of the Higgs boson in 2012 at the LHC [4, 5]. This discovery meant that all theoretically predicted particles in the SM were experimentally observed, marking a significant milestone in particle physics research. Since then, there have been a number of studies done on the properties [237] of the Higgs boson to provide a thorough understanding of this particle. This includes the analysis of the Higgs boson production cross-section, the measurement of its decay width and the interaction of the Higgs boson with other particles [238, 239]. Since the strength of the Higgs interaction is proportional to the mass of the particle it is interacting with, the largest coupling strength is obtained from its interaction with the heaviest fermion, the top quark.

This analysis measures the top-Yukawa coupling modifier Y_t, defined as the ratio of the top-Yukawa coupling strength over its Standard Model value, i.e., $Y_t = \frac{g_t}{g_t^{SM}}$. This is measured using the $t\bar{t}$ cross-section in the single-leptonic decay channel. The theoretical foundation of this measurement relies on the estimation of the electroweak correction which enters the cross-section at loop-induced order from the virtual Higgs exchange in between the top quarks. This correction is a function of the top-Yukawa coupling strength and hence, it is used to obtain corrections to the kinematic distributions sensitive to it. The `HATHOR v2.1-b3` tool is used to evaluate the differential cross-sections and the electroweak corrections for the $t\bar{t}$ process. These corrections are obtained as functions of Y_t, initial parton state, $m_{t\bar{t}}$, and cosine of the scattering angle of the top quark in the partonic rest frame. Considering that the electroweak corrections factorise with the QCD corrections, weights are derived from the `HATHOR` tool and are multiplied to the weight of each event in the $t\bar{t}$ signal sample.

At detector level, top quarks need to be reconstructed from the available event information. A $t\bar{t}$ reconstruction method is devised that requires at least four jets in the event with at least two jets identified to be b-flavoured jets. After a detailed analysis of the algorithm, the distribution for the invariant mass of the two top quarks is obtained. Using the weights obtained for the electroweak corrections, $m_{t\bar{t}}$ distributions for different Y_t values are obtained as well. With $t\bar{t}$ as the signal, the background contribution mostly comes from processes producing a single top quark, followed by other small backgrounds. The analysis is signal dominated, with the overall background contribution amounting to only 5.5% of the full Monte Carlo prediction.

Due to limited theoretical knowledge and experimental precision, the kinematic observables are subject to a range of uncertainties. These are systematic uncertainties that are derived from dedicated analyses of the parameters associated with the experimental resolution of the detector and the modelling of the Monte Carlo samples. A good assessment of these uncertainties is crucial because they serve as parameters that allow for flexibility in the Monte Carlo fit with data.

Run-2 data from the ATLAS detector with an integrated luminosity of $\mathcal{L} = 140$ fb^{-1} from proton-proton collisions at $\sqrt{s} = 13$ TeV are used. The comparison of this data with the Monte Carlo prediction shows a good agreement. A likelihood is constructed so as to include statistical and systematic constraints to perform a fit to data. The parameter of interest used in the fit is Y_t^2 since the electroweak correction has a quadratic dependence on Y_t, making the yield for each $m_{t\bar{t}}$ bin a linear function of Y_t^2. Hence, $m_{t\bar{t}}$ distribution templates for Y_t^2 are included in the fit. The fitting procedure results in an observed Y_t^2 of $2.26^{+1.84}_{-1.75}$, and the expected Y_t^2 of $1.00^{+1.81}_{-1.71}$. An observed upper limit of 2.32 is obtained on Y_t at 95% confidence level, along with the corresponding expected 95% confidence level limit of 2.06. This result is compared to the previous measurements for the top-Yukawa coupling value. The obtained limit is not as precise as the previous indirect measurements [13, 236], nevertheless, a possible combination of the obtained result with these measurements is well motivated.

The top-Yukawa coupling reflects the strength of the interaction of the Higgs boson with the top quark. Any deviation from the SM expectation opens a portal to the vast domain of new physics beyond the SM. Although most of the particle physics observations can be explained by the SM, the mystery of dark matter, hierarchy problem and other open questions in particle physics serve as strong motivations for new physics models. Because of the sensitivity of this analysis to loop corrections, the models that predict heavy Higgs particles—such as the two Higgs doublet model—are particularly intriguing.

The objective of particle physics is to understand the theory of the universe, and with each new observation that expands our understanding, we advance one step closer to achieving it.

Reconstructing neutrino p_z

This appendix shows how the z-component of neutrino momentum is reconstructed. Considering the decay of W-boson for the leptonic part, from the conservation of four-momenta, we have:

$$p^W = p^\nu + p^l$$

Squaring both sides,

$$\Rightarrow m_W^2 = (p^\nu + p^l)^2 = m_l^2 + 2p^l p^\nu = m_l^2 + 2(E^l E^\nu - p_x^l p_x^\nu - p_y^l p_y^\nu - p_z^l p_z^\nu)$$

$$\Rightarrow m_W^2 - m_l^2 + 2(p_x^l p_x^\nu + p_y^l p_y^\nu) + 2p_z^l p_z^\nu = 2E^l E^\nu = 2E^l \sqrt{(p_x^\nu)^2 + (p_y^\nu)^2 + (p_z^\nu)^2}$$

$$\text{(A.1)}$$

Taking $\alpha = m_W^2 - m_l^2 + 2(p_x^l p_x^\nu + p_y^l p_y^\nu)$, and squaring both sides again, we get,

$$\Rightarrow \frac{\alpha^2}{4} + (p_z^l)^2(p_z^\nu)^2 + \alpha p_z^l p_z^\nu = (E^l)^2[(p_x^\nu)^2 + (p_y^\nu)^2 + (p_z^\nu)^2]$$

$$\Rightarrow [(p_z^l)^2 - (E^l)^2](p_z^\nu)^2 + \alpha p_z^l p_z^\nu - (E^l)^2[(p_x^\nu)^2 + (p_y^\nu)^2] + \frac{\alpha^2}{4} = 0 \qquad \text{(A.2)}$$

Therefore, we obtain a quadratic equation as a function of p_z : $A(p_z^\nu)^2 + Bp_z^\nu + C = 0$ where,

$$A = (p_z^l)^2 - (E^l)^2$$
$$B = \alpha p_z^l$$
$$C = -(E^l)^2[(p_x^\nu)^2 + (p_y^\nu)^2] + \frac{\alpha^2}{4} \qquad \text{(A.3)}$$
$$\text{with} \quad \alpha = m_W^2 - m_l^2 + 2(p_x^l p_x^\nu + p_y^l p_y^\nu)$$

Therefore, the two possible solutions to the neutrino momentum p_z are:

$$p_z^\nu = \frac{-B \pm \sqrt{B^2 - 4AC}}{2A} \qquad \text{(A.4)}$$

For solutions with $B^2 < 4AC$, we get imaginary solutions, for which we approximate the solution using scaling + rotation.

Studying qg events

This appendix summarises the treatment of quark-gluon events in the $t\bar{t}$ signal sample. The number of quark-gluon events in the sample amounts to around 2.5%.

At leading order, a qg process can not be obtained, therefore one has to translate the NLO qg initial state to a $q\bar{q}$ or gg state at LO. There are two possibilities for such a process to exist. The first one in which a spectator quark radiates a gluon and interacts with the gluon from the PDF, i.e., the process depicted in Figure B.1(a). Or the second one in which a gluon splitting into a pair of quarks interacts with another quark from the PDF, depicted by Figure B.1(b). Studies done looking into the correlation of the incoming particles with the outgoing radiated quark show that the energy of the outgoing quark is usually similar but a bit smaller than the incoming quark (Figure B.2(a)), while there is little correlation with the incoming gluon as shown in Figure B.2(b). This concludes that most of the qg events have a behaviour similar to the process shown in Figure B.1(a) at NLO, acting as a qg event in the POWHEG MC sample.

(a)   (b)
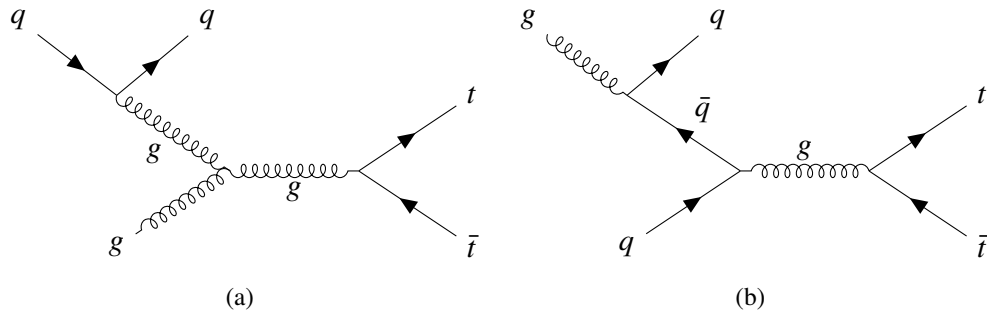
Figure B.1: Example of possible Feynman diagrams for a qg process from POWHEG generator. These figures serve as the possible cases for a qg process.
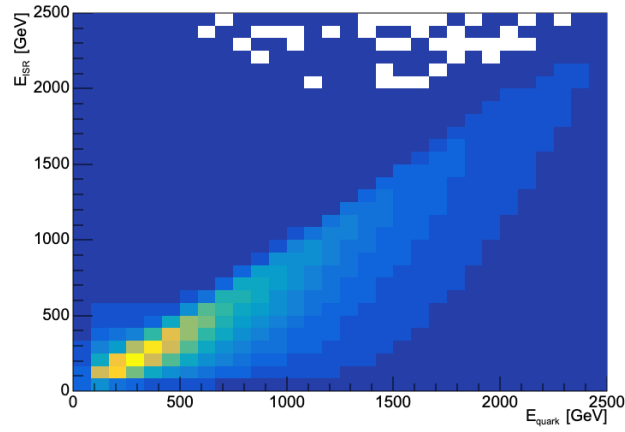
(a)
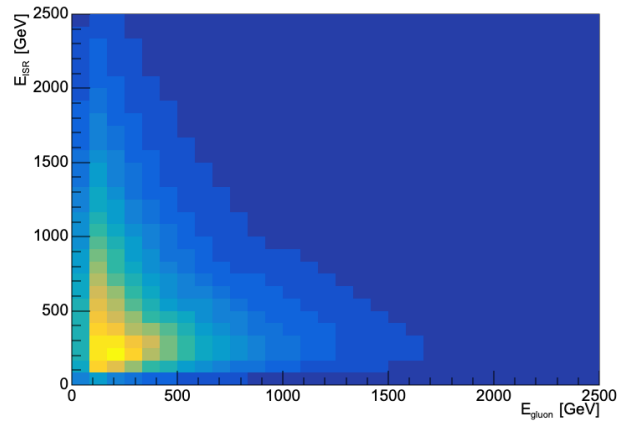
(b)

Figure B.2: Energy of the emitted ISR with respect to B.2(a) the energy of incoming quark, and with respect to B.2(b) the energy of the incoming gluon

Bibliography

[1]   M. K. Gaillard, P. D. Grannis and F. J. Sciulli, *The standard model of particle physics*,
      Reviews of Modern Physics **71** (1999) S96,
      URL: http://dx.doi.org/10.1103/RevModPhys.71.S96.

[2]   ATLAS Collaboration, *A detailed map of Higgs boson interactions by the ATLAS
      experiment ten years after the discovery*, Nature **607** (2022) 52,
      URL: https://doi.org/10.1038/s41586-022-04893-w.

[3]   CMS Collaboration,
      A portrait of the Higgs boson by the CMS experiment ten years after the discovery.,
      Nature **607** (2022) 60, URL: https://doi.org/10.1038/s41586-022-04892-x.

[4]   ATLAS Collaboration, *Observation of a new particle in the search for the Standard
      Model Higgs boson with the ATLAS detector at the LHC*,
      Physics Letters B **716** (2012) 1, URL: https://www.sciencedirect.com/science
      /article/pii/S037026931200857X.

[5]   CMS Collaboration,
      Observation of a new boson at a mass of 125 GeV with the CMS experiment at the LHC,
      Physics Letters B **716** (2012) 30, ISSN: 0370-2693, URL: https://www.sciencedire
      ct.com/science/article/pii/S0370269312008581.

[6]   D. M. Webber et al.,
      *Publisher's Note: Measurement of the Positive Muon Lifetime and Determination of the
      Fermi Constant to Part-per-Million Precision [Phys. Rev. Lett. 106, 041803 (2011)]*,
      Phys. Rev. Lett. **106** (7 2011) 079901,
      URL: https://link.aps.org/doi/10.1103/PhysRevLett.106.079901.

[7]   Particle Data Group and R. L. Workman and Burkert, *Review of Particle Physics*,
      Progress of Theoretical and Experimental Physics **2022** (2022) 083C01,
      ISSN: 2050-3911, URL: https://doi.org/10.1093/ptep/ptac097.

[8]   ATLAS Collaboration,
      $t\bar{t}H$ *Coupling Measurement with the ATLAS Detector at the LHC*,
      EPJ Web Conf. **182** (2018) 02052,
      URL: https://doi.org/10.1051/epjconf/201818202052.

[9]   CMS Collaboration, *Search for* $t\bar{t}H$ *production in the* $H \rightarrow b\bar{b}$ *decay channel with
      leptonic* $t\bar{t}$ *decays in proton-proton collisions at* $\sqrt{s} = 13$ *TeV*,
      Journal of High Energy Physics **2019** (2019) 26,
      URL: https://doi.org/10.1007/JHEP03(2019)026.

[10] ATLAS and CMS Collaborations, *Measurements of the Higgs boson production and decay rates and constraints on its couplings from a combined ATLAS and CMS analysis of the LHC pp collision data at $\sqrt{s}$ = 7 and 8 TeV*,
Journal of High Energy Physics **2016** (2016) 45,
URL: https://doi.org/10.1007/JHEP08(2016)045.

[11] J. H. Kühn, A. Scharf and P. Uwer,
Weak interactions in top-quark pair production at hadron colliders: An update,
Physical Review D **91** (2015), ISSN: 1550-2368,
URL: http://dx.doi.org/10.1103/PhysRevD.91.014020.

[12] J. H. Kühn, A. Scharf and P. Uwer,
Weak interaction effects in top-quark pair production at hadron colliders,
The European Physical Journal C **51** (2007) 37,
URL: https://doi.org/10.1140/epjc/s10052-007-0275-x.

[13] CMS collaboration, *Measurement of the top quark Yukawa coupling from $t\bar{t}$ kinematic distributions in the lepton+jets final state in proton-proton collisions at $\sqrt{s}$ = 13 TeV*,
Phys. Rev. D **100** (2019) 072007,
URL: https://doi.org/10.1103/PhysRevD.100.072007.

[14] CMS Collaboration, *Measurement of the top quark Yukawa coupling from $t\bar{t}$ kinematic distributions in the dilepton final state in proton-proton collisions at $\sqrt{s}$ = 13 TeV*,
Phys. Rev. D **102** (9 2020) 092013,
URL: https://link.aps.org/doi/10.1103/PhysRevD.102.092013.

[15] T. Kobayashi, *Experimental verification of the standard model of particle physics*,
Proceedings of the Japan Academy, Series B Physical and Biological Sciences **97** (2021) 211,
URL: http://inis.iaea.org/search/search.aspx?orig_q=RN:53050883.

[16] H. M. Gray, "TASI 2022 lectures on LHC experiments", 2023,
URL: https://doi.org/10.48550/arXiv.2307.01894.

[17] G. Altarelli, *The Higgs and the Excessive Success of the Standard Model*,
Frascati Phys. Ser. **58** (2014) 102, ed. by R. Fusco Femiano and G. Mannocchi,
URL: https://doi.org/10.48550/arXiv.1407.2122.

[18] J. Woithe, G. J. Wiener and F. F. V. der Veken,
Let's have a coffee with the Standard Model of particle physics!,
Physics Education **52** (2017) 034001,
URL: https://dx.doi.org/10.1088/1361-6552/aa5b25.

[19] M. Y. Khlopov, *Conspiracy of BSM physics and cosmology*, 2019,
URL: https://doi.org/10.48550/arXiv.1911.03294.

[20] E. Halkiadakis, G. Redlinger and D. Shih,
Status and Implications of BSM Searches at the LHC, 2014,
URL: https://doi.org/10.48550/arXiv.1411.1427.

[21] O. Fischer et al., *Unveiling hidden physics at the LHC*,
The European Physical Journal C **82** (2022), ISSN: 1434-6052,
URL: http://dx.doi.org/10.1140/epjc/s10052-022-10541-4.

[22] *Standard Model of Elementary Particles*, Figure 2.1,
URL: https://en.wikipedia.org/wiki/File:Standard_Model_of_Elementary_Particles.svg (visited on 22/12/2023).

[23] S. Ujevic, V. Zampronio, B. R. de Abreu and S. A. Vitiello,
Properties of fermionic systems with the path-integral ground state method,
SciPost Physics Core **6** (2023), ISSN: 2666-9366,
URL: http://dx.doi.org/10.21468/SciPostPhysCore.6.2.031.

[24] S. Biswas, *Fermi-Dirac Statistics*, 2015,
URL: https://doi.org/10.48550/arXiv.1402.3370.

[25] C. S. Unnikrishnan,
Bosons, Fermions, Spin, Gravity, and the Spin-Statistics Connection, 2019,
URL: https://doi.org/10.48550/arXiv.1906.07656.

[26] V. Mittar, *Bose-Einstein condensation: what, how and beyond*, 2022,
URL: https://doi.org/10.48550/arXiv.2203.07038.

[27] Y.-R. Liu, H.-X. Chen, W. Chen, X. Liu and S.-L. Zhu,
Pentaquark and Tetraquark States,
Progress in Particle and Nuclear Physics **107** (2019) 237,
URL: http://dx.doi.org/10.1016/j.ppnp.2019.04.003.

[28] R. Loll, G. Fabiano, D. Frattulillo and F. Wagner, *Quantum Gravity in 30 Questions*,
2022, URL: https://doi.org/10.48550/arXiv.2206.06762.

[29] S. L. Glashow, *The renormalizability of vector meson interactions*,
Nuclear Physics **10** (1959) 107, ISSN: 0029-5582, URL: https://www.sciencedirect.com/science/article/pii/0029558259901968.

[30] S. L. Glashow, *Partial symmetries of weak interactions*, Nuclear Physics **22** (1961) 579,
ISSN: 0029-5582, URL: https://www.sciencedirect.com/science/article/pii/0029558261904692.

[31] S. Weinberg, *A Model of Leptons*, **19** (1967) 1264,
URL: https://ui.adsabs.harvard.edu/abs/1967PhRvL..19.1264W.

[32] A. Salam, *Weak and electromagnetic interactions*,
Il Nuovo Cimento (1955-1965) **11** (1959) 568,
URL: https://api.semanticscholar.org/CorpusID:15889731.

[33] M. E. Peskin and D. V. Schroeder, *An Introduction to quantum field theory*,
Reading, USA: Addison-Wesley, 1995, ISBN: 978-0-201-50397-5.

[34] A. Francis et al., *Study of the Couplings of QED and QCD from the Adler Function*,
2014, URL: https://doi.org/10.48550/arXiv.1412.6934.

[35] P. W. Phillips, *Fifty years of Wilsonian renormalization and counting*, 2023,
URL: https://doi.org/10.48550/arXiv.2309.02484.

[36] F. L. Wilson, *Fermi's Theory of Beta Decay*,
American Journal of Physics **36** (1968) 1150, ISSN: 0002-9505,
URL: https://doi.org/10.1119/1.1974382.

[37] W. J. Marciano, *Fermi constants and "new physics"*, Physical Review D **60** (1999),
ISSN: 1089-4918, URL: http://dx.doi.org/10.1103/PhysRevD.60.093006.

[38] M. Thomson, *Modern particle physics*, New York: Cambridge University Press, 2013, ISBN: 978-1-107-03426-6.

[39] C. S. Wu, E. Ambler, R. W. Hayward, D. D. Hoppes and R. P. Hudson, *Experimental Test of Parity Conservation in Beta Decay*, Phys. Rev. **105** (4 1957) 1413, URL: https://link.aps.org/doi/10.1103/PhysRev.105.1413.

[40] E. C. G. Sudarshan and R. E. Marshak, *Origin of the Universal V-A theory*, AIP Conference Proceedings **300** (1994) 110, ISSN: 0094-243X, URL: https://doi.org/10.1063/1.45454.

[41] A. Franklin, *Experiment and the Development of the Theory of Weak Interactions: Fermi's Theory*, PSA: Proceedings of the Biennial Meeting of the Philosophy of Science Association **1986** (1986) 163, URL: https://doi.org/10.1086/psaprocbienmeetp.1986.2.192798.

[42] S. Descotes-Genon and P. Koppenburg, *The CKM Parameters*, Annual Review of Nuclear and Particle Science **67** (2017) 97, URL: http://dx.doi.org/10.1146/annurev-nucl-101916-123109.

[43] H. P. R, P. Kielanowski and S. R. J. W, *Cabibbo–Kobayashi–Maskawa matrix: rephasing invariants and parameterizations*, Journal of Physics: Conference Series **485** (2014) 012058, URL: http://dx.doi.org/10.1088/1742-6596/485/1/012058.

[44] A. Pich, *The Standard Model of Electroweak Interactions*, 2012, URL: https://doi.org/10.48550/arXiv.1201.0537.

[45] M. A. Faessler, *Weinberg Angle and Integer Electric Charges of Quarks*, 2013, URL: https://doi.org/10.48550/arXiv.1308.5900.

[46] *Tevatron Run II combination of the effective leptonic electroweak mixing angle*, Physical Review D **97** (2018), URL: https://doi.org/10.1103/PhysRevD.97.112007.

[47] J. Horejsi, *Fundamentals of electroweak theory*, 2022, URL: https://doi.org/10.48550/arXiv.2210.04526.

[48] F. Englert and R. Brout, *Broken Symmetry and the Mass of Gauge Vector Mesons*, Phys. Rev. Lett. **13** (9 1964) 321, URL: https://link.aps.org/doi/10.1103/PhysRevLett.13.321.

[49] P. W. Higgs, *Broken Symmetries and the Masses of Gauge Bosons*, **13** (1964) 508, URL: https://ui.adsabs.harvard.edu/abs/1964PhRvL..13..508H.

[50] G. S. Guralnik, C. R. Hagen and T. W. B. Kibble, *Global Conservation Laws and Massless Particles*, Phys. Rev. Lett. **13** (20 1964) 585, URL: https://link.aps.org/doi/10.1103/PhysRevLett.13.585.

[51] A. Abokhalil, *The Higgs Mechanism and Higgs Boson: Unveiling the Symmetry of the Universe*, 2023, URL: https://doi.org/10.48550/arXiv.2306.01019.

[52] ATLAS Collaboration, *Observation of a new particle in the search for the Standard Model Higgs boson with the ATLAS detector at the LHC*, Physics Letters B **716** (2012) 1.

[53] CMS Collaboration, *Observation of a new boson at a mass of 125 GeV with the CMS experiment at the LHC*, English (US), Physics Letters, Section B: Nuclear, Elementary Particle and High-Energy Physics **716** (2012) 30, ISSN: 0370-2693.

[54] J. I. Illana and A. J. Cano, *Quantum field theory and the structure of the Standard Model*, 2022, URL: https://doi.org/10.48550/arXiv.2211.14636.

[55] R. A. Wilson, *A discrete model for Gell-Mann matrices*, 2024, URL: https://doi.org/10.48550/arXiv.2401.13000.

[56] T.-M. Yan and S. D. Drell, *The parton model and its applications*, International Journal of Modern Physics A **29** (2014) 1430071, ISSN: 1793-656X, URL: http://dx.doi.org/10.1142/S0217751X14300713.

[57] Del Debbio, Luigi, *Parton distributions in the LHC era*, EPJ Web Conf. **175** (2018) 01006, URL: https://doi.org/10.1051/epjconf/201817501006.

[58] V. N. Gribov and L. N. Lipatov, *Deep inelastic e p scattering in perturbation theory*, Sov. J. Nucl. Phys. **15** (1972) 438.

[59] Y. L. Dokshitzer, *Calculation of the Structure Functions for Deep Inelastic Scattering and e^+e^- Annihilation by Perturbation Theory in Quantum Chromodynamics.*, Sov. Phys. JETP **46** (1977) 641.

[60] G. Altarelli and G. Parisi, *Asymptotic Freedom in Parton Language*, Nucl. Phys. B **126** (1977) 298.

[61] N. Kidonakis and B. D. Pecjak, *Top-quark production and QCD*, The European Physical Journal C **72** (2012), ISSN: 1434-6052, URL: http://dx.doi.org/10.1140/epjc/s10052-012-2084-0.

[62] J. C. Collins, D. E. Soper and G. F. Sterman, *Factorization of Hard Processes in QCD*, Adv. Ser. Direct. High Energy Phys. **5** (1989) 1, URL: https://doi.org/10.48550/arXiv.hep-ph/0409313.

[63] T. Lappi, H. Mäntysaari, H. Paukkunen and M. Tevio, *Evolution of structure functions in momentum space*, The European Physical Journal C **84** (2024) 84, URL: https://doi.org/10.1140/epjc/s10052-023-12365-2.

[64] A. D. Martin, *Proton structure, Partons, QCD, DGLAP and beyond*, 2008, URL: https://doi.org/10.48550/arXiv.0802.0161.

[65] C. Lange, *A novel approach to precision measurements of the top quark-antiquark pair production cross section with the ATLAS experiment*, Humboldt U., Berlin, 2013, URL: https://cds.cern.ch/record/1602266.

[66] J. F. Donoghue, "The effective field theory treatment of quantum gravity", *AIP Conference Proceedings*, AIP, 2012, URL: http://dx.doi.org/10.1063/1.4756964.

[67] E. W. Kolb and M. S. Turner, *The Early Universe*, vol. 69, 1990, ISBN: 978-0-201-62674-2, URL: https://doi.org/10.1201/9780429492860.

[68] C. D. Froggatt and H. B. Nielsen, *Hierarchy Problem and a new Bound State*, 2004, URL: https://doi.org/10.48550/arXiv.hep-ph/0312218.

[69] N. Arkani–Hamed, S. Dimopoulos and G. Dvali,
The hierarchy problem and new dimensions at a millimeter,
Physics Letters B **429** (1998) 263,
URL: http://dx.doi.org/10.1016/S0370-2693(98)00466-3.

[70] M. Lisanti, "Lectures on Dark Matter Physics", *New Frontiers in Fields and Strings*,
WORLD SCIENTIFIC, 2016,
URL: http://dx.doi.org/10.1142/9789813149441_0007.

[71] The ATLAS and CDF and CMS and D0 Collaborations,
First combination of Tevatron and LHC measurements of the top-quark mass, (2014),
URL: https://doi.org/10.48550/arXiv.1403.4427.

[72] J. Yoh, R. A. Burnstein, D. M. Kaplan and H. A. Rubin,
The Discovery of the B quark at Fermilab in 1977: The Experiment coordinator's story,
AIP Conf. Proc. **424** (1998) 29, ed. by R. A. Burnstein, D. M. Kaplan and H. A. Rubin,
URL: https://ui.adsabs.harvard.edu/abs/1998AIPC..424...29Y.

[73] F. Abe et al., *Observation of Top Quark Production in $\bar{p}p$ Collisions with the Collider
Detector at Fermilab*, Phys. Rev. Lett. **74** (14 1995) 2626,
URL: https://link.aps.org/doi/10.1103/PhysRevLett.74.2626.

[74] S. Abachi et al., *Observation of the Top Quark*, Phys. Rev. Lett. **74** (14 1995) 2632,
URL: https://link.aps.org/doi/10.1103/PhysRevLett.74.2632.

[75] J. Gao, C. S. Li and H. X. Zhu,
Top-Quark Decay at Next-to-Next-to-Leading Order in QCD,
Phys. Rev. Lett. **110** (4 2013) 042001,
URL: https://link.aps.org/doi/10.1103/PhysRevLett.110.042001.

[76] A. Valishev, *Tevatron accelerator physics and operation highlights*, 2012,
URL: https://doi.org/10.48550/arXiv.1202.5525.

[77] A. D. Roeck, *Top production at hadron colliders*,
Pramana Journal of Physics **79** (4 2012) 643,
URL: https://www.ias.ac.in/article/fulltext/pram/079/04/0643-0658.

[78] CDF and D0 Collaborations, *Combination of measurements of the top-quark pair
production cross section from the Tevatron Collider*, Phys. Rev. D **89** (7 2014) 072001,
URL: https://link.aps.org/doi/10.1103/PhysRevD.89.072001.

[79] ATLAS Collaboration, *Measurement of the $t\bar{t}$ production cross-section in pp collisions
at $\sqrt{s}$ = 5.02 TeV with the ATLAS detector*, JHEP **06** (2023) 138,
URL: https://doi.org/10.1007/JHEP06%282023%29138.

[80] CMS Collaboration, *Measurement of the inclusive $t\bar{t}$ production cross section in
proton-proton collisions at $\sqrt{s}$ = 5.02 TeV*, JHEP **04** (2022) 144,
URL: https://doi.org/10.1007/JHEP04%282022%29144.

[81] The ATLAS and CMS Collaborations,
*Combination of inclusive top-quark pair production cross-section measurements using
ATLAS and CMS data at $\sqrt{s}$ = 7 and 8 TeV*, JHEP **07** (2023) 213,
URL: https://doi.org/10.1007/JHEP07(2023)213.

[82] ATLAS Collaboration, *Inclusive and differential cross-sections for dilepton $t\bar{t}$
production measured in $\sqrt{s}$ = 13 TeV pp collisions with the ATLAS detector*,
JHEP **07** (2023) 141, URL: https://doi.org/10.1007/JHEP07%282023%29141.

[83] CMS Collaboration, *Measurement of the $t\bar{t}$ production cross section, the top quark mass, and the strong coupling constant using dilepton events in pp collisions at $\sqrt{s}$ = 13 TeV*, The European Physical Journal C **79** (2019) 368, URL: https://doi.org/10.1140/epjc/s10052-019-6863-8.

[84] ATLAS Collaboration, *Measurement of the $t\bar{t}$ production cross-section in the lepton+jets channel at $\sqrt{s}$ = 13 TeV with the ATLAS experiment*, Phys. Lett. B **810** (2020) 135797, URL: https://doi.org/10.1016/j.physletb.2020.135797.

[85] CMS Collaboration, *Measurement of differential $t\bar{t}$ production cross sections in the full kinematic range using* lepton + *jets events from proton-proton collisions at $\sqrt{s}$ = 13 TeV*, Phys. Rev. D **104** (9 2021) 092013, URL: https://link.aps.org/doi/10.1103/PhysRevD.104.092013.

[86] ATLAS Collaboration, *Measurement of the $t\bar{t}$ cross section and its ratio to the Z production cross section using pp collisions at s=13.6 TeV with the ATLAS detector*, Phys. Lett. B **848** (2024) 138376, URL: https://doi.org/10.1016/j.physletb.2023.138376.

[87] CMS collaboration, *First measurement of the top quark pair production cross section in proton-proton collisions at $$ \sqrt{s} $$= 13.6 TeV*, Journal of High Energy Physics **2023** (2023) 204, URL: https://doi.org/10.1007/JHEP08(2023)204.

[88] M. Czakon, P. Fiedler and A. Mitov, *Total Top-Quark Pair-Production Cross Section at Hadron Colliders Through $O(\alpha_S^4)$*, Phys. Rev. Lett. **110** (25 2013) 252004, URL: https://link.aps.org/doi/10.1103/PhysRevLett.110.252004.

[89] *LHC Top Working Group sumary plots*, URL: https://twiki.cern.ch/twiki/bin/view/LHCPhysics/LHCTopWGSummaryPlots (visited on 01/02/2024).

[90] *Branching ratio for $t\bar{t}$ decay*, Figure 2.6, URL: https://tikz.net/wp-content/uploads/2023/09/SM_decay_piechart-007.png (visited on 26/01/2023).

[91] ATLAS Collaboration, *Combined measurements of Higgs boson production and decay using up to 80 fb^{-1} of proton-proton collision data at $\sqrt{s}$ = 13 TeV collected with the ATLAS experiment*, Phys. Rev. D **101** (1 2020) 012002, URL: https://link.aps.org/doi/10.1103/PhysRevD.101.012002.

[92] CERN, *CERN Yellow Reports: Monographs, Vol 2 (2017): Handbook of LHC Higgs cross sections: 4. Deciphering the nature of the Higgs sector*, 2017, URL: https://e-publishing.cern.ch/index.php/CYRM/issue/view/32.

[93] L. Evans and P. Bryant, *LHC Machine*, Journal of Instrumentation **3** (2008) S08001, URL: https://dx.doi.org/10.1088/1748-0221/3/08/S08001.

[94] ATLAS Collaboration, *The ATLAS Experiment at the CERN Large Hadron Collider*, Journal of Instrumentation **3** (2008) S08003, URL: https://dx.doi.org/10.1088/1748-0221/3/08/S08003.

[95] *European Council for Nuclear Research: about*, URL: https://home.web.cern.ch/about (visited on 28/01/2024).

[96] O. S. Brüning et al., *LHC Design Report*, CERN Yellow Reports: Monographs, Geneva: CERN, 2004, URL: http://cds.cern.ch/record/782076.

[97] N. A. Ky and N. T. H. Van, *Was the Higgs boson discovered?*, (2015), URL: https://doi.org/10.15625/0868-3166/25/1/5941.

[98] ATLAS Collaboration, *ATLAS detector and physics performance: Technical Design Report, 1*, Technical design report. ATLAS (1999), URL: https://cds.cern.ch/record/391176.

[99] ATLAS Collaboration, *ATLAS detector and physics performance: Technical Design Report, 2*, Technical design report. ATLAS (1999), URL: https://cds.cern.ch/record/391177.

[100] CMS Collaboration, *CMS Physics: Technical Design Report Volume 1: Detector Performance and Software*, Technical design report. CMS (2006), URL: https://cds.cern.ch/record/922757.

[101] CMS Collaboration, *CMS Physics: Technical Design Report Volume 2: Physics Performance*, J. Phys. G **34** (2007) 995, revised version submitted on 2006-09-22 17:44:47, URL: https://cds.cern.ch/record/942733.

[102] ALICE Collaboration, *ALICE: Physics Performance Report, Volume 1*, Journal of Physics G: Nuclear and Particle Physics **30** (2004) 1517, URL: https://dx.doi.org/10.1088/0954-3899/30/11/001.

[103] ALICE Collaboration, *ALICE: Physics Performance Report, Volume 2*, Journal of Physics G: Nuclear and Particle Physics **32** (2006) 1295, URL: https://dx.doi.org/10.1088/0954-3899/32/10/001.

[104] LHCb Collaboration, *LHCb : Technical Proposal*, Geneva: CERN, 1998, URL: https://cds.cern.ch/record/622031.

[105] *Luminosity determination in pp collisions at $\sqrt{s}$ = 13 TeV using the ATLAS detector at the LHC*, tech. rep., CERN, 2019, URL: https://cds.cern.ch/record/2677054.

[106] P. Grafström and W. Kozanecki, *Luminosity determination at proton colliders*, Progress in Particle and Nuclear Physics **81** (2015) 97, ISSN: 0146-6410, URL: https://www.sciencedirect.com/science/article/pii/S0146641014000878.

[107] *CAS - CERN Accelerator School: Intermediate Course on Accelerator Physics*, CERN, Geneva: CERN, 2006, URL: http://cds.cern.ch/record/603056.

[108] ATLAS Collaboration, *Luminosity determination in pp collisions at $\sqrt{s}$ = 13 TeV using the ATLAS detector at the LHC*, The European Physical Journal C **83** (2023) 982, URL: https://doi.org/10.1140/epjc/s10052-023-11747-w.

[109] *Total Integrated Luminosity and Data Quality in 2015-2018*, URL: https://twiki.cern.ch/twiki/bin/view/AtlasPublic/LuminosityPublicResultsRun2 (visited on 27/01/2024).

[110] G. Soyez, *Pileup mitigation at the LHC: A theorist's view*, Physics Reports **803** (2019) 1, ISSN: 0370-1573, URL: http://dx.doi.org/10.1016/j.physrep.2019.01.007.

[111] *Number of Interactions per Crossing*, URL: https://twiki.cern.ch/twiki/bin/view/AtlasPublic/LuminosityPublicResultsRun2 (visited on 27/01/2024).

[112] ATLAS Collaboration, *The ATLAS Experiment at the CERN Large Hadron Collider*, Journal of Instrumentation **3** (2008) S08003, URL: https://doi.org/10.1088%2F1748-0221%2F3%2F08%2Fs08003.

[113] *Pseudorapidity values in the yz-plane*, Figure 3.5(b), URL: https://tikz.net/axis2d_pseudorapidity/ (visited on 28/01/2023).

[114] ATLAS Collaboration, *ATLAS magnet system: Technical Design Report, 1*, Technical design report. ATLAS, Geneva: CERN, 1997, URL: https://cds.cern.ch/record/338080.

[115] ATLAS Collaboration, *ATLAS central solenoid: Technical Design Report*, Technical design report. ATLAS, Electronic version not available, Geneva: CERN, 1997, URL: https://cds.cern.ch/record/331067.

[116] ATLAS Collaboration, *ATLAS barrel toroid: Technical Design Report*, Technical design report. ATLAS, Electronic version not available, Geneva: CERN, 1997, URL: https://cds.cern.ch/record/331065.

[117] ATLAS Collaboration, *ATLAS end-cap toroids: Technical Design Report*, Technical design report. ATLAS, Electronic version not available, Geneva: CERN, 1997, URL: https://cds.cern.ch/record/331066.

[118] J. J. Goodson, *Search for supersymmetry in states with large missing transverse momentum and three leptons including a Z-boson*, State University of New York at Stony Brook, 2012.

[119] ATLAS Collaboration, *ATLAS inner detector: Technical Design Report, 1*, Technical design report. ATLAS, Geneva: CERN, 1997, URL: https://cds.cern.ch/record/331063.

[120] ATLAS Collaboration, *ATLAS inner detector: Technical Design Report, 2*, Technical design report. ATLAS, Geneva: CERN, 1997, URL: https://cds.cern.ch/record/331064.

[121] ATLAS Collaboration, *The ATLAS Inner Detector commissioning and calibration*, The European Physical Journal C **70** (2010) 787, URL: https://doi.org/10.1140/epjc/s10052-010-1366-7.

[122] G. Hall, *Semiconductor particle tracking detectors*, Reports on Progress in Physics **57** (1994) 481, URL: https://dx.doi.org/10.1088/0034-4885/57/5/002.

[123] W. R. Leo, *Techniques for Nuclear and Particle Physics Experiments*, Heidelberg: Springer Berlin, 2012, ISBN: 978-3-642-57920-2, URL: https://doi.org/10.1007/978-3-642-57920-2.

[124] The ATLAS Collaboration, *The ATLAS Experiment at the CERN Large Hadron Collider*, Journal of Instrumentation **3** (2008) S08003, URL: https://dx.doi.org/10.1088/1748-0221/3/08/S08003.

[125] ATLAS Collaboration, *IBL Efficiency and Single Point Resolution in Collision Events*, tech. rep., CERN, 2016, URL: https://cds.cern.ch/record/2203893.

[126] ATLAS Collaboration, *Performance of the ATLAS Transition Radiation Tracker in Run 1 of the LHC: tracker properties*, Journal of Instrumentation **12** (2017) P05002, URL: https://dx.doi.org/10.1088/1748-0221/12/05/P05002.

[127] A. Bingül, *The ATLAS TRT and its Performance at LHC*, Journal of Physics: Conference Series **347** (2012) 012025, URL: https://dx.doi.org/10.1088/1742-6596/347/1/012025.

[128] ATLAS Collaboration, *ATLAS Calorimeter: Run 2 performance and Phase-II upgrades*, PoS EPS-HEP2017 (2017) 485, ed. by P. Checchia et al., URL: https://doi.org/10.22323/1.314.0485.

[129] V. Tisserand, *Optimization of the ATLAS detector for the search of Higgs boson decaying into two photons at the LHC*, Theses: Université Paris Sud - Paris XI, 1997, URL: https://theses.hal.science/tel-00544731.

[130] C. W. Fabjan and F. Gianotti, *Calorimetry for Particle Physics*, Rev. Mod. Phys. **75** (2003) 1243, URL: https://cds.cern.ch/record/692252.

[131] Z. Meng, *Performance of the ATLAS Liquid Argon Calorimeter*, tech. rep., CERN, 2010, URL: https://cds.cern.ch/record/1304279.

[132] R. Wigmans, "30The Physics of Shower Development", *Calorimetry: Energy Measurement in Particle Physics*, Oxford University Press, 2017, ISBN: 9780198786351, URL: https://doi.org/10.1093/oso/9780198786351.003.0002.

[133] ATLAS Collaboration, *ATLAS Muon Detector Commissioning*, 2009, URL: https://doi.org/10.48550/arXiv.0910.2767.

[134] F. Kuger, *Signal Formation Processes in Micromegas Detectors and Quality Control for large size Detector Construction for the ATLAS New Small Wheel*, 2017, URL: https://doi.org/10.48550/arXiv.1708.01624.

[135] J. Snuverink, *The ATLAS muon spectrometer: commissioning and tracking*, Presented on 16 Oct 2009, Twente U., Enschede, Enschede, 2009, URL: http://dx.doi.org/10.3990/1.9789036529129.

[136] S. Artz et al., *Upgrade of the ATLAS Central Trigger for LHC Run-2*, Journal of Instrumentation **10** (2015) C02030, URL: https://dx.doi.org/10.1088/1748-0221/10/02/C02030.

[137] Atlas Collaboration, *Performance of the ATLAS trigger system in 2015*, The European Physical Journal C **77** (2017) 317, URL: https://doi.org/10.1140/epjc/s10052-017-4852-3.

[138] ATLAS collaboration, *Operation of the ATLAS trigger system in Run 2*, Journal of Instrumentation **15** (2020) P10004, URL: https://dx.doi.org/10.1088/1748-0221/15/10/P10004.

[139] ATLAS Collaboration, *Technical Design Report for the Phase-I Upgrade of the ATLAS TDAQ System*, tech. rep., 2013, URL: https://cds.cern.ch/record/1602235.

[140] Atlas Collaboration,
       ATLAS high-level trigger, data-acquisition and controls: Technical Design Report,
       Technical design report. ATLAS, Geneva: CERN, 2003,
       URL: https://cds.cern.ch/record/616089.

[141] A. Buckley et al., *General-purpose event generators for LHC physics*,
       Physics Reports **504** (2011) 145, ISSN: 0370-1573,
       URL: http://dx.doi.org/10.1016/j.physrep.2011.03.005.

[142] M. Dobbs and J. B. Hansen,
       The HepMC C++ Monte Carlo event record for High Energy Physics,
       Computer Physics Communications **134** (2001) 41, ISSN: 0010-4655, URL: https://ww
       w.sciencedirect.com/science/article/pii/S0010465500001892.

[143] T. Sjöstrand and P. Z. Skands,
       Transverse-momentum-ordered showers and interleaved multiple interactions,
       The European Physical Journal C - Particles and Fields **39** (2005) 129,
       URL: https://doi.org/10.1140/epjc/s2004-02084-y.

[144] M. Savitskyi,
       *Measurements of differential cross sections for $t\bar{t}$ production in proton-proton collisions
       at $\sqrt{s}$ = 13 TeV using events containing two leptons with the CMS experiment*,
       Hamburg U., 2018.

[145] S. Hoeche et al., *Matching Parton Showers and Matrix Elements*, 2006,
       URL: https://doi.org/10.48550/arXiv.hep-ph/0602031.

[146] B. Andersson, G. Gustafson, G. Ingelman and T. Sjöstrand,
       Parton fragmentation and string dynamics, Physics Reports **97** (1983) 31,
       ISSN: 0370-1573, URL: https://www.sciencedirect.com/science/article/pi
       i/0370157383900807.

[147] B. Andersson, G. Gustafson and B. Söderberg, *A general model for jet fragmentation*,
       Zeitschrift für Physik C Particles and Fields **20** (1983) 317,
       URL: https://doi.org/10.1007/BF01407824.

[148] B. Andersson, *The Lund Model*, vol. 7,
       Cambridge Monographs on Particle Physics, Nuclear Physics and Cosmology,
       Cambridge University Press, 2023.

[149] T. Sjöstrand, *Jet fragmentation of multiparton configurations in a string framework*,
       Nuclear Physics B **248** (1984) 469, URL: https://www.sciencedirect.com/scien
       ce/article/pii/0550321384906072.

[150] D. Amati and G. Veneziano, *Preconfinement as a property of perturbative QCD*,
       Physics Letters B **83** (1979) 87, ISSN: 0370-2693, URL: https://www.sciencedirec
       t.com/science/article/pii/0370269379908967.

[151] R. D. Field and S. Wolfram, *A QCD model for e^+e^- annihilation*,
       Nuclear Physics B **213** (1983) 65, ISSN: 0550-3213, URL: https://www.sciencedire
       ct.com/science/article/pii/055032138390175X.

[152] T. Sjöstrand and M. van Zijl,
       A multiple-interaction model for the event structure in hadron collisions,
       Phys. Rev. D **36** (7 1987) 2019,
       URL: https://link.aps.org/doi/10.1103/PhysRevD.36.2019.

[153] S. Alioli, P. Nason, C. Oleari and E. Re, *A general framework for implementing NLO calculations in shower Monte Carlo programs: the POWHEG BOX*,
Journal of High Energy Physics **2010** (2010),
URL: http://dx.doi.org/10.1007/JHEP06(2010)043.

[154] S. Frixione, P. Nason and C. Oleari, *Matching NLO QCD computations with parton shower simulations: the POWHEG method*,
Journal of High Energy Physics **2007** (2007) 070,
URL: http://dx.doi.org/10.1088/1126-6708/2007/11/070.

[155] P. Nason, *A new method for combining NLO QCD with shower Monte Carlo algorithms*,
Journal of High Energy Physics **2004** (2004) 040,
URL: https://dx.doi.org/10.1088/1126-6708/2004/11/040.

[156] J. Alwall et al., *The automated computation of tree-level and next-to-leading order differential cross sections, and their matching to parton shower simulations*,
Journal of High Energy Physics **2014** (2014) 79,
URL: https://doi.org/10.1007/JHEP07(2014)079.

[157] R. Frederix et al.,
Erratum to: The automation of next-to-leading order electroweak calculations,
Journal of High Energy Physics **2021** (2021) 85,
URL: https://doi.org/10.1007/JHEP11(2021)085.

[158] T. Sjöstrand et al., *An introduction to PYTHIA 8.2*,
Computer Physics Communications **191** (2015) 159, ISSN: 0010-4655, URL: https://www.sciencedirect.com/science/article/pii/S0010465515000442.

[159] M. Bähr et al., *Herwig++ physics and manual*,
The European Physical Journal C **58** (2008) 639,
URL: https://doi.org/10.1140/epjc/s10052-008-0798-9.

[160] J. Bellm et al., *Herwig 7.0/Herwig++ 3.0 release note*,
The European Physical Journal C **76** (2016) 196,
URL: https://doi.org/10.1140/epjc/s10052-016-4018-8.

[161] E. Bothmann et al., *Event generation with Sherpa 2.2*, SciPost Physics **7** (2019),
ISSN: 2542-4653, URL: http://dx.doi.org/10.21468/SciPostPhys.7.3.034.

[162] D. J. Lange, *The EvtGen particle decay simulation package*,
Nuclear Instruments and Methods in Physics Research Section A: Accelerators, Spectrometers, Detectors and Associated Equipment **462** (2001) 152, BEAUTY2000, Proceedings of the 7th Int. Conf. on B-Physics at Hadron Machines, URL: https://www.sciencedirect.com/science/article/pii/S0168900201000894.

[163] *ATLAS Pythia 8 tunes to 7 TeV data*, tech. rep., CERN, 2014,
URL: https://cds.cern.ch/record/1966419.

[164] ATLAS Collaboration, *The ATLAS Simulation Infrastructure*,
The European Physical Journal C **70** (2010) 823,
URL: https://doi.org/10.1140/epjc/s10052-010-1429-9.

[165] S. Agostinelli et al., *Geant4—a simulation toolkit*,
Nuclear Instruments and Methods in Physics Research Section A: Accelerators,
Spectrometers, Detectors and Associated Equipment **506** (2003) 250, ISSN: 0168-9002,
URL: https://www.sciencedirect.com/science/article/pii/S0168900203
013688.

[166] J. Allison et al., *Geant4 developments and applications*,
IEEE Transactions on Nuclear Science **53** (2006) 270,
URL: https://doi.org/10.1109/TNS.2006.869826.

[167] D. Froidevaux, L. Poggioli and E. Richter-Was,
ATLFAST 1.0 A package for particle-level analysis, tech. rep., CERN, 1996,
URL: https://cds.cern.ch/record/682460.

[168] S. Marzani, G. Soyez and M. Spannowsky, *Looking Inside Jets: An Introduction to Jet
Substructure and Boosted-object Phenomenology*,
Springer International Publishing, 2019, ISBN: 9783030157098,
URL: http://dx.doi.org/10.1007/978-3-030-15709-8.

[169] J. Pequenao and P. Schaffner,
How ATLAS detects particles: diagram of particle paths in the detector, 2013,
URL: https://cds.cern.ch/record/1505342 (visited on 07/02/2024).

[170] A. D. Yaghjian, *Maxwell's derivation of the Lorentz force from Faraday's law*, 2020,
URL: http://dx.doi.org/10.2528/PIERM20040202.

[171] ATLAS Collaboration, *Performance of the ATLAS track reconstruction algorithms in
dense environments in LHC Run 2*, The European Physical Journal C **77** (2017) 673,
URL: https://doi.org/10.1140/epjc/s10052-017-5225-7.

[172] ATLAS collaboration,
A neural network clustering algorithm for the ATLAS silicon pixel detector,
Journal of Instrumentation **9** (2014) P09009,
URL: https://dx.doi.org/10.1088/1748-0221/9/09/P09009.

[173] T. Cornelissen et al.,
Concepts, Design and Implementation of the ATLAS New Tracking (NEWT), tech. rep.,
CERN, 2007, URL: https://cds.cern.ch/record/1020106.

[174] R. Fruehwirth, *Application of Kalman filtering to track and vertex fitting*,
Nuclear Instruments and Methods in Physics Research Section A, Accelerators,
Spectrometers, Detectors and Associated Equipment **262** (1987) 444,
URL: http://inis.iaea.org/search/search.aspx?orig_q=RN:19055820.

[175] ATLAS Collaboration, *Performance of primary vertex reconstruction in proton-proton
collisions at $\sqrt{s}$ =7 TeV in the ATLAS experiment*, tech. rep., CERN, 2010,
URL: https://cds.cern.ch/record/1281344.

[176] ATLAS Collaboration,
Vertex Reconstruction Performance of the ATLAS Detector at $\sqrt{s}$ = 13 TeV, tech. rep.,
CERN, 2015, URL: https://cds.cern.ch/record/2037717.

[177] ATLAS Collaboration, *Electron reconstruction and identification in the ATLAS
experiment using the 2015 and 2016 LHC proton–proton collision data at $\sqrt{s}$ = 13 TeV*,
The European Physical Journal C **79** (2019) 639,
URL: https://doi.org/10.1140/epjc/s10052-019-7140-6.

[178] ATLAS Collaboration, *Topological cell clustering in the ATLAS calorimeters and its performance in LHC Run 1*, Eur. Phys. J. C **77** (2017) 490,
URL: https://doi.org/10.1140/epjc/s10052-017-5004-5.

[179] ATLAS Collaboration, *Performance of the ATLAS Tile Calorimeter*,
Journal of Physics: Conference Series **623** (2015) 012014,
URL: https://dx.doi.org/10.1088/1742-6596/623/1/012014.

[180] ATLAS Collaboration, *Electron and photon performance measurements with the ATLAS detector using the 2015–2017 LHC proton-proton collision data*,
Journal of Instrumentation **14** (2019) P12006,
URL: https://dx.doi.org/10.1088/1748-0221/14/12/P12006.

[181] ATLAS Collaboration, *Electron and photon reconstruction and performance in ATLAS using a dynamical, topological cell clustering-based approach*, tech. rep., CERN, 2017,
URL: https://cds.cern.ch/record/2298955.

[182] ATLAS Collaboration, *Electron efficiency measurements with the ATLAS detector using the 2015 LHC proton-proton collision data*, tech. rep., CERN, 2016,
URL: https://cds.cern.ch/record/2157687.

[183] ATLAS Collaboration, *Muon reconstruction and identification efficiency in ATLAS using the full Run 2 pp collision data set at $\sqrt{s}$ = 13 TeV*,
The European Physical Journal C **81** (2021) 578,
URL: https://doi.org/10.1140/epjc/s10052-021-09233-2.

[184] ATLAS Collaboration, *Muon reconstruction performance of the ATLAS detector in proton–proton collision data at $\sqrt{s}$ = 13 TeV*,
The European Physical Journal C **76** (2016) 292,
URL: https://doi.org/10.1140/epjc/s10052-016-4120-y.

[185] G. P. Salam, *Towards jetography*, The European Physical Journal C **67** (2010) 637,
URL: https://doi.org/10.1140/epjc/s10052-010-1314-6.

[186] M. Cacciari, G. P. Salam and G. Soyez, *The anti-k_t jet clustering algorithm*,
Journal of High Energy Physics **2008** (2008) 063,
URL: http://dx.doi.org/10.1088/1126-6708/2008/04/063.

[187] S. D. Ellis and D. E. Soper, *Successive combination jet algorithm for hadron collisions*,
Phys. Rev. D **48** (7 1993) 3160,
URL: https://link.aps.org/doi/10.1103/PhysRevD.48.3160.

[188] Y. Dokshitzer, G. Leder, S. Moretti and B. Webber, *Better jet clustering algorithms*,
Journal of High Energy Physics **1997** (1997) 001,
URL: https://dx.doi.org/10.1088/1126-6708/1997/08/001.

[189] M. Cacciari, G. P. Salam and G. Soyez, *FastJet user manual*,
The European Physical Journal C **72** (2012) 1896,
URL: https://doi.org/10.1140/epjc/s10052-012-1896-2.

[190] ATLAS Collaboration,
Jet reconstruction and performance using particle flow with the ATLAS Detector,
The European Physical Journal C **77** (2017) 466,
URL: https://doi.org/10.1140/epjc/s10052-017-5031-2.

[191] ATLAS Collaboration, *Performance of algorithms that reconstruct missing transverse momentum in $\sqrt{s}$ = 8 TeV proton–proton collisions in the ATLAS detector*,
The European Physical Journal C **77** (2017) 241,
URL: https://doi.org/10.1140/epjc/s10052-017-4780-2.

[192] ATLAS Collaboration, *Jet energy scale and resolution measured in proton–proton collisions at $\sqrt{s}$ = 13 TeV with the ATLAS detector*,
The European Physical Journal C **81** (2021) 689,
URL: https://doi.org/10.1140/epjc/s10052-021-09402-3.

[193] ATLAS Collaboration, *Performance of pile-up mitigation techniques for jets in pp collisions at $\sqrt{s}$ = 8 TeV using the ATLAS detector*,
The European Physical Journal C **76** (2016) 581,
URL: https://doi.org/10.1140/epjc/s10052-016-4395-z.

[194] ATLAS Collaboration,
ATLAS flavour-tagging algorithms for the LHC Run 2 pp collision dataset,
The European Physical Journal C **83** (2023) 681,
URL: https://doi.org/10.1140/epjc/s10052-023-11699-1.

[195] I. H. Witten, E. Frank, M. A. Hall and C. J. Pal, "Chapter 10 - Deep learning",
Data Mining (Fourth Edition), ed. by I. H. Witten, E. Frank, M. A. Hall and C. J. Pal,
Fourth Edition, Morgan Kaufmann, 2017 417, ISBN: 978-0-12-804291-5, URL: https://www.sciencedirect.com/science/article/pii/B9780128042915000106.

[196] ATLAS Collaboration, *Optimisation and performance studies of the ATLAS b-tagging algorithms for the 2017-18 LHC run*, tech. rep., CERN, 2017,
URL: https://cds.cern.ch/record/2273281.

[197] ATLAS Collaboration,
Optimisation of the ATLAS b-tagging performance for the 2016 LHC Run, tech. rep.,
CERN, 2016, URL: https://cds.cern.ch/record/2160731.

[198] ATLAS Collaboration, *Identification of Jets Containing b-Hadrons with Recurrent Neural Networks at the ATLAS Experiment*, tech. rep., CERN, 2017,
URL: https://cds.cern.ch/record/2255226.

[199] ATLAS Collaboration,
Secondary vertex finding for jet flavour identification with the ATLAS detector,
tech. rep., CERN, 2017, URL: https://cds.cern.ch/record/2270366.

[200] ATLAS Collaboration, *Topological b-hadron decay reconstruction and identification of b-jets with the JetFitter package in the ATLAS experiment at the LHC*, tech. rep.,
CERN, 2018, URL: https://cds.cern.ch/record/2645405.

[201] ATLAS Collaboration, *Performance of missing transverse momentum reconstruction with the ATLAS detector using proton–proton collisions at $\sqrt{s}$ = 13 TeV*,
The European Physical Journal C **78** (2018) 903,
URL: https://doi.org/10.1140/epjc/s10052-018-6288-9.

[202] ATLAS Collaboration,
Performance of electron and photon triggers in ATLAS during LHC Run 2,
The European Physical Journal C **80** (2020) 47,
URL: https://doi.org/10.1140/epjc/s10052-019-7500-2.

[203]   ATLAS Collaboration, *Performance of the ATLAS muon triggers in Run 2*,
        Journal of Instrumentation **15** (2020) P09015,
        URL: https://dx.doi.org/10.1088/1748-0221/15/09/P09015.

[204]   R. D. Ball et al., *Parton distributions with LHC data*, Nuclear Physics B **867** (2013) 244,
        ISSN: 0550-3213, URL: https://www.sciencedirect.com/science/article/pi
        i/S0550321312005500.

[205]   M. Aliev et al., *Hathor version 2.1-b3*,
        URL: https://www.physik.hu-berlin.de/de/pep/tools/hathor.html.

[206]   M. Czakon and A. Mitov,
        Top++: A program for the calculation of the top-pair cross-section at hadron colliders,
        Computer Physics Communications **185** (2014) 2930, ISSN: 0010-4655, URL: https:
        //www.sciencedirect.com/science/article/pii/S0010465514002264.

[207]   L. A. Harland-Lang, A. D. Martin, P. Motylinski and R. S. Thorne,
        Parton distributions in the LHC era: MMHT 2014 PDFs,
        The European Physical Journal C **75** (2015) 204,
        URL: https://doi.org/10.1140/epjc/s10052-015-3397-6.

[208]   ATLAS Collaboration, *Studies on the improvement of the matching uncertainty
        definition in top-quark processes simulated with Powheg+Pythia 8*, tech. rep.,
        CERN, 2023, URL: https://cds.cern.ch/record/2872787.

[209]   J. Rojo, *PDF4LHC recommendations for Run II*, 2016,
        URL: https://doi.org/10.48550/arXiv.1606.08243.

[210]   J. Butterworth et al., *PDF4LHC recommendations for LHC Run II*,
        Journal of Physics G: Nuclear and Particle Physics **43** (2016) 023001, ISSN: 1361-6471,
        URL: http://dx.doi.org/10.1088/0954-3899/43/2/023001.

[211]   N. Kidonakis, *Next-to-next-to-next-to-leading-order soft-gluon corrections in
        hard-scattering processes near threshold*, Physical Review D **73** (2006),
        ISSN: 1550-2368, URL: http://dx.doi.org/10.1103/PhysRevD.73.034001.

[212]   N. Kidonakis, *Next-to-next-to-leading logarithm resummation for s-channel single top
        quark production*, Physical Review D **81** (2010), ISSN: 1550-2368,
        URL: http://dx.doi.org/10.1103/PhysRevD.81.054028.

[213]   E. Re, *Single-top Wt-channel production matched with parton showers using the
        POWHEG method*, The European Physical Journal C **71** (2011), ISSN: 1434-6052,
        URL: http://dx.doi.org/10.1140/epjc/s10052-011-1547-z.

[214]   T. Gleisberg et al., *Event generation with SHERPA 1.1*,
        Journal of High Energy Physics **2009** (2009) 007,
        URL: https://dx.doi.org/10.1088/1126-6708/2009/02/007.

[215]   J. Butterworth et al.,
        Single Boson and Diboson Production Cross Sections in pp Collisions at $\sqrt{s} = 7$ TeV,
        tech. rep., CERN, 2010, URL: https://cds.cern.ch/record/1287902.

[216]   J. M. Campbell and R. K. Ellis,
        Update on vector boson pair production at hadron colliders,
        Physical Review D **60** (1999), ISSN: 1089-4918,
        URL: http://dx.doi.org/10.1103/PhysRevD.60.113006.

[217] ATLAS Collaboration, *Tools for estimating fake/non-prompt lepton backgrounds with the ATLAS detector at the LHC*, 2022,
URL: https://doi.org/10.48550/arXiv.2211.16178.

[218] J. H. Kuhn, A. Scharf and P. Uwer,
Electroweak corrections to top-quark pair production in quark-antiquark annihilation,
Eur. Phys. J. C **45** (2006) 139,
URL: https://doi.org/10.48550/arXiv.hep-ph/0508092.

[219] J. H. Kuhn, A. Scharf and P. Uwer,
Electroweak effects in top-quark pair production at hadron colliders,
Eur. Phys. J. C **51** (2007) 37,
URL: https://doi.org/10.48550/arXiv.hep-ph/0610335.

[220] Y. Sumino and H. Yokoya,
Bound-state effects on kinematical distributions of top quarks at hadron colliders,
Journal of High Energy Physics **2010** (2010), ISSN: 1029-8479,
URL: http://dx.doi.org/10.1007/JHEP09(2010)034.

[221] W.-L. Ju et al., *Top quark pair production near threshold: single/double distributions and mass determination*, Journal of High Energy Physics **2020** (2020), ISSN: 1029-8479,
URL: http://dx.doi.org/10.1007/JHEP06(2020)158.

[222] L. Lista, *Statistical Methods for Data Analysis*, 3rd ed., Springer Cham, 2023,
URL: https://doi.org/10.1007/978-3-031-19934-9.

[223] G. Cowan, *Statistical data analysis*, Oxford University Press, USA, 1998.

[224] K. Cranmer, G. Lewis, L. Moneta, A. Shibata and W. Verkerke,
HistFactory: A tool for creating statistical models for use with RooFit and RooStats,
(2012), URL: https://cds.cern.ch/record/1456844.

[225] W. Verkerke and D. Kirkby, *The RooFit toolkit for data modeling*, 2003,
URL: https://doi.org/10.48550/arXiv.physics/0306116.

[226] L. Moneta et al., *The RooStats Project*, 2011,
URL: https://doi.org/10.48550/arXiv.1009.1003.

[227] F. James,
MINUIT Function Minimization and Error Analysis: Reference Manual Version 94.1,
(1994), URL: https://inspirehep.net/literature/1258343.

[228] Marshall, Z. and the ATLAS Collaboration,
Simulation of Pile-up in the ATLAS Experiment,
Journal of Physics: Conference Series **513** (2014) 022024,
URL: https://dx.doi.org/10.1088/1742-6596/513/2/022024.

[229] ATLAS Collaboration, *Tagging and suppression of pileup jets with the ATLAS detector*,
tech. rep., 2014, URL: https://cds.cern.ch/record/1700870.

[230] ATLAS Collaboration, *Electron and photon energy calibration with the ATLAS detector using data collected in 2015 at $\sqrt{s} = 13$ TeV*, tech. rep., CERN, 2016,
URL: https://cds.cern.ch/record/2203514.

[231] ATLAS Collaboration, *ATLAS b-jet identification performance and efficiency measurement with $t\bar{t}$ events in pp collisions at $\sqrt{s} = 13$ TeV*,
The European Physical Journal C **79** (2019) 970,
URL: %7Bhttps://doi.org/10.1140/epjc/s10052-019-7450-8%7D.

[232] ATLAS Collaboration,
E_T^{miss} performance in the ATLAS detector using 2015-2016 LHC p-p collisions,
tech. rep., CERN, 2018, URL: https://cds.cern.ch/record/2625233.

[233] M. Botje et al., *The PDF4LHC Working Group Interim Recommendations*, 2011,
URL: https://doi.org/10.48550/arXiv.1101.0538.

[234] A. Ghosh and B. Nachman, *A cautionary tale of decorrelating theory uncertainties*,
The European Physical Journal C **82** (2022) 46,
URL: https://doi.org/10.1140/epjc/s10052-022-10012-w.

[235] I. Nitsche, *Search for $t\bar{t}H$ and tH production with $H \rightarrow \gamma\gamma$ at $\sqrt{s} = 13$ TeV with the ATLAS experiment*, 2017, URL: https://doi.org/10.48550/arXiv.1711.08211.

[236] CMS Collaboration, *Search for standard model production of four top quarks with same-sign and multilepton final states in proton–proton collisions at $\sqrt{s} = 13$ TeV*,
The European Physical Journal C **78** (2018) 140,
URL: https://doi.org/10.1140/epjc/s10052-018-5607-5.

[237] CERN, LHC Higgs Cross Section Working Group,
Handbook of LHC Higgs Cross Sections: 4. Deciphering the Nature of the Higgs Sector,
CERN Yellow Reports: Monographs, 2017,
URL: https://doi.org/10.23731/CYRM-2017-002.

[238] CERN, LHC Higgs Cross Section Working Group,
Handbook of LHC Higgs Cross Sections: 1. Inclusive Observables, 2011,
URL: http://cds.cern.ch/record/1318996.

[239] CERN, LHC Higgs Cross Section Working Group,
Handbook of LHC Higgs Cross Sections: 2. Differential Distributions, 2011,
URL: https://doi.org/10.5170/CERN-2012-002.

List of Figures

List of Tables